UNIVERSITY OF THE WITWATERSRAND

OPTO-ELECTRICAL CHARACTERISATION OF CARBON-BASED THIN FILM SOLAR CELLS OF EXCITONIC DESCENT IN BULK HETEROJUNCTION ARCHITECTURE

LORDWELL JHAMBA

A thesis submitted to the Faculty of Science, University of the Witwatersrand, Johannesburg, in fulfilment of the requirements for the degree of Doctor of Philosophy.

Johannesburg, September, 2017.

Declaration

I declare that this Thesis is my own, unaided work. It is being submitted for the Degree of Doctor of Philosophy, in the Faculty of Sciences, at the University of the Witwatersrand, Johannesburg. It has not been submitted before for any degree or examination at any other University.

_____

(Signature of candidate)

_____day of _____20_____at_____

Abstract

Organic photovoltaic cells (OPVCs) continue to be intensively investigated due to their low cost and high utility potential. However, their low power conversion efficiency (PCE) has limited their full commercialization. The efficiency of the OPVCs is dependent on charge injection mechanisms, morphology and their underlying kinetics and energetics. Understanding the mechanisms that influence the efficiency of conjugated polymer solar cells is therefore pivotal to the enhancement of the devices' performance and the implementation of low priced fabrication technologies. In this regard, we investigated the dependence of the efficiency of organic solar cells on light intensity (I) using thin films of P3HT:PCBM blends, sandwiched between ITO/PEDOT:PSS and Al electrodes, the assembly of which was subjected to differing illumination intensities. Since charge transport through interfaces of such devices depends on charge carrier injection mechanisms, charge injection mechanisms at metal-organic active layer (here-in referred to as 'metal-active layer') interfaces in the devices were studied under changing external voltage bias. Use was made of the Richardson-Schottky (R-S) thermionic emission currents and those due to Fowler-Nordheim (FN) tunneling in generating complete J(V) curves which were compared with those obtained through combined graphical representations of the variation of open circuit voltage (V_{oc}) and efficiency (η) with light intensity. This led to the findings that under forward bias, the metal- active layer junction of an organic solar cell becomes ohmic after a certain threshold electrical field ($E_{thresh\ tunn}$) associated with quantum mechanical tunneling of charge carriers through the device's respective interfaces. Furthermore, we found that the open circuit voltage at which efficiency starts to decrease ($V_{oc\ thresh\ eff.\ decay}$) approximates in magnitude the internal threshold open circuit voltage ($V_{oc\ thresh\ tunn}$) at which FN quantum mechanical tunneling starts within the device at the electrode (a metal)- active layer interface.

Explanatory findings were that for photoactive P3HT:PCBM composite devices, increasing white light intensity incident on them increases the photogenerated open circuit voltages that increasingly bias them with voltages, which with effect from the thresholds due to opto-electrical mechanisms at the devices' metal-active layer interfaces, are sufficient to greatly increase the dark currents. The increased dark current reduces the short circuit current density significantly, which in turn inflicts a likewise decrease in the power conversion efficiency of the devices.

The theme of the next set of investigations was on the characteristic changes in the opto-electrical properties of the 1:1 blend of P3HT:PCBM with thickness of the active layer in ITO/PEDOT:PSS/P3HT:PCBM/Al solar cells, with intentions of finding out their effect on the threshold voltage at which efficiency starts to decrease ($V_{threshold\ eff\ decay}$) and also for purposes of optimizing the thickness of the active layer. To obtain different active layer thicknesses (ALTs), each sample was cast at different spin-coat speeds. The thicknesses determined by surface profilometer through variation of spin-coating speeds were 61.5, 69.4, 77.1 and 84.5 nm. Whilst this study's empirical results demonstrated optimal performance at approximately 77.1 nm active layer thickness, the overall findings have been that the existence of a static universal optimum active layer thickness is not practical. Such an optimum rather exhibits contextual dependence.

Annealing investigations revolved around attempts to empirically broaden and deepen the presently scarce understanding of the fundamental mechanisms defining thermal annealing process in conjugated polymers. To achieve this, we studied the opto-electrical effects of post-fabrication thermal annealing of bulk heterojunction ITO/PEDOT:PSS/P3HT:PCBM/AL solar cells at different heat treatment temperatures in the range 65 – 180 °C. The photoactive P3HT:PCBM layer was cast in air. The effect of air exposure has been found to chemically dope the polymer. Dedoping brought in by thermal annealing has been demonstrated to be responsible for the aggravated drop of efficiency. Summary findings lead to the generalisation that annealing of polymers is a two-step process, the first of which causes a decrease in conductivity, followed by its increase. Although impurity dedoping decreases 'under dark' current density in certain regions of the active P3HT:PCBM composite layer during annealing, it has beneficial aftermaths, some of which surface upon illumination of the P3HT:PCBM-based solar cell. When illuminated, photogenerated current density in the illuminated device immediately increases. This happens so, because of less electron capture and immobilization during illumination of the annealed device. Morphologically, thermal annealing has been found to enhance the formation of the deeply quenched bicontinuous network at the nanoscale between P3HT and PCBM, leading to high efficiency devices. We propose that the beneficial structure formation in P3HT:PCBM blends, is initiated by the crystallization of P3HT as it segregates PCBM, possibly to the amorphous P3HT. Thermal annealing renders significant enhancement in Jsc, Voc and FF of the annealed device. The optical absorbance was found to increase with increase in annealing temperature.

In unison with nature: To my wife Gladys, my daughter Norah and my sons Leonel Maropafadzo and Russel Tawedzegwa

Acknowledgements

This study would not be complete without me expressing my gratitude and indebtedness to many who contributed either directly or indirectly to its completeness. I am particularly indebted to my supervisor Dr Daniel Wamwangi who diligently did the arduous tasks of supervising my work every now and then. It is through his competent advices, suggestions, constructive criticism, patience, encouragement and outstanding scholarly tact both during the experimental and writing periods that this study owes success. Through this section, I particularly register my heartfelt gratitude to him and through him, I extend my thank you to the University of the Witwatersrand (Wits), Faculty of Science, the School of Physics and Material Physics Research Institute, for the provision of a very enabling environment to conduct this work. To Dr Zivayi Chiguvare (my former co-supervisor in the School of Physics at Wits) who introduced me to the field of study, suggested the topic and guided me immensely during the time he was in the school and even after he had left, I take this opportunity to thank him so much. My heartfelt thanks further goes to Prof Neil Coville and Prof Nosipho Moloto for allowing and arranging for me to do some of the experiments and talks on my results in the School of Chemistry. To the University of Venda (my university), I thank you immensely for providing me with very helpful financial support through the Research Department and further register my indebtedness for the moral support, encouragement and many times affording me time to be away from the university carrying out measurements and compilations at Wits.

To the growing photovoltaic group at Wits, in particular Ranganathan Kamalakannan, Francis Otieno and Lesias Kotane, I thank you greatly for at times working together to trace and solve equipment affiliated problems whenever they arose in the laboratories. I also owe you thanks for the motivating discussions in our field, encouragement and patience, especially in laboratory organisations, where we had to give each other chance to conduct some of the experiments. To many colleagues in the Wits Schools of Physics and Chemistry, in particular: George Bepete, Ibrahim Usman, George Chimowa, Isaac Motochi, Jonah Kuria, Ross McIntosh and Siphephile Ncube, I thank you all for the great support and help in many different ways.

To my nuclear and extended family, I say, “Thank you utmost for the encouragement, patience, tolerance and endurance during those long periods of my absence from home or no sleep while home, over something that at times seemed never to be achieved and end.”

Contents

Chapters

List of Figures

List of Tables

Nomenclature and Symbols

BHJ	Bulk heterojunction
AFM	Atomic Force Microscope
ϕ_B	Potential barrier
ϕ_{Be}	Electron blocking Schottky barrier,
ϕ_{Bh}	Hole blocking Schottky barrier,
E_F	Fermi level
C_n	Electron capture rate constant
ϕ_s	Work function
PCE	Power conversion efficiency
FB	Forward bias
RB	Reverse bias
RS	Richardson-Schottky
FN	Fowler-Nordheim
SCLC	Space charge limited current
OSC	Organic solar cells
MS	Metal-semiconductor
TFSCLC	Trap free space charge limited current
LUMO	Lowest unoccupied molecular orbital
HOMO	Highest occupied molecular orbital
E_{Dn}	Demarcation level for electron traps
CT	Charge transfer
HH	Head-to-head
D-A	Donor Acceptor

R_S	Series resistance
R_{SH}	Shunt resistance

Chapter 1

Introduction

1.1 Motivational background to the problem

Central to all development is energy. However, the disturbing part is that most of the current energy resources are fossil fuels, whose recoverable amount is estimated to last less than 150 years.[1-3] Furthermore, burning fuels for energy generation has negative environmental impacts. The public, on the other hand, generally fears nuclear energy, because the risk of hazardous emissions from radioactive sources is high. Life threatening manifestations such as acidification of the water cycle and ozone layer depletion (greenhouse effect) are on the increase, mainly because of continued and increased fossil fuel usage. At present, only one out of four of the inhabitants of this planet has access to electricity.[4] Therefore, the challenge now is to identify and develop sustainable alternatives, in the form of a secure 'energy generation mix' to meet the increasing energy demand. Green energy research, which is broadening, is good enough assurance that the bigger portion of the 'mix' option to fill the gap aptly has to increasingly come from renewable energy sources. Renewable energy based technologies encompass solar systems (photovoltaic and solar thermal), micro-hydro power plants, wind energy systems like wind mills (grist mills and wind pumps) and wind turbine systems for electricity generation, biomass/biogas plants, geothermal plants and oceanic systems (wave and tidal).

Due to the abundance of solar energy, the photovoltaic aspect becomes even more promising, hence the need for informed and continual developments of its technology and for casting the net wide, because the resource is unlimited. Therefore, the approach to efficiently utilize the clean and unlimited resource of energy from the sun remains a challenge. In this regard, organic solar cells (OSCs) are being pursued with much anticipation of them viably complementing inorganic (for example, silicon) solar cells, which dominate today's market at inhibitive costs. Since organic semiconductors allow a higher degree of disorder, they are cheaper and easier to process. The other advantage of organic solar cells over their inorganic counterparts is that they can be fabricated at low temperatures, whereas the latter often require temperatures exceeding $1000^{o}C$ and a clean room environment. Furthermore, organic semiconductors can be processed from solution by printing or spin coating at room temperature.

However, practical utilization of OSCs is still shrouded in many technological imperfections which account for their very low power conversion efficiency (PCE), inferior stability under ambient operating conditions and lack of processing technologies for mass production. The problem seems to be two-fold:

- lack of a clear understanding of the physics regarding the morphology and operation of OSCs
- inadequate knowledge of the proper materials of choice, coupled with their optimal configuration.

This has been the motivation for this research undertaking, which seeks to contribute towards the understanding of the operation of organic conjugated polymer solar cells under different conditions, for improvement of their efficiency and stability. Hence, this study seeks to explore the inclusion of low dimensional carbon-based materials in these solar cells, namely: poly (3-hexylthiophene 2,5 diyl) (P3HT), [6,6]-phenyl-C61 butyric acid methyl ester (PCBM) and poly(3,4-ethylenedioxythiophene)-polysytrenesulphonate (PEDOT:PSS).

Since the selected materials exhibit outstanding opto-electronic properties, a study of their behaviour under various combinations and conditions will most likely fill the knowledge gap and result in improved efficiency and stability of organic solar cells. It is against this background that we formulate and investigate the following statements of the problem.

1.2 Statements of the problem

Due to the need for an empirical and systematic study of the functioning of organic solar cells, the following statements of the problem direct the problematic pathways through which the present study is centred:

- Effect of charge injection mechanisms at metal-polymer interfaces on the efficiency of conjugated polymer-fullerene blend devices. Specifically, we seek to make a contribution in bringing to light, fundamental interface physics accounting for the observed decrease in the efficiency of organic solar cells at high incident light intensity and extend our investigations to finding out how the observed open circuit voltage (V_{oc}) $_{\text{threshold efficiency decay}}$ is quantitatively linked to the device's internal voltage regimes at the metal-organic active layer junctions (herein referred to as 'metal-active layer junctions/interfaces').

- Determination of the effect of active layer thickness on the opto-electrical characterisation of P3HT:PCBM based solar cells for performance optimisation endeavours and response of $V_{oc\ threshold\ efficiency\ decay}$ to variation in active layer thickness.
- Conduction of in-depth study of mechanisms involved in post-fabrication thermal annealing at different temperatures in solar cells based on polymer-fullerene blend and the influence of the same (annealing) on the opto-electrical behaviour of the devices. The problem is broadened to encompass heat treatment temperature optimization.

1.3 Hypothesis

From a holistic perspective, this research hypothesises that viable optimal power conversion efficiency in organic solar cells can be attained through a clearer understanding of the physics underpinning opto-electronic behaviour of the carbon-based polymer-fullerene solar cells and such understanding can be achieved through opto-electrical characterisation of low-dimensional carbon-based solar cells. The characterisation enables in-depth study of the fundamentals directing stimulus-response mechanisms ascribed to the excitonic solar cells. This enriched understanding, achieved through such empirical and systematic investigation into the operation of the photoactive devices, leads to improved device architecture and performance.

1.4 Aims and Objectives

1.4.1 Aims

The aim of this research is to gain insight into the fundamental issues regarding the fabrication, surface morphology, operation and opto-electronic behaviour of low-dimensional carbon-based conjugated polymer devices, in particular the organic solar cell, the knowledge of which will contribute towards the understanding of the bulk-heterojunction concept in order to improve the performance, stability and life time of the fabricated bulk-heterojunction organic solar cells. Such devices, which are based on a phase-separated mixture of donor and acceptor materials, have the potential to provide lightweight, flexible, inexpensive and efficient solar cells.

1.4.2 Objectives

1. To validate and check the reliability of the methods and instrument calibrations used to fabricate and opto-electrically characterise polymer-fullerene photovoltaic devices by developing and characterising bulk heterojunction organic solar cells based on the polymer regioregular P3HT and the soluble fullerene derivative PCBM as detailed in the methodologies section.

2. To develop **metal / organic active layer / metal** OSCs of the form: **Electrode** (ITO/PEDOT:PSS) / **Active bulk heterojunction polymer-fullerene layer** (P3HT:PCBM) / **Electrode** (Al) and characterise them to gain insight into charge injection mechanisms at metal-active layer (polymer/fullerene) interfaces in the dark and under illumination, the knowledge of which is applied to demonstrate and explain the negative correlation between organic solar cell efficiency and increase in light intensity.

3. To fabricate and conduct opto-electronic characterisation of bulk heterojunction organic solar cell devices of the form: ITO/PEDOT:PSS/P3HT:PCBM/Al, having different active layer thicknesses and use them in determining the effect of active layer thickness on the opto-electrical behaviour and threshold open circuit voltages of such devices.

4. To investigate the effect of post-fabrication thermal annealing processes at different temperatures in ITO/PEDOT:PSS/P3HT:PCBM/Al devices through the conduction of opto-electronic characterization to gain insight into the thermal annealing mechanisms in the devices as well as the behaviour changes due to heat treatments at different temperatures.

5. To conduct atomic force microscope (AFM) imaging and study the obtained images for purposes of gaining insight into the nanoscale morphological changes in the devices: (i) due to different active layer thicknesses and (ii) due to post-fabrication thermal annealing at different temperatures.

1.5 Challenges

There are three main ones:

1.5.1 Power Conversion Efficiencies

First is the crucial efficiency value, in which OSCs are still inferior to all inorganic counterparts. Fortunately, one major advantage of using semiconducting conjugated polymers is that there are endless combinations that could possibly be used as potential photoactive layers.[5-6] If properly engineered, these semiconducting polymers can fine tune their properties such as band gap and charge mobility, which in turn have a bearing on absorption and efficiency.[7]

1.5.2 Device stability

One of the greatest obstacles that must be overcome before organic photovoltaics become commercially viable is the inability to produce stable solar cells with long life times. Device stability under ambient operating conditions is problematic for many thin film solar cells (organic and inorganic alike). The manufacturers of commercial crystalline silicon solar cells usually assure a 25-year lifetime warranty. However, so far there are few OSC devices that can pass a 1000-hour test in damp heat (85 °C and 85% RH) with < 10% degradation of PCE.[8]

1.5.3 Processing technologies for mass production

Another challenge for OPVs is that efficiencies decrease as the size of the cell increases. The record holding Konarka cell is a small device (1 cm^2), as are all organic solar cells with high efficiencies. Increasing size of the cell results in higher sheet resistivity and greater defects in the organic films.[9] State-of-the-art OSCs with high efficiencies are usually made in research laboratories. These champion cells usually have very small active areas (less than 1 cm^2) and are typically fabricated by multiple steps utilizing many different processing techniques.

1.6 Scope

This section defines the scope of the dissertation through the provision of summary outlines of the concerns of each chapter of the write-up.

Chapter 2 identifies, explains and reviews fundamental theory prerequisite to an informed undertaking of this study. Underlying attributes of semiconductors, the p-n junction theory, band theory, as well as other core concepts like electrical contacts, Fermi-levels, potential barriers and electric conduction, just to mention a few, are treated via illustrations and explanations tailored to make understanding of the concepts easy without compromising detail. Knowledge gaps necessitating and justifying the present study are identified. The origin of semiconductor behaviour in carbon-based polymers is extensively discussed along the lines of atomic hybridization for purposes of elucidating such core concepts as morphology, conjugation and opto-electrical characteristics of conjugated polymers, leading to charge carrier generation and conduction mechanisms in polymers. In elucidating charge conduction in polymer-fullerene based solar cells, charge injection mechanisms at metal-polymer interfaces and current limiting mechanisms ascribed to charge flow across electrical contacts and in the bulk are discussed. Furthermore, in-depth considerations are made about surface states, charge carrier mobility, traps and recombinations. Models which bring to light how charge carriers pass metal-active layer interfaces and the nature of their subsequent diffusion in the bulk are brought to the fore and explained for use in the experimental analysis. Of these models, the main ones are the Richardson-Schottky (RS), Fowler-Nordheim (FN) and space charge limited current (SCLC).

Chapter 3 explores and explains underlying physical principles and attributes of solar cells based on conjugated polymers. Included are descriptions of such phenomena as built-in electric fields, singlet and triplet states. These are followed by elaborated step by step illustrations and explanations of competing mechanisms of photon-to-electron conversion processes in polymer-fullerene bulk heterojunction solar cells. The chapter extends to illustrate and explain charge generation and the associated $J(V)$ characteristics. Solar cell figures of merit are also discussed in the chapter.

Chapter 4 outlines the materials and methods used for the fabrication of metal-semiconductor (MS) interfaces and organic solar cells (OSCs). The main experimental materials were ITO, PEDOT:PSS, P3HT, PCBM, Al and chlorobenzene which was the solvent . Each of the materials is described in terms of its structural formula and properties. The other section of Chapter 4 gives a description of how the experimental organic solar cell was generally fabricated. Modifications

if any, to suit requirements of a specific investigation are then stated. The chapter also presents illustrative descriptions and analyses of the generated interfaces.

Chapters 5, 6 and 7 form the mainstream experimental chapters in which the investigation themes are distributed as follows:

- Chapter 5 reports on investigations into the effect of charge injection mechanisms at metal-active layer interface on the efficiency of thin-film photoactive P3HT:PCBM blend devices subjected to increasing incident light intensity. Associated results, analyses, findings and generalisations are presented. Link of $V_{\text{oc threshold efficiency decay}}$ to charge injection (flow) mechanisms at metal–active layer interfaces was determined and explained. The linked behaviour was found to account for the observed decrease in efficiency of organic solar cell devices as incident light intensity increases.
- The theme in Chapter 6 is - Opto-electrical performance analysis of nano-composited P3HT:PCBM bulk heterojunction photoactive solar cells of differing active layer thicknesses for optimization and nanoscale behaviour analyses. Under this theme photoluminescence and extinction coefficient analyses as well as morphological modifications due to active film thickness variations are conducted. The effect of active layer thickness on charge injection mechanisms at electrical contacts is examined in relation to RS thermionic emission; FN field emission and threshold open circuit voltages. Charge conduction in the bulk is also investigated to a great extent for the different regions and active layer thickness (ALTs). Mobility values are determined in trap free space charge limited current (TFSCLC) regions of the different film thicknesses and are compared.
- In Chapter 7, the influence of post fabrication thermal annealing on the opto-electrical characteristics of P3HT:PCBM based solar cells is investigated for different annealing temperatures in the range 65°C–180°C. Optical absorption properties for different annealing temperatures are studied alongside morphological modifications in the thin films as the heat treatment changes. Descriptions of experiments conducted to determine dark and illuminated J(V) characteristics of the polymer-fullerene solar cells are laid down in the chapter.

  Chapter 8 presents the Conclusions and Recommendations.

Chapter 2

Review of fundamental theory

2.1 Underlying Attributes of Inorganic/Organic Semiconductors

Semiconductors are materials whose conductivity (σ) at 300 K is intermediate between that of most conductors (generally metals) and insulators (such as, ceramics), either due to addition of an impurity (doping) or because of temperature effects. Quantitatively, their electrical conductivities range from 10^3 to 10^{-9} $(\Omega cm)^{-1}$, as compared to a maximum conductivity of about 10^7 $(\Omega cm)^{-1}$ for good conductors and a minimum conductivity of 10^{-17} $(\Omega cm)^{-1}$ for good insulators. At room temperature (300 K), the conductivity of metals ranges from about 10^6 to 10^7 $(\Omega cm)^{-1}$, while for good dielectrics at room temperature $\sigma < 10^{-10} \rightarrow 10^{-12}$ $(\Omega cm)^{-1}$. In semiconductors, charge transport (which is characterised by the conductivity σ) is thermally activated according to the expression

$$\sigma = \sigma_0 \exp\left(\frac{\varepsilon_A}{k_B T}\right) = \sigma_0 \exp\left(\frac{E_g}{2k_B T}\right) \qquad (2.1)$$

where σ_0 is the proportionality factor, k_B is Boltzmann constant, ε_A is the activation energy for charge transport in intrinsic semiconductors and is related to the bandgap energy E_g by the relation $\varepsilon_A = E_g/2$. Equation (2.1) shows that the conductivity depends only on the semiconductor bandgap and the operating temperature T.

A semiconductor can be a pure element such as carbon, conjugated polymer, silicon, germanium or a compound such as gallium arsenide or cadmium selenide. At high temperatures, the conductivity of a semiconductor approaches that of a metal and at low temperatures it acts as an insulator. While the density of free electrons is of the same order of magnitude as the density of atoms in a conductor, in an insulator, the density of free electrons is negligible compared to the density of atoms. The ratio of free electron density per atom in insulators is less than 10^{-20}, but is greater than 10^{-20} in semiconductors.[10]

The incorporation of certain impurities (that is, donor and acceptor atoms collectively) in a semiconductor enhances its conductive properties. {This doping (replacing or adding of certain

donor or acceptor atoms to the semiconductor) process can produce more free electrons than holes or vice versa if a group V or III element is used as a dopant. The impurities either add free electrons or create holes (electron deficiencies) in the structures of the host substances. The doping is mostly in the order of 1 impurity per 10 million (or more) native atoms of the semiconductor.}

2.1.1 The p-n junction theory and its placement in photovoltaic effect

In a piece of semiconductor material, if half is doped by p-type impurity and the other half is doped by n-type impurity, a p-n junction is formed. The same happens if a p-doped semiconductor and an n-doped material are brought into intimate contact. The plane dividing the two zones is called the p-n junction. In the region adjacent to the junction, free electrons diffuse across the junction from the n-type to the p-type and by so doing, the donor ions become positively charged. As a result, a positive space charge or depletion region is formed on the n side of the junction. The free electrons that cross the junction fill in the holes of the negative acceptor ions. Therefore, a net negative charge is established on the p-side of the junction. This net negative charge on the p-side prevents further diffusion of electrons into the p-side. Similarly, the net positive charge on the n-side repels further hole migration from p-side to n-side. A barrier potential which prevents further migration of charge carriers is therefore set-up. As a result of the induced electric field across the depletion layer, an electrostatic built in potential difference V_j is established between the p and n regions. This built in potential (or contact potential) has been found to be given by

$$V_j = \frac{kT}{e} \ln\left(\frac{N_A N_D}{n_i^2} \right) \tag{2.2}$$

where, N_A is the acceptor density, N_D is the donor density, n_i is the intrinsic concentration, k is Boltzmann's constant, T is the thermodynamic temperature and e is the electronic charge.

2.2 Electronic Band Structure Concept → Band Theory

In this study, the term energy band (or simply band) is used to refer to the range of energies that an electron within the solid may have. The forbidden band (or band gap) describes the range of energies that an electron may not occupy. This electronic band structure concept stems from the

(solid state) band theory's examination of the eigenfunctions for an electron in a large periodic lattice of atoms or molecules.[11-13] The band theory is the result of a development of the Schrödinger equation and describes the energy of the electrons in a metal or solid.[14] The theory postulates that in organic materials, the electrons are located in well-defined energetic levels which form bands. An electron can be promoted towards other vacant levels upon external stimuli.[15] The highest occupied molecular orbital (HOMO) and the other occupied levels which are lower in energy are collectively named the valence band, because they hold the valence electrons. The lowest unoccupied molecular orbital (LUMO) and the empty continuum levels above it are collectively called the conduction band, because an electron energised to that band contributes to the electrical conductivity of the material. The band theory is therefore concerned with the description of a material's energetic structure. Based on this energetic structure, three different kinds of materials can be distinguished and these are: metals, semiconductors and insulators[14] (see Figure 2.2). These are explained in conjunction with the Fermi level in the next section.

Where appropriate, we shall use band diagrams to help explain the operation of our devices. Band diagrams (for example, Figures 2.1 – 2.5) are plot diagrams (not drawn to scale) of the principal energy levels (Fermi level and energy band edges in the neighbourhood) as a function of position in space, which may pass through many materials. To explain the local changes in the energy offset of the material's band structure due to accumulated charges near a junction, band bending illustrations shall be utilised. Band bending arises in conjunction with the electric field force. Knowledge of how energy bands will bend when two different types of materials are brought in contact is critical to understanding whether the junction will be rectifying (Schottky) or Ohmic. The extent of band bending depends on the relative Fermi levels and carrier concentrations of the materials forming the junction.

2.3 Electrical Contacts, Fermi Level, Work Functions, Potential Barriers and Electric Conduction

An electrical contact generally refers to a contact between a metal and a non-metallic material which may be an insulator or a semiconductor.[16] In this study, we shall delimit our investigation to the metal–semiconductor configuration. The role of an electrical contact is either to make possible or to impede charge carrier injection from a metal into an insulator or a semiconductor

or vice versa across the junction of the two concerned materials. A fundamental difference between a semiconductor and a metal is that the former houses both electrons and holes, whereas the latter has electrons only. As such, the conduction of electric current in metals is characterised by the drift of electrons driven by the application of a voltage source across the metal, whereas that in semiconductors is due to the simultaneous mobility of both electrons and holes without a powering voltage source. Furthermore, metals unlike semiconductors are characterised by an overlap of the valence and conduction bands, resulting in a higher charge carrier density.[17-18] One of the easily configured contacts between a metal and a non-metallic material is the contact between a metal and a vacuum. Figure 2.1 shows the corresponding energy band diagram. The work function, which is given by the difference between the Fermi energy and the vacuum level, consists of two parts, which are: the energy binding the electron and the energy needed to move the electron through an electrostatic double layer at the surface. The vacuum level is the energy of an electron at rest at a point infinitely far away from the metal.

A potential barrier is bound to build up at the metal - semiconductor interface. This arises, because when two materials with different Fermi levels are brought into contact, free net charge carriers will flow from one material into the other until the Fermi levels of the two materials are aligned. What it means is that at the achievement of this electrodynamic equilibrium status, the Fermi levels for electrons in both materials will be equal at the contact. Furthermore, the net flow of charge carriers accumulates a positive space charge on one side and a negative space charge on the other side of the junction, resulting in the establishment of an electric double layer called potential barrier. The potential across this barrier is termed the contact potential.[16] The double layer is significant in that it sets up an electric field which opposes and stops the net flow of charge carriers from one material to the other (although there will still be continued flow of free carriers thermodynamically in both directions under thermal equilibrium). An example of the electrical contact between a metal and a vacuum is shown in Figure 2.1. The Fermi level E_F basically refers to the electrochemical potential (or simply the chemical potential) at absolute zero temperature (0 K.).[16] It represents a reference electron energy level depicting a state of energy E_F whose probability to be occupied or to be vacant is half (50%). This can be deduced from an examination of the Fermi-Dirac distribution (equation) for the probability of a state of energy E to be occupied by an electron, which is,

$$f(E)=\frac{1}{e^{(E-E_F)/k_BT}+1}, \tag{2.3}$$

where $f(E)$ is the Fermi-Dirac (probability) distribution function, E_F is the Fermi level energy, k_B is the Boltzmann constant and T is the thermodynamic temperature. At $T \neq 0$ and $E = E_F$, $f(E)$ is found to be equal to half (1/2).

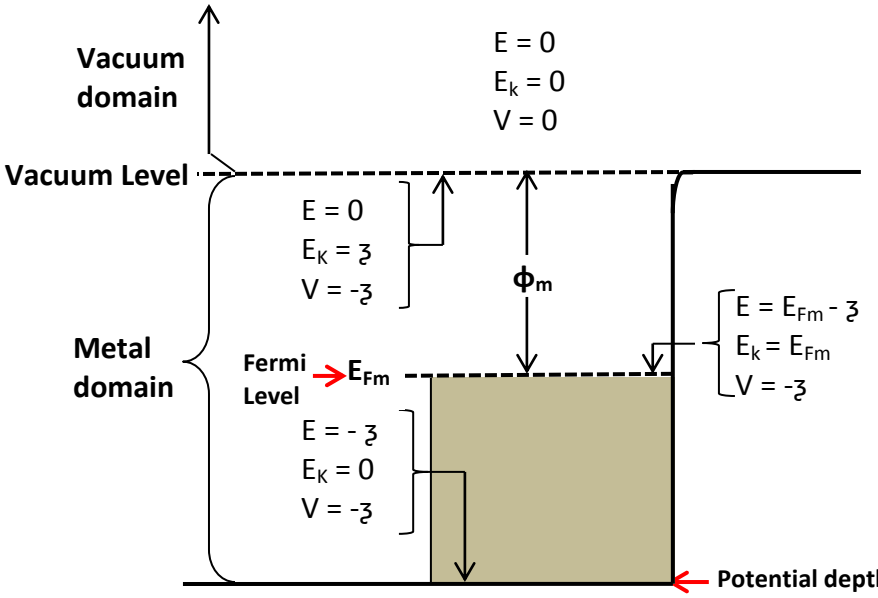

Figure 2.1 *Energy band diagram showing the electrical contact between a metal and a vacuum, as well as the associated Fermi level* E_{Fm} *and work function* ϕ_m *of a metal.* E_k *and V are the kinetic and potential energies, respectively of the electrons and* $ʒ$ *is the difference in potential energy of the electrons between the inside and the outside of the metal.* $ʒ$ *depends on the structure of the crystal and the condition of the surface*

Frequently though, the Fermi level is defined as the topmost energy level occupied by electrons at 0 K. In semiconductors this would correspond to the top of the valence band, which is in contrast with the electrochemical potential that certainly lies in the forbidden gap (Figure 2.2).

We suggest that the Fermi level can simply be considered as a hypothetical energy level of an electron which does not necessarily correspond to an actual energy level, but is a reference level necessary for providing information about whether states (if they exist between the valence band V_b maximum and the Fermi level) would be filled or not. The probability for a state (orbital) at

the level ΔE above E_F to be occupied by an electron would be equal to that at the level ΔE below E_F to be vacant. This would mean equal densities of conduction band electrons and free valence band holes. If the Fermi energy is exactly in the middle of the gap, electron density at the bottom of the conduction band would be the same as the hole density at the top of the valence band. If the Fermi level is biased toward the conduction band, the electron density at the bottom of the conduction band would be higher than the hole density at the top of the valence band.

In a nutshell, in any system, the density of free holes in the valence band and electrons in the conduction band defines the Fermi level.

In metals, the valence and conduction bands overlap and the Fermi level lies inside one of the bands. The existence of this valence – conduction bands overlap region in conductors, as illustrated in Figure 2.2(c), ensures that for metals, there is no energy gap to overcome for an electron in the valence band to pass to the conduction band. This allows electrons to be promoted to the conduction band without an additional source of energy and explains why metals are inhabited by quasi-free electrons in the conduction band and are very good conductors.

The poor conductivity of insulators is explained by their property of having an energetically forbidden gap (see Figure 2.2(a)) between the valence and conduction bands, which is so large (typically more than 4 eV) that it becomes very difficult to excite electrons towards the conduction band. The amount of energy required to overcome this forbidden energy gap is too high and would lead to degradation of the material.[16]

For semiconductors, there is a small energy gap between the valence and conduction bands. The states in the gap are not available to the electrons. Since this forbidden gap is so small for semiconductors, (Figure 2.2(b)) their properties lie between those of conductors and insulators, but unlike metals, semiconductors increase their conductivity with temperature, because the forbidden gap dwindles, leading to the birth and growth of the overlap between the two bands as the temperature T increases. Figure 2.2(b) also shows that for a semiconductor, the Fermi level lies in its forbidden band (mid-gap for the intrinsic semiconductor). This means that occupied and unoccupied states in its valence and conduction band respectively are energetically separated. In fact, the width of the separation (width measured in energy units) determines whether the material is a metal, semiconductor or insulator.

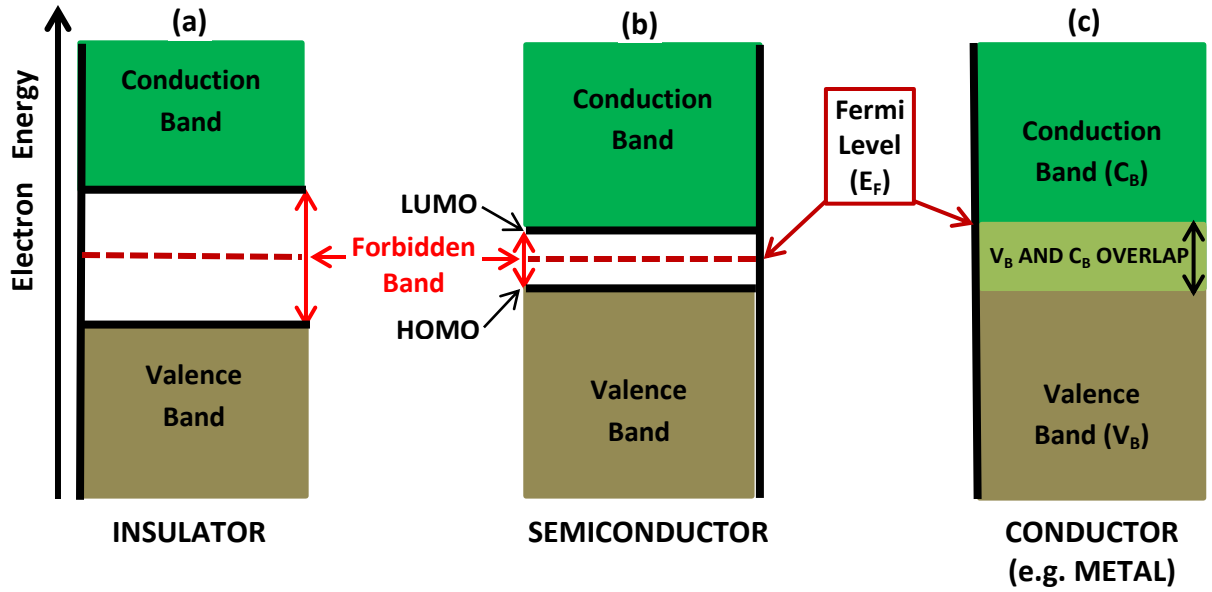

Figure 2.2 *Categorisation of solids on the basis of electronic energy bands and corresponding Fermi level E_F configurations*

If at room temperature range, the electrons in a pure semiconductor gain sufficient energy to overcome the forbidden band gap energy E_g, then the semiconductor is an intrinsic semiconductor. The smallness of the energetically forbidden gap in semiconductors allows excitation of electrons via thermal or light activation.

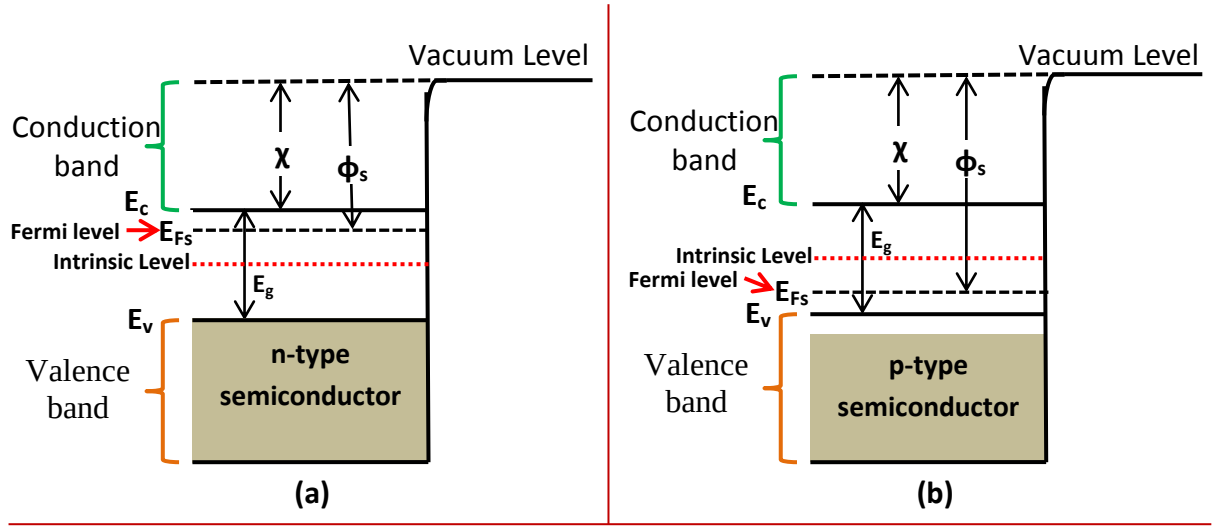

Figure 2.3 *Context of Fermi level E_{Fs}, work function ϕ_s and electron affinity χ for* (a) *n-type semiconductor and* (b) *p-type semiconductor relative to the energy bands*

An extrinsic semiconductor is a doped semiconductor. The dopant will be a specific impurity which significantly alters the electrical properties of the semiconductor and makes it suitable for optoelectronic applications (for example, diodes and transistors). The interesting peculiarity of a semiconductor is that its Fermi level can be shifted within the gap if it is either n-doped or p-doped (extrinsic semiconductor). As shown in Figure 2.3, for an n-doped semiconductor the Fermi level shifts to the region above the intrinsic level (nearer the conduction band) and for a p-doped semiconductor it shifts to below the intrinsic level (nearer the valence band). Impurity concentration (of which doping is part) as well as temperature and external pressure are amongst the key factors which determine the exact position of the Fermi level.

2.3.1 Electron emission from semiconductors

Conditions for electron emission from a semiconductor or insulator differ appreciably from those of metals. In semiconductors, there are no electrons at the Fermi level. As such, electrons which may be removed from the interior of a semiconductor must be either in the conduction band or in the valence band or in the impurity levels. After an electron has left the semiconductor, the remaining electrons in the semiconductor restore their statistical distribution.

If an electron in the conduction band receives energy greater than χ and leaves the semiconductor, its place is immediately taken by an electron either from the impurity levels or from the valence band.

2.4 Types of Electrical Contacts

2.4.1 Neutral Contact

A neutral contact is one at which the charge carrier concentration at the contact is equal to that in the bulk of the semiconductor. The regions adjacent to such a contact are electrically neutral. Neither space charge nor band bending will be existent within the semiconductor. This implies that both the conduction and valence band edges will be flat throughout to the interface. A neutral contact may arise when $\phi_m = \phi_s$, where ϕ_m and ϕ_s are the work functions of the metal and semiconductor, respectively. Such a contact is neutral because when the two surfaces are brought into contact, the probability for the electrons to flow from the metal to the semiconductor is

equal to the reverse direction flow probability. As such, there is no net flow of charge carriers; hence no space charge is formed near the interface.

It is also possible to establish a neutral contact when $\phi_m \neq \phi_s$ at low temperatures (due to low thermionic emission) or with an electron-trapping level at a sufficient distance above E_F (or a hole-trapping level below E_F) in wide band gap semiconductors.[19-20] The contact can be neutral because the trapped space charge in the traps will be too small to cause significant band bending under such conditions.

2.4.2 Blocking Contact

A blocking contact (sometimes referred to as a Schottky or rectifying contact) is one in which the semiconductor bulk can carry away more charge carriers than the contact can supply to the bulk. The current is then determined by the maximum rate at which the contact can supply carriers. Figure 2.4 shows the energy band diagram for an electron-blocking contact. Interesting features are the respective Fermi levels E_{Fm} and E_{Fs} as well as their alignment after contact, potential barrier ϕ_B (often called the Schottky barrier or simply the energy barrier) and band bending.

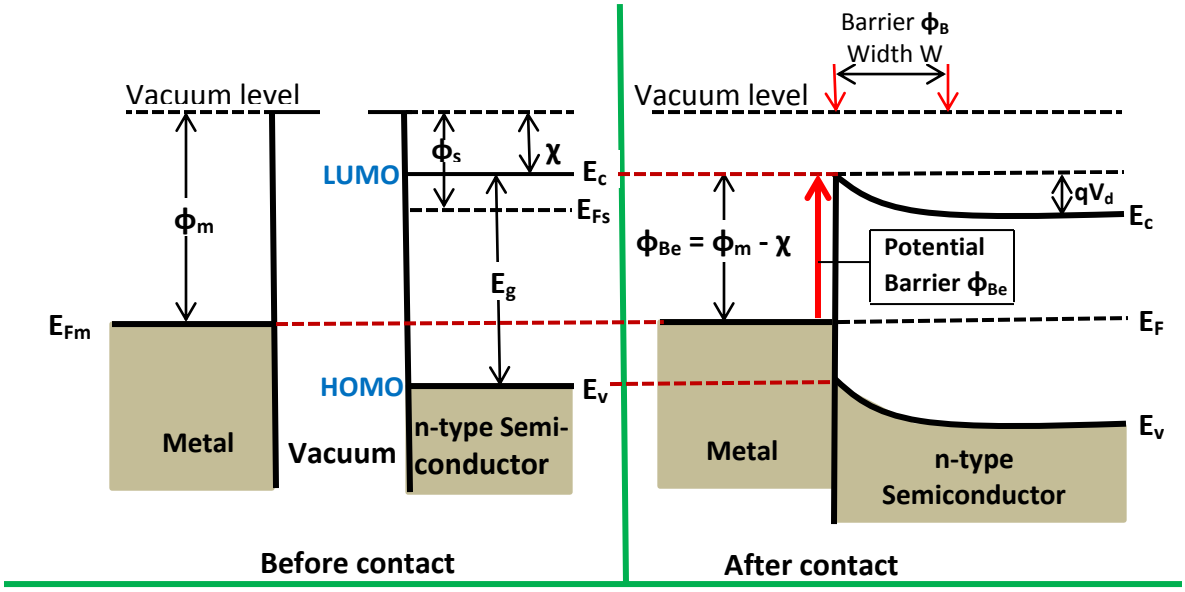

Figure 2.4 *Electron-blocking contact for condition* ($\phi_m > \phi_s$) → (*blocks electrons from metal from passing into the semiconductor*)

The potential barrier is given by the difference between the Fermi level E_{Fm} in the metal and the bottom of the conduction band in the semiconductor. With reference to Figure 2.4, a Schottky barrier is formed by an electron blocking contact for which $\phi_m > \phi_s$. Therefore, the condition for a contact to be blocking as seen by electrons from the metal is $\phi_m > \phi_s$ for a metal-n-type semiconductor. Under this condition, electrons will flow from the semiconductor to the metal leaving a positive space charge region (thus electron depletion region) in the semiconductor in which W is the width of the depletion region. ϕ_B is the height of the potential barrier which an electron in the metal has to surmount in order to pass into the semiconductor. Such a contact is referred to as a rectifying contact, because under forward bias, electrons can flow easily from the semiconductor to the metal, while under reverse bias the flow of electrons from the metal into the semiconductor is limited by the electrons available over the Schottky barrier, which block electrons in the metal from crossing over to the semiconductor and whose density is much smaller than that in the bulk of the semiconductor.

As for the metal-p-type semiconductor junction, the establishment of a hole blocking contact from the perspective of holes from the metal side (or electron blocking contact as seen by electrons from the semiconductor side) is subject to $\phi_m < \phi_s$.

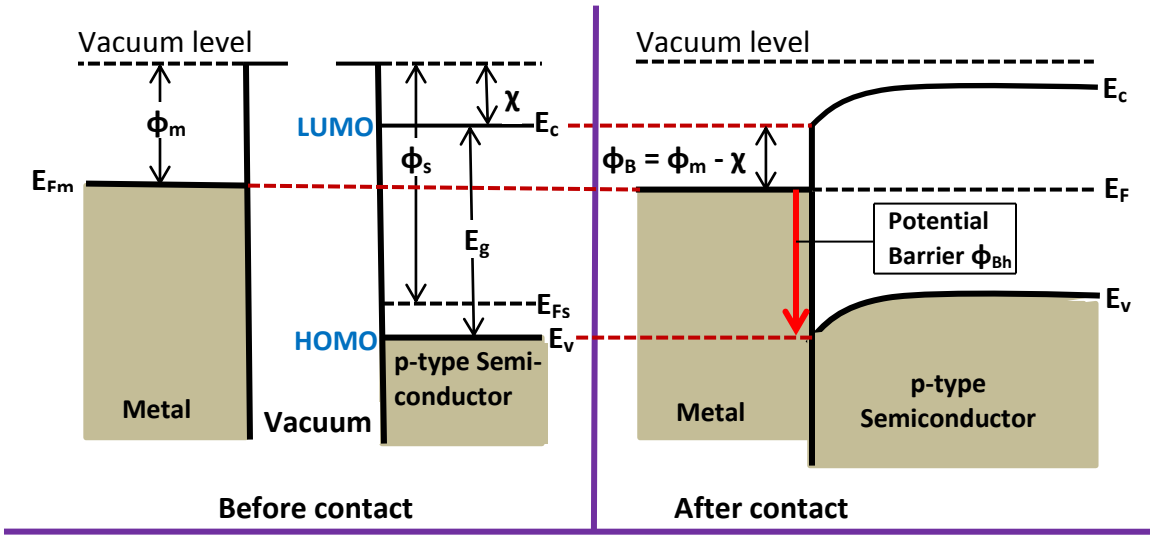

Figure 2.5 *Hole-blocking contact* ($\phi_m < \phi_s$) → (*blocks holes from metal from passing into the semiconductor*)

Under this contact, holes from the semiconductor side easily diffuse across the junction into the metal until the associated Fermi levels are aligned. This creates a depletion of holes in the p-type semiconductor (thus the potential barrier) which blocks holes from the metal side (Figure 2.5). Therefore a blocking contact can be considered as one which creates a charge depletion region extended from the interface to the inside of the semiconductor.

A necessary, but not sufficient condition for a contact to be blocking is that $\phi_B >> k_B T$. This shows that, with such a contact, thermionic emission from the metal tends to be saturated (i.e. screened) since negligible thermally generated current is conducted under reverse bias. There are two possible ways in which charge carriers can be injected from a metal electrode into a semiconductor across a blocking contact and these are thermionic emission and quantum mechanical tunneling. These will be discussed in Section 2.5.

Based on our discussion in this section and analyses of Figures 2.4 and 2.5, we can generalise that the height of a potential barrier is always given by the difference between the electrode (metal) work function and the corresponding transport levels of the polymer. It is always measured from the Fermi level of the metal (which is pinned and coincides with that of the semiconductor after contact) to the LUMO ($\mathbf{E_c}$ in Figure 2.4) of the polymer in the case of an electron blocking contact and to the HOMO ($\mathbf{E_v}$ in Figure 2.5) of the polymer in the case of a hole blocking contact.

Image force: The image force tends to attract the emitted electrons back to the metal, while the driving force due to the applied field tends to drive the emitted electrons away from the metal. The combination of the applied electric field and the image force (the so called Schottky effect) lowers the potential barrier.

2.4.3 Ohmic Contact

A contact between a metal and a semiconductor is classified as ohmic if its impedance in comparison with the series impedance of the bulk of the semiconductor is negligibly small. The implication is that the associated free charge density at and in the vicinity of the contact would be very much greater than that in the bulk of the semiconductor (for example, the thermally generated carriers in the bulk). Under such configuration, the contact may act as a reservoir of

carriers. The broader perspective would be to view an ohmic contact as one which creates a charge accumulation spanning from the interface to the inside of the semiconductor. However, the current-voltage relationship is non-linear at the contact.

Generally, the conduction is ohmic at low fields if the metal does not inject more carriers into the semiconductor than those thermally generated by the semiconductor, because excess charge carrier injection from the electrode results in predominance of the space charge effect in the semiconductor, thus instigating non-ohmic conduction.

There are two ways of making ohmic contacts. One way is to choose a metal of low work function such that $\phi_m < \phi_s$ (for metal-n-type semiconductor junction) for electron injection by diffusion from the metal to the semiconductor as illustrated in Figure 2.6. As a result, there is negative charge accumulation in the n-type semiconductor and no barrier forms.

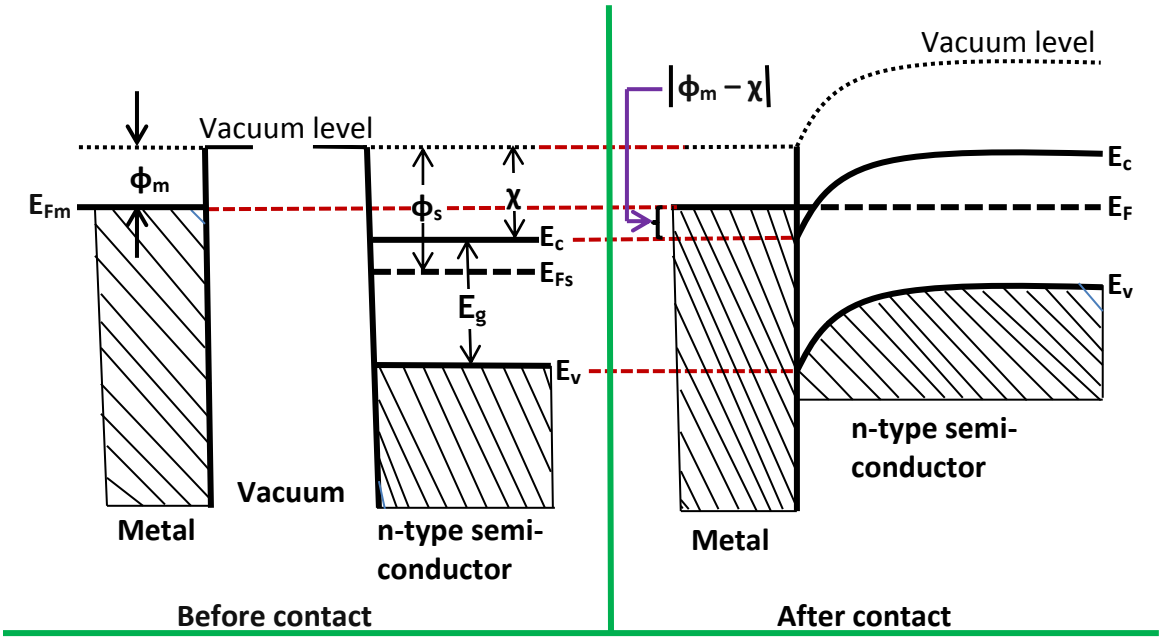

Figure 2.6 *Electron Ohmic contact*
($\phi_m < \phi_s$)

The alternative is to choose a metal of high work function such that $\phi_m > \phi_s$ (for metal-p-type semiconductor junction) for hole injection by diffusion from the metal to the p-type

semiconductor as illustrated in Figure 2.7. The mechanism is equivalent to electron diffusion from the p-type semiconductor to the metal, the end point of which is positive charge accumulation in the p-type semiconductor with no barrier formation.

Therefore an ohmic contact can be considered to be one which generates a charge accumulation region extended from the interface to the inside of the semiconductor.

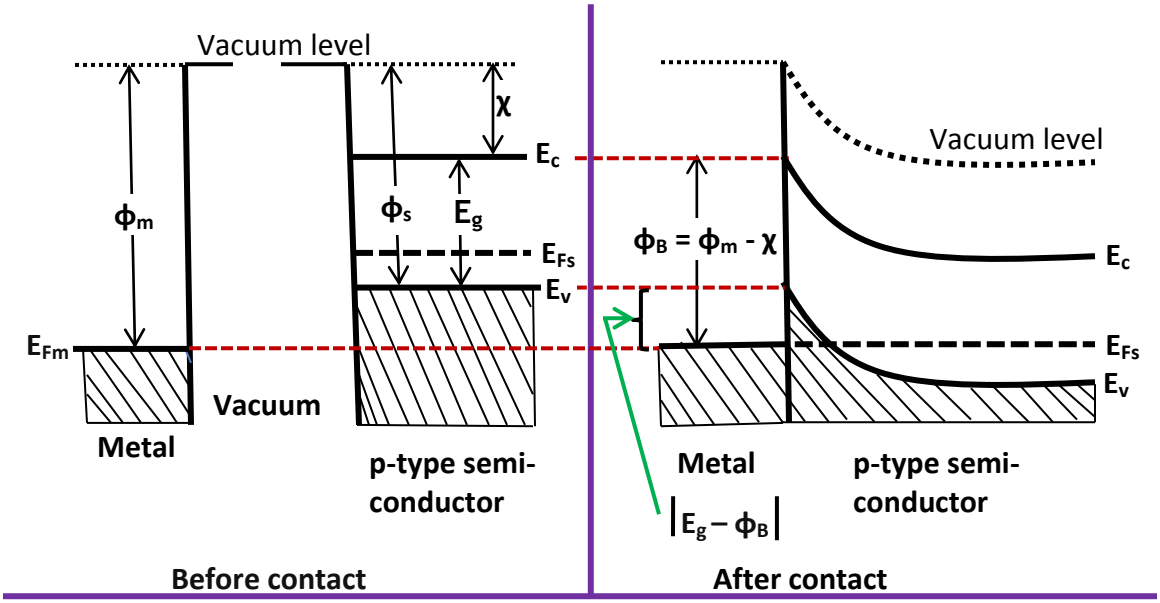

Figure 2.7 *Hole Ohmic contact* ($\phi_m > \phi_s$)

The second way of making an ohmic contact is to use a degenerate semiconductor (or dope the semiconductor surface heavily) near the contact to make the potential thin enough for efficient quantum mechanical tunneling.[16]

2.5 Surface States (at Junctions and Structural Imperfections/Defects)

Surface states (which basically are electronic states/orbitals found at the surface of materials) greatly affect the efficiency of carrier injection at the interface. Concerning a metal-semiconductor contact, in which the structures or interparticle distances of the intimate materials are different, localized surface states with energies lying in the forbidden energy gap may arise due to dangling bonds, H_2 terminated bonds or due to the interruption (or discontinuity) of the periodic lattice structure at the interface.[21] The sudden termination of the lattice of the solid crystal at its surface usually results in the distortion of the band structure near the surface and

causes the bending of energy bands in an attempt to bring the solid to an equilibrium state in which the Fermi level at the surface would be identical to that in the bulk.(Surface recombination minimises the internal energy.) In this regard, surface states can be generalized to partly emanate from the alluded discontinuities at the surface leading to the so-called 'Tamm states'.[22] which are associated with an asymmetric termination of the periodic potential and a large separation or weak interaction between surface atoms or molecules. Conversely, the discontinuities accounting for surface states may lead to the so called 'Shockley states'[23] which are associated with symmetrical termination of the periodic potential and a small separation or strong interaction between atoms or molecules. Furthermore, surface states partly blossom from foreign materials (impurities) adsorbed on the surface or flaws on the surface such as abrasions on the surface due to cutting, grinding, etching, polishing, defects/dislocations, etc. Such surface imperfections are connected to the development of dangling bonds at the surface. A dangling bond results from chemical binding at the surface of the material in a manner which creates a domain from which an electron normally participating in chemical binding in the solid has been removed in creating the surface [16]. Such a domain is the dangling bond. To exemplify a dangling bond, one can consider a four valence atom (for example, carbon) which at a given surface is bonded to two neighbours, leaving two of the four covalent bonds unsaturated. It will then be these two unsaturated bonds that will generally be referred to as dangling bonds and act as acceptors tending to capture electrons available in the vicinity.

2.6 Impediments/Hindrances to charge carrier mobility in the bulk

As long as the charge carrier injecting contact can provide a reservoir of carriers, the subsequent behaviour and fate of the injected carriers, which form the electric current, is controlled by the properties of the material in which the charge carriers are flowing. In the main, it will be the charge carrier mobility in the space inside the bulk (active material, which in this study is the polymer-fullerene bulk-heterojunction blend) that will determine the current.

2.6.1 Charge carrier mobility

Qualitatively, carrier mobility is concerned with how quickly a charge carrier can move through a given material under the pull by an applied electric field, specifically the carrier's average velocity (in cm/sec) per unit potential difference applied across one centimeter of the material

(volt/cm). Amongst the key factors which determine carrier mobility in organic semiconductors (or their blends, as in polymer-fullerene composites) are distribution of energies of the injected carriers, magnitude of the applied electric field, concentration of shortcomings/defects (for example, in-homogeneity of the blend and impurity concentrations, which account for the distribution of traps and recombination centres).

Some of the injected carriers in the material will either be temporarily captured at trapping centres (the trap and release mechanisms) or lost permanently through recombination centres. Since no perfect crystals exist, materials always contain localized states. Such localized states form the so called trapping and recombination centres. Low charge carrier mobility significantly lowers the efficiency of devices.

2.6.2 Traps

A trapping centre (or simply a trap) is any centre formed by a localized state, which is capable of capturing a free charge carrier and after a while this captured (or trapped) carrier has a greater probability of being thermally re-excited to the nearest allowed band to become a free carrier again than recombining with a carrier of opposite sign at the centre. The behaviour of traps can be categorized into three types, namely, Coulombic attractive centres, Coulombic neutral centres and Coulombic repulsive centres.[16] Based on this, a trap can be considered to be an empty entity with a certain charge, positive, neutral or negative when unoccupied. Those trapping centres which capture electrons only are called electron traps and those which capture holes only are hole traps. The occupancy (occupation period) or life time is determined by the thermal equilibrium interchange of the carriers of one particular sign between the centres and the nearest allowed band.[16]

Traps are created by all types of imperfections present in the material and since they may capture some of the injected carriers from (ohmic) contacts, they in a way control the carrier flow accounting for the J/V characteristics. Trapping can be viewed as a process of energy storage in the sense that it spatially localises electrons and holes at certain sites and by so doing hinders them from moving freely, thereby preventing them from contributing to electric current conduction. The magnitude of the trapping potential V_t determines the nature of the interaction (that is, whether long range or short range). We guess that for short range, it should likely be that

$V_t \geq k_B T$ and the charge will most likely be bound (or may tunnel). If $V_t < k_B T$, there should then be greater chances of the charge escaping thermionically.

Generally, the trap densities in solid materials range from about 10^{12} cm^{-3} in the highly pure single crystals to about 10^{19} cm^{-3} in the imperfect large band gap insulators [16]. We note that no consideration of the level (whether deep or shallow) distribution is explicit in the assertion. In organic crystals, two types of carrier trap distributions have been identified. One type is that of traps confined in discrete energy levels in the forbidden energy gap, as illustrated in Figure 2.8. The second type is that of traps with a quasi-continuous distribution of energy levels (normally following an exponential or Gaussian form) with a peak trap density near the band edges.[24-26] However, despite several investigations, no explicit information on the possible physical nature of traps has so far been provided.

The probability for a trap to capture an electron follows the Fermi-Dirac statistics

$$f_n(E) = \left[1 + g_n^{-1} \exp\left[\{(E - E_{Fn})\}\right] / kT\right]^{-1} \tag{2.4}$$

and that for a trap to capture a hole follows

$$f_p(E) = \left[1 + g_p \exp\left[\{(E_{Fp} - E)\}\right] / kT\right]^{-1} \tag{2.5}$$

where, $f_n(E)$ is the negative carrier (electron) Fermi-Dirac distribution function

$f_p(E)$ is the positive carrier (hole) Fermi-Dirac distribution function

g_n and g_p are the degeneracy factors of trap states for electrons and holes respectively

E is the energy level

E_{Fn} and E_{Fp} are the Quasi-Fermi levels for electrons and holes respectively

k is Boltzmann constant and T is the absolute temperature

Based on the energy levels for the traps, the traps can be classified into shallow and deep traps.[16] The electron capture rate, which refers to the rate at which electrons are captured from the conduction band is given by

$$\frac{dn}{dt} = -C_n n N_n \tag{2.6}$$

where, n is the free electron density in the conduction band, N_n is the density of empty electron traps and C_n is the electron capture rate constant (or electron capture coefficient)

2.6.3 Recombinations

A recombination centre is a centre which also captures a free carrier, but the captured carrier has a greater probability of recombining with a carrier of opposite sign, resulting in annihilation of both, than of being thermally re-excited to the nearest allowed band.[16] The recombination centres in which the localized states are normally empty capture electrons first and then recombine with holes, while those in which localized states are normally filled capture holes (or in other words, give up electrons to the valence band) first and then recombine with electrons). The occupancy of such centres is determined by the kinetic recombination process.[16] Analysis of Figure 2.8 leads to the deduction that a localized state may act as a trapping or a recombination centre depending on its location in the forbidden energy gap (which is determined by the nature of impurities and temperature). Other contributing factors to the localized state's action nature are concentrations of electrons or holes and the capture cross-sections σ_n and σ_p for the electrons and holes respectively.

The demarcation level for electron traps E_{Dn} is defined as the level at which a captured electron has equal probabilities of being excited into the conduction band and of recombining with a hole from the valence band.[27-28] Likewise, the demarcation level for hole traps E_{Dp} is defined as the level at which a captured hole has equal probabilities of being excited into the valence band and of recombining with an electron from the conduction band. Furthermore, the localized states between E_c and E_{Dn} will act mainly as electron traps, those located between E_v and E_{Dp} will act mainly as hole traps and those between E_{Dp} and E_{Dn} will act exceedingly as recombination centres.[16], [28-29]

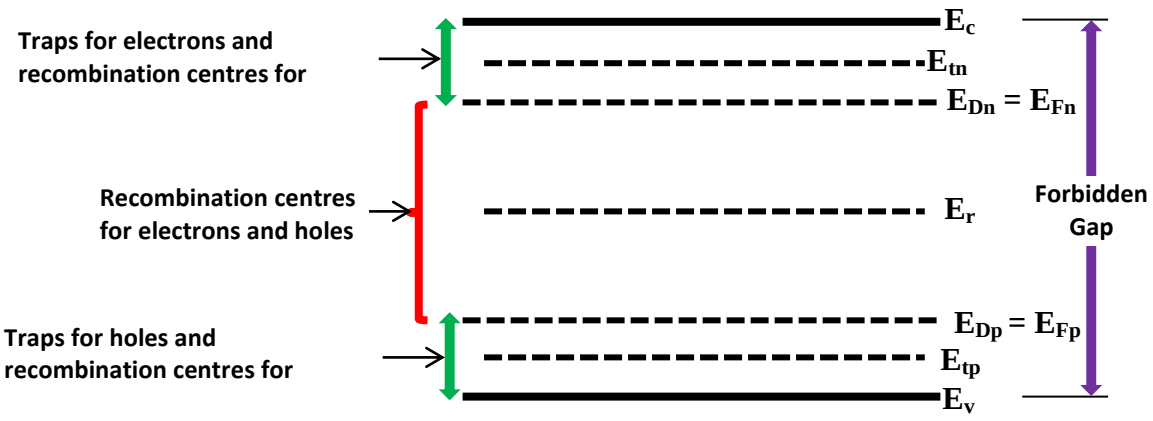

Figure 2.8 *Semiconductor demarcation levels, Fermi levels and energy levels for trapping and recombination centres for* $n\sigma_n = p\sigma_p$, *where: n and p are the carrier densities,* E_c *and* E_v *are the energy levels at conduction band and valence band edges respectively,* E_{tn} *and* E_{tp} *are the electron and hole trapping energy levels respectively,* E_{Dn} *and* E_{Dp} *are the electron and hole demarcation levels respectively,* E_{Fn} *and* E_{Fp} *are the Quasi-Fermi levels for electrons and holes respectively.*

Recombination process may conveniently be divided into two major divisions, which are radiative transition and non-radiative transition.[16] Under radiative transition, the released energy is emitted as radiation which can lead to luminescence and in the case of non-radiative transition, the released energy is dissipated ultimately as heat by various mechanisms.

2.7 The Origin of opto-electrical/semiconductor behaviour in carbon-based polymers

Preamble: A polymer is a macromolecule (with a molecular weight in excess of 10,000 g/mol) formed when the same type of smaller molecules, the monomer, combine through a polymerization process.

2.7.1 Prerequisites: Simple molecular orbitals – Sigma (σ) and Pi (π) bonds in molecules

An atomic orbital is associated with a single atom. When two (or more) atomic orbitals overlap in bond formation, the perspective changes to include all the bonded atoms and the overlapping orbitals. Such orbitals are referred to as molecular orbitals since more than one atom is involved. The total number of atomic orbitals mixed is always the same as the number of orbitals generated.

2.7.1.1 Creation of σ and σ* bonds → σ-bonding and σ*-anti-bonding molecular orbitals [the σ-HOMO and σ*-LUMO]

The first covalent bond between two atoms is always a sigma (σ) bond. In a σ-bond, the shared electron density lies directly between the nuclei of the bonding atoms, along the bond axis. The bonding (simply, bond) axis or inter-nuclear axis is the imaginary straight line that connects the nuclei of two atoms bonded to each other in a molecule. The interaction of the two bonded atoms with the bonding electrons produces a more stable arrangement for the atoms than when they are separated and the potential energy is lowered by an amount referred to as the bond energy. The lower the potential energy, the more is the stability. In a covalent bonding process, involving two atoms, the first shared electrons are those in the s orbitals, that is, 1s, 2s, etc., depending on the valence shell for each of the interacting atoms. In the case of two hydrogen atoms, for example, the addition (combination) of the two atomic 1s orbitals together produces a σ (bonding) molecular orbital, the bond of which is called a σ bond (ref. Figure 2.9). A simplistic mathematical perspective would go thus:

$\{\sigma_{molecular\ orbital} = (1s_a + 1s_b)\}$, where *a* and *b* are the respective hydrogen atoms.

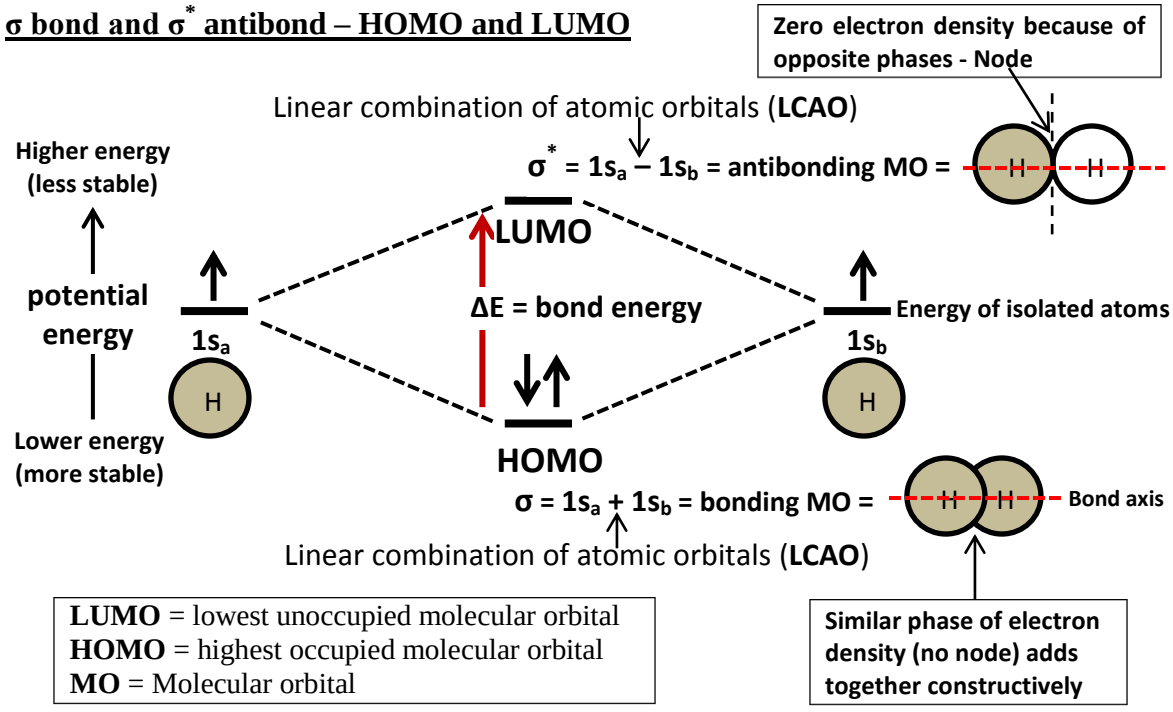

Figure 2.9 *Sigma (σ) and sigma-star(σ*) illustrated pictorially and energetically for hydrogen molecule*

The electrons in this 'new' orbital $(1s_a + 1s_b)$ are more stable than on the individual atoms. Other σ molecular orbitals could be $(1s_a + 2s_c)$, $(2s_c + 2s_h)$, $(2s_e + 3s_m)$, etc. Electrons usually occupy these orbitals and such electrons are so strongly bonded that they do not break loose to become electric conduction members. A second molecular orbital, which can simplistically be shown as a subtraction of the two atomic 1s (or 2s or 3s, etc.) orbitals is also created. For the two hydrogen atoms (Figure 2.9), this second molecular orbital (symbolized sigma-star (σ^*)) would be formed of $(1s_a - 1s_b)$. The adding and subtracting of atomic orbitals is referred to as linear combination of atomic orbitals (LCAO). The σ^* orbital is less stable than the two separated constituent atoms and is called the anti-bonding molecular orbital, because electrons in this orbital (if they do) would be less stable than the two separated individual atoms. Normally this orbital is empty, but if it happens to be occupied, then the wave nature of electron density (when present) would be out of phase (destructive interference) and cancelling in nature. There will be a node between the bonding atoms (zero electron density). Nodes produce repulsion between the two interacting atoms when electrons are present.

Two molecular orbitals (MO's), σ and σ^* have now been created from two atomic orbitals. There are two electrons to fill these orbitals, so the lower energy molecular orbital (σ) will be filled and the higher energy molecular orbital (σ^*) will be empty (in conformity with the Aufbau Principle). While there are only two molecular orbitals in this example, there may be many molecular orbitals formed in a more general example. Of all the possible molecular orbitals in a (molecular) structure, two special ones are selected and given names. One is called the highest occupied molecular orbital (HOMO), because it is the highest energy orbital housing electrons. The other is called the lowest unoccupied molecular orbital (LUMO), because it is the lowest energy orbital without any electrons. Therefore the σ-HOMO is the bonding orbital resulting from the σ bond and the σ^*-LUMO is the antibonding orbital resulting from the σ^* antibond (Figure 2.9). There are a number of reactions in which the electron density is transferred into the LUMO antibonding orbital.

2.7.1.2 Creation of π and π^* bonds →π-bonding and π^*-anti-bonding molecular orbitals [the π-HOMO and π^*-LUMO]

While a σ bond is always the first bond between two atoms, a pi (π) bond is always the second bond between the two atoms (…and third bond, if present). Pi bonds overlap the sigma bond

formed first. Therefore, in a double or triple bond, the first is always a σ bond and the subsequent ones are π bonds. These π bonds are formed of 2p orbitals, which overlap in a bonding and antibonding way, producing a π bonding molecular orbital when the two 2p orbitals are added and a π^* antibonding molecular orbital when the 2p orbitals are subtracted. As illustrated in Figure 2.10, mathematical (linear) representation would go thus:

$$\pi = 2p_a + 2p_b \qquad \text{and} \qquad \pi^* = 2p_a - 2p_b$$

For brevity, the basics of generating π and π^* bonds, as well as the associated molecular orbitals and the respective π-HOMO and π^*-LUMO are analogous to the σ-molecular orbitals discussed about under section 2.7.1.1 (which can be revisited in conjunction with Figure 2.10 for adaptation to π).

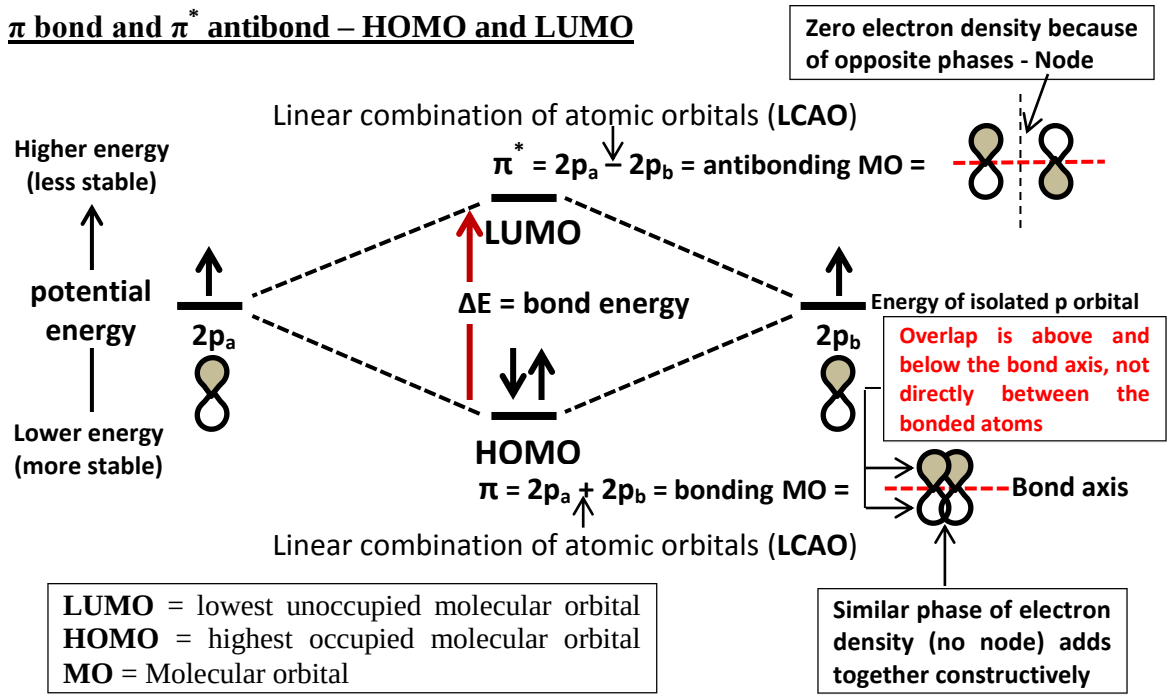

Figure 2.10 *Energetic and pictorial mechanisms of two interacting 2p orbitals a and b*

The big difference between a σ-bond and a π-bond, is that in a π-bond, there is no electron density directly between the bonding atoms (their nuclei) since 2p orbitals do not have any electron density at the nucleus. There is a node. As such, the overlap of 2p orbitals (that is, the bonding electron density) lies above and below, or in front and in the back of the bonding axis,

with no electron directly on the bonding axis. As depicted in Figure 2.10, π-bonds are characterized by side-to-side overlap. The interaction of the two bonded atoms with the bonding electrons produces a more stable arrangement for the 2p orbitals than for the atoms when separated. Electrons usually occupy these orbitals, when available/present. The HOMO of a π-system is of significant interest. There are many reactions (some of which are core to this research) which will be explained by the transfer of electrons from the HOMO (specifically π-HOMO) to the LUMO (π^*-LUMO) of another reactant.

The π^* antibonding molecular orbital is normally empty, but should it be inhabited, then the wave nature of electron density will be out of phase and result in destructive interference. This cancellation produces a second node (with zero electron density) between the bonding atoms, in addition to the usual 2p orbital node at the nucleus. This generates repulsion between the two interacting atoms, when electrons are occasionally present. There are also a number of reactions in which the electron density is transferred into the π^*-LUMO antibonding orbital.

2.7.2 Atomic Hybridization

Contextual to organic chemistry, hybridization is the mixing of two orbitals of the same atom to form new orbitals suitable for bonding. The new creations evolving from such mixtures are termed hybrids. These new hybrid atomic orbitals will be having different energies, shapes, etc., than the component atomic orbitals, but will have features which exhibit contributions of those component atomic orbitals from which they are created. For example, because a 2p orbital is very directional (along *x*, *y*, or *z* axis) and its two oppositely phased lobes lie along a single axis, in a linear way, the newly created sp hybrid orbitals will also lie along a straight line in a linear manner, with oppositely phased lobes, due to the 2p's contribution. We focus on orbital mixtures involving simple combinations of the valence electrons in the 2s and 2p orbitals of an isolated carbon atom, to form hybrid orbitals associated with the same (single) atom. The orbitals can be mixed in three ways to generate the three common shapes of organic chemistry: linear [2s + 2p], trigonal planar [2s + 2p + 2p] and tetrahedral [2s + 2p + 2p + 2p]. The number of atomic orbitals mixed together is the same as the number of new hybrid (mixed) orbitals created. In this section we qualitatively demonstrate the conceptual framework underpinning hybridization of two orbitals (2s and 2p) of a carbon atom, producing two sp hybrid orbitals of the same atom. As unfolded in the next section, the same framework can be used again to explain the generation of

three sp^2 hybrid (atomic) orbitals from three atomic orbitals [(2s and two 2p's) – specifically, 2s, $2p_x$ and $2p_y$] and four sp^3 hybrid (atomic) orbitals from four atomic orbitals [(2s and three 2p's) – specifically, 2s, $2p_x$, $2p_y$ and $2p_z$].

2.7.2.1 sp hybridization of a carbon atom

Under sp hybridization, a 2s and a 2p atomic orbital are mixed to form two sp hybrid orbitals. During the hybridization process, a 2s electron is energised and promoted to an empty 2p orbital (as shown in Figure 2.11). This unpairing of the 2s electrons allows the carbon atom to make two additional bonds, thus creating four unpaired electrons ready for bonding to attain the neon noble gas (octet) configuration when it shares with four more electrons from other atoms or molecules.

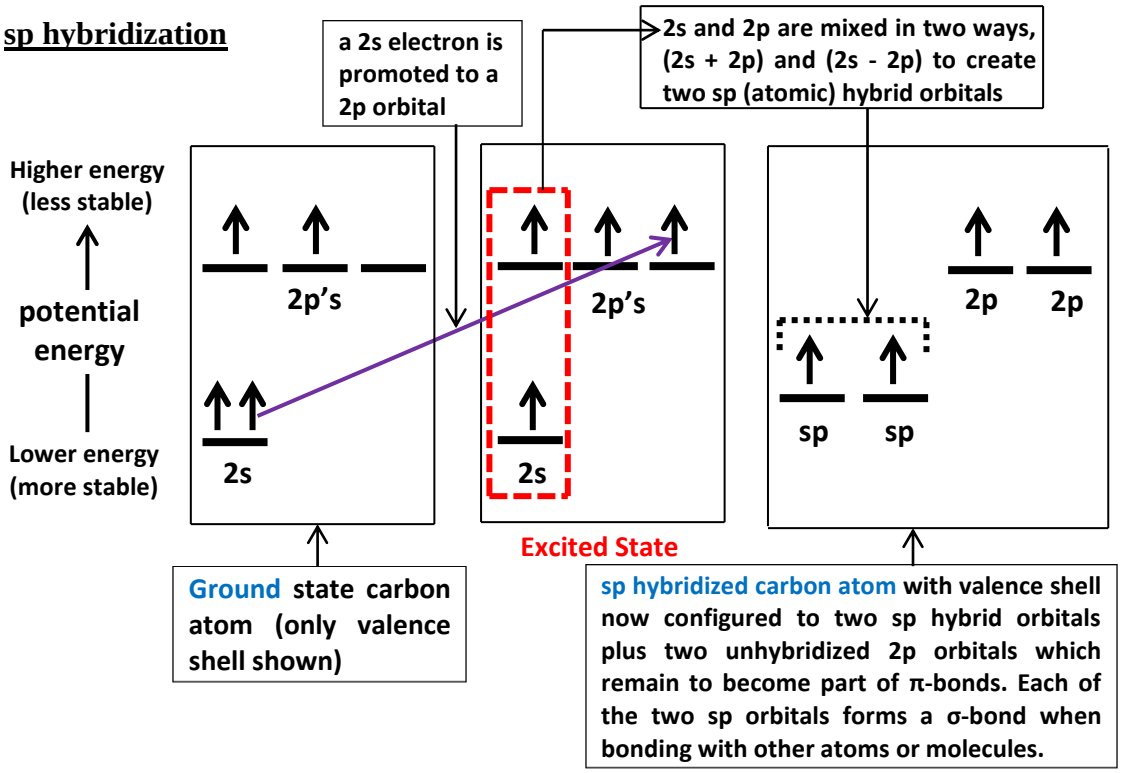

Figure 2.11 *Energetic representation of the process of changing an isolated carbon atom into an sp hybridized carbon atom, in which orbital mixing created two sp hybrid orbitals*

As Figure 2.11 shows, the 2s and 2p orbitals (contained in the red rectangular catchment) are then mixed (combined linearly) to produce two sp hybrid orbitals, which point in opposite directions. From a mathematical perspective, the mixing can be represented by the addition of

the two orbitals (2s + 2p), which produces one sp hybrid orbital and the subtraction of the two orbitals (2s - 2p), which produces the second sp hybrid orbital. This second sp hybrid orbital points 180º in the opposite direction from the first sp hybrid orbital, because of the change of the phase of the 2p orbital (which is symbolically shown by its subtraction from the 2s orbital).

The same phase adds constructively and results in bonding, but opposing phase adds destructively and results in antibonding. This will produce a larger lobe on the bonding side of the sp hybrid orbital (which implies more electron density to the hold atoms together when bonding with other atoms) and a smaller lobe on the antibonding side of the same sp hybrid orbital (which implies less electron density). The greater the electron density between bonded atoms, the stronger is the bond produced. The other two 2p orbitals do not participate in the mixing (hybridization) and they remain to become part of π-bonds. Each of the two sp hybrid orbitals forms a σ-bond when bonding with other atoms or molecules.

The vertical (energy) scale in Figure 2.11 indicates potential energy changes as the electron migrates farther from the nucleus. Though the promotion of the 2s electron to a 2p orbital is at the expense of energy, the combination of all the energy changes is more supportive for the hybridized carbon atom (whether sp, sp^2 or sp^3) than the initial one. The overall gain is in the formation of the more directional hybrid orbitals, which have better overlap of electron density between the bonding atoms and therefore form stronger bonds. This is evident from Figure 2.11, which shows that the electrons in the two newly formed sp hybrid orbitals are held more tightly than those in the non-participant 2p orbitals (though less tightly than the 2s electrons) since they are closer to the nucleus, on average.

2.7.3 Electrical, Optical and Morphological Properties in Conjugated Polymers

2.7.3.1 The origin of semiconducting behaviour in conjugated carbon-based polymers

The type of bonds made by the valence electrons of carbon with other carbon atoms (C-atoms) or with atoms of other elements determines the overall electronic characteristics of the resultant polymer. This is so, because the main building block of most polymers is the carbon atom. Generally, polymers can be classified as saturated and unsaturated based on the number and type of the carbon valence electrons involved in the chemical bonding between adjacent C-atoms

along the main chain of the polymer.[30] Saturated polymers are insulators since all the four valence electrons of the C-atom are exhausted (localized) in the covalent bonds. It is the unsaturated nature of the carbon backbone which makes conjugated polymers mostly conductive. Conjugated polymers, like other polymers, are macromolecules that consist of long chains of repeated units called monomers. These monomers mostly consist of carbon and hydrogen atoms, but other atoms like nitrogen, oxygen and sulphur can be part of the monomer (Figure 2.12).

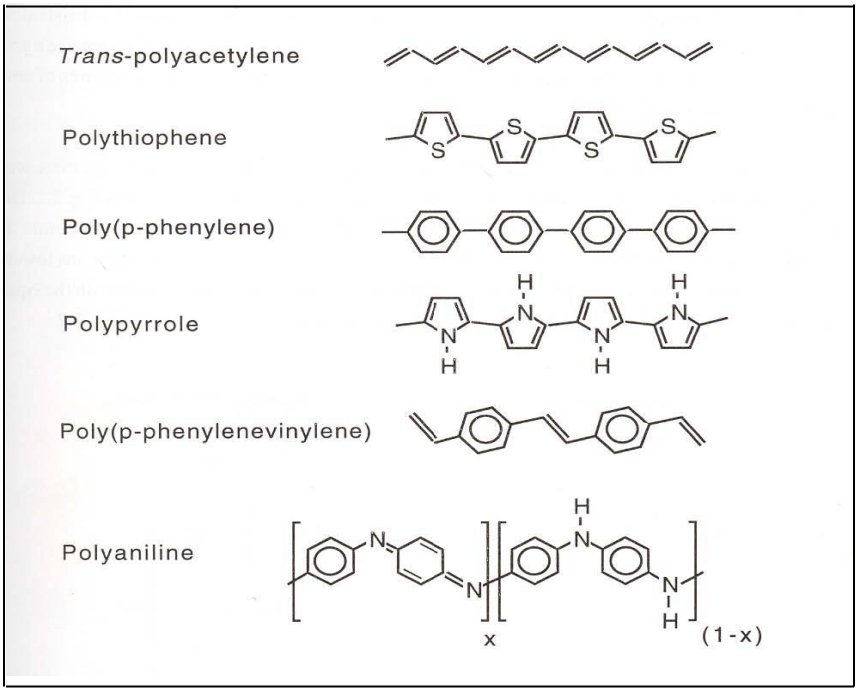

Figure 2.12 *Some common conjugated polymers*[33]

The difference between conjugated polymers and other polymers lies in the backbone of the polymer, which in the case of conjugated polymers consist of alternating single and double covalent bonds between the carbon atoms. The single bond is a σ-bond and the double bond consists of a σ-bond and a π-bond overlapping the σ-bond. Fundamentally, it is from within the overlap of the molecular orbitals formed by the valence electrons of the chemically bonded C-atoms that the organic semiconducting property of conjugated polymers originates.

The ground state electronic configuration of a carbon atom is $1s^2\ 2s^2\ 2p^2$, which can be depicted as shown below.

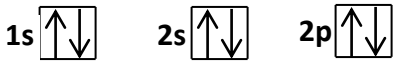

The atomic orbitals of carbon are altered into hybrid orbitals as they form covalent bonds. As explained earlier (section 2.7.3), during hybridization, a 2*s*-electron is promoted to the vacant 2*p*-orbital leading to an intermediate $2s^1 2p_x^1 2p_y^1 2p_z^1$ excited state configuration of the nature depicted in Figures 2.13 and 2.14 for sp^3 and sp^2 respectively. These electronic orbitals do not bond in this excited state form, but first hybridize (that is, mix in the linear combinations previously explained).

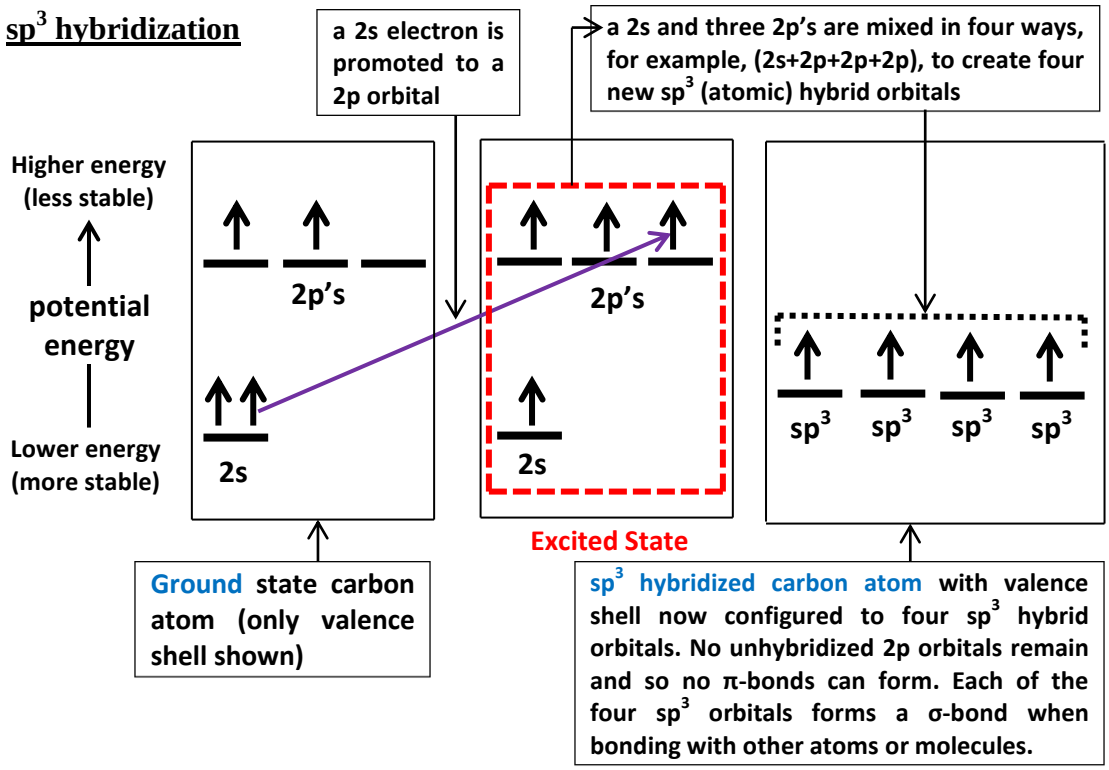

Figure 2.13 *sp^3 hybridization of the valence shell electrons of a carbon atom*

As shown in Figure 2.13, sp^3 hybridization produces set of four sp^3 hybrid orbitals oriented towards the corners of a regular tetrahedron [a four surfaced figure of equilateral triangles (not shown)]. This geometric configuration is explained by the realization that the three 2p orbitals (which constitute the greater part of their creation) fill all three dimensions and so the four

orbitals created from them also fill all three dimensions. There are no π bonds, because no 2p orbitals remain to make them. Since all the bonding orbitals are hybrid orbitals, they form σ bonds when bonding with orbitals of other atoms. Sigma bonds enjoy strong degrees of overlap in bond formation with other atoms. As a result, molecules with strong bonds and increased stability are generated whenever sp^3 hybridized atoms participate in their production process. The arrangement of bonds emanating from overlap with sp^3 hybrid orbitals on adjacent atoms is the one which gives rise to the tetrahedral structure that is found in the lattice of diamond and in some alkanes like ethane, C_2H_6.[30] In these structures, all electrons are engaged in the σ-bonds (which in effect are the strong covalent bonds). As such, all hydrocarbons containing σ bonds formed from sp^3 hybrid orbitals are saturated molecules and are therefore insulators, with the characteristic high band gaps.[15], [31-32] Therefore sp^3 hybrid orbitals have no contribution to the electronic behaviour in carbon-based polymers.

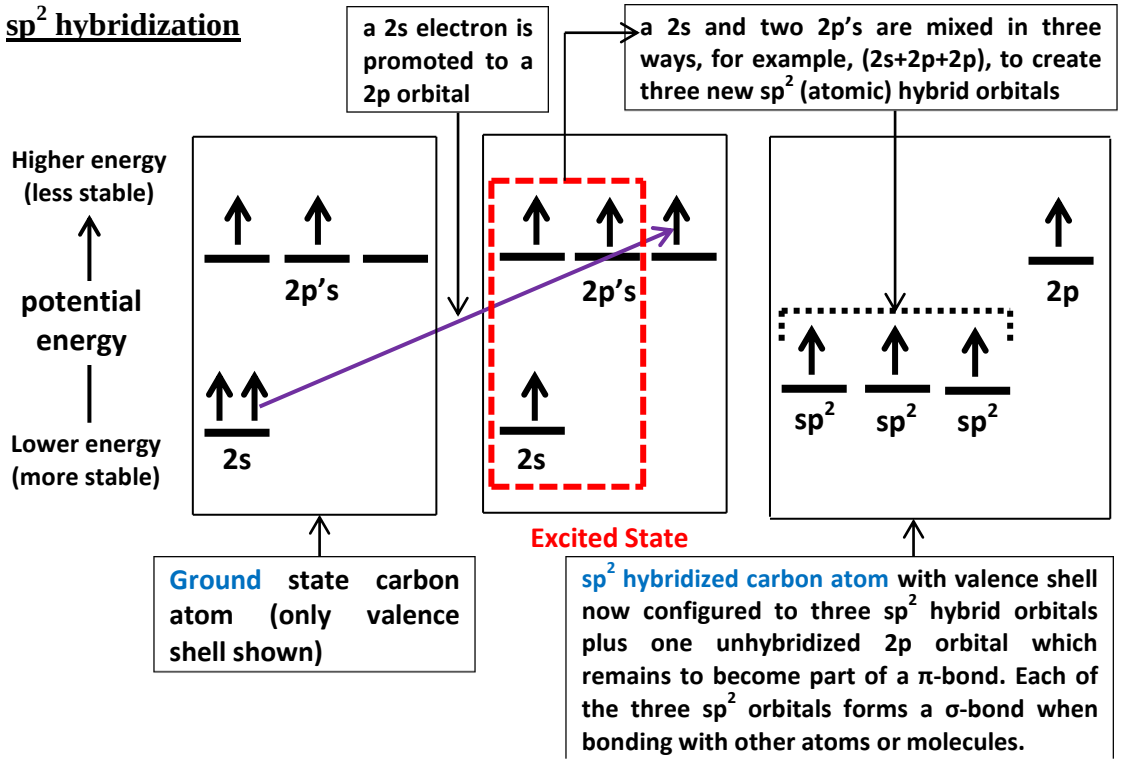

Figure 2.14 *sp^2 hybridization of the valence shell electrons of a carbon atom*

Actually it is the sp^2 hybridization of the carbon atoms of the organic polymer which accounts for the semiconducting behaviour of the polymer. Under sp^2 atomic hybridization, the 2s orbital mixes with two 2p atomic orbitals ($2p_x$ and $2p_y$) creating three new hybrid orbitals, as shown in Figure 2.14.

The relative energy framework showing electron promotion and orbital mixing is almost identical to the sp (and also sp^3) hybridization explained earlier. The major difference is the addition of a second 2p orbital ($2p_y$) in the mixing.

The unmixed $2p_z$ orbital remains unchanged and will be perpendicular to the plane panned by the three sp^2 hybrid orbitals. It takes part in the formation of a π-bond. The valence electron in this $2p_z$ orbital interacts with a neighboring $2p_z$ electron in the adjacent $2p_z$ orbital belonging to the next sp^2 hybridized carbon atom and forms a π-bond (Figure 2.14). This process is replicated along the carbon chains within the polymer. The two electrons in the π-bond occupy the space above and below the σ-bond,[33-34] as illustrated in Figure 2.14.The added $2p_y$ orbital alters the hybrid creations from linear to planar, as shown in Figure 2.15. Since the two 2p orbitals ($2p_x$ and $2p_y$) lie in a (horizontal) plane, the three sp^2 hybrid orbitals created also lie in the same plane and arrange themselves in a trigonal planar shape of 120 ° bond angles between any two of the orbitals. The three hybrid orbitals form σ-bonds when bonding with other atoms or molecules as depicted in Figure 2.16. The trigonal configuration allows the electrons in the σ-bonds to be as far apart in space as possible and minimizes the electron-electron repulsion. This results in greater bond strength and stability of the hybridized atom.

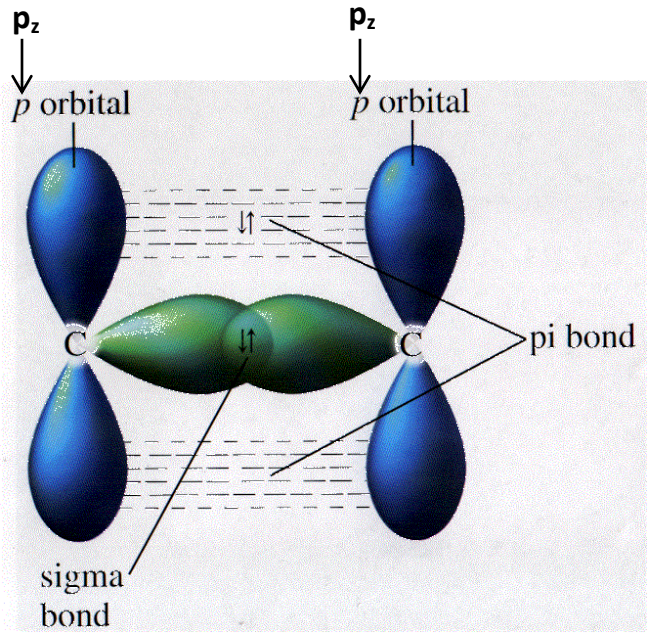

Figure 2.15 *Sigma (σ) and Pi (π) bonds between two sp^2 hybridized carbon atoms. Only one hybridized lobe (green) is shown for each atom*[34]

Compared to sp^3 hybrid orbitals, the sp^2 hybrid orbitals of the hybridized carbon atom form a different bond length, strength and geometry when combining with other atoms or molecules. This leads to conjugation along the backbone carbon chain of the polymer.

Conjugation refers to the alternation of single and double bonds between the carbon atoms[35-36] and is characterised by π-bond overlap across the intervening σ-bonds. As can be deduced from Figure 2.15, conjugation creates a region of overlapping $2p_z$ orbitals (the π-molecular orbitals)

bridging the adjacent single bonds (σ-bonds). The σ-bonds will have been formed by the bonding between the sp^2 hybrid orbitals of the consecutive carbon atoms along the spinal chain of the polymer. This overlapping of double bonds over single bonds is the so called mesomerization.

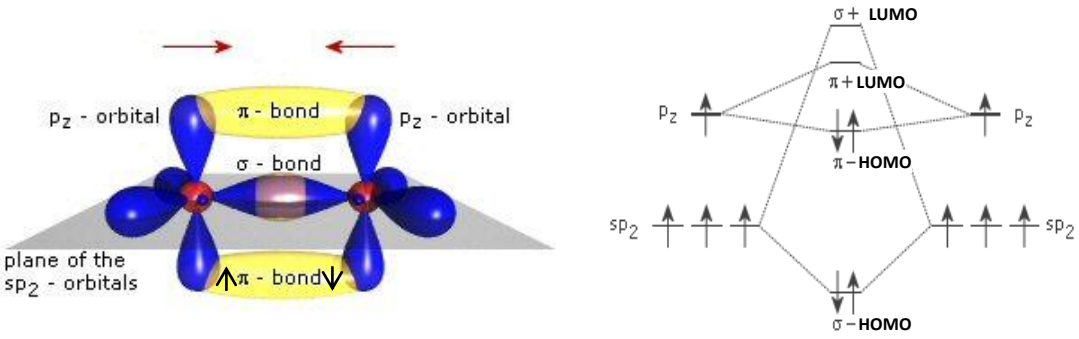

Figure 2.16 *Scheme of the orbitals, bonds and associated energy diagram (not to scale) for two sp^2 hybridized carbon atoms*[12]

Figure 2.17 shows the alternating double and single bonds in polyacetylene, which is one example of a simple conjugate polymer. It has a linear structure and exhibits a degenerate state.

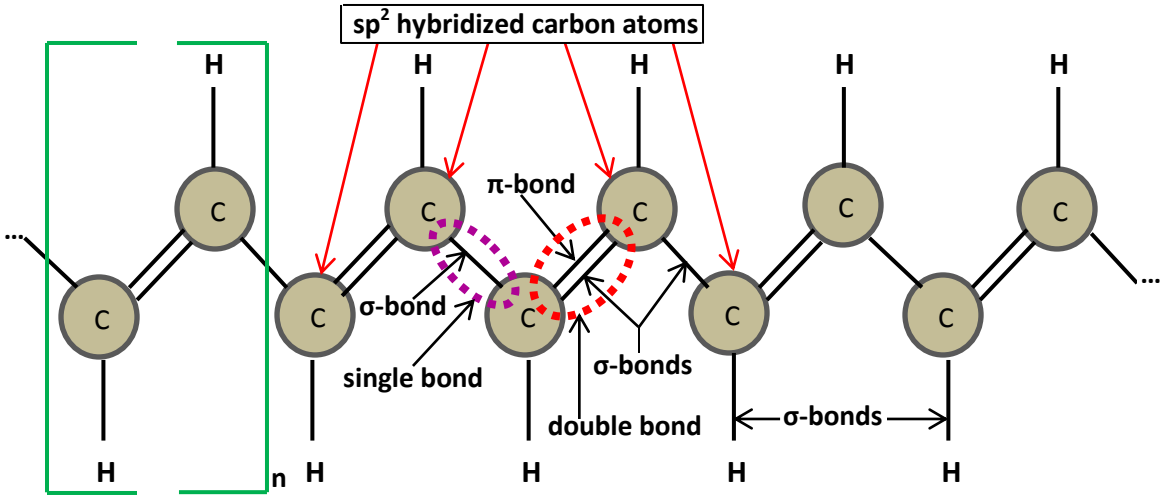

Figure 2.17 *Polyacetylene molecule's alternating double and single bonds along its backbone carbon chain, which shows that the polymer is conjugated*

Since π-bonds are weak bonds, the overlapping of their p_z electron wavefunctions causes delocalization of the π-electrons along the polymer chain, which is the origin of semiconducting

behaviour in these carbon-based polymers.[31], [35], [37-40] Therefore π-bonds can be considered to be the fundamental source of band transport in the conjugated systems.[30] The delocalization of the π-bonds over the entire molecule is followed by the quantum mechanical overlap of the p_z orbitals, which due to the Peierls instability, produces two delocalized energy bands, the bonding π and the antibonding π* orbitals. The lower energy π-orbitals constitute the valence band (π-state), and the higher energy orbitals π^*-orbitals form the conduction band (π*-state).[10] Of the valence band orbitals, the highest occupied molecular orbital is the HOMO and of the conduction band orbitals, the lowest unoccupied molecular orbital is the LUMO. In this regard, the ionization potential of the molecule corresponds to the HOMO and the electron affinity corresponds to LUMO. Electrons usually occupy the valence band and the conduction band is usually empty. As explained in section 2.7.4.5, there is a correlated match between the band gaps of conjugated polymers and the optical light energy range, which favours UV and visible light absorption by the polymers. This original property makes conjugated polymers ideally suited for use as photoactive materials in opto-electronic devices operating in the optical light range.

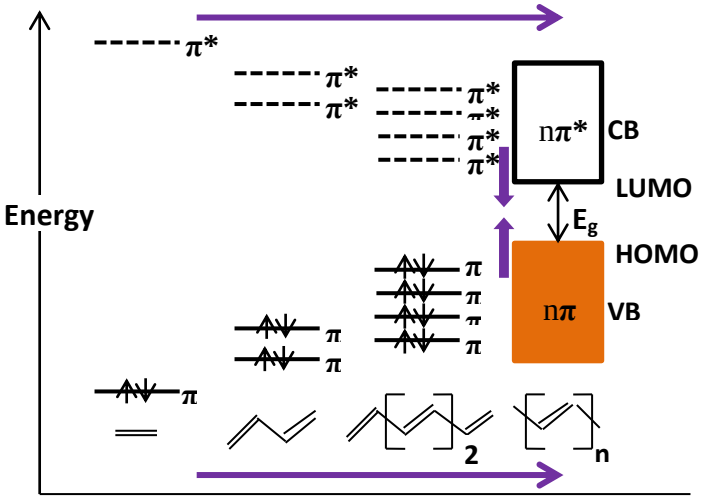

Figure 2.18 ***Extension of the π-system results in the creation of the valence band (VB) and conduction band (CB).Valence band is filled with electrons, whereas conduction band is empty. The energetically forbidden gap (E_g) decreases as the π-network increases.***

Orbital overlap increases the concentration of orbitals on adjacent atoms in the same region of space. Due to the overlapping of π-orbitals, delocalized π-electrons roam over the developed valence band which extends over the entire polymer molecule. The electrons may occasionally migrate into the created conduction band upon appropriate energy absorption. Additional advantages of π-electrons are that they can be moved without destroying the chemical structure of the polymer material and (due to their weak bonds) require less energy to be removed from their bonding state. Since the σ-bonds do not dismantle (because of their strength), the polymer molecule keeps the rest of its atoms linked together. Only π conjugated electrons become delocalized and move freely throughout the molecule, without being associated

with a particular atom or covalent bond. Furthermore, increasing the degree of conjugation (number of alternated multiple bonds) results in the development of molecular orbitals which are very close in energy (Figure 2.18). This leads to the formation of energetic bands (valence and conduction bands), because the energetic structure of the material is no longer composed of discrete levels. In addition, the energetically forbidden gap between the HOMO and the LUMO is narrowed (Figure 2.18). For example, ethylene (or ethane) monomer molecule has an energetic (forbidden) gap of 7.6 eV[15] between its HOMO and LUMO levels. This is too large to obtain semiconductor behaviour. When polymerized, conjugation effect arises (that is, polymer molecule develops and contains delocalized π-electrons/bonds) and further decreases the energetic gap, to the extent that the polymer may start to exhibit semiconductor behaviour. In fact, such parameters as molecular arrangement (for example, linear, planar, etc.), geometry of the molecule, aromaticity or substituents effect, etc. are known to alter the band gap of the polymer. It is from such endowed electronic properties that conjugated polymers exhibit semiconductor behaviour.

2.7.3.2 Band structure of conjugated polymers

Two possible band structures emerge from the alternation of single and double bonds in conjugated polymers. The first class consists of polymers which possess a degenerate ground state (simply, degenerate) and the second class is composed of polymers with a non-degenerate ground state (simply, non-degenerate). Our discussion of the two classes is based on trans-polyacetylene (simply, polyacetylene) for the degenerate category and polythiophene for the non-degenerate group.

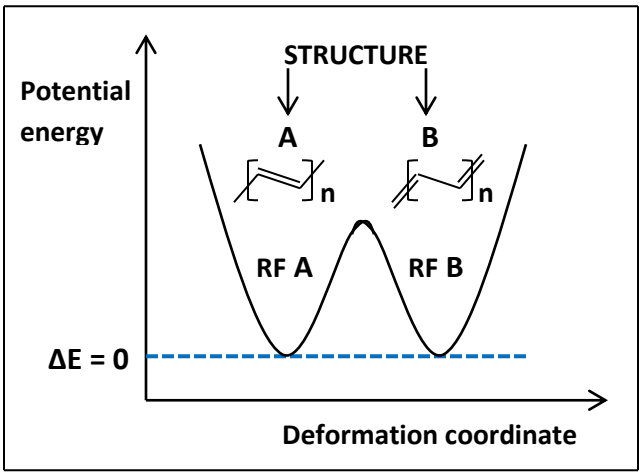

Figure 2.19 *Sketch of the potential energy curve for a degenerate system* (*for example, polyacetylene*)

Degenerate: Degenerate structures like polyacetylene are energetically equivalent. Figure 2.19 illustrates this phenomenon on a sketch of the potential energy curve for a degenerate system (for example, polyacetylene). The monomer of polyacetylene is made up of only one carbon atom and one hydrogen atom. If the carbon atoms in the chain were equally spaced, the system of the 2p-orbitals would create a half-

filled π-band. This half–filled π-band would result in a metallic state of the polymer. Fortunately, such a state does not arise in polyacetylene (as in other polymers of the same class) because of its creation of conjugated bonds (that is, altering strong and weak bonds). These creations of altering bonds result in non-equal spacing of the carbon atoms. The double bonds assume a length of 1.36 Å and the single bonds pick up a length of 1.44 Å.[41]

This change in the lattice is explained by Peierls' distortion which states that a one dimensional metal will be unstable, and that an energy gap will form at the Fermi level, because of the lattice distortion so that the material becomes an insulator or a semiconductor.[10] The theorem describes a spontaneous lowering of the symmetry of the lattice in order to minimise the ground state energy.[41] The break in the continuity of the energy bands is caused by the use of elastic energy during lattice distortion, which is compensated by a lowering of the electronic energy and formation of a band gap.[10] The displacement of every second atom reduces the translation symmetry and halves the first Brillouin zone. After the periodic distortion, two new π-bands are generated: one filled (π) and the other empty (π^*). The two bands repel each other and open up a band gap at the Brillouin zone boundary. This band gap is caused by the conjugation (altering single and double bonds), which leads to a periodic perturbation of the potential.[33], [41] The band gap in trans-polyacetylene is about 1.8 eV at the Brillouin zone boundary.[41] As can be seen in Figure 2.20, polyacetylene has two ground state configurations, A and B. Configuration B can be obtained from A by exchange of the single and double bonds. Since all the carbon atoms are equivalent if the chain is infinite, the energies of the two phases (configurations) are equal, which implies degeneracy of the ground state of the polymer.

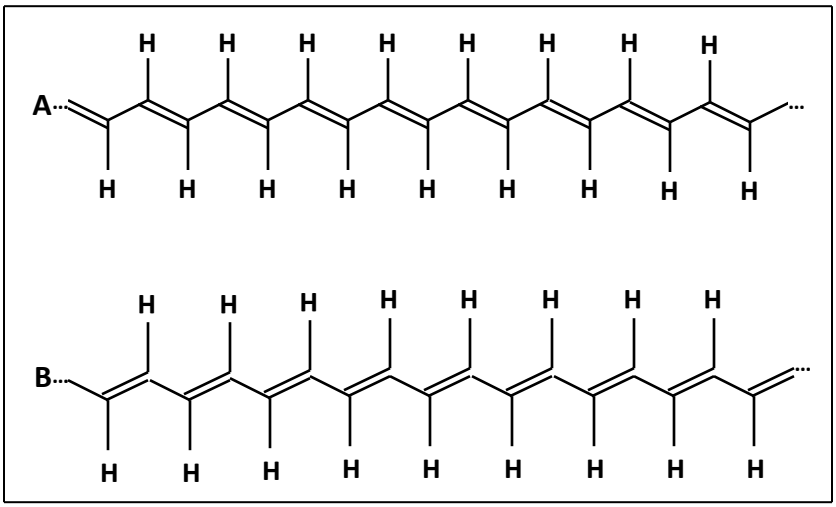

Figure 2.20 *The two ground state configurations of trans-polyacetylene*

Non-degenerate: Polyparaphenylene is an example of a conjugated polymer with a non-degenerate ground state. This polymer belongs to the structure of aromatic-based semiconducting conjugated polymers. These materials have σ-bonds and delocalized π-electrons between the carbon atoms which form the (so called benzene) rings. Such conjugated polymers show a difference in energy (Δ**E**) between the two resonance forms RF C and RF D shown in Figure 2.21. The second energetic structure D (obtained from C by the exchange of the single and double bonds) is now of the quinoid form, which ordinarily reveals higher potential energy (Figure 2.21). Another example of a conjugated polymer with a non-degenerate ground state is polythiophene, whose monomer is a thiophene (ring). Figure 2.22 shows two connected thiophene rings. The left hand ring E has two non-equivalent carbon sites designated C_α and C_β. C_α connects the thiophene ring E to a neighbouring ring through covalent σ-bonding with a carbon C atom in the backbone chain of that neighbour. C_β bonds to a hydrogen side group. The hydrogen atoms on neighbouring rings repel each other, which leads to rotation of the rings around the chain axis.[33], [41] In the ground state configuration of polythiophene, the neighbouring C_β and C_β atoms are doubly bonded. The C_α - C_α and the C_α - C_β are both connected with single bonds. Since the C_α and the C_β are non-equivalent, an exchange of the double and single bonds along the chain will lead to another state of energy, which means that the ground state of the polymer is non-degenerate.

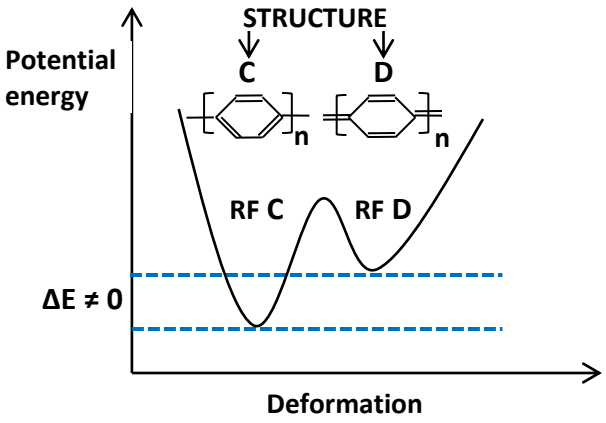

Figure 2.21 *Sketch of potential energy curve for a non-degenerate system* (*for example, polyparaphenylene*)

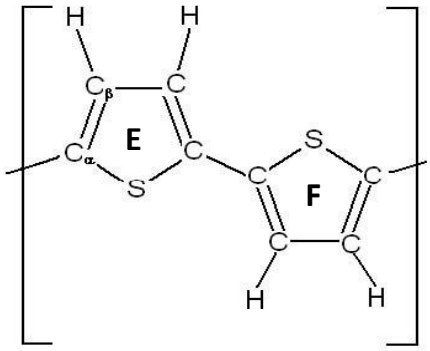

Figure 2.22 *Two connected thiophene rings E and F. The left ring E has two non-equivalent carbon sites,* C_α *and* C_β [41]

2.7.3.3 Correlation of conjugated polymer chain distributions with optical phenomena

Each chain of a conjugated polymer does not elongate endlessly, but rather builds up twists and coiled structures which significantly account for the amorphous nature of the polymer. This disordered morphology limits the delocalization length of the π-spread of electrons to a definite length called the conjugation length. This characteristic length is bounded by an energy barrier which may be created by defects or kinks.[30], [42] Besides, the conjugation length segments have random distributions, which lead to different energies of the π-electrons. This explains why conjugated polymers exhibit broad absorption and emission spectra. Assuming a one-dimensional particle-in-a-box picture, the longer segments will have a low π-π^* energy gap and the shorter segments will have a much higher energy gap.[30], [42] The emission spectrum of conjugated polymers is highly Stokes-shifted (Figure 2.23). This may be understood from the consideration that Coulomb-bound electron-hole pairs on high-energy chain segments will undergo rapid energy transfer to lower-energy segments, so that nearly all the emission comes from low energy, long conjugation length segments.[30] Therefore, chain distributions, play an important role in determining the HOMOs and LUMOs of conjugated polymers. The difference in energy (band gap) between the HOMO and the LUMO gives the optical properties of the polymer. It is determined from optical, electrochemical and other spectroscopic measurements. Excitingly, for conjugated polymers, the band gap (which lies between 1.5 and 4.0 eV[43]) has been found to be within the semiconductor range of 1.0 – 4.0 eV,[10], [31] which covers the whole light spectrum range from infrared to ultraviolet, thus making conjugated polymers ideally suited for opto-electronic applications operating in the visible range.[10]

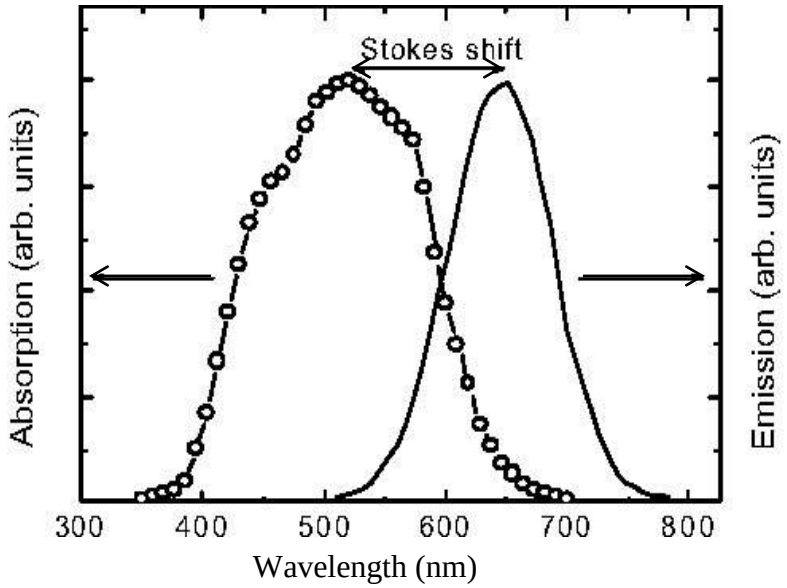

Figure 2.23 *Sketch of a polymer's absorption and emission spectra, which is Stokes-shifted towards low energy*[30]

2.7.3.4 Morphological Properties of Conjugated Polymers

Side chains mushroom from the principal (or backbone) chain of most conjugated polymers. These branches are welcome, because they help in increasing the solubility of the polymer in common solvents like chlorobenzene and chloroform. The enhanced solubility is attributed to separation of the side chains from the conjugated backbone and thereby reduces the rigidity of the backbone, which enhances flexibility. Furthermore, the backbone separation decreases the intermolecular overlap of neighbouring chains, which in turn hinders the hopping of charges between molecules.[44] The sides chains also lower the melting temperature and in most cases hinder the conjugated chain packing in solid films of many conjugated polymers.

However, the effect of the separation of the conjugated backbones in a given polymer depends on whether the polymer is amorphous or well-ordered crystalline structure. For molecules which are designed to form amorphous films, like those for light emitting diodes (LEDs), this separation is beneficial in that it reduces intermolecular overlap, the increase of which promotes excimer formation (see Appendix 1) in such molecules (for example, polyfluorene). As such, for molecules of this nature, increased intermolecular overlap, which results in more packing associated with high crystalline density, decreases the power efficiency of the polymer molecule due to excimers.[44] These molecules typically have asymmetric, bulky side chains that cause the molecules to twist and fail to pack efficiently.[44]

On the other hand, the impact of increased intermolecular overlap in conjugated polymers that crystalize is of positive correlation. Most of these molecules are used in the fabrication of organic solar cells. In films made of these polymers, charge transfer depends upon the degree of inter-chain overlap or chain packing.[30], [45] Efficiently packed chain structures provide well-ordered crystalline phases, which increase electron delocalization length, leading to high charge carrier mobility.[30], [44] Conjugated polymers that crystallize tend to be more rigid and planar.

A well behaved example of a conjugated polymer whose members constitute a mixture of the two structural versions (amorphous and crystalline) is poly(3-hexylthiophene) (P3HT). Some of the P3HT conjugated polymers are amorphous while others can be crystalline. The regiorandom P3HT version has a twisted chain conformation with poor packing and low crystallinity with solid films having amorphous phases. On the other hand, the regioregular P3HT version is

characterised by a planar conformation, better intermolecular overlap with increased efficient packing that promotes well-ordered and increased crystalline phases.[30], [46-50] Required optical and electrical parameter value range conformities can be achieved in conjugated polymers through the tuning of morphology as a function of regularity in molecular structures. Regioregular P3HT's response to such adjustments is much more favourable than that of the regiorandom P3HT form. For example, several orders of magnitude higher charge carrier mobility was recorded in films from regioregular P3HT as compared to its regiorandom counterpart.[30], [44], [51-53] As described in Chapter 3, regioregular P3HT is the donor used in the fabrication of the organic solar cells investigated in this research.

Nanoscale morphology plays a very decisive role in producing efficient donor/acceptor (D/A) based photovoltaic devices (PVDs). Even if the donor and acceptor have a favourable electronic relationship, their composite performance will be a dismal failure if their spatial regimes of the morphology are not constituted of conducive inter-penetrable network, with increased donor /acceptor (D/A) interface and large clusters of separate D/As. This is so, because the performance of such devices (for example, bulk-heterojunction (BJH) organic solar cells heavily depends on the physical interaction of the donor conjugated polymer and the acceptor (conjugated) fullerene components, which is manifested by the composite morphology.[54-57] The morphology of the active layer depends on the interaction between a number of intrinsic and extrinsic properties. Intrinsic properties are those that are inherent to the polymer and the fullerene, including the fundamental interaction parameters between the components.[55] These include the crystallinity of the two materials as well as their relative miscibility. The extrinsic factors incorporate all the external influences which have a bearing on device fabrication. These include choice of the solvent, overall concentration of the blend components, deposition technique (that is, whether spin coating and if so → spin coating speed, drop casting, ink-jet printing, roll casting or blade coating, etc.), evaporation rate of the organic solvents and thermal treatments (for example, thermal evaporator employment for cathode formation) as well as solvent annealing.[30], [55], [58-59] High evaporation rates produce highly packed films, which imply increased inter-chain interaction that promotes efficient charge transport processes[51], [53] and reduced photoluminescence efficiency.[60] Such polymer films are best suited for use in PVDs. Slowly evaporating solvents result in slow film growth rate, which aggravates formation of porous films.

It is evident that the number of factors impacting on the morphology of the active layer is huge and contextual to the specific polymer-fullerene blend. The composite should be formed from skillfully prepared solution and self-assemble into the most favourable morphology with high minimal retrograde treatments from external, because the opto-electrical behaviour of conjugated polymer based electronic devices heavily depends on the solid state film morphology of the composite polymers.

2.7.3.5 Metal-active layer interface (e.g. metal-polymer interface)

When two materials with different Fermi levels are brought into contact, due to Seeback effect, net free charge carriers flow into the other side of the junction until the Fermi levels for electrons in both materials are aligned and therefore equal at the contact. In the case of a metal being brought into intimate contact with an insulator or semiconductor, an electrical contact is formed,[10], [16] which for the case of a metal and a polymer is referred to as a metal-polymer (m-p) interface (or m-p junction). The so formed junction either enables or impedes charge carrier flow from the metal into the polymer or vice versa across the junction of the two materials concerned. Therefore, at such a contact, either a rectifying Schottky or an ohmic contact is created. A Schottky contact is a charge blocking contact. The development of such a contact is accompanied by the build-up of a Schottky (blocking) potential barrier which extends from the interface into the semiconductor. The barrier blocks (impedes/slows) the cross-over of charge carriers from the metal into the semiconductor polymer. Therefore at a blocking metal-polymer junction, the bulk polymer can carry away more charge carriers than the contact can supply to the bulk.[61-62]

For an n-type semiconductor, the condition for the formation of an electron blocking contact (that is, an electron blocking metal-polymer interface in this case) is that $\phi_m > \phi_s$ (Figure 2.4), where ϕ_m and ϕ_s are the work functions of the metal and semiconductor (polymer) respectively. Under such a configuration, it is electrons from the metal that are confronted by a repelling electric potential from the semiconductor side, which hinders them from entering the semiconductor, but electrons easily diffuse from the n-type semiconductor to the metal and therefore cause electron depletion in the semiconductor. Charge depletion is characteristic of a Schottky barrier. If the work function of the n-type semiconductor is greater than that of the

metal (that is, $\phi_m < \phi_s$), then the metal-polymer interface (that is, electrical contact) would be ohmic. In such a case, electrons diffuse from the metal to the semiconductor and cause electron accumulation within the semiconductor in the region adjacent to the junction, which is characteristic of an ohmic contact.

In the case of a p-type semiconductor, the condition for the formation of a hole blocking metal-polymer junction is that $\phi_m < \phi_s$. Holes from the semiconductor therefore diffuse into the metal and cause a depletion of holes in the semiconductor, which is characteristic of a hole blocking contact. It is holes from the metal side which are blocked from entering the p-type semiconductor. If ϕ_s of the p-type semiconductor is smaller than ϕ_m (that is, $\phi_m > \phi_s$), then the contact (that is, the metal-polymer interface) is ohmic and will be characterised by accumulation of holes in the p-type semiconductor.

2.8 Charge carrier generation mechanisms in conducting polymers

2.8.1 Generation of charges in semiconducting polymers through 'doping'

A small amount of energy, like ambient temperature energy (25 meV), is capable of enhancing electrical conductivity in intrinsic (pure) semiconductors, because their band gap is narrow enough to allow promotion of electrons from the valence band to the conduction band. Insulators have already been illustrated to have a much wider band gap. Extrinsic semiconductors are formed from doping intrinsic semiconductors. Polymers have the electronic profiles of either insulators or semiconductors; thus the band gap in a fully saturated polymer like polyethylene is 5.0 eV and decreases to about 1.5 eV in the conjugated system polyacetylene.[10] As explained in earlier sections, the uniqueness of polymers is that atoms of polymers are covalently bonded to one another and form polymeric chains that experience weak intermolecular interactions. In view of this profile, it means that the band theory cannot be completely exhaustive in describing the electronic conduction in polymers, because macroscopic conduction in polymers is intricate in that it demands electron movement not only along chains, but also hopping from one chain to another.[10] As is customary to all extrinsic semiconductors, polymers whose band gaps are similarly high can be converted into conducting polymers by reducing the sizes of their band gaps.

Doping can be executed either by injecting charges with an electric current sent to the material, or via the inclusion of a dopant (that is, a material of a different nature).[15] A semiconductor can be either n-doped, or p-doped. An n-doping process involves the addition of electrons in the conduction band or in newly created energetic levels below the LUMO and a p-doping process corresponds to the creation of holes (that is, electron vacancies) in the valence band or in newly created energetic levels above the HOMO.[32] In inorganic materials, doping is usually performed by substituting several atoms with elements of the previous group (which implies, generation of a valence electron vacancy, $\Rightarrow$p-doping) or the next group (which implies, creation of an extra free valence electron, $\Rightarrow$p-doping). In the case of organic materials (focusing on polymers, particularly conjugated polymers), a redox process is usually employed to generate charges.[10] [15], [32] By this process, the band gaps are thus modified chemically.[41], [43] Whilst the term 'doping' is usually used to describe the whole process, in reality it only covers the physical part of adding the donor or acceptor molecule of the chemical to the polymer. The reaction which actually takes place is either an oxidising one or a reducing one,[10] thus a chemical process, which is different from the commonly termed doping of a semiconductor like silicon or germanium where an atom in the lattice is substituted.[10] In light of this, a compromise term, 'chemical doping', shall be used when referring to polymers. Electrical conductivity in conjugated polymers upon chemical doping was brought to the lime light by the pioneering work of Heeger et al. in 1977.[63] The chemical doping of a conductive polymer is characterised by the formation of a polymer salt. This is achieved either by immersing the polymer in a solution of the reagent or via electrochemical methods.[10] A polaron can be formed when an electron is removed (or injected) from the neutral chain by chemical doping. This introduced charge polarizes the surrounding chain and creates local deformation of the lattice. The charge and the surrounding deformation are quantum mechanically referred to as a polaron. This local deformation of the chain lowers the conducting state and raises the valence state,

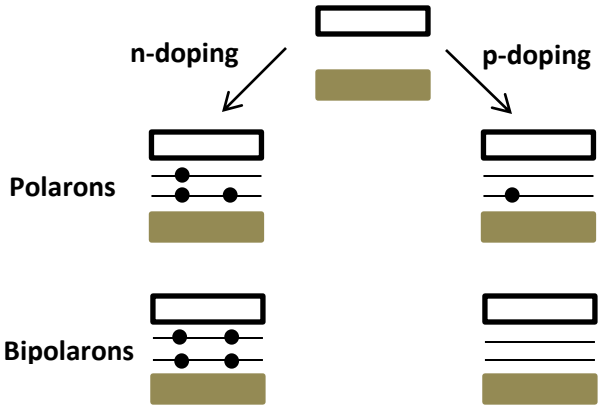

Figure 2.24 *Schematic illustration of an electron polaron and bipolaron to the left and a hole polaron and bipolaron to the right*[32], [33]

thereby moving two electronic states into the band gap.[33] Depending on the type and level of chemical doping, different polarons can be created. A hole polaron is formed when the polymer is p-doped (that is, an electron has been removed from the chain). In the absence of an electron, the lower level only contains one electron and the upper level is empty (Figure 2.24). An electron polaron is formed when the polymer is n-doped (that is, an electron has been introduced into the chain). In the presence of an extra electron, the lower level is filled with two electrons and the upper level gains an electron.[33] At high doping level of the polymer, two polarons can recombine to form a double charged bipolaron (Figure 2.24).[33] The generalized oxidation process can be represented by the chemical equation (2.7)

$$P_n = \underset{Red}{O_x/A^-} \rightleftharpoons [P_n^+A^-] \rightleftharpoons \underset{Red}{O_x/A^-} \rightleftharpoons [P_n^{2+}2A^-]^{[10]} \qquad (2.7)$$

where P_n represents a section of a polymer chain.

The summary steps are: A cation radical, formed by p-doping or an anion radical formed by n-doping (which is the polaron) is first formed. This is followed by a second electron transfer with the formation of a dication (or dianion), which is the bipolaron.[10] An alternative representation is that of Equation (2.8), in which charge transfer complexes may form between charged and neutral segments of the polymer when the situation allows.[10]

$$P_n^+A^- + P_m \rightarrow [(P_nP_m)^+A^-]^{[10]} \qquad (2.8)$$

As explained in the next section, the absorption of light by a conjugated polymer may lead to charge generation. Light is an example of an external stimulus.

2.8.2 Generation of charges through external stimulus-response mechanisms of conjugated polymers

In intrinsic semiconductors, electrical conductivity may be induced through intrinsic excitation of the material.[10], [32] The stimulus can be thermal energy (which is temperature dependent), electric field, or solar light. Extrinsic semiconductors require doping (see Section 3.2) to enhance conductivity. Charge carriers may alternatively be injected into the material from the electrodes.[10] There is also the necessary field assisted charge generation in polymers. When an exciton has been generated in a (conjugated) polymer based solar cell, it has to be dissociated into an electron and a hole. When dissociated, each of the two charge carriers has to be

transported to its respective electrode in order for it to enable the device to deliver current to an external circuit. For the two processes (dissociation to generate 'isolated' charges and charge transport) to be achieved, the polymer based solar cell must have some built-in driving electrostatic field to assist and enable the processes. The assisting field accumulates the dissociations and generates a charge transport.[41], [64]

2.9 Charge conduction/flow mechanisms in conducting polymers

Semiconductors are distinctively marked by the simultaneous presence of both electrons and holes, whereas in metals, only electrons are present. This means that current conduction in polymers (as is the case for all semiconductors) is characterised by the motion of both charge carriers (that is, electrons and holes) in opposite directions. For metals, current conduction involves the flow of electrons only. An organic photovoltaic device of the metal/polymer/metal assembly has the structural presence of metal/polymer junctions sandwiching a bulk semiconductor (or semiconductor blend) material. Potential barriers have illustratively been explained to develop at these interfaces, leading to the creation of rectification phenomena (that is, diode characteristics) which are now understood to be associated with potential barriers at metal/polymer interfaces (or in general metal/organic semiconductor interfaces). This means that in the absence of illumination (that is in the dark) an organic photovoltaic device (for example, organic solar cell) is a diode. This characteristic can be used to distinguish between a well fabricated solar cell and one with many shortcomings.

The fundamental electric current conduction (that is, simultaneous flow of electrons and holes) processes in metal/polymer/metal devices are mainly explained by two theories, which are, charge carrier injection from the metal electrode into the polymer and vice versa at metal/polymer/metal interfaces and charge transport in the bulk polymer material. The domination of one over the other depends on the particular settings of the experimental parameters, such as temperature, electrode workfunction, external bias, surface density of states, trap density, transport and trapping levels of the polymer.[10] One of the two processes may occur at a much lower rate than the other. Since the two contribute to the carrier flow through the device, it means that the slower process limits the carrier dynamics and therefore controls (or dominates) the characteristics of the current through the device. To emphasise that the current

characteristics are ascribed to the lower rate mechanism, the current is referred to as either injection limited, if the carrier cross-over at the interface is of lower rate or bulk transport limited,[10], [16] if the carry-through transportation rate by the polymer material is weaker. The transition between injection limited and bulk transport limited depends upon the bias (field) and the temperature. Core variables that have a significant bearing on whether the current is injection limited or bulk transport limited (commonly short- termed bulk limited or transport limited) are the externally applied electric field and the height of the potential barrier to be overcome (see Figures 2.5 and 2.6). Currently, the widely applied understanding is that of taking barrier heights of less than 0.2 eV to be presenting insignificant hindrance to the injection and therefore, the associated current is generalized as bulk limited. Barrier heights between 0.2 eV and 0.5 eV account for the transition range, whilst those above 0.5 eV and with non-extreme biases have corresponding currents described as injection limited.[65]

The preceding introductory remarks in this section converge at the realisation that the current-voltage J(V) characteristics of metal-polymer-metal devices are in many ways controlled by the charge carrier injection processes from the injecting contacts and the transport mechanisms in the bulk polymer material. We present a deeper discussion about these phenomena in the next subsections in order to contribute to the enhancement of the understanding of the physics of such conjugated polymer assemblies and also for subsequent use in the characterisation of our devices.

For charge transport in the bulk, it is the morphology of the bulk which contributes greatly to the way in which charge flows through the active material/blend. Once the carrier injecting contact can provide a reservoir of carriers, the behaviour of the injected charge carriers and hence the current, is controlled by the properties of the bulk material in which the charge carriers will now be flowing. Charge transport in the bulk may be of space charge limited current (SCLC), hopping and/or percolation forms. These forms are however not exhaustive, because transport mechanisms in such devices of organic origin are still not clearly understood. Each of the transport forms may be accomplished through diffusion, drift, etc., processes. For SCLC, the condition is that one of the electrodes must be ohmic. This means that it should be capable of supplying charge carriers to the bulk polymer (semiconductor) material at a rate which surpasses the rate at which the bulk can transport the handed over carriers. Since the bulk material fails to

immediately transport all the injected charge, the result is that charge delays and piles up (accumulates) in the polymer region near the injecting electrode and builds up an electric field that hinders further injection. Such heaped up cloud of charge, spreading over a significant region of space in the active material, is referred to as space charge. It is the one which slows down (limits) or determines the rate of charge flow (that is, current) within the device. Since space charge is limiting the current in this case, it is for this reason that such current is referred to as space charge limited current (SCLC).

2.9.1 Charge carrier injection mechanisms at metal/active layer/metal interfaces

Whilst the following charge flow mechanisms can be generalized for semiconductors, we confine our discussion to conducting polymers of the conjugated form and fullerenes.

In Section 2.4 we deliberated that the function of an electrical contact is either to enable or to block charge carrier injection. There are two possible ways in which charge carriers (electrons and holes) can be injected from an electrode (metal) into a polymer (or vice-versa) across the metal-polymer interface and these are: thermionic emission and quantum mechanical tunneling. There is also the diffusion theory which accounts for the charge carrier drift/diffusion process from the depletion region (adjacent to the junction, in the semiconductor) into the metal.[66] The theory assumes a bias drop inside the depletion region, in which case, the barrier does not present an obstacle to the flow of charge across the junction and we shall therefore not consider it.

In order for charge carriers to be injected from the metal into the polymer, they must overcome the potential barrier at the metal-polymer junction. If the potential barrier ϕ_B is of small enough height $\left(\phi_B >> \sqrt{k_B T/m_e}\right)$ or at high temperatures T $\left(T >> e\phi_{sc}/k_B\right)$, many charge carriers energetically surmount the junction barrier and cross over into the (organic) semiconductor. Note that this is a classical process enabled by the charge carrier's possession of high enough thermal energy. Such thermally induced flow of charge carriers over a potential energy barrier is termed thermionic emission.[10], [67] The process occurs, because the thermal energy given to the charge carrier overcomes the work function of the material (metal, in the case of injection from metal into polymer). In this regard, thermionic emission theory assumes that charge carriers, which have energy larger than the top of the barrier, will cross the barrier, provided they move towards

the barrier. In this regard, the theory assumes an abrupt bias drop at the metal/semiconductor interface and neglects scattering adjacent to the barrier.[66]

At low temperatures or high electric fields , the dominant transport across a Schottky barrier is quantum mechanical tunneling, which can either be direct tunneling (field emission) at the quasi-Fermi level, or thermally assisted tunneling (thermionic field emission). Whilst direct tunneling takes place at the quasi-Fermi level, thermally assisted tunneling occurs above the Fermi level, but below the top of the barrier.[66] Figure 2.25, depicts these exchange injection mechanisms at a metal-organic semiconductor (active layer) junction.

The type of injection is predominantly dependent on the potential barrier height. In the event of the charge carriers being confronted by a potential barrier of a large value, a small number of the carriers will likely have energies greater than the potential barrier height. As such, negligible thermionic emission across the junction will take place. The injection can then only occur through quantum mechanical tunneling of the charge carriers through the potential barrier. The mechanism is that the charge carriers tunnel from the metal to the empty states at the LUMO or HOMO level of the polymer. On the other hand, if the concentration of impurities in the polymer layer is high, tunneling may occur from the metal to the empty localized states in the polymer layer and constitute a kind of hopping process. The smallest barrier at any given metal- organic semiconductor junction always dominates the injection.[68-69]

The tunneling current may also show rectifying behaviour, but the polarity of the rectification is opposite that observed in thermionic current. In thermionic emission, the large positive current is a result of the lowering of the band bending in the semiconductor, which implies easier flow of charge carriers from the semiconductor into the metal.[66] Charge conduction in the tunneling regime has some dependence on the magnitude of the bias. For very small bias, the current in both directions should be linear. However, when the bias is smaller than the barrier height, tunneling in the reverse biased contact may be larger, because the tunneling distance is smaller than in the forward biased contact.[66]

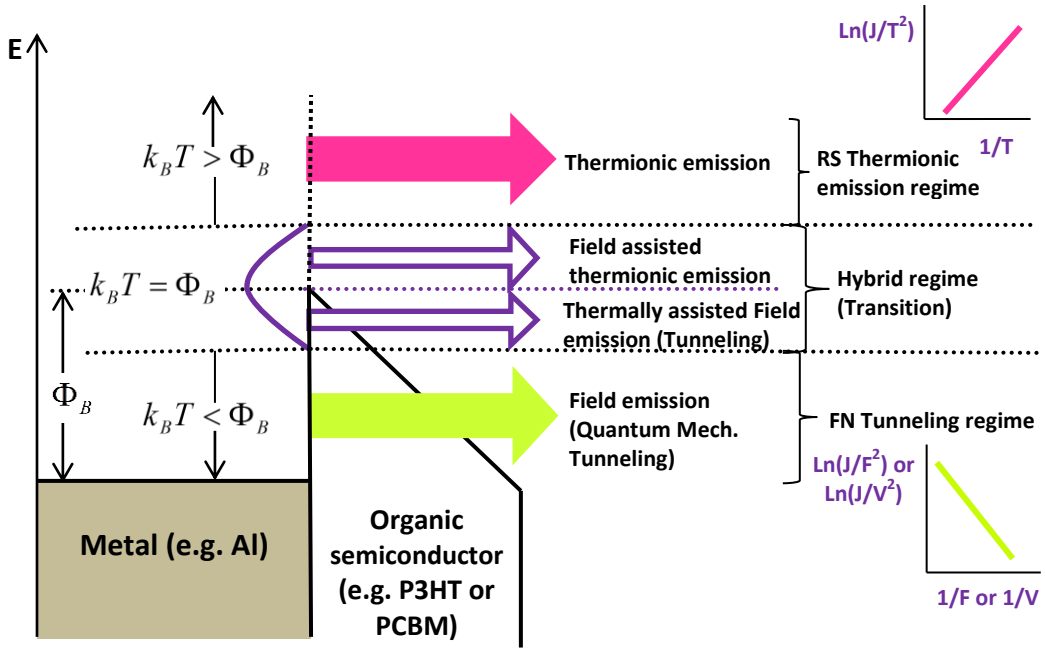

Figure 2.25 *Injection mechanisms through and above a triangular potential barrier at a metal-organic active layer interface. Φ_B is the potential barrier height.*

Assuming no presence of surface states at the metal-organic semiconductor interface (which may pin the Fermi level between a dielectric and the electrode) and also no depletion layer due to impurity doping, the energy barriers that regulate hole and electron injection are respectively (refer to Figures 2.5 and 2.6): $\phi_{Bh} = \phi_{m\,(anode)} - I = (E_g + \chi)$ and $\phi_{Be} = \phi_{m\,(cathode)} - \chi$ (2.9)

where

$\phi_{m\,(anode)}$	is the workfunction of the (positive metal) electrode
$\phi_{m\,(cathode)}$	is the workfunction of the (negative metal) electrode
$I = (E_g + \chi)$	is the ionization energy of the organic dielectric (semiconductor)
χ	is the electron affinity of the organic dielectric (semiconductor)
E_g	is the (forbidden) energy gap of the dielectric (semiconductor)

The parameters in Eq. (2.27) help to show at which energy levels hole and electron transport proceed (which in effect indicates where the HOMO and LUMO are located energetically).

Depending on the magnitude of the bond energy ΔE, between HOMO and LUMO, the measured current can either be injection limited or (bulk) transport limited. The bulk transport limited characteristics are treated in Section 2.9.2.2.

Current is injection limited if the bulk (active material) clears away and transports all the charge carriers injected into it and performs these clearing and transportation chores at a rate that prevents any accumulation of the injected charge near the injecting electrode. In this study, the term 'charge injection' refers to 'charge flow across a metal-polymer junction. Connected to this is the term 'injection limited', which we use in reference to the impedance to/hindrance to/delay in charge flow within the device, strictly imposed by the electrical contacts (that is, metal-polymer interfaces in this case).

The models which describe charge injection mechanisms (that is, thermionic emission and quantum mechanical tunneling) at metal/polymer junctions are Richardson-Schottky (RS) and Fowler-Nordheim (FN) respectively. The two are briefly described in the next subsections and are used in characterising the electrical behaviour of the solar cells fabricated in our study.

2.9.1.1 The Richardson-Schottky (RS) Thermionic Emission current model

Thermionic emission model is based on the premise that only those electrons with energies higher than the conduction band energy at the metal-polymer junction have a share in the resultant current. According to the RS model, if an electron from the metal acquires enough thermal energy to surmount the maximum potential barrier formed by the superposition of the external potential (due to the applied (bias) voltage) and the image charge potential, it can then be injected into the polymer.[10], [16], [70-71] The model holds for low (applied) electric fields and higher temperatures. With consideration of the lowering effect of the image force on the potential height, The Richardson-Schottky Emission Model is the Schottky equation (which is the RS model) is given by,[10], [16], [70-72]

$$J = A^{*}T^{2}\exp\left(\frac{-\phi_B}{k_B T}\right)\exp\left[\left(\frac{q^3 V}{4\pi\varepsilon_0\varepsilon_r d}\right)^{\frac{1}{2}} / k_B T\right] \tag{2.10}$$

where ϕ_B, d, ε_0 and ε_r are the interface potential barrier height, active film thickness, permittivity of free space and relative permittivity (optical dielectric constant) respectively; k_B is Boltzmann's constant, q is the elementary (electronic) charge, T is the thermodynamic temperature, V is the applied (bias)voltage (which is positive for forward bias and negative for reverse bias) and A^* is the Richardson-Schottky constant. For free electrons,

$$A^* = 4\pi q m^* k_B^2/h^3 = 120 \text{ A/cm}^2\text{K},^{[10]}$$

where, h is Planck's constant. The effective mass of the carrier m^*, which actually depends on the anisotropy of the (polymer) material,[71] is assumed to be equal to that of the free electron.

For the case in which temperature *T* is constant, RS thermionic emission can still be investigated for by variation of bias voltage at constant temperature through rearrangement of Equation (2.10), followed by taking the natural logarithm of the rearranged equation. This leads to the equation

$$Ln\,J = Ln\,A^* + 2\,LnT - \frac{\phi_B}{k_B T} + \left[\left(\frac{q^3 V}{4\pi\varepsilon_0\varepsilon_r d}\right)^{(1/2)} \frac{1}{k_B T}\right]$$

which can be rewritten as

$$Ln\,J = Ln\,A^* + 2\,LnT - \frac{\phi_B}{k_B T} + \left[\left(\frac{q^3}{4\pi\varepsilon_0\varepsilon_r d}\right)^{(1/2)} \frac{1}{k_B T}\right]\sqrt{V} \qquad (2.11)$$

Based on Equation (2.11), RS plot of $Ln\,J$ versus $\sqrt{V}$ is made. This RS plot must be a straight line with positive slope/gradient if the injection of charge through the potential barrier at the metal-polymer interface is by thermionic emission.

From Equation (2.11), the slope of the RS curve is given by $\frac{1}{k_B T}\sqrt{\frac{q^3}{4\pi\varepsilon_0\varepsilon_r d}}$ (2.12)

The intercept on *Ln J* axis = $Ln\,A^* + 2\,LnT - \frac{\phi_B}{k_B T}$ (2.13)

From Equation (2.13), the potential barrier ϕ_B corresponding to injection by thermionic emission at the metal-polymer junction of the device kept at constant temperature T is then given by

$$\phi_{B(RS\ thermionic\ emission\ at\ constant\ temp)} = \left(Ln A^* + 2\,LnT\right)k_B T \tag{2.14}$$

Since $F = V/d \Rightarrow V = Fd$, where F is the electric field due to V. Substituting V in Equation (2.11) gives $Ln J = Ln A^* + 2\,LnT - \frac{\phi_B}{k_B T} + \left[\left(\frac{q^3}{4\pi\varepsilon_0\varepsilon_r d}\right)^{(1/2)} \frac{1}{k_B T}\right]\sqrt{Fd}$, which leads to

$$Ln J = Ln A^* + 2\,LnT - \frac{\phi_B}{k_B T} + \left[\left(\frac{q^3}{4\pi\varepsilon_0\varepsilon_r}\right)^{(1/2)} \frac{1}{k_B T}\right]\sqrt{F} \tag{2.15}$$

Equation (2.15) is the alternative for Equation (2.11) if the variable parameter in the experimentation is the applied electric field F, in which case, the plot of $Ln\ J$ vs $\sqrt{F}$ should also be a straight line of positive slope if RS thermionic emission is taking place at the metal polymer interface of the isothermal device.

2.9.1.2 The Fowler-Nordheim (FN) Tunneling (Field Emission) current model

If the barrier height is large and the applied electric field is sufficiently high, the potential barrier may become so thin that field emission (quantum mechanical tunneling) becomes significant. Field emission therefore refers to the quantum mechanical tunneling (penetration) through a potential barrier, by charge carriers (electrons or holes) from a metal to a semiconductor or insulator when the assembly is subjected to an intense electric field, which however, is not high enough to cause breakdown. As alluded to in Section 2.9.1, quantum mechanical tunneling can also occur at low temperatures. At such favourably low temperatures, most electrons tunnel at the Fermi level of the metal, thus constituting strict field emission (F-emission). At intermediate temperatures, most electrons tunnel at an energy level E_m above the Fermi level of the metal, which constitutes the so-called thermionic field or thermally assisted field emission (T-F emission). When at very high temperatures (but not so high to damage (degrade) the assembly) the main contribution is thermionic emission (see Figure 2.25).

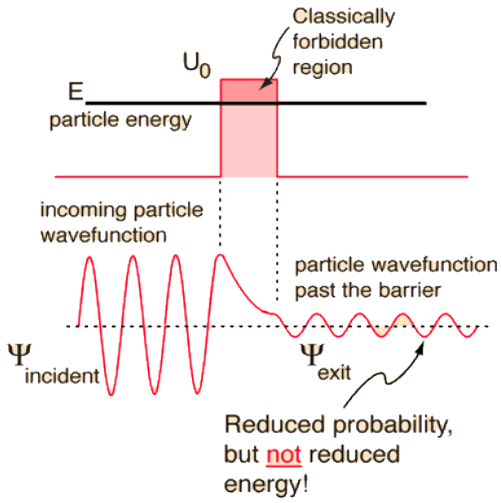

Figure 2.26 *Illustration of the quantum mechanical tunneling phenomenon* [73]

Figure 2.26[73] illustrates the quantum mechanical (wave-mechanical) tunneling phenomenon in a simple form. Though shown for a rectangular barrier, the phenomenon is the same for all barrier types. Quantum mechanically, a quantum particle (like an electron) that impinges on a potential barrier whose height is larger than its incident kinetic energy (Figure 2.26) will definitely penetrate a certain distance into the barrier. This is contrary to the classical perspective, but quantum mechanics asserts the behaviour by taking into account the wave-particle duality of matter, which is significantly pronounced in quantum particles. The FN formulation derives the tunneling current by starting from the one dimensional (along x axis) time independent Schrödinger equation for the wave-function of an electron (or other quantum particle). A parallel derivation can be the following:

The time independent Schrödinger equation is

$$-\frac{\hbar^2}{2m}\frac{\partial^2\psi}{\partial x^2}+V(x)\psi(x)=E\psi(x) \tag{2.16}$$

which can be written as

$$\frac{\partial^2\psi(x)}{\partial x^2}=\frac{2m(V(x)-E)}{\hbar^2}\psi(x) \tag{2.17}$$

If we assume that $V(x) - E$ is independent of position in the interval between x and $x + dx$ and that the potential $V(x)$ varies slowly with distance x, we can engage the Wentzel-Kramers-Brillouin (WKB) approximation and arrive at the solution of Equation (2.17), which is shown in Equation (2.18) for the infinitesimal distance dx.

$$\psi(x+dx)=\psi(x)\exp\left(-\frac{\sqrt{2m[V(x)-E]}}{\hbar^2}dx\right) \tag{2.18}$$

The negative sign inserted in the equation is to reinforce our assumption that the quantum particle is moving from left to right. Since the potential $V(x)$ varies slowly with distance x, the probability amplitude of the wave function at $x = x_1$ can be related to the probability amplitude of the wave function at $x = 0$ by the WKB approximation

$$\psi(x_1) = \psi(0)\exp\left(-\int_0^{x_1} \frac{\sqrt{2m[V(x)-E]}}{\hbar}\,dx\right) \tag{2.19}$$

where $\psi(0)$ is the probability amplitude of the incident wave function (that is, the wave incident to the potential barrier at $x = 0$, where tunneling starts). Since the incident electron energy E is smaller than the potential $V(x)$, the classical expectation would be that of no penetration. Interestingly, this is not so for the quantum particle, whose wave ceases to oscillate sinusoidally as shown in Figure 2.26 before incidence, but decays exponentially in probability amplitude as it penetrates the barrier. Since there is no scattering, its energy E remains constant, as Figure 2.26 shows. By further engagement of the WKB approximation, the tunneling probability $T(E)$ can be estimated for the assumed triangular potential barrier for which $V(x) - E = q\phi_B\left(1 - \dfrac{x}{x_1}\right)$

$$T(E) = \frac{\psi(x_1)\psi^*(x_1)}{\psi(0)\psi^*(0)} \approx T(0)\exp\left(-2\int_0^{x_1} \frac{\sqrt{2m}}{\hbar}\sqrt{q\phi_B\left(1-\frac{x}{x_1}\right)}\;dx\right) \tag{2.20}$$

where x is the distance into the barrier between zero (0) and x_1. Equation (2.20) can be rewritten in the form

$$T(E) = T_0\exp\left\{-2\int_0^{x_1}\sqrt{\frac{2m}{\hbar^2}[V_B(x)-E]}\;dx\right\} \tag{2.21}$$

where $V_B(x)$ the barrier energy as a function of the distance x, m is the mass of the tunneling particle, E is the total energy of the quantum particle (which is smaller than the barrier potential $V(x)$) and T_0 is the tunneling probability when the energy of the particle is larger than the barrier height (which is virtually equal to 1). The tunneling probability then becomes

$$T(E) = \exp\left(-\frac{4}{3}\frac{\sqrt{2qm}}{\hbar}\frac{\phi_B^{3/2}}{F} \right) \tag{2.22}$$

where F is the electric field given by $F = \frac{\phi_B}{x_1}$.

In a given metal-polymer interface, a combination of diffusion current, thermionic emission current and tunneling current can exist, but typically only one current mechanism dominates. When field emission dominates, the Fowler-Nordheim model, which ignores image charge effects, assumes the quantum tunneling of electrons from the metal through a triangular potential barrier into unbound continuum states[10] and postulate that the tunneling injection current density J is given by

$$J = AF^2 \exp\left(-\frac{8\pi\sqrt{2m^*}\,\phi_B^{3/2}}{3hqF} \right) \tag{2.23}$$

where m^* is the effective charge carrier mass, F is the applied electric field and A (in A/V^2) is a rate coefficient that contains a tunneling prefactor and rate of current back-flow, h is the Planck constant equal to 6.62607004 × 10^{-34} m^{2}kg/s and q is the electronic charge. Equation (2.23) is the Fowler-Nordheim tunneling current, which can also be expressed in terms of the applied (bias) voltage V by substituting F with V/d. The model is used in the $J(V)$ characterisation of our devices. The tunneling current therefore depends exponentially on the square root of the cube of the barrier height. The expression for A has been deduced to be[10] $A = q^3 / 3\pi h\phi_B$.

Equation (2.23) can be rewritten as $J = AF^2 \exp\left(\frac{-\kappa}{F}\right)$ (2.24)

where k is a constant given by[10] $k = \frac{8\pi\left(\sqrt{2m^*}\right)(\phi_B)^{\frac{3}{2}}}{3hq}$ (2.25)

The barrier height is then given from (2.25) by $\phi_B = \left(\frac{3hqk}{8\pi\sqrt{2m*}}\right)^{\frac{2}{3}}$ (2.26)

The tunneling current density J may also be obtained from

$$J = q\nu_R \rho T(E), \qquad \text{where } \nu \text{ is the Richardson velocity} \tag{2.27}$$

Equation (2.24) can be rewritten as $$\frac{J}{F^2} = A\exp\left(-k\left(\frac{1}{F}\right)\right) \tag{2.28}$$

from which we obtain $$Ln\left(\frac{J}{F^2}\right) = Ln\,A - k\left(\frac{1}{F}\right) \tag{2.29}$$

Therefore if quantum mechanical tunneling is ongoing, the graph of $Ln\left(\frac{J}{F^2}\right)$ against $\frac{1}{F}$ should be a straight line of negative slope equal to $-k$. With known k, the barrier height ϕ_B during tunneling can then be obtained from Equation (2.26).

However, use of this method to obtain ϕ_B does not explicitly expose the dependence of ϕ_B on the thickness d of the active layer, because d is implicit in the applied electric field F (from $F = \frac{V}{d}$, where V is the applied (bias) voltage). Therefore, for practical applications, it is convenient to express the Fowler-Nordheim tunneling model in terms of the applied (bias) voltage V by substituting F with V/d. Following on this, it implies that Equation (2.29) becomes

$$Ln\left(\frac{J}{\left[\frac{V}{d}\right]^2}\right) = Ln\,A - k\frac{1}{\left[\frac{V}{d}\right]} \tag{2.30}$$

from where we arrive at $$Ln\left(\frac{J}{V^2}\right) = Ln\,A - Ln\,d^2 - kd\left(\frac{1}{V}\right) \tag{2.31}$$

This implies that the graph of $Ln\left(\frac{J}{V^2}\right)$ vs $\frac{1}{V}$ is a straight line of negative slope (or gradient) equal to $-kd$ if tunneling is overwhelming. Therefore, in the tunneling regime,

$$Gradient\,of\ Ln\left(\frac{J}{V^2}\right) vs \frac{1}{V} plot = -kd = \frac{-8\pi\left(2m^*\right)^{\frac{1}{2}}\left(\phi_B\right)^{\frac{3}{2}} d}{3hq} \tag{2.32}$$

From equation (2.32), $$\phi_B = \left\{ -\frac{3hq.(gradient)}{8\pi d\sqrt{2m*}} \right\}^{\frac{2}{3}} \quad (2.33)$$

2.9.2 Charge transport mechanisms, in the bulk conducting polymer

In polymer solar cells, charge carriers either photo-generated or injected into the bulk active layer have to reach the electrodes. Various charge transport mechanisms accounting for their motion (to the electrodes) while inside the polymer material or composite have been identified, the main ones being diffusion, drift or both, which can be of hopping, percolation, etc. form. These various transport mechanisms are dependent upon the device and the polymer material attributes such as, crystallinity, nature/level of disorder, amorphousness, etc. This shows that once the carrier injecting contact can provide a reservoir of carriers, the behaviour of the injected carriers and hence the current is controlled by the properties of the material in which the charge carriers are flowing. In this section we delimit our discussion to hopping and space charge limited current (SCLC), which contribute significantly to transport mechanisms in the bulk.

2.9.2.1 Hopping Mechanism

The random distribution of conjugation length of polymer chains in the bulk of the material gives rise to the distribution of electronic states where regular lattice arrangement is lacking. This implies that a polymer film can be described as a discontinuously distributed amorphous phase, in which the discontinuity is introduced by the small crystalline like ordered phases of small dimensions. This variation in molecular morphology leads to the broadening of the electronic density of states and results in hopping[30]. Hopping transport can be approximated by a random walk which is restricted by energetic and spatial disorders. Its transport mechanism is characterised by a considerable activation energy, which renders its transport mobility to be field and temperature dependent. The mobility obeys the Poole-Frenkel law[74]

$$\mu = \mu_0 \, exp\left(\gamma\sqrt{E}\right) \quad (2.34)$$

where μ_0 is the zero field mobility, γ is the field activation factor and E is the net electric field.

Hopping mechanism in polymers considers electrons or hole to be hopping from one chain fragment (section) to another of the same chain or from one chain to anther chain as illustrated in Figure 2.27.

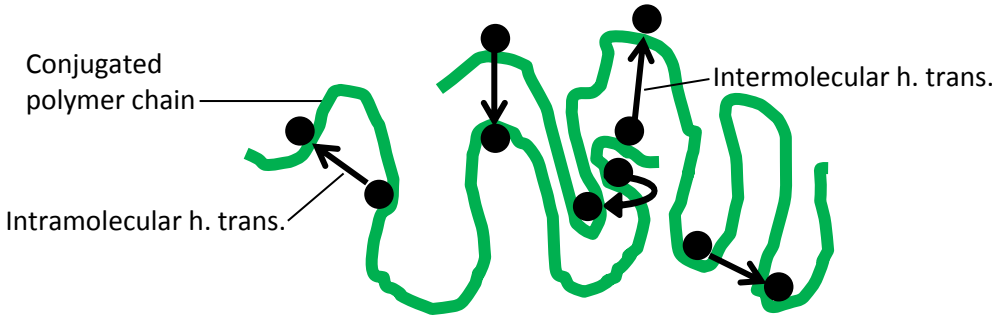

Key: Black spheres ● ⇒ charge carriers of the same kind (either all electrons or all holes)

Figure 2.27 *Intramolecular* (*intrachain*) *and intermolecular* (*interchain*) *hopping transport*

Hopping is considered as the main phenomenon contributing to charge transport in semiconducting polymers. Most of the conducting polymers show a better hole transport than electron transport.[41] Such disordered systems are subject to an energetic spread of the charge transport sites, which are often approximated in shape by a Gaussian density of states (GDOS or simply DOS).[74] The charge carriers, which are initially relaxed to equilibrium states, are sometime later excited to higher energy states through thermal stimulation. The Gaussian disorder model (GDM) was developed through a Monte Carlo simulation that assumes a Gaussian distribution of transport site energy[75] given by

$$\rho(\varepsilon) = (2\pi\rho_{DOS}^2)^{-1/2} exp\left(-\frac{\varepsilon^2}{2\sigma_{DOS}^2}\right) \tag{2.35}$$

where σ_{DOS} is the width of the Gaussian site energy distribution and the energy ε is measured relative to the centre of the DOS. In the GDM formalism, the jump rate υ_{ij} between adjacent sites i and j of the energyε_i and ε_j, respectively. The separation distance R_{ij} is the Miller-Abraham's type, which is.[30], [76-77]

$$\upsilon_{ij} = \upsilon_0 exp\left(-2\gamma a \frac{\Delta R_{ij}}{a}\right) \begin{cases} \exp\left(-\frac{\varepsilon_{j-}\varepsilon_i}{k_B T}\right), & \varepsilon_j > \varepsilon_i \\ 1, & \varepsilon_j < \varepsilon_i \end{cases} \tag{2.36}$$

Charge carriers that hop to locations higher in energy are thermally promoted or accelerated by a field. The effective potential energy barrier for hops to higher energy is given by the difference between the two states.

2.9.2.2 Space Charge Limited Current (SCLC) Theory/Model

Current is injection limited if the bulk clears away and transports all the charge carriers injected into it and performs these clearing and transportation chores at a rate that prevents any accumulation of the injected charge near the injecting electrode. If the injection rate outweighs the transportation rate, then the current is said to be transport limited (or bulk-transport limited or simply, bulk limited). This situation implies that the bulk (polymer material) is failing to cope with the injection pace, since it cannot at once sweep away and transport the injected carriers. As such, the 'stranded' charges accumulate inside the polymer, in the region adjacent to the injecting electrode and gradually develop an electric field that hinders continued injection. This accumulated cloud of charge, spreading over a significant region of space, is referred to as space charge and the corresponding current is called space charge limited current (SCLC). In a photovoltaic device, if at least one contact can inject (within the locality) higher charge densities than those of the material in thermal equilibrium without carrier injection, then space charge limited currents can surface.[78]

The space charge limited (SCL) dark current conduction (not resulting from light absorption or thermal perturbations) takes place when the contacting electrodes (under bias) are able to inject either electrons into the conduction band or holes into the valence band of a semiconductor or an insulator and when the initial rate of such carrier injection is higher than the rate of recombination, so that the injected carriers will form a space charge to limit the current flow.[16]
Carrier injection into a solid material is generally categorized into two divisions, which are single injection and double injection. In single injection, the current flow is mainly due to one type of carrier (electrons or holes) injected from a contacting electrode into the solid. The injected carriers gradually develop a space charge resulting in single carrier SCLC. For double injection, the current flow is comprised of two different types of charge carriers; electrons injected from the cathode and holes from the anode. In double injection, all the electrical properties are controlled by recombination kinetics. The recombination process may either be bimolecular (which implies band-to-band electron-hole recombination) or it may take place

through one or more sets of localised recombination centres. The J(V) characteristics strongly depend on the concentration and the distribution function of traps inside the active material and other boundary conditions. Since a few of our devices will be of the one-carrier current injection class, with the majority belonging to the two-carrier current (double) injection category, we present a brief discussion of both processes. We start with single injection and then treat double injection thereafter. Actually, the space charge electric conduction is quite intricate, because many competing processes are at play and so to tone down the otherwise burdensome solution, we resort to simplifying assumptions.

2.9.2.2.1. Modeling (single carrier) SCLC: Many transport parameters such as, charge carrier mobility, concentration of traps, parasitic resistances, etc., can be estimated from models of the transport of charge carriers in the SCLC region. In this section a formulation of the space charge limited (SCL) model (the current of which is the SCLC) is described, due to its application in the electrical characterisation of the bulk regions of our devices. Furthermore, the model/formalism provides a deeper understanding of the efficiency-limiting factors in polymer solar cells.

Since the active material in a polymer solar cell (and light emitting devices) is thin (nano-scale order of magnitude), charge transport in such devices is assumed to be a one dimensional mechanism. We can therefore invoke Poisson's one dimensional and continuity equations for electrons and holes, which constitute the fundamental transport equations modeling charge transport behaviour. Assuming negligible effect of traps, the drift-diffusion current equations and the Poisson's equation are respectively given by[30]

$$J_n = e\left[-\mu_n(x)n(x)\frac{d\psi}{dx} + D_n\frac{dn}{dx}\right] \tag{2.37}$$

$$J_p = e\left[-\mu_p(x)p(x)\frac{d\psi}{dx} + D_p\frac{dp}{dx}\right] \tag{2.38}$$

$$\frac{dE(x)}{dx} = \frac{e}{\epsilon}[p(x) - n(x)] \tag{2.39}$$

where J_n and J_p are the electron and hole current densities respectively

$n(x)$ and $p(x)$ are the respective electron and hole densities

D_n and D_p are the respective electron and hole diffusion constants

μ_e and μ_p are the electron and hole mobilities respectively

$\varepsilon = \varepsilon_0 \varepsilon_r$ is the permittivity of the polymer material blend or single component D/A

The electric field $E(x)$ and the electrostatic potential $\psi(x)$ are connected by the equation

$$E(x) = -\frac{d\psi}{dx} \tag{2.40}$$

The Einstein equation $$D = \mu k_B T \tag{2.41}$$

connects the mobility and diffusion coefficients. In Equation (2.41), k_B is Boltzmann's constant and T is the thermodynamic temperature.

In the SCL transport regime, the drift current dominates the net current flow and the diffusion component is often considered negligible.

2.9.2.2.1.1 The ideal case – Without traps (trap free solids): If we assume negligible trap density or traps free bulk, we can obtain an analytical expression of SCLC through simultaneous solution of the current equation (2.37) or (2.38) with the Poisson equation (2.39). This yields the practical equation

$$J = J_{SCL} = \frac{9}{8} \varepsilon \mu \frac{V^2}{d^3} \tag{2.42}$$

where μ is the charge carrier (electron or hole) mobility and d is the film thickness.

Equation (2.42) is true for a trap free SCL transport. It is referred to as Child's law for solids and is also often known as the Mott and Gurney equation or the square law for trap-free SCL currents (TFSCLC),[16], [79] Child's law is modeled on the basis of stringent adherence to the quadratic dependence of current (⇒ current density) on voltage. This means that if a Log J vs Log V plot has slope 2, then the behavior is characteristic of Child's law. However, this does not literally mean that there are no traps in the active material, but rather means that the traps are all filled.[80] A strikingly clear and undoubted difference between SCL currents and injection limited currents is that SCLCs depend on the thickness of the active layer (as can be deduced from Equation (2.42)), but injection limited currents do not. This characteristic difference provides an informed guidance to valid experimental set-ups and the subsequent analyses of results of conjugated

polymer-based photovoltaic devices. The dependence of current on the electric field is in most cases not enough basis of differentiating (TF)SCL currents from injection limited currents.

Equation (2.42) assumes no effect of the thermally generated carriers. At low applied voltages, the J(V) characteristics may follow Ohm's law if the density of the thermally generated free carriers ρ_0 is predominant such that[16]

$$q\rho_0\mu\frac{V}{d} \gg \frac{9}{8}\varepsilon\mu\frac{V^2}{d^3} \tag{2.43}$$

The start of the departure from Ohm's law or the start of the SCL conduction occurs when the inequality (2.43) becomes equal and $V = V_{th\ SCLC}$, where $V_{th\ SCLC}$ is the minimum (threshold or lower limit) bias voltage required for the transition from ohmic to SCL regime to take place. Therefore, using equation (2.43), the minimum applied (bias) voltage for this transition to take place is

$$V_{th\ SCLC} = \frac{8}{9}\frac{q\rho_0 d^2}{\varepsilon} \tag{2.44}$$

If equation (2.44) is rearranged in the form

$$\frac{d^2}{\mu V_{th\ SCLC}} = \frac{9}{8}\frac{\varepsilon}{q\rho_0\mu} \tag{2.45}$$

we can have the approximation

$$t_t \simeq \tau_d \tag{2.46}$$

where t_t is the charge carrier transit time and τ_d is the dielectric (or ohmic) relaxation time, which is a measure of the time required for the injected carriers to re-establish equilibrium. From Equations (2.45) and (2.46), we can deduce that when the transition from the ohmic regime to the SCL regime takes place, the carrier transit time t_t can be given by

$$t_t = \frac{d^2}{\mu V_{th\ SCLC}} \text{ at } V_{th\ SCLC} \tag{2.47}$$

and

$$\tau_d = \frac{\varepsilon}{q\rho_0\mu} \tag{2.48}$$

If the applied voltage V is less than $V_{th\ SCLC}$, then $t_t > \tau_d$, which implies that the injected carrier density ρ is less than the thermally generated carrier density ρ_0. Therefore, the injected carriers

will redistribute themselves with an inclination to maintain electric charge neutrality internally in a time comparable to τ_d and have no chance to travel across the specimen (material).[16]. The redistribution of the charge is termed the dielectric relaxation. In this case, the density of the carriers ρ_0 is not changed by the injected carriers, because the injection of ρ would be accompanied by a net space charge, which according to Gauss' law would generate an electric field that would exert an attractive force on nearby carriers of opposite charge. The attracted charges then accelerate in and neutralise the space charge. As a result, carriers of the same charge as the ones being injected, for example, holes in all regions of the specimen begin to drift in such a manner that the injected holes now do the business of replacing those holes flowing out at the contacting electrode. This leads to no significant change in the carrier (for example, hole) density everywhere within the polymer material.

Therefore, when $t_t > \tau_d$ the ohmic process is predominant and the effect of injected space charge is suppressed and when $t_t < \tau_d$ the SCL conduction is predominant and the ohmic process is suppressed. The transition from ohmic to the SCL conduction is not a sudden change, but rather a gradual change.[16] When the density of the thermally carriers ρ_0 inside the polymer material is larger than that of the injected carriers, the ohmic conduction becomes predominant and we can therefore set $V = V_\Omega$. The total current can then be qualitatively expressed as,[16]

$$J = q\rho_0\mu\frac{V_\Omega}{d} + \frac{9}{8}\varepsilon\mu\frac{V_\Omega^2}{d^3} \quad = q\rho_0\mu\frac{V_\Omega}{d} + q\rho_0\mu\frac{V_\Omega}{d} \quad = q(2\rho_0)\mu\frac{V_\Omega}{d}$$

$$\Rightarrow \qquad J_\Omega = q\rho\mu\frac{V_\Omega}{d} \tag{2.49}$$

which is Ohm's law equation.[16], [79] The parameter ρ is the overall (injected plus thermally generated) free charge carrier density of the active material, J_Ω is the ohmic current density and V_Ω is the applied (bias) voltage in the ohmic regime. If the slope of a $Log - Log$ plot of J(V) or I(V) at low voltages equals 1, then the behaviour can be attributed to Ohm's law. However, the bottom line is that ohmic compliance breaks down at the space charge limit when the injected charge carrier density is comparatively so large that the electric field generated in the polymer specimen (by the created space charge) overwhelms that due to the applied bias and result in the space charge limit characteristics taking centre stage.

2.9.2.2.1.2 The Real Case - With traps: When traps are present, most of the injected charge carriers are localised and do not contribute to current flow. Under such situations, the J(V) characteristics are determined by the density and energy distribution of the trap sites. However the considerations of this case are so huge that due to time constraints, its detailed treatment is beyond the scope of this study. Many factors come into play in different trap distribution categories like, traps confined in single or multiple discrete energy levels, traps distributed exponentially within the forbidden energy gap, traps distributed Gaussianly within the forbidden energy gap, whether shallow traps or deep traps, whether trap distribution is homogeneous or inhomogeneous, density of unfilled traps, etc. As such, we delimit most of our analyses to the ideal case blended with checks for the presence and impact of traps. Small inroads into quantitative considerations are only done for a few isolated cases which thus demand.

Also, in the case of traps confined in single or multiple discrete energy levels, the ohmic conduction predominates when the density of thermally generated free charge carriers ρ_0 inside the polymer material is greater than the density of injected carriers ρ. The onset of the transition from the ohmic to the SCL conduction follows the same principle discussed for the ideal case and takes place when the applied voltage becomes,

$$V_{th\,SCLC} = \frac{9}{8}\frac{q\rho_0 d^2}{\theta_a \varepsilon} \tag{2.50}$$

where θ_a is the ratio of the free carrier density to the total carrier (free and trapped) density and is given by

$$\theta_a = \frac{\rho}{\rho + \rho_t} \tag{2.51}$$

where ρ_t is the density of the trapped charge carriers.

Thus, for the trap free case, $\rho_t = 0$ and therefore, $\theta_a = 1$. Equation (2.50) shows that with all traps, θ_a is always less than unity. In fact, it could be as small as 10^{-7}.[16] For simplicity, equation (2.50) ignores the effect of the inhomogeneous (non- uniform) spatial distribution of traps.

From Equation (2.50) we can extract that: $V_{th\ SCL}$ increases with increasing ρ_0; the higher the concentration of traps, the higher is the value of $V_{th\ SCL}$. At quasi-thermal equilibrium of trapping and detrapping (when trapping and detrapping have reached steady state) the total density of injected carriers ρ_T is given by $\rho_T = \rho + \rho_t$. Therefore the effective mobility is

$$\mu_{eff} = \frac{\rho}{\rho_T}\mu = \left(\frac{\rho}{\rho + \rho_t}\right)\mu = \theta_a \mu \qquad (2.52)$$

where μ is the usual (trap free) mobility of the free carriers. In fact, ρ_T is the effective carrier density for electric conduction. Extending from Equation (2.52), the effective carrier transit time can be expressed in terms of free carrier transit time t_t at V_Ω (with the remembrance that $V_\Omega = V_{th\ SCLC}$) as[16]

$$t_{t\ eff} = \frac{t_t}{\theta_a} = \frac{d^2}{\theta_a \rho V_\Omega} = \frac{d^2}{\mu_{eff} V_\Omega} \qquad (2.53)$$

This means that the change from the ohmic to the SCL regime takes place when $t_{t\ eff}$ is approximately equal to τ_d.

There is always a transient supply of injected carriers when a voltage is applied across a polymer material. Even if $V < V_\Omega$(when ohmic conduction is normally predominant in the steady state), the ohmic behaviour can be observed only after these space charge carriers become trapped.[27] The SCL current for this case of traps confined in a single discrete energy level has been found to be given by.[16], [24]

$$J_{SCLC} = \frac{9}{8}\varepsilon\mu\theta_a \frac{V^2}{d_{eff}^3} \qquad (2.54)$$

which shows that $J_{SCL} \propto \frac{V^2}{d_{eff}^3}$, where d_{eff} is the effective thickness, which takes into account the effect of non-uniform spatial distribution of traps.

For traps distributed exponentially within the forbidden energy gap, the combined SCL current *J* is estimated by[16]

$$J = q^{1-l}\mu N_v \left(\frac{2l+1}{l+1}\right)^{l+1} \left(\frac{l}{l+1}\frac{\varepsilon}{H_b'}\right)^{l} \frac{V^{l+1}}{d_{eff}^{2l+1}} \tag{2.55}$$

which shows that $J_{SCL} \propto \frac{V^{l+1}}{d^{2l+1}}$

By setting $J = q\rho_0\mu\frac{V}{d}$ equal to equation (2.55) we obtain the applied voltage for the onset of the transition from the ohmic to the SCL conduction, which is given by

$$V_\Omega = \frac{qd^2H_b'}{\varepsilon}\left(\frac{\rho_0}{N_t}\right)^{1/l}\left(\frac{l+1}{l}\right)\left(\frac{l+1}{2l+l}\right)^{l+1/l} \tag{2.56}$$

When all the traps are filled up, a transition from the trapped SCL current to a trap-free SCL current will take place. By setting $J = \frac{9}{8}\varepsilon\mu\frac{V^2}{d^3}$ (which is the trap-free current $\langle Equation\ (2.42)\rangle$) equal to Equation (2.55) we obtain the trap-free limited (TFL) threshold voltage (V_{TFL})[81]

$$V_{TFL} = \frac{qd^2}{\varepsilon}\left[\frac{9}{8}\frac{H_b'^l}{N_t}\left(\frac{l+1}{l}\right)^{l}\left(\frac{l+1}{2l+l}\right)^{l+1}\right]^{1/(l-1)} \tag{2.57}$$

where, l is defined in terms of a characteristic trap distribution constant.[16], [67], [76], [82]

2.9.2.2.2 Space Charge Electric Conduction (SCLC) for Double (two carrier current) Injection

Double injection is characterised by charge carriers being injected into a semiconductor (or insulator) through simultaneous emission of electron and hole from the contacting electrodes. Electrons are emitted from the cathode, whilst holes are emitted from the anode. Such charge emitted upon absorption of light increases the electric conductivity of the polymer material. Under such conditions, $np > n_i^2$, where $n_i^2 = n_0p_0$, n_0 and p_0 are the thermally generated electron and hole densities respectively inside the polymer specimen, n_i is the electron (or hole) density of the intrinsic semiconductor, n and p are the free electron and hole densities respectively. Since all materials always have imperfections resulting in localised states, it means that the injected carriers in the material will either be temporarily captured at trapping centres or lost completely through recombination centres.[16]

Chapter 3

Underlying physical principles of organic solar cells

Prior to the presentation and analysis of our experimental settings and results obtained from fabrications of the carbon-based solar cells, it is crucial to get an insight into the fabrication of an organic solar cell (OSC), the underlying physics governing its operation, its characterisation techniques, optical limitations, response and behaviour, which impact on its power conversion efficiency. As such, the purpose of this chapter is to bring to light such prerequisites. As we do so, we confine our treatment to the bulk heterojunction (BHJ) polymer-fullerene solar cell, because it is central to this study. Our presentation is of a general approach and we leave the focus on specific materials used for the next chapter.

3.1 Organic solar cells (OSCs)

3.1.1 Structural configurations of OSCs

Two different structural configurations commonly adopted in organic photovoltaics (OPVs) are the normal and the inverted.[8-9], [83-85] Geometrically normal organic solar cells are of the structure: **substrate/semitransparent high workfunction cathode-hole collector/ active layer/ low workfunction anode-electron collector.**[8] (See Figure 3.1.) Under this structure, the anode is deposited as the last layer on top of the organic semiconductor blend.[8]

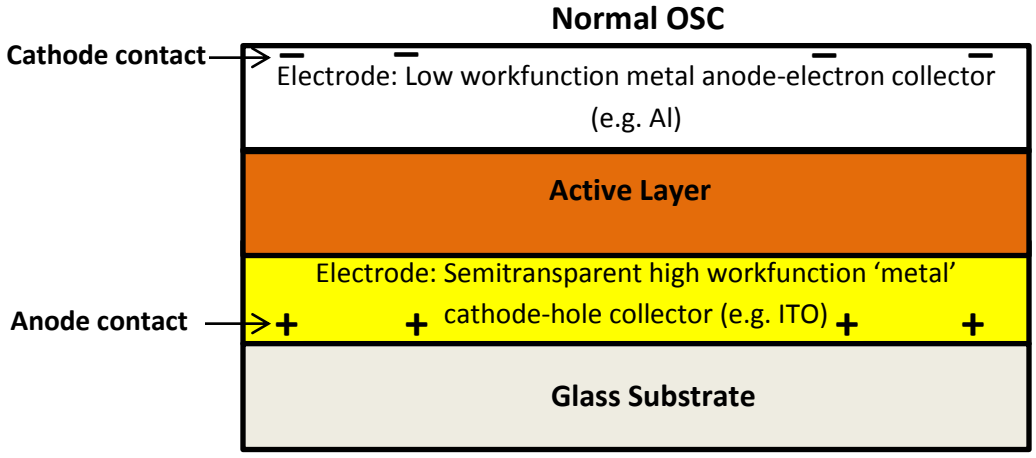

Figure 3.1 *Normal structure organic solar cell*

The down side of this architecture is that the low workfunction metal electrode can be easily oxidised in air, which lowers the device performance. As such, encapsulation of the device becomes necessary to protect it from oxidation. Alternatively, an inverted structure is used. An inverted OSC is of the structure: **substrate/cathode contact-electron collector/active layer/hole collector-anode.**[8] (See Figure 3.2.) Under this structural configuration, the low workfunction metal is in contact with the substrate, while the high workfunction metal is exposed to air.[8]

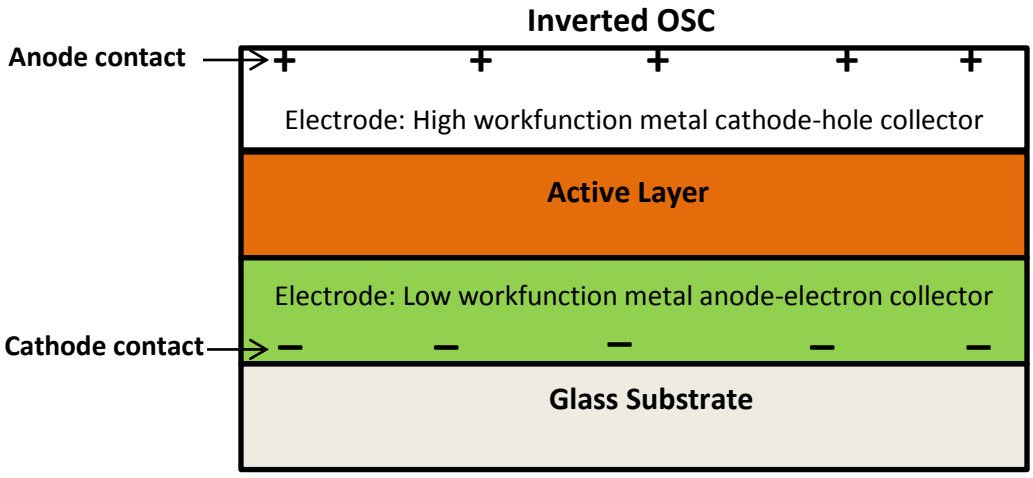

Figure 3.2 *Inverted structure organic solar cell*

For organic solar cells with one of the electrodes being transparent conducting oxide (such as ITO), a normal cell would have indium tin oxide being the hole collecting electrode ($\phi_{ITO} \approx 4.7$eV) and the electron collecting electrode would be a metal with a lower workfunction than ITO (like aluminium (Al, $\phi_{Al} \approx 4.2$ eV)). In inverted organic solar cells, ITO is the electron collecting electrode and a metal with a work function greater than ITO (like silver or gold) serves as the hole collecting.[8], [85] When an ITO substrate is used in the inverted structure, its role is flipped from collecting holes (which it does under normal architecture) to collecting electrons. This is possible, because the workfunction of ITO (4.5 to 4.7 eV) lies between the typical HOMO and LUMO of common active composites (like P3HT:PCBM).[8] As such, ITO can collect either holes or electrons depending principally on the contact properties of the coating layer on top of its (that is, ITO) surface.[8] In the normal structure, a relatively higher workfunction layer, mostly PEDOT:PSS, which collects holes, is cast on top of ITO, whereas in

the inverted architecture, the workfunction of ITO is lowered by coating with a low workfunction material and it collects electrons.[8] One advantage of the inverted structure is that the need for using PEDOT:PSS, which is acidic in nature, is circumvented. This study uses the normal structure.

3.1.2 Attributes of the normal structure bulk heterojunction organic solar cell

Figure 3.3 is a schematic illustration of the geometrical structure of the layers of a normal polymer-fullerene bulk heterojunction solar cell with a high workfunction buffer layer. (Also refer to Figure 3.1.)

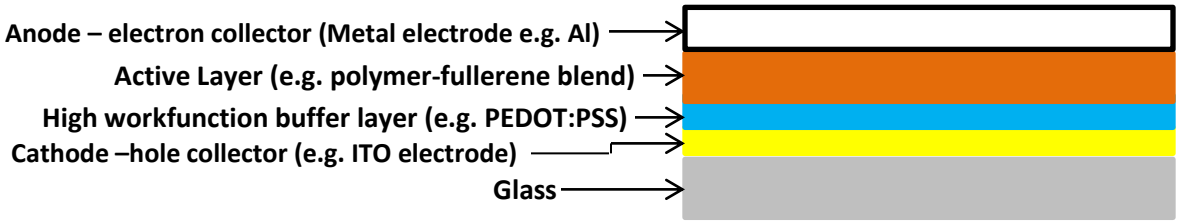

Figure 3.3 *Normal structure organic solar cell with high workfunction buffer layer*

This type of solar cell fundamentally consists of five layers, which are: glass, semitransparent hole collector electrode, high workfunction buffer layer, active layer and electron collector electrode. In OSCs, as in an electrochemical cell, the terminological concept of what electrode is anode and what is cathode is based on the direction of flow of electrons. Electrons flow to the anode electrode. In an electrochemical cell, the anode is the electrode at which oxidation occurs and electrons flow from the electrolyte to it. Analogously, in a normal OSC, the anode electrode is the low workfunction metal or metallic electrode to which electrons from the active layer flow to.[8] Therefore, in the case of an **ITO/PEDOT:PSS/ACTIVE LAYER/Al** solar cell, the anode (electron collector) electrode is Al and the cathode (hole collector) is ITO. This means that under this geometry, the indium tin oxide (ITO) terminal is an anode contact, whilst the Al terminal is a cathode contact (See Figure 3.1. Also note the difference between cathode/anode electrode and cathode/anode contact.)

The glass (or other suitable rigid body) serves as a support base (foundation) for the solar cell and the crucial prerequisite is high transparency (> 90%) in the visible spectrum, because this is the light that the solar cell harnesses for power generation. In addition to their use as electrodes, ITO and Al importantly generate a built-in electric field that arises due to the difference in the

work functions of the two metals. This electric field spans across the solar cell from the ITO electrode to the Al electrode. A detailed description of this physical quantity (the built-in electric field) is presented in the next section. ITO is chosen, because it also fulfills the 'transparency to visible light' requirement. Such material, which is coated on a glass substrate, must allow all light from the glass substrate to pass through to the active layer.

PEDOT:PSS (poly[3,4-(ethylenedioxy)-thiophene]:poly(styrene sulfonate) is a buffer layer which has multiple enhancement functions in a polymer solar cell. An elaborate description of this chemical as well as many of its utilities is given in Chapter 4, where all materials incorporated in our devices are significantly treated. For now, the extraction that PEDOT:PSS's inclusion in the polymer solar cell increases the built-in electric field, which thus improves the performance of the solar cell'[86] suffices for the present needs.

The active layer is a polymer-fullerene blend, whose function is to generate charge carriers upon absorption of light. The fullerene derivative, like [6,6]-phenyl-C61 butyric acid methyl ester (PCBM) is the electron acceptor for a donor conjugated polymer material, like poly-3-hexylthiophene-2,5-diyl (P3HT). These organic materials are not crystalline (like silicon or germanium) and when mixed in a common solvent, they form a disordered blend of electron-donor and electron-acceptor materials, hence the name bulk heterojunction. Donor polymer materials show high light absorbance, whilst the acceptor fullerenes exhibit strong affinity for electrons.

Currently, there are three donor-acceptor bulk morphologies: the bilayer, the bulk heterojunction and the "comb" structure. However, our focus is on the bulk heterojunction, which provides many polymer-fullerene interfaces for improved charge dissociation. In a bulk heterojunction device, charge generation can occur throughout the bulk and charge transport mainly depends on the transport properties of the individual components. The collection efficiency of these polymer-fullerene photovoltaic devices is greatly increased by controlling the morphology of the phase separation within the bulk material, so that an interpenetrating phase separated donor-acceptor (D/A) network composite is formed. Such maneuvering ensures the establishment of a large interfacial area within the bulk material, such that any point within the composite gets to a few nanometers of donor-acceptor interface, where electron transfer takes place. Additionally, it is best that the network is bicontinuous (doubly running) with the constituent materials adjacent

and parallel to each other in such a manner that pathways to the respective electrodes exist for the separated charge carriers. The bicontinuous configuration guarantees efficient hand over of the electron by the donor to the acceptor, as well as efficient collection (receiving) of the electron by the acceptor at the interface of the two materials. Such a composite is effectively the ideal bulk D/A heterojunction material.

In a bilayer device, the p-n junction is the origin of rectification, while for a bulk heterojunction; rectification has to be introduced via selective contacts and the subsequent built-in electric field. The creation of bulk D/A heterojunctions is a milestone step towards the creation of efficient nanostructured p-n junctions in organic materials.

3.2 The built-in electric field and its band bending mechanism

When a bound exciton has been generated in a polymer solar cell, it has to be dissociated into an electron and a hole. Each of the two charge carriers (electron and hole) has to reach its respective electrode so that the cell can be enabled to deliver current to an external circuit. For this to happen, the polymer solar cell must have some kind of built-in driving force, which promotes the dissociations (at the D/A interfaces) and the subsequent charge transport (in appropriate material phases) to the different electrodes. This built-in driving force can be created through spatial variations in the electronic environment, which practically is done through junctions of materials with different electronic properties,[41], [87] (that is, different work functions).

For a deeper understanding, we can imagine a simple polymer solar cell that consists of a polymer layer sandwiched between two metals, the assembly of which forms a heterojunction. The two metals generate an electric field inside the polymer due to their different (asymmetrical) work functions. This built-in electric field generates a built-in driving force, which if large enough, can dissociate the Coulomb-bound excitons by pulling the electrons and holes in opposite directions.[88] Therefore the built-in electric field is that force on unit charge, which is created, because of the difference in the work functions of the two materials (metals or semiconductors) in electrical contact. In the case of polymer photovoltaic devices, the built-in electric field's functions can be two fold. Firstly, the force field can be used to dissociate the generated excitons into holes and electrons. Secondly, it pulls (drives) the separated (lone)

charges to their respective electrodes. The creation of a built-in electric field causes band bending, the physics of which is epitomized as follows:

Before the polymer solar cell is built, the Fermi levels of the two electrodes (for example, ITO and Al) are independent of each other. When assembled, as explained in Chapter 2, a redistribution of charge carriers begins and the diffusion continues until thermal equilibrium, which is marked by the alignment of the Fermi levels of the two metals, has been reached. This redistribution of charges results in the establishment of an electric field, which affects the valence and conduction bands. Depending on the conductivity of the polymer, two different profiles (shown in Figure 3.4) can be created.[89]

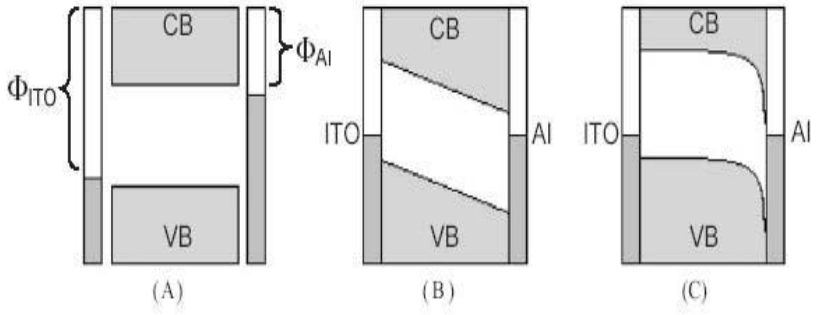

Figure 3.4 *Illustration of two possible band bending profiles in a polymer solar cell. ITO is the high work function electrode and Al is the low work function electrode. (A) depicts the energy levels before the solar cell assemblage, while (B) and (C) show the energy levels after assemblage. In (B), the polymer is an insulator and so the electric field changes linearly through the cell. (C) polymer is hole conducting and so a Schottky barrier is formed between the polymer and the low work function electrode*.[88]

If the polymer is an insulator, it will have no free charges to participate in the redistribution. Therefore charge carriers which can diffuse are only those from the electrodes. This means that electrons from the low work function electrode (Al in this case) diffuse to the high work function electrode (ITO in Figure 3.4) in order to align the Fermi levels and establish a thermal equilibrium.[41] As a result, the low work function electrode is left positively charged and the high work function electrode becomes negatively charged, thus the creation of a built-in potential difference between the two electrodes, which generates the built-in electric field under present

discussion. If the sandwiched polymer is an insulator, this field changes (builds up) linearly throughout the solar cell and in so doing, pulls the valence and conducting bands in skewed form, as shown in Figure 3.4 (B).[89] The skew direction of the polymer bands at each metal-polymer contact, is the direction in which the Fermi level of the adjacent metal goes in order to establish thermal equilibrium, with the Fermi levels of the two metals aligned. For insulator polymer (B), this implies, downward on the Al side and upward on the ITO side).

At this stage, it is crucial not to be trapped in the misconception of interpreting this band bending to be referring to the physical bending of the conduction and valence bands of the polymer, because it does not. Rather, it is used to illustrate a local change in the energy of electrons in a semiconductor caused by an applied electric field,[41] (which happens to be the built-in electric field in this case).

If the polymer is a hole conducting semiconductor, the hole conducting properties of the polymer allow holes to freely redistribute within the polymer and therefore participate in the alignment of the Fermi levels. At the junction between the polymer and the low work function electrode, holes from the polymer will diffuse into the electrode in order to lower their energy. This diffusion of holes leaves a region of negatively charged acceptor atoms in the polymer and creates a positively charged domain in the electrode.[41] An electric field (Schottky barrier) is therefore created across the interface. This development causes the valence and conduction bands in the polymer region close to the polymer-low work function electrode interface to bend as shown in Figure 3.4 (C). Holes tend to drift upwards as also explained in Chapter 2. If the polymer was an electron conductor, the band bending would have taken place at the junction between the polymer and the high work function electrode. In this instance the valence band (VB) and conduction band (CB) bend upwards as the electrons flow from the polymer to the metal.

3.3 Singlet and Triplet states

According to Pauli Exclusion Principle, electrons in a molecular orbital are paired with equal but opposite spins. When an electron absorbs enough energy it will be excited to a higher energy state; but will keep the orientation of its spin. The molecular electronic state in which electrons are paired is called a singlet (transition) state (Figure 3.5). On the other hand, the molecular electronic state in which the two electrons are unpaired is called a triplet state. The triplet state is

achieved when an electron is transferred from a singlet energy level into a triplet energy level, by a process called intersystem crossing; accompanied by a flip in spin (Figure 3.5).

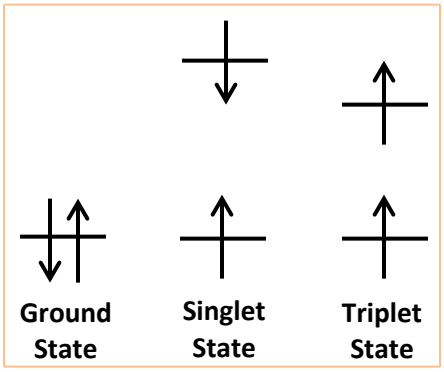

Figure 3.5 *Ground, singlet and triplet states*

In a singlet state, the spins of the two electrons are paired and thus exhibit no magnetic field and are called diamagnetic. Diamagnetic molecules, containing paired electrons, are neither attracted nor repelled by a magnetic field. On the other hand, molecules in the triplet state have unpaired electrons and are thus paramagnetic, which means that they are either repelled or attracted to magnetic fields. The terms singlet and triplet stem from the definition of multiplicity where: Multiplicity = 2S+1, where, S is the total spin. The total spin for a singlet state is zero since electrons are paired, which gives a multiplicity of one (the term singlet state), given by:

$$\text{Multiplicity} = (2 * 0) + 1 = 1 \Rightarrow \text{singlet}$$

In a triplet state, the total spin is one (the two electrons are unpaired) and the multiplicity is three, given by:

$$\text{Multiplicity} = (2 * 1) + 1 = 3 \Rightarrow \text{triplet}$$

The probability of a singlet to triplet transition is much lower than a singlet to singlet transition.

3.4 Mechanisms of photon-to-charge carrier conversion process in polymer-fullerene BHJ Solar Cells

The backbone steps whose consecutive operational involvement generates the photovoltaic effect in BHJ polymer-fullerene SC are: in-coupling of the photon; absorption of the photon in the donor/acceptor of lower band gap; exciton creation; exciton migration by diffusion; exciton configuration to electron transfer complex (polaron formation) at polymer–fullerene interface; electron-hole dissociation →enforced by the built-in electric field across the polymer-fullerene interface; charge carrier (bulk) transport to the junction of the polymer or fullerene[90] with the metal electrode; charge injection at the electrode (metal)-active layer interface and subsequent collection at the electrodes; and finally, electric power extraction by the external circuit. Although significant progress has been made in improving the performance of organic solar

cells, there are still many gray areas embedded in each of the outlined steps. Basically, these steps converge to four fundamental processes, which we here treat for the regioregular conjugated polymer-P3HT:PCBM fullerene BHJ SC.

We start from the encouragement that the photon absorption likelihood is high in organic donor materials (for example, conjugated polymers), because these materials often exhibit very high thickness dependent absorption coefficients, which are above 10^7 m^{-1}.[36] As a result, very low active material thicknesses of between 100 and 300 nm suffice for good absorption yield in organic photovoltaic devices.[36] Unfortunately, on the downside, many organic materials have a rather narrow absorption band width. Conjugated polymers commonly used in organic solar cells typically cover the visible optical spectrum only,[36], [91-92] although polymers with wider absorption bands exist.[93-94] In contrast, the inorganic semiconductors, silicon and $CuInSe_2$, absorb across the whole spectrum of the sunlight and beyond to more than 1000 nm (optical bandgap 1.1 eV),[36] but the costs involved in fabricating solar cells based on these materials are inhibitive, hence the need to continue studies on the much cheaper organic counterparts. Therefore, the advantageous optical property of high absorbance in the visible range for conjugated polymers is utilised.

Figure 3.6 shows a simplified energetic sketch diagram illustrating the fundamental mechanisms of the photon-to-charge carrier conversion operations. Upon absorption of a photon, a valence electron of the donor molecule (polymer) undergoes photo-induced excitation, which excites it from the HOMO to the LUMO, usually of the same molecule of the organic (polymer) material and in the process leaves a hole behind; thus creating a Coulombically bound electron (e^-)-hole (h^+) pair called a (singlet) exciton (or Frenkel exciton) (see Figure 3.6). The absorption efficiency (η_A) is then equivalent to the ratio of the generated Frenkel excitons (in terms of absorbed energy) to the total incident photons energy-wise. In organic materials, excitons usually reside on one molecule or along an extended polymer segment (intrachain excitons).[95] However, interchain excitons which reside on adjacent molecules have been reported. Singlet excitons (which are the ones usually generated upon illumination) have a resulting spin of zero and triplet excitons have a spin of one.[96] The lifetime of a singlet exciton is in the order of 1 ns, after which it recombines radiatively with photoluminescence as the decay path. Triplet excitons have a relatively longer life time of up to milliseconds.[36], [96-97]

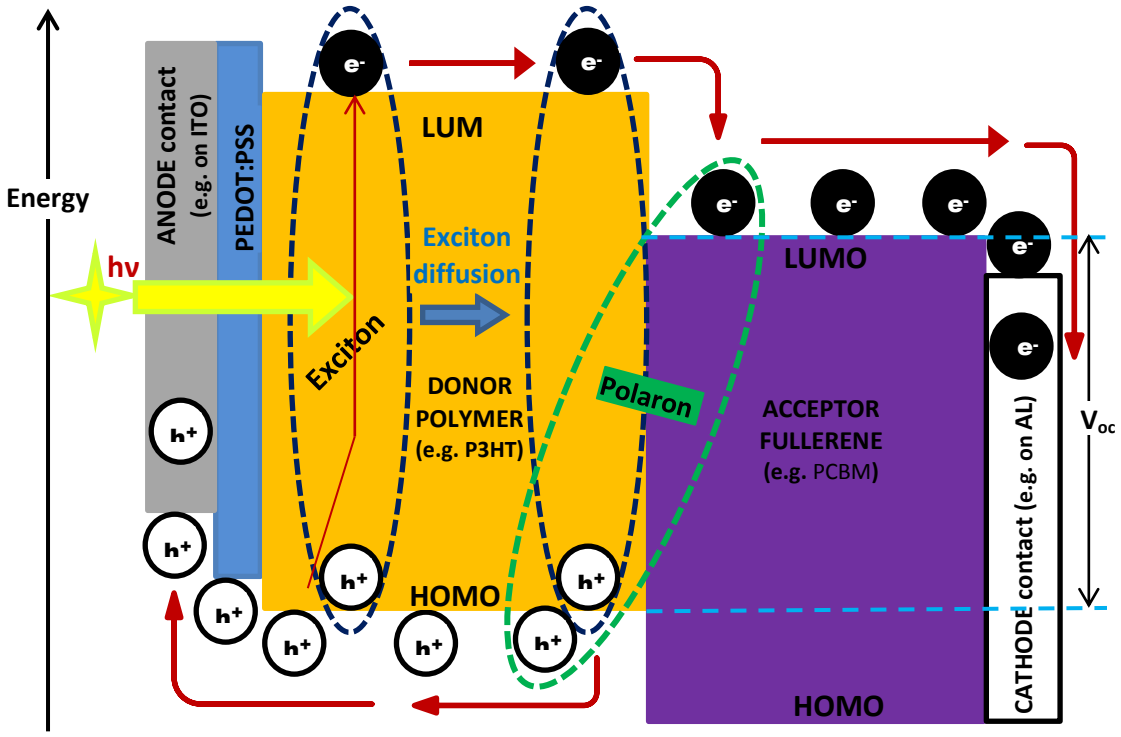

Figure 3.6 *Underlying mechanisms of the photon-to-charge carrier conversion process in a bulk heterojunction solar cell incorporating a conjugated polymer as the absorber material*.

The created exciton exhibits a significant amount of binding energy (several tenths of electron volts,[98]) which is much larger than the thermal energy and therefore precludes the possibility of it being dissociated by thermal energy at 300K (25 meV). Since the exciton binding energy by far exceeds the thermal energy at room temperature, it is commonly referred to as a Frenkel exciton, which distinguishes it from the weakly bound type, called Wannier-Mott.[99] Typical values of the binding energy of excitons in organic materials are 0.5 to 1.0 eV.[100] This is so, because organic materials exhibit low dielectric permittivities (or constants) that range from 3 – 4, which makes the screening length larger.[36] For example, an exciton of radius 1 nm, in a material with a dielectric constant of 3, has a Coulomb binding energy of 0.5 eV.[36] In comparison, thermal energy $(k_B T)$ at room temperature (298 K) is approximately 0.025 eV,[101]

which is much lower than that of an exciton in an organic material. Therefore to achieve dissociation of the bound charges, another driving force is needed. This force is brought about by the introduction of a second organic semiconductor, which is more electronegative and thus lower in energy. The material is introduced either in a bilayer or bulk heterojunction assembly. It therefore serves as an electron acceptor and due to different work functions of the two organic materials, the acceptor also incites the creation of a built-in (internal) electric field at the donor-acceptor interface of the two materials (as explained in Chapter 2). This built-in electric field is usually large enough to dissociate any excitons that diffuse into the interface location. In fact the difference between the electron energy on the LUMO of the donor molecule and the corresponding LUMO of the acceptor molecule has to be larger than the exciton binding energy, in order to bring about an electron transfer from the LUMO of the donor (molecule) to LUMO of the acceptor (molecule). The commonly used electron acceptors are the (Buckminster) fullerenes, C60 and its derivatives,[102-103] like [6,6]-phenyl-61 butyric methyl ester (PCBM) and a popular donor is a conjugated polymer like poly (3-hexylthiophene 2,5 diyl (P3HT). Fullerenes have greater electron affinities than those of polymers or small molecules.[102-103]

In most cases the exciton reaches the donor-acceptor heterointerface by diffusion (within the donor) towards this planar interface to the acceptor, since it is neutral.[104-105] However, this journey to the interface is shrouded in problematic challenges. The main challenge is that the diffusion length (L_D) of an exciton in most conjugated polymer films ranges from 5 to 10 nm,[9], [106] which is quite low. The $L_D = 10$ nm approximation is mostly considered to be the standard.[41], [36] This implies that the exciton creation must take place at a distance from the donor-acceptor (D-A) interface, which is within the exciton diffusion length, in order to guard against recombination losses (often radiative). This requirement further bottlenecks free charge carrier generation. Therefore, dimensions of the active layer must be chosen meticulously. The bulk heterojunction concept, which features a distributed D-A interface over the whole spread of the active layer attempts to implement the guideline. The phase separation should be as small as possible. When polymers and fullerenes are mixed well at the molecular level, photo-generated excitons are next to the heterojunction and often do not need to diffuse that much to the interfaces for charge transfer process.[101] The ratio of the number of excitons that reach the D-A interface to the total number of excitons generated through photoexcitation is termed the exciton diffusion efficiency (η_{ED}). Formation of donor and acceptor clusters lead to Schottky barriers.

The simplified diagram of Figure 3.7 shows the photovoltaic effect for a bulk heterojunction solar cell whose active layer composite is a blend of conjugated polymer and fullerene. Many competing processes are at play.

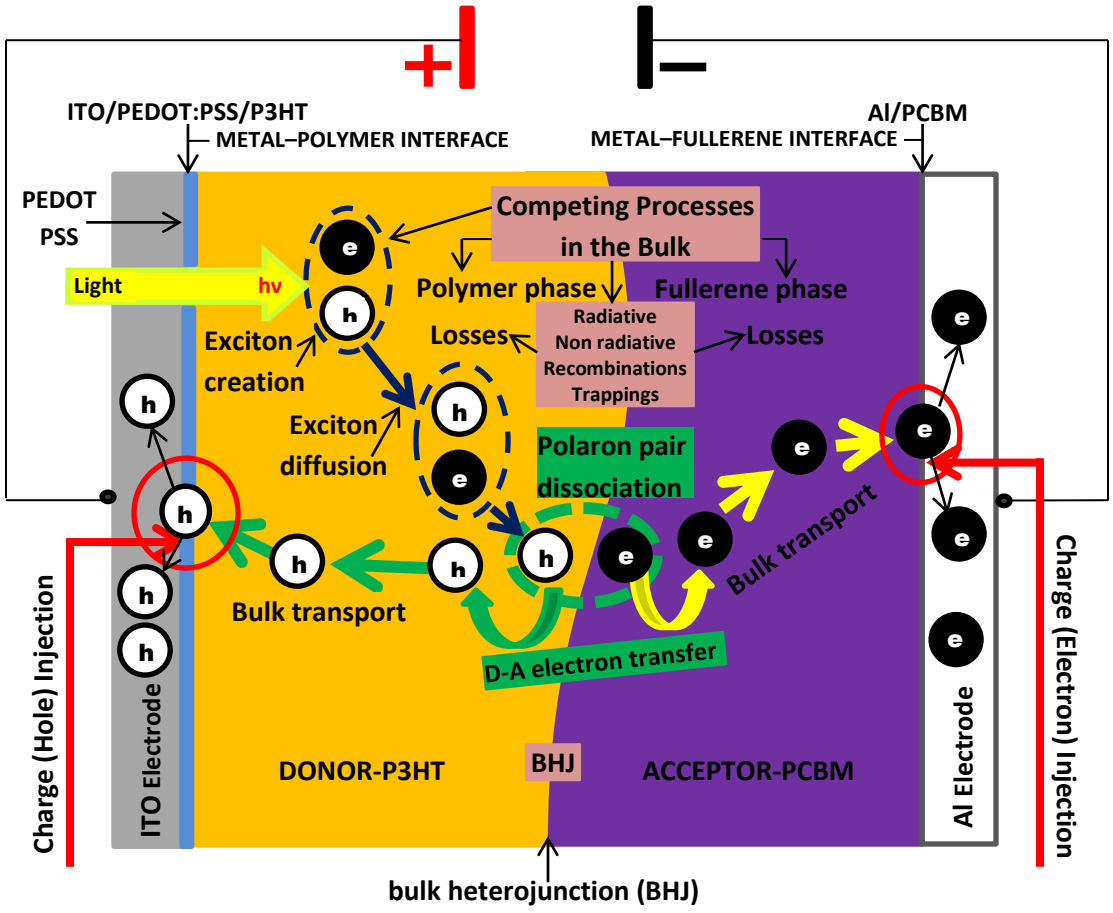

Figure 3.7 *Competing processes associated with a bulk heterojunction (BHJ) polymer-fullerene solar cell in its photovoltaic effect*

At the interface, the electron transfer process is reported to be at an ultrafast pace[30], [107] (100 fs) in polymer-fullerene assemblies and very efficient, whereas the alternative loss mechanisms are relatively much slower.[36] In fact, separation process times of 40 fs have been recorded in polyphenylene vinylene (PPV)/PCBM composites,[10] with the back-transfer process exhibiting heavy hindrance resulting in the establishment of metastable charge separated states with lifetimes in the fs timescale. Thus, the stabilization of radical ions is intrinsic in this system. This fast electron transfer process minimises various forms of losses at the D-A interfaces. In

suitable material combinations, the charge transfer is much faster than any competing loss processes such as radiative-photoluminescence or intersystem crossing.[36] The charge-transfer (CT) process yields a polaron (Figure 3.7), where the hole and electron still remain Coulombically bound, but are now in the donor and acceptor phases, respectively. The polaron finally dissociates as a result of the pull on the mutually bound charges by the built-in electric field, which splits them into free holes and electrons in their respective phase for bulk transportation to their respective electrodes. This means that the hole remains in the HOMO of the donor and the electron is offloaded into the LUMO of the acceptor, from where they are transported, mainly by hopping along these energy levels until they reach their electrodes (Figures 3.4 and 3.7). The charge separation efficiency (η_{CS}) is defined as the ratio of the number of excitons that have undergone the charge transfer (CT) to the number of excitons that have reached the D-A interface.

Electrons and holes have different mobilities in the bulk material. The dangers (loss mechanisms) in the bulk materials are that the charges may fall prey to localised trappings and recombinations, the risks of which increase with distance travelled. This diminishes the charge transport efficiency. While a thin active layer minimises the losses, its downside is that it simultaneously reduces the optical absorption, which is proportional to film thickness. This calls for an optimization trade-off. An electron or hole that reaches the interface of the electrode (metal) and the polymer/fullerene is still not guaranteed of reaching the electrode, because it must overcome the potential barrier at the interface. All the mechanisms (for example, quantum mechanical tunneling) associated with charge carrier injection at metal-active layer interface have to deal with the crossing problems presented by the potential barrier height and width, interface imperfections, geometry and topology, etc. As such, some of the charge carriers are eliminated (screened) during the cross over. It is only after surmounting all the junction hindrances that the charge carrier passes and is collected at the electrode. It can then participate in electric conduction in the external circuit. Interestingly, despite all the transport hitches, the transport of free charge carriers to the respective electrodes occurs within a period of time ranging from nano to microseconds.[101] The charge collection efficiency (η_{CC}) is defined as the ratio of the number of charge carriers that have collected at the electrode to the number of excitons that have undergone the charge transfer process.

3.4.1 Some of the factors affecting performance of organic solar cell (Summary)

Materials used in fabricating the organic solar cell are important**.** For example, the band gap of the absorber material should be within UV and visible range. Only photons with photon energy ≥ band gap of the material can be absorbed and can excite an electron from HOMO to LUMO of the material. The ability of the material to absorb solar radiation (as shown by the material's absorbance spectra) is fundamental, as it plays the crucial role in the generation of excitons. These play crucial roles in the generation of excitons. Essential attributes of the acceptor material have been explained in the preceding section (3.3). Other factors, which are mainly morphological dependent, have been explained to be exciton separation (which generates charge carriers) and charge transport to electrodes (which partly depends on the transport properties of the active ingredients). The electrical properties of electrodes are core to charge injection processes at metal-organic semiconductor interfaces. Recombinations, series and parallel/shunt resistances and maintenance are also among many other determinants of the performance of an OSC.

3.5 Current Generated in a Solar Cell

3.5.1 Dark Current

A diode is a device that admits (or conducts) much larger current in one direction, following the application of a voltage in that direction (forward bias) than in the other (reverse bias). A solar cell acts as a diode under bias. For a solar cell, the external voltage needed to deliver electrical energy to the external circuit (or the load) creates a bias across the solar cell, which drives current, the so called dark current, within the cell, even when the cell is not under illumination (that is, in the dark) – hence the descriptive term 'dark' for such currents. Therefore, dark current is current generated within the diode, by the photogenerated voltage, which biases across the diode solar cell. As a result, the dark current will flow in the opposite direction of the photogenerated current and reduce the net current. It stems from injection movements of electrons and holes driven by the bias electric filed (generated by the bias voltage) which occur within the bulk of the active material and which ultimately result in the charge carriers recombining. A single exponential formula, based on the Shockley equation for an ideal diode and which adequately approximates the dark current is [108]

$$I_D(V) = I_o\left[\exp\frac{qV}{nkT} - 1\right] \qquad \text{with } 1 < n < 2 \tag{3.1}$$

where $I_D(V)$ is the dark current in terms of the applied voltage *V*, *n* is the ideality factor, I_o is the reverse saturation current, which is a constant for a given solar cell, *q* (or *e*) is the elementary charge, *k* is Boltzmann's constant and *T* is the thermodynamic temperature. At low voltages, the ideality factor *n* approaches 2 ($n \rightarrow 2$) which indicates activities dominated by recombination behaviour within the space charge region. At high voltages, $n \rightarrow 1$ and this corresponds to recombination behaviour dominated by diffusion in the quasi neutral regions.[108] Values of *n* greater than 2 have been reported for many solar cells at low bias voltages. However, there have been many unexplained practical observations involving organic and other solar cells in which values of $n > 2$ at low bias voltages have surfaced. These may partly be explained as being due to current leakages that can be modeled as a parallel resistance.[10], [108] Other different causes such as the tunnel effect, breakdown by micro-plasmas, leaks along surface channels, etc., have been suggested.

3.5.2 Photogenerated current

Regarding an illuminated solar cell in the absence of a load, the current drawn through the circuit is the short circuit current, I_{sc}. When a load is included, the current that flows will be between 0 and I_{sc}. This current will be the net result of two components of internal current acting against each other. The components are:

- The photogenerated current I_L resulting from the generation of carriers by light.
- The diode or dark current, I_D, due to the recombination of carriers driven by the external voltage. This external voltage across the solar cell terminals (or electrodes) is the photogenerated voltage that will be delivering power to the load.

Assuming the two currents to be superimposed linearly, as is the case in many practical cases and taking the photocurrent as positive, it means that the current *I* in the external circuit can be approximated as the difference between the two components as shown in equation (3.2).

$$I(V) = I_L - I_D(V) \tag{3.2}$$

At sea level, under clear conditions, atmospheric absorption modifies the solar spectrum typically to air mass 1.5 (AM1.5) and the irradiance becomes reduced to 100 mW/cm^2 under clear conditions.

The number of photogenerated electron-hole pairs is equal to the number of photons absorbed, because only one electron-hole pair is created for each photon absorbed, regardless of the energy of the photon. Based on this, the photogenerated current may be calculated as:[108]

$$I_L = e A_C \int_{E_G}^{\infty} S(E)\alpha'(E,W)dE \tag{3.3}$$

which can be rewritten as:

$$I_L = e A_C \int_{E_G}^{\infty} S(E)\left[1-\rho(E,W)-\tau(E,W)\right]dE \tag{3.4}$$

where, $\alpha'(E,W)$ is equal to the term in the square bracket in Eq. (3.4) and denotes the spectral absorbance α', which depends on photon energy E and layer thickness W, E_G is the bandgap of the semiconductor material of thin film (layer) thickness W, $S(E)$ is the number of photons of energy E, A_C is the area of the illuminated cell, e is the electronic charge, $\rho(E,W)$ is the reflectance and $\tau(E,W)$ is the transmittance. Under careful device architecture, reflection and transmission losses may in principle be reduced to zero, but non-absorption losses are inevitable since these depend only on the properties of the semiconductor material. With these considerations, the theoretical maximum photocurrent from a solar cell then becomes:

$$I_L \leq e A_C \int_{E_G}^{\infty} S(E)\, dE \tag{3.5}$$

Equation (3.5) shows that the current depends only on the bandgap and the solar emission spectrum $(S(E))$. The current therefore decreases as the bandgap E_G is increased. Not all the photogenerated carriers contribute to the generation of electricity in the external circuit, because even under short circuit conditions (no voltage existing across the device), a small fraction of the photogenerated carriers that is generated far from the area of high electric field recombines before being collected. This becomes so, because such carriers have to travel some distance towards the area of high electric field before being separated and collected across the junction. The fraction of the carriers that is collected is termed the collection efficiency, $\eta_{coll}(E)$ and

depends on the optical and electrical properties of the material as well as the structure of the device. Consideration of this brings the photocurrent to:

$$I_L = eA_c \int_{E_G}^{\infty} S(E)\,\alpha'(E)\,\eta_{coll}(E)\,dE \qquad (3.6)$$

The collection efficiency depends on the region of the device being considered.

3.6 Solar cell characterisation parameters

3.6.1 Quantum efficiency $\eta_{qe}(E)$

The external quantum efficiency (*EQE*) of a solar cell is a property parameter of a photoactive device that measures the fraction of incident photons that result in actually collected electron-hole pairs under short circuit conditions. From a practical perspective, the quantum efficiency (QE) can be viewed as the ratio of the number of charge carriers collected by the solar cell to the number of photons of a given energy incident on the solar cell. It may be given either as a function of energy E or wavelength λ, since $\lambda = \frac{hc}{E}$, where h is Planck's constant and c is the speed of light in free space. If all photons of a certain wavelength are absorbed and the resulting minority carriers are all collected, then the quantum efficiency of that particular wavelength is unit. Figure 3.8 shows sketch curves of (external) quantum efficiency versus wavelength for an ideal and a practical solar cell.

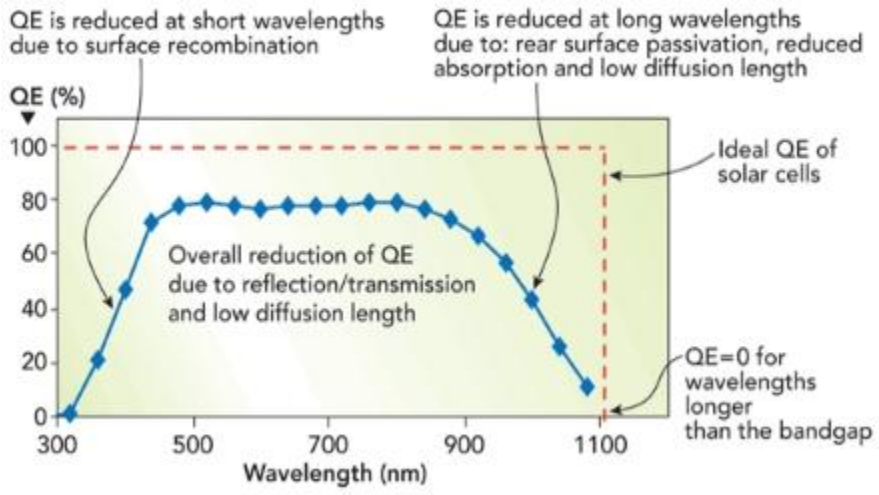

Figure 3.8 *Variation of external quantum efficiency with incident wavelength for ideal and practical cases of a solar cell*[109]

As Figure 3.8 shows, while quantum efficiency ideally has a square shape shown in red dashes above, the quantum efficiency of most solar cells is reduced due to recombination effects. The mechanisms which affect the collection probability also affect the quantum efficiency. For example, the front surface passivation affects carriers generated near the surface and since the blue light is absorbed very close to the surface, high front surface recombination will affect the blue portion of the quantum efficiency. Similarly, green light is absorbed in the bulk of a solar cell and a low diffusion length will affect the collection probability from the solar cell bulk and reduce the quantum efficiency in the green portion of the spectrum. Likewise, the quantum efficiency is reduced at long wavelengths due to rear surface passivation, reduced absorption and low diffusion length.[110] As the figure shows, the quantum efficiency is equal to zero ($QE = 0$) for wavelengths longer than the bandgap wavelength $\lambda_g = hc / E_g$, because no light is absorbed below the bandgap E_g (that is, light spectrum region $\lambda > \lambda_g$).

The carriers travel by diffusion once they are created. The minority diffusion length L_m represents the average distance, which a (generated) minority carrier will travel before it recombines. The diffusion length is related to the minority carrier lifetime τ, and the diffusion constant D, by the equation:

$$L_m = \sqrt{D_m \tau_m} \tag{3.7}$$

where, the subscript m can either be n for electrons or p for holes.

The quantum efficiency can be viewed as the collection probability due to the generation profile of a single wavelength, integrated over the device thickness and normalized to the incident number of photons.

The 'external' quantum efficiency of a solar cell often includes the effect of optical losses such as transmission and reflection. However, it is often useful to look at the quantum efficiency of the light left after the reflected and transmitted light has been lost. 'Internal' quantum efficiency (IQE) refers to the efficiency with which photons that are not reflected or transmitted out of the cell can generate collectable carriers.[110] By measuring the reflection and transmission of a device, the external quantum efficiency curve (like the blue plot curve in Figure 3.6) can be corrected to obtain the internal quantum efficiency curve. As such, when the term quantum efficiency is used, it often refers to the external quantum efficiency, unless distinctly stated to

mean otherwise. In a nutshell, quantum efficiency includes the effect of optical losses such as transmission through the cell and reflection of light from the cell, whereas internal quantum efficiency refers to the efficiency devoid of transmitted and reflected light by the cell. The narrowing down to internal quantum efficiency, where more precise analysis is needed, is based on the premise that only the absorbed portion of light can generate charge carriers which can constitute photocurrent.

The monochromatic external quantum efficiency (EQE_λ) is defined as:

$$EQE_\lambda = \frac{I_{SC\lambda}}{eN_{0\lambda}} \tag{3.8}$$

where, $I_{SC\lambda}$ is the short-circuit photocurrent due to incident photons of wavelength λ, e is the elementary charge, and $N_{0\lambda}$ which is the incident photon flux density at wavelength λ is given by.

$$No\lambda = \frac{P(light)\lambda}{P(photon)\lambda} = \frac{E(light)_\lambda \lambda}{hc} \tag{3.9}$$

Each photon absorbed is capable of generating only one electron-hole pair. The short circuit current density per wavelength $J_{SC\lambda}$ is then given by

$$J_{SC\lambda} = \frac{qE(light)_\lambda \lambda}{hc} EQE_\lambda \tag{3.10}$$

In terms of the solar flux of photons $n(\omega)$ with energy $E = h\omega$ and quantum efficiency $QE(E)$, the load carrying short circuit current is given by

$$I_{SC} = \int QE(E)n(\omega)dE \tag{3.11}$$

where $\omega = E/h = 2\pi\nu$ and ν is the photon frequency.

As a function of external quantum efficiency, the photocurrent I_L of a given solar cell may be determined from:

$$I_L = eA_C \int S(E).(EQE_\lambda).EdE \tag{3.12}$$

3.6.2 Current-Voltage Characteristics

The overall current (or current density) of a solar cell as a function of the applied voltage is called the current-voltage $I(V)$ {or $J(V)$} characteristic. This current is given by the difference between the photocurrent I_L and the dark (or recombination) current $I_D(V)$. Note that the round bracketed V is to remind that I_D is a function of V (or 'depends upon V' in other words). This is so from the dark current equation, Eq. (3.1), which is based on the Shockley equation for an ideal diode. $I_D(V)$ is due to the bias from the photogenerated voltage.

Following from Eq. (3.1), the current-voltage characteristics of an illuminated solar cell becomes:

$$I(V) = I_L - I_0\left[\exp\left(\frac{eV}{nk_BT}\right) - 1\right] \tag{3.13}$$

Eq. (3.13) is for simplicity based on the assumption that the current in the diode (the solar cell in our case) can be expressed by a single exponential. The greatest value of current, with the solar as a generator, is obtained under short circuit conditions, when $V = 0$. Substituting V in Eq. (3.13) with zero (0) gives

$$I(V=0) = I(0) = I_L = \textit{the short circuit current } I_{SC} \tag{3.14}$$

This shows that the photogenerated current I_L can be approximated by I_{SC}, which when applied to Eq. (3.13) yields

$$I(V) = I_{SC} - I_0\left[\exp\left(\frac{eV}{nk_BT}\right) - 1\right] \tag{3.15}$$

Therefore, the overall (or net) current $I(V)$ of a solar cell can be approximated as the algebraic sum of the short circuit and dark currents. Note that Eqs. (3.1), (3.2), (3.13) and (3.15) are valid for an ideal diode. Practical settings require the consideration of resistances. Short circuit current refers to the maximum electric current produced when the negative and positive terminals of a cell are short-circuited (or bridged with a good conductor). Current flow through the bridging conductor is maximum (thus the short circuit current) because the load resistance is zero under the configuration. In this case, load resistance corresponds to series resistance R_S. The bridging (or joining) of the two terminals ensures that the voltage (potential difference) between the terminals is zero.

The short-circuit current depends on a number of factors some of which are:

- area of the solar cell - To remove the dependence of the solar cell area, use is made of the short-circuit current density (J_{sc} in mA/cm^2) rather than the short-circuit current.
- charge carrier mobility
- power of the incident light source
- spectrum of the incident light - For most solar cell measurement, the spectrum is standardized to the AM1.5 spectrum.
- optical properties (absorptance, reflectance and transmittance) of the active material of the device
- collection probability of the solar cell, which mainly depends on the surface passivation and the minority carrier lifetime in the base.

The -1 in Eqs. (3.13) and (3.15) can be neglected, because the exponential term is usually much greater than one (>>1) except for voltages below 100 mV. Also, at low voltages the photogenerated current I_L dominates the $I_0\left(eV/nk_BT\right)$ term, so the term -1 may be neglected under illumination as shown by the following proof: $e^{\frac{qV}{nkT}} \approx \sum_{i=0}^{\infty} \frac{\left(\frac{eV}{nkT}\right)^i}{i!} \approx 1+\frac{eV}{nkT}\ for\ V << 0.1$

When under open circuit conditions, it means that the positive and negative terminals of the device are either not connected or are equivalent to those of a device whose terminals are bridged by a material of infinite resistance (such as a potentiometer) which will not allow current to flow between them. Therefore, the device will not be delivering any current under this condition. If the solar cell device is kept in open-circuit condition (implying current $I = 0$), it biases itself with a voltage that is the greatest possible for the device. This voltage is called the open circuit voltage V_{OC} and ideally corresponds to a load resistance (commonly termed shunt resistance R_{SH}) of infinity. As the equivalent circuit of the solar cell shows in Figure 3.7, R_{SH} is analogous to parallel resistance in the conventional electric circuit diagrams. The value of the open circuit voltage is such that the photogenerated current corresponding to it is completely negated (cancelled) by the dark (bias) current {that is, $I_L = I_D\left(V_{OC}\right)$} under open circuit

conditions. From Eq. (3.13), the open circuit voltage can be derived and is displayed in Eq. (3.16).

$$V_{OC} = n\frac{k_B T}{e}\ln\left[\frac{I_L}{I_0} - 1\right] \tag{3.16}$$

Eq. (3.16) can be approximated by I_{SC} as

$$V_{OC} = n\frac{k_B T}{e}\ln\left[\frac{I_{SC}}{I_0} - 1\right] \tag{3.17}$$

Eqs. (3.16) and (3.17) show that at constant temperature, V_{OC} depends on the saturation current I_0 of the solar cell and the photogenerated current. While I_{SC} typically has a small variation, the crucial effect is due to the saturation current, since this may vary by orders of magnitude. The saturation current depends on recombination in the solar cell. As such, the open circuit voltage is a measure of the amount of recombination in the device. Higher I_0 implies higher recombination. In an electric circuit due to a solar cell, the solar cell is equivalent to a current source connected in parallel with a diode as shown in Figure 3.9. The placement of parasitic resistances is briefly explained towards the end of this section and more extensively in Chapter 5. When a voltage is applied, the current will be divided between the load and the diode.

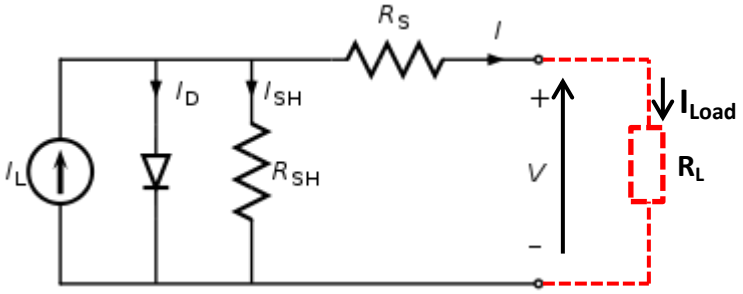

Figure 3.9 *Electrical model of a practical solar cell with parasitic resistances modeled as a parallel shunt resistance (R_{SH}) and series resistances (R_S). For an ideal solar cell, R_{SH} would be infinite and would not provide an alternative route for current to flow, while R_S would be zero, so that there would be no voltage drop and/or power loss before the load*

The power P generated by a solar cell at any given voltage is the product of the voltage and the corresponding current, as expressed in Eq. (3.18).

$$P = VI \tag{3.18}$$

The solar cell can only operate at a voltage between 0 and V_{OC}. The highest efficiency corresponds to the point where the cell delivers maximum power. This point can be arrived at by

varying the load resistance from zero (short circuiting) to infinity (open circuiting). Although I_{SC} and V_{OC} are both highest, at both of these operating points, the power of the cell is zero, because the two counter-peak, that is, at I_{SC}, $V = 0$ and at V_{OC}, $I = 0$, which by Eq. (3.18) yields zero power in each case. On the *I*(*V*) curve, the maximum power point (MPP) occurs at the point where the product of voltage and current (or current density) is a maximum and the wish is to locate this point. As shown in Figure 3.10, the power will increase with increasing voltage until a maximum is reached at V_M and I_M or J_M, then drop to zero at V_{OC}. The solar cell dissipates maximum power at about the 'knee' of the *I*(*V*) or *J*(*V*) curve. This is the point at which the solar cell operates at its maximum efficiency in converting light energy into electrical energy. This behaviour is described by the fill factor, FF, which in mathematical from is defined by Equation (3.19) as:

$$FF = \frac{V_M I_M}{V_{OC} I_{SC}} = \frac{V_M J_M}{V_{OC} J_{SC}} \qquad (3.19)$$

The fill factor characterises how "square" the J-V curve is and it gives a measure of how difficult or how easy the photogenerated charge carriers can be extracted out of the photoactive device.

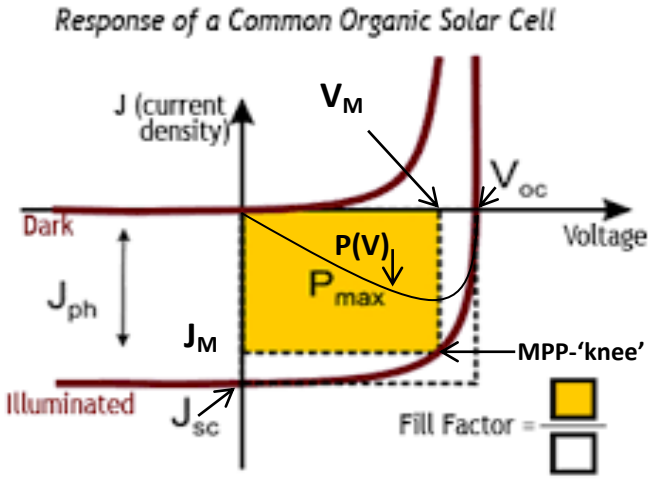

Figure 3.10 *Simulated J(V) characteristics of a solar cell at a particular light level and in darkness: Performance parameters*

Such behaviour is quantitatively indicated by the comparative extent of the difference between I_M and I_{SC} as well as the degree of the difference between V_M and corresponding V_{OC} at the maximum power point. Figure 3.10 graphically illustrates the degree of matching. A higher fill factor indicates greater squareness and nearness of the yellow $J_M - MPP - V_M - 0$ square to the

white $J_{SC} - V_{OC} - 0$ square, which implies higher power conversion efficiency. In terms of the fill factor *FF*, P_{MAX}, V_{OC}, I_{SC}, V_M and I_M, the efficiency η and maximum power P_{MAX} of the SC are given by: $\eta = \frac{P_{MAX}}{P_{in}} = \frac{I_M V_M}{P_{in}} = \frac{FF\left(V_{OC} I_{SC}\right)}{P_{in}}$ …(a) and $P_{MAX} = FF\left(V_{OC} I_{SC}\right)$…(b) (3.20)

where P_{in} is the incident power. From Eqs. (3.20), the efficiency of a solar cell can be viewed as the fraction of the incident power which is converted to electricity.

3.6.3 Parasitic resistances (series and parallel)

Resistive effects in solar cells decrease the fill factor and hence the efficiency of the solar cell through power dissipation (a loss mechanism) in the resistances. The most common parasitic resistances are series resistance (R_S) and shunt (parallel equivalent) resistance (R_{SH}). The inclusion of the series and shunt resistances in the solar cell model is shown in Figure 3.9. In practice, power will be lost in the contacts through leakage currents within and around the cell. These flaws are the ones simulated with the two parasitic resistances. To model the power loss due to leakage currents plying the polymer bulk sheet layer (inclusive of active material properties and polymer-polymer junctions), a parallel connected or shunt resistance R_{SH} is fitted as shown in Figure 3.9. To mimic power lost in contact resistance at the polymer-electrode interfaces and within the electrodes, a series resistance R_S is included as in Figure 3.9. To derive the $I(V)$ $\{or\ J(V)\}$ characteristic of the solar cell inclusive of the effects of parasitic resistances, use is made of Ohm's $V = IR$ and Kirchoff's laws of currents at a junction in a circuit and potential changes in a loop.[41] The modified $I(V)$ characteristic which accounts for the effect of parasitic resistances then becomes[81]

$$I(V) = \frac{\left[I_{SC} - I_0\left\{\exp\left(\frac{e\left(V - I(V)R_S\right)}{n k_B T}\right) - 1\right\}\right]R_{SH} - V}{R_S + R_{SH}} \tag{3.21}$$

Eq. 3.21 can be rewritten in the form

$$I(V) = I_L - I_0\left[\exp\left(\frac{e\left(V - IR_S\right)}{nkT}\right) - 1\right] - \frac{V + IR_S}{R_{SH}} \tag{3.22}$$

Chapter 4

Materials and methodologies

4.1 Materials

4.1.1 Indium Tin Oxide (ITO)

Indium tin oxide (ITO) is more of a composite alloy of indium, tin and oxygen in varying proportions (about 74% Indium (In), 18% Oxygen ($O_{2)}$, and 8% Tin (Sn) by weight).[111-113] Its general molecular formula is **In_2O_5Sn** or **In_2O_3/SnO_2**.[111-113] It is transparent and colorless in thin layers, but in bulk its colour ranges from pale yellow to greenish yellow (see Figure 4.1) depending on SnO_2 concentration. The oxide is widely used as a transparent conducting electrode in many organic devices, because of its two main properties, which are; good electrical conductivity and high optical transparency over the visible region.[8], [83-84] In many applications, these two properties outweigh its disadvantages. It is also easy to deposit it as a thin film and its patterning is easy. During its deposition onto glass, for purposes of forming the anode electrode, at the (commercial) manufacturing stage, a compromise is made between conductivity and transparency, because increasing the thickness increases its electrical conductivity, but decreases its optical transparency.[8], [83-84], [111-113]

Figure 4.1 *Indium tin oxide, from left*: *first→general structural formula, second→dust form and third→after deposition on glass substrates.*[111-113] *Smallest (square) glass substrate shown in picture is of the size purchased with side measurement of 2.50 cm and then cut into 4 smaller squares each of side dimensions 1.25 cm.*

However the downside the material is that high quality ITO is too expensive, has a low work function (~ 4.6 eV), contains indium that is too limited in supply for widespread use in solar

energy applications, cannot be solution processed, is brittle and cracks easily and is therefore unsuitable for use on flexible substrates.[8], [84]

Indium tin oxide (ITO) coated on glass is generally employed as the high work function anode electrode in organic photovoltaic (OPV) cells, because of its good electrical conductivity.

4.1.2 Poly(3,4-ethylenedioxythiophene)-poly(styrenesulfonate) (PEDOT:PSS)

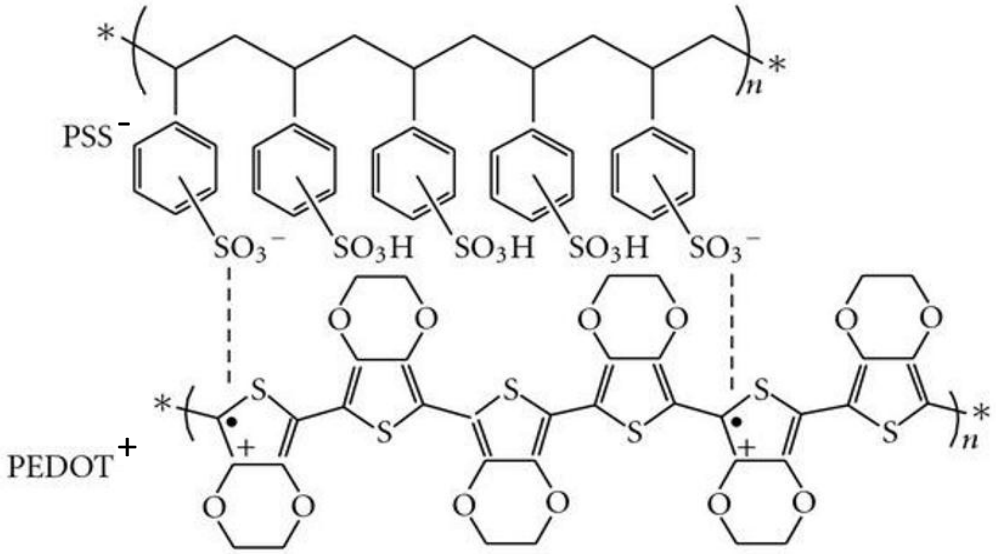

Figure 4.2: *Chemical structure of PEDOT:PSS showing PEDOT+ and PSS–,*[84], [114] *The fixed negative charges on the PSS chain are balanced by polarons existing on the PEDOT chain, giving rise to enhanced electronic conductivity. The "dot" and "plus" represent the unpaired electron and positive charge on the PEDOT chain, respectively*.[114]

PEDOT is a conjugated polymer that is positively doped and neutralised with the PSS polyanion. The material PEDOT:PSS (Figure 4.2) assists in band bending for the anode and so enhances the performance of the solar device. Furthermore, PEDOT:PSS is highly transparent in the visible range, has excellent thermal stability and is processable in aqueous solution. As a result it is widely used as a buffer layer for anodes in OSCs to improve hole extraction and block the flow of electrons to the anode. In the process, it prevents electrical shorting of devices by reducing pinhole defects.[8] The material helps to smooth the ITO surface, decreasing the density of pinholes and stifling current leakage that occurs along shunting paths.[8], [84], [114-115]

4.1.3 Poly (3-hexylthiophene 2,5 diyl) (P3HT)

In all our experimental fabrications we used the > 98% head-to-tail regioregular poly (3-hexylthiophene-2,5-diyl) (P3HT) purchased from Sigma-Aldrich in South Africa, but being a product of USA (P Code1001366532). The regioregularity aspect refers to the percentage of sterio-regular head-to-tail (HT) attachments of the alkyl side chains to the three-position of the thiophene rings. Figure 4.3 shows the structural formula of one of the P3HT isomers. The regioregular P3HT was our donor material and we chose it primarily because of its end-to-end arrangement of side chain, which allows efficient stacking of the conjugated backbones, leading to superior conductivities,[116] charge carrier mobilities,[117] optical non-linearity and magnetic properties over the regiorandom head-to-head (HH) conjugated polymers. P3HT is soluble in a variety of solvents, which enables easy and cheap processing. The rigidity and planar conformation of its conjugated backbone further ensures efficient packing, crystallization and development of functional properties with a characteristic absorption in the low energy part of the spectrum.[118] However, a precise crystallization mechanism of conjugated polymers has not yet been fully established. On account of the alkyl side group, P3HT is rendered hydrophobic in neutral state. Our HT P3HT was prepared by the Rieke method,[119] which is commercially available from the Aldrich Chemical Co.

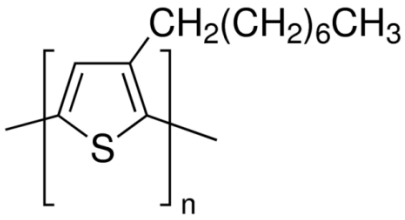

Figure 4.3 *Structural formula of P3HT*

4.1.4 Fullerenes and PCBM

4.1.4.1 Fullerenes

Fullerenes are a class of closed-cage carbon molecule, C_n, characteristically containing 12 pentagons and a variable number of hexagons.[90] Fullerenes composed of less than 300 carbon atoms, or endohedral fullerenes, are commonly known as "buckyballs", and include the most common fullerene, buckminsterfullerene, C_{60}. Giant fullerenes, or fullerenes with more than 300 carbon atoms, include single-shelled or multi-shelled carbon structures, onions, and nanotubes.[90]

Form: As individual molecules, fullerenes are about 1 nm in diameter. This compares to 0.16 nm for a water molecule. During manufacture, these molecules come together to form small particles (10 nm to several microns).[90], [102-103] They are readily handled, or can be easily pelletized. Buckminsterfullerene is the smallest fullerene molecule in which no two pentagons share an edge (which can be destabilizing, as in pentalene). It is also the most common in terms of natural occurrence, as it can often be found in soot. The structure of C_{60} is a truncated (T = 3) icosahedron, which resembles an association football ball of the type made of twenty hexagons and twelve pentagons, with a carbon atom at the vertices of each polygon and a bond along each polygon edge.[90], [102-103] The suffix "ene" indicates that each C atom is covalently bonded to three others (instead of the maximum of four), a situation that classically would correspond to the existence of bonds involving two pairs of electrons ("double bonds")

4.1.4.2 [6,6]-phenyl-C61-butyric acid methyl ester (PCBM)

The fullerene PCBM stands in as the electron acceptor in the active bulk heterojunction (BHJ) solution of its blend with a donor like P3HT. Its structural form is of the configuration shown in Figure 4.4. [90], [102-103] PCBM has the capacity to accept as many as six electrons into its structure. P3HT,[10] the dominant solar radiation absorber material has been found to have sufficient band gap to absorb radiation within the UV and visible. Also, the synthesis of these solution processable conjugated polymers with different band-gaps provides a wide potential to absorb the insolation.[10] C_{60} is a molecule that consists of 60 carbon atoms arranged as 12 pentagons and 20 hexagons.[10], [90] The carbon atoms within each C_{60} molecule are held together by strong covalent bonding. Van der Waals interactions are the dominant intermolecular forces in C_{60} crystals.[120] Our experimental PCBM was purchased from Sigma Aldrich in South Africa, but being a product of Netherlands. Its electronic grade was > 99 %.

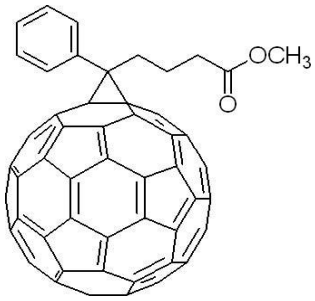

Figure 4.4 *Structural form of PCBM*

4.1.5 Chlorobenzene (C_6H_5Cl)

Chlorobenzene is an aromatic organic compound with the chemical formula C_6H_5Cl and has a structural formula of the build shown in Figure 4.5. It is a colorless, flammable liquid that is commonly used as a solvent. In all our making of the active blend, we used chlorobenzene as the solvent for P3HT and PCBM, since it had empirically demonstrated superiority in $I(V)$ characterisation over others like chloroform. Our Chlorobenzene was in a dark brown tinted bottle inscribed: Koch-Light Laboratories Ltd; Colnbrook Berks England; 1009-57; CHLOROBENZENE; **C_6H_5Cl**; purics; M.W.11-56; Fl.p.30 °C; ML 055-01.

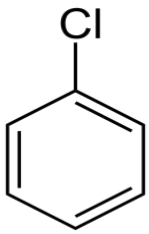

Figure 4.5
Chlorobenzene structural formula

4.1.6 Aluminium (Al)

For all our fabrications, aluminium metal formed the electron collecting electrode (cathode). Aluminium is a low work function metal (~ 4.1 eV).

4.2 Methods

4.2.1 Optical responses of glass, ITO and PEDOT:PSS

We first investigated the optical characteristics of the auxiliary materials in the conjugated polymer solar cell assembly by conducting absorbance measurements of the individual materials involved. These materials are glass, ITO and PEDOT:PSS. The information helps us to determine whether the incorporation of such materials significantly reduces or does not reduce the light targeted for the active material. The absorbance of glass was measured with air as the reference. For ITO, glass was the reference and for PEDOT: PSS, glass and ITO were the references.

4.2.1.1 Results and Discussion

Figure 4.6 shows the ITO plot superimposed on the glass plot (the zero baseline), which basically means that it does not absorb any light in the visible region, since glass is seen not absorb any light in the same region. More importantly, both materials dot not absorb in the

region absorbed by the active materials P3HT, PCBM and P3HT:PCBM. This characteristic is picked up from the comparison of the graphs of Figures 4.6 and 4.7. The behaviour is as expected and is good, because the light is let to pass to the active layer where its absorption is needed most.

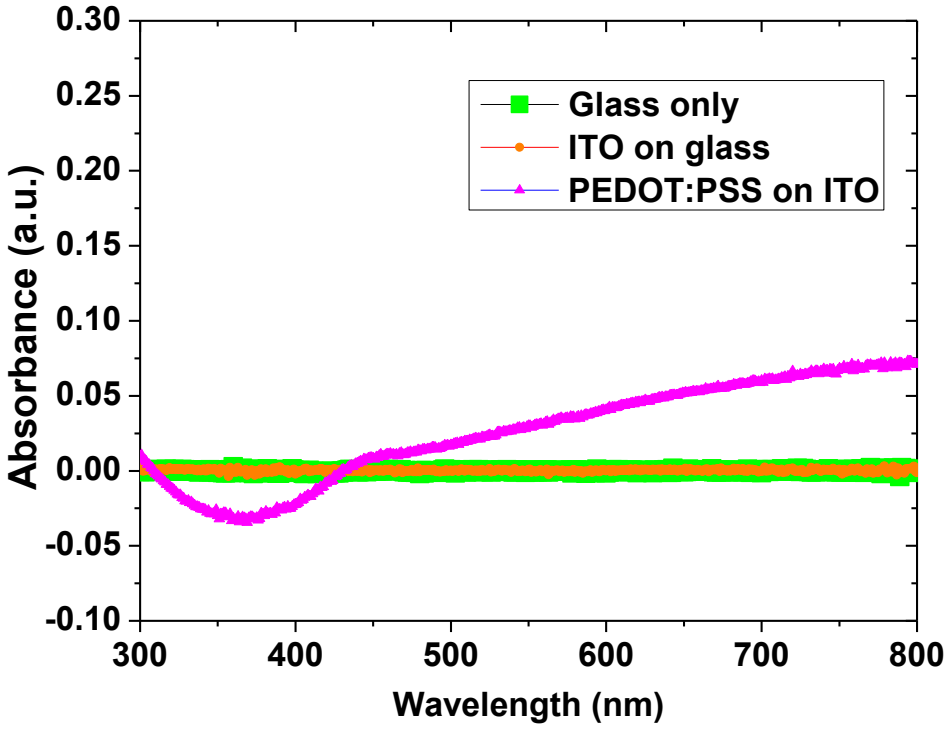

Figure 4.6 *Comparative optical absorbances of glass, ITO and PEDOT:PSS*

PEDOT:PSS shows a generally very low absorbance, which becomes negative in the approximate wavelength range of 300 nm to 440 nm. The interpretation of the negative absorbance range helps us identify a unique optical behaviour characteristic of PEDOT:PSS. The conjugated polymer (PEDOT:PSS) removes some of the reflective ability of glass and thereby makes more light pass through to the active layer. The low absorbance must also be due to the very thin layer of PEDOT:PSS spun over the substrate. Although PEDOT:PSS has a broad absorbance area (deduced from Figure 4.6), the light it absorbs is negligibly small, such that we can safely treat it as a material transparent to light in all (organic) photovoltaic endeavours.

4.2.2 Enhanced optical absorbance of P3HT, PCBM and P3HT:PCBM blend due to thin film cast of PEDOT:PSS on ITO substrate

The optical absorption enhancement of PEDOT:PSS was foremost investigated to establish the optical superiority of using PEDOT:PSS based substrates, as opposed to depositing the active layer on top of bare ITO substrates and obtained the results shown graphically in Figure 4.7.

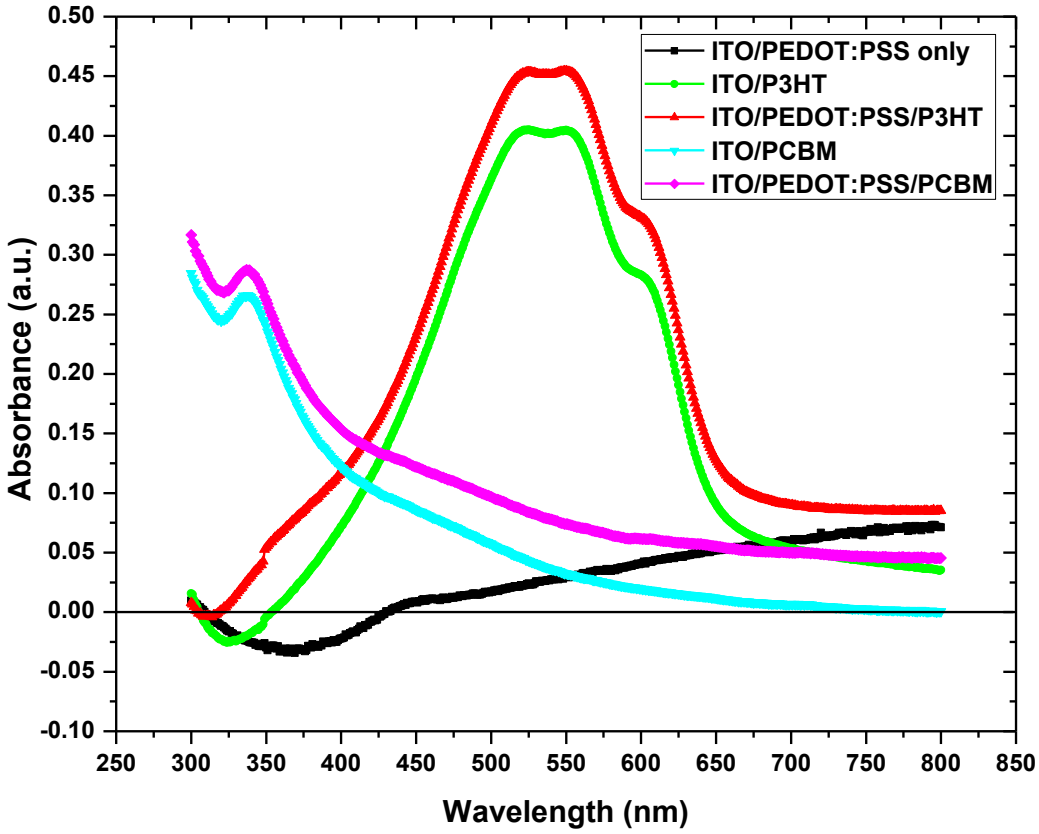

Figure 4.7 *Optical absorbance enhancement effect of PEDOT:PSS on polymer P3HT and fullerene PCBM with base substrate ITO on glass*

Both P3HT and PCBM show significantly enhanced absorbances under PEDOT:PSS incorporated assemblies than under those without PEDOT:PSS. Based on the findings, all the experimental devices were spin cast on ITO/PEDOT:PSS substrates. Explanation of the behaviour and role of PEDOT:PSS is presented in section 4.2.4.1.

4.2.3 Generalised fabrication of the experimental organic (carbon-based) solar cells

Figure 4.8 displays the composite building blocks of the backbone experimental activities undertaken in the device fabrications and in the subsequent performance tests (characterisation measurements) of the organic (carbon-based) solar cells.

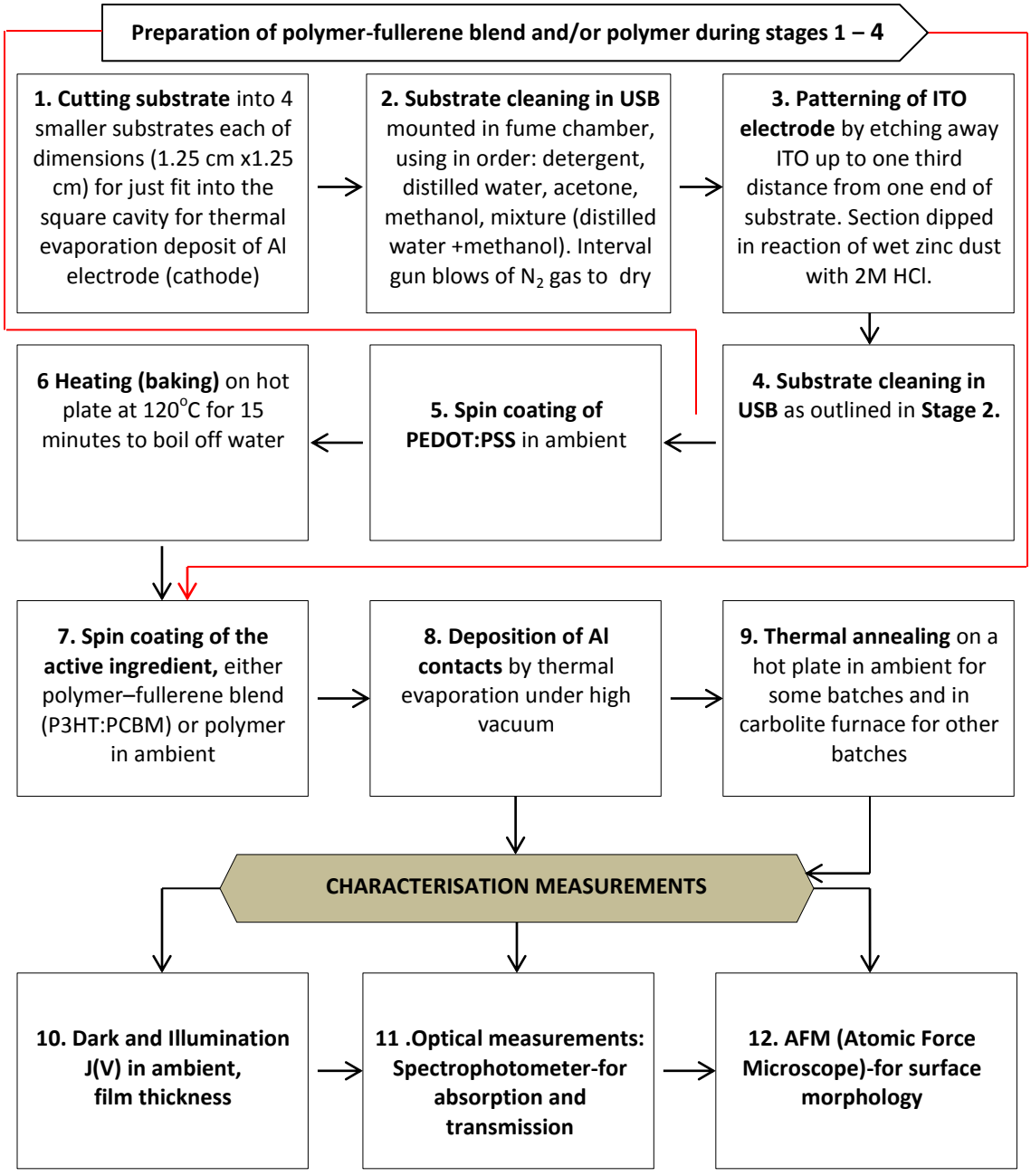

Figure 4.8 *Composite building blocks of the backbone experimental activities undertaken*

Prior to cutting and cleaning the substrates, preparations of the active ingredient solutions were conducted and left to run (under monitoring) while carrying out stages 1 to 4 (as Figure 4.8 shows).

4.2.3.1 Fabrication of the experimental polymer-fullerene bulk heterojunction solar cell

We used the commercial 703184-10PAK indium tin oxide (ITO) coated transparent glass slide squares as the substrates. ITO formed the high work function anode electrode. The ITO glass substrates were purchased from SIGMA-ALDRICH and each was of the following specifications: side dimension: 2.50 cm, surface resistivity ρ: 30-60 Ω/square slide and Lot # MKBQ1819V. Each of the purchased substrates was carefully cut into 4 named smaller square substrates (collectively referred to as a batch) each of side length 1.25 cm. We however remark that the smaller square area A of the substrate resultant from the cutting brings in the problem of increased resistance R, since the resistivity ρ remains constant in the relation $R = \rho L/A$, where L is the side length of the square. In our case, the surface resistance theoretically doubled in the smaller substrate due to cutting.

The substrates (in their batches) were then subjected to thorough cleaning in hot ($\approx 50℃$) ultrasonic (water) bath (USB) mounted under fume hood. The cleaning activities (each of which was run for 5 minutes) involved the sequential use of distilled water and solvents according to the listing: **detergent →distilled water →acetone $(\times 2)$ →methanol →mixture (in equal proprtions) of distilled water and methanol.** At the end of each 5 minutes cleaning interval and still under fume hood, each substrate was dried by gun blowing it with nitrogen.

In order to guard against short circuiting and control the effective surface area, the ITO electrode was patterned by etching away ITO one third distance from the end bearing the inscribed identity of the device. The ITO section to be spared was covered with kapton tape and etching of the other section was achieved by dipping it into the reaction of wet zinc dust with 2M HCl. The zinc dust [< 10 μm ≥ 98%], was purchased from SIGMA-ALDRICH. The 2M HCl had been prepared by adding 16.4 ml of 32% hydrochloric acid (HCl) to 83.6 ml of distilled water, which produced 100 ml of 2M HCl. After etching all the substrates constituting the batch, the substrates were again thoroughly cleaned as described earlier in this section (and also outlined in stage 2 of Figure 4.8). The clean substrates were then subjected to spin coating and Al electrode deposition

activities. Poly(3,4-ethylenedioxythiophene)-polystyrenesulphonate (PEDOT:PSS) was the first to be spin coated on each of the thoroughly cleaned ITO coated glass substrates. This was done at a constant speed of 2000 rpm for 60 seconds, followed by baking each of them (on a hot plate) at 120^{o}C for 15 minutes. The thermal drying process was done in order to evaporate water from the PEDOT:PSS solution and build up stability in the PEDOT:PSS interfaces, which in turn enhances the opto-electrical properties of the device.[8], [121]

In forming the active composite, each of 7.5 mg of regioregular head-to-tail poly(3-hexylthiophene-2,5-diyl) (P3HT), the electron donor, purchased from Sigma Aldrich and 7.5 mg of [6,6]-phenyl C_{61} butyric acid methyl ester (PCBM), the electron acceptor, also purchased from Sigma Aldrich and having the capacity to accept as many as six electrons into its structure, was dissolved in 0.5 ml of chlorobenzene and stirred by use of a magnetic stirrer for 3 hours in ambient. P3HT is the conjugated polymer and PCBM is the fullerene). The active blend solution of P3HT and PCBM was then made by mixing the two solutions (in the matrix P3HT:PCBM = 1:1 by mass and concentration 15 mg/ml) and subjecting the mix to magnetic stirring for a further 2 hours in ambient. For experiments in Chapters 5 and 7, we then cast the active polymer-fullerene heterojunction matrix layer by spin coating the prepared 1:1 P3HT:PCBM blend solution on top of the dry PEDOT:PSS film, also at 2000 rpm for 1 minute in ambient. For Chapter 6 experiments, we varied the spin coat speeds of the 1:1 P3HT:PCBM blend as given in the chapter.

Each active layer spin coating was followed by deposition of the Al electrode (~ 100 nm thick) by thermal evaporation under high vacuum of the order of 1.5×10^{-6} mbar, at the deposition rate of 0.1 – 0.2 nm s^{-1}, which was monitored by a quartz crystal thickness monitor. This was the final stage of the fabrication process. High vacuum is essential for impurity free evaporation. A deposition power in the order of 300 W was set across the molybdenum resistance wire on which an Al strip to be melted was hung. The Al electrode deposition completed the fabrication process, which produced a polymer-fullerene bulk heterojunction solar cell of the structure shown in Figure 4.9. The assembly was left in the vacuum chamber to cool for 30 minutes, after which the devices were either subjected to opto-electrical characterisation or further treated (for example post-fabrication annealing) as per specific investigation requirements, before and/or after opto-electrical characterisation.

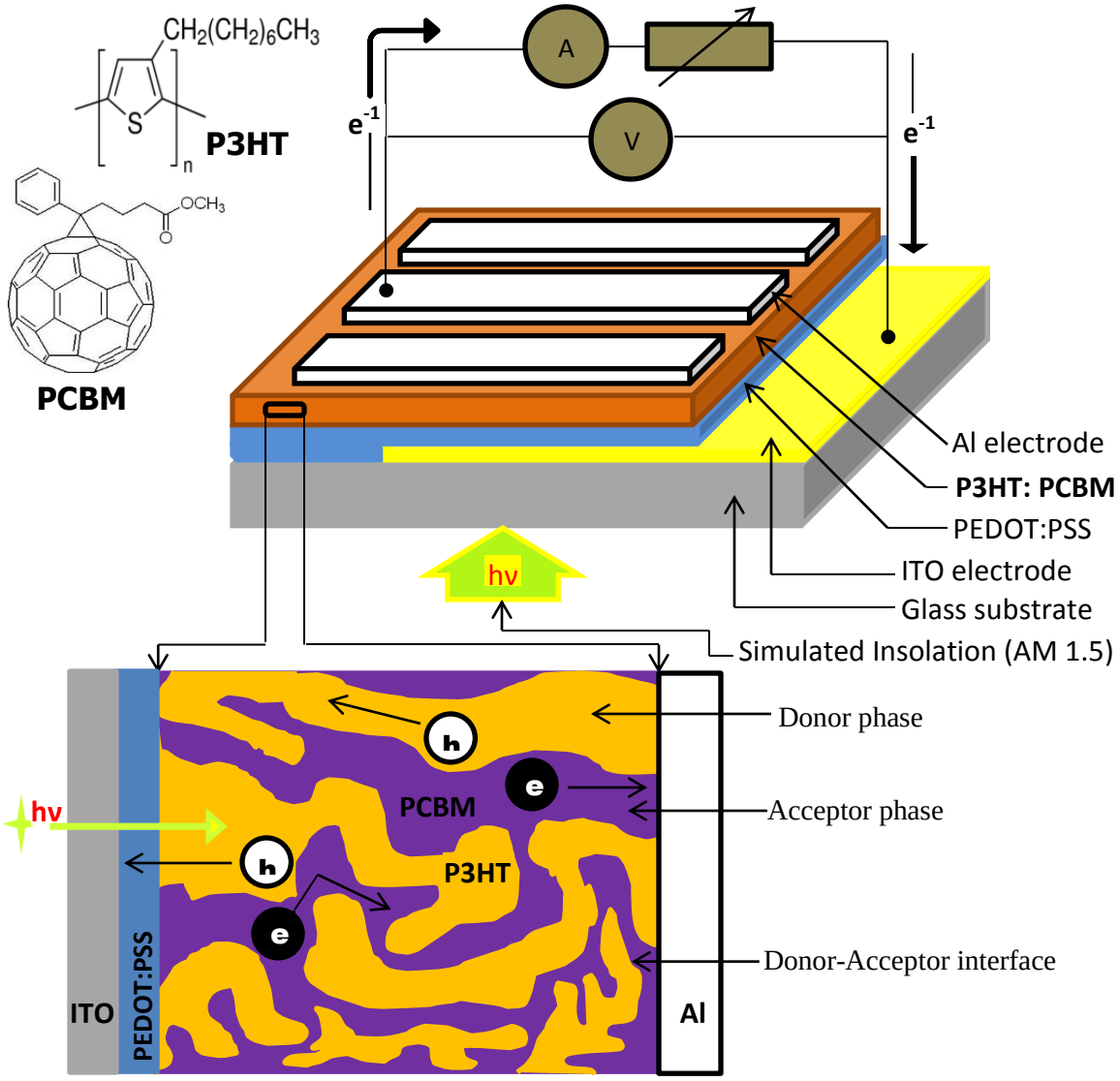

Figure 4.9 *Structure of the fabricated bulk heterojunction polymer-fullerene solar cells as well as the chemical formulae of the materials forming the active thin film composite* (*P3HT:PCBM*)

4.2.3.1.1 Characterisation techniques

Characteristic current-voltage measurements were obtained in the dark and under the solar simulated white light illuminations (AM 1.5) of varying intensities. The illumination was from a ThermoOriel 150-W solar simulator with AM1.5G filters. A dc current-voltage HP 4141B Source/Monitor Unit was used to obtain the results. Automated (I-V) measurements were retrieved via a connected computer which performed corresponding current-voltage sweeps through use of the Lab-View program.

A Varian Cary UV-VIS-NIR visible spectrophotometer (Cary 500 scan) was used to measure the optical absorption responses of the P3HT:PCBM blend films, which formed the opto-active components of the devices. This photo-detector (which is available in the University of the Witwatersrand School of Physics) is able to measure different wavelengths of a light beam sent through the sample under investigation for absorption and/or transmission by determining the optical excitations of the sample upon dispersion. The measurements were confined to the 300-800 nm wavelength range and were then used to produce the absorption spectra of the active blends.

Morphological studies of the active layers of chosen devices were conducted through imaging engagements of the Veeco Dimension 3100 Atomic Force Microscope (AFM) instrument available in MMMU at the University of the Witwatersrand.

Film thickness measurements were done by the use of a surface profilometer available at the Council for Scientific and Industrial Research (CSIR) centre in Pretoria, South Africa.

4.2.4 Analyses of the generated interfaces, energy levels, charge transport levels and energetic mechanisms of the experimental device

In general, our fabrications of the bulk heterojunction (conjugated) polymer-fullerene solar cells created the following interfaces and electrical contacts: ITO/PEDOT:PSS interface, ITO/PEDOT:PSS/P3HT interface, P3HT/PCBM interface in the bulk, ITO/PEDOT:PSS/PCBM interface P3HT/Al junction and the PCBM/Al junction. We discuss about these in the next sections and start with the ITO/PEDOT:PSS interface, which we used as the anode electrode in most of our devices.

4.2.4.1 ITO/PEDOT:PSS interface (and electrode)

The stability of the ITO/organic interfaces (like ITO/P3HT interface in our case) greatly influences the performance characteristics of the device.[122-123] There are many problems associated with direct electrical contacts of such materials. For example, in single-layer organic light emitting diodes (OLEDs) some of the problems include:

- oxidation of the organic emitting layer by oxygen diffusing out of the ITO
- evolution of electric shorts aggravated by the rough ITO surface

- an imbalance in electron-hole injection at the electrical contacts of the two materials involved.

Such problems curtail the life-time of the device.[124] To circumvent or minimise these problems, a thin film of hole injecting PEDOT:PSS is applied between ITO and the active layer. Since the introduced PEDOT:PSS layer will be very thin (~ 60 nm) , it will virtually be transparent to visible light and will therefore not reduce the light output. Instead, its presence will significantly enhance the durability as well as the optical performance of the device and also promote a reduction in the operating voltage.[10], [125] Some of the enhancement outcomes of PEDOT:PSS include: the smoothing effect it renders onto the ITO surface (which impressively reduces the chances of occurrence of short circuiting, by blocking electrons from filtering into ITO, in addition to inflicting significant reduction in the brittleness of ITO) and the reduction of the hole-injecting barrier due to the high energy of the occupied electronic levels of PEDOT:PSS in comparison with that of ITO,[10] (also illustrated in Figure 4.11). In this regard, PEDOT:PSS enhances the mobility of holes. It is possible that PEDOT:PSS may undergo interfacial chemistry with ITO.[123-124] Since PEDOT:PSS is a stable emulsion in water, it is easy to spin-coat it onto ITO. On the downside, when PEDOT:PSS film is exposed to air, it absorbs atmospheric water (water vapour) and forms an aqueous acid environment as a result of the reaction: $H_2O + PSS(SO_3H) . H_3O^+ + PSS(SO_3^-)$ which facilitates the etching of ITO.[10] Furthermore, the sheet resistance of PEDOT:PSS can reduce the short circuit current J_{SC}.

4.2.4.2 Metal-active layer interfaces, energy levels, charge transport levels and energetic mechanisms of the experimental device

In Figure 4.10, we show the same fabricated BHJ solar cell, but with display of the identified interfaces affecting the performance of the solar cell. We note that each of the electrodes (metallic ITO/PEDOT:PSS and metal Al) is in contact (electrical contact) with both P3HT and PCBM. These contacts constitute the metal-active layer (or metal-organic semiconductor) interfaces, from which we identify those active during forward bias (FB) and those active during reverse bias (RB).

As shown in Figure 4.10, the FB active are the Al-PCBM and ITO/PEDOT:PSS/P3HT interfaces and the RB active are the Al/P3HT and ITO/PEDOT:PSS/PCBM interfaces.

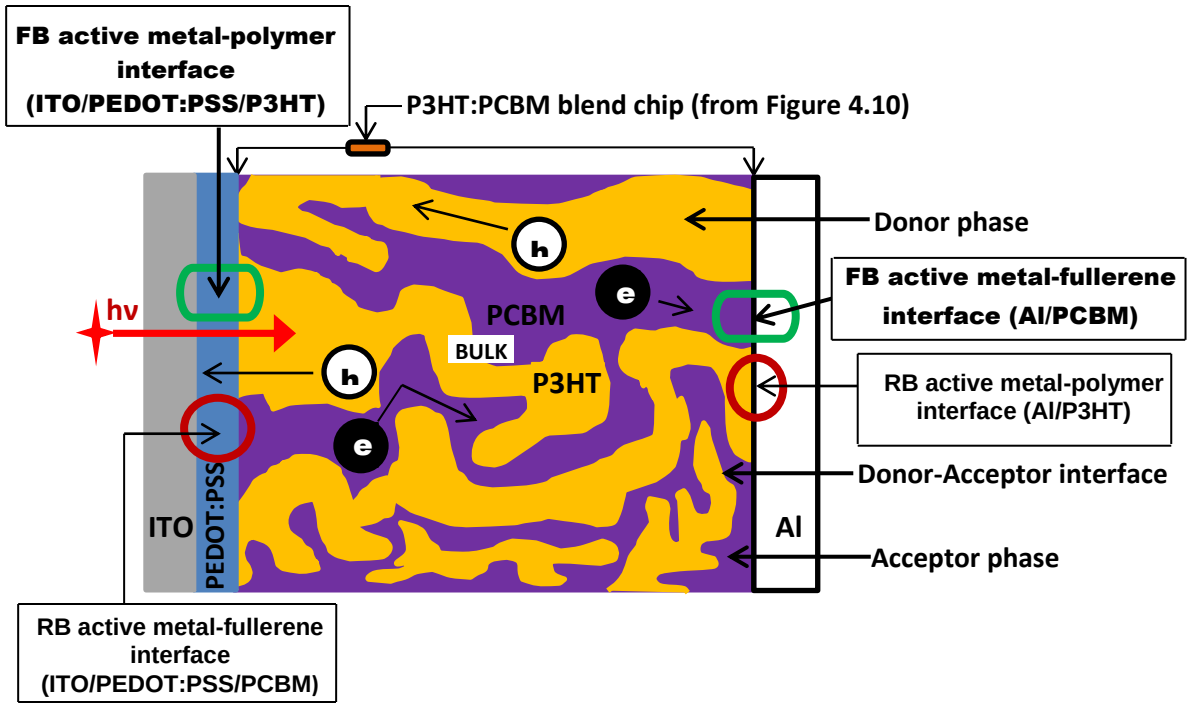

Figure 4.10 *Identified metal-organic semiconductor interfaces, donor-acceptor interfaces, as well as the transport phases formed of the bicontinuous composite of donor and acceptor of the BHJ device*

The zoomed P3HT:PCBM blend chip (from Figure 4.9) which is shown in Figure 4.10 portrays the desired bicontinuous composite of donor and acceptor, which should phase segregate on a suitable length scale to allow maximum ordering and effective charge transport in continuous pathways to the electrodes.[126-127] Such ordering also minimises recombination of free charges. We also note that the bulk heterojunction polymer-fullerene blend is fraught with many polymer-fullerene junctions. These account for the dissociation of the photogenerated excitons within the active blend.

Figure 4.11 shows an energy level diagram of the device under non-equilibrium conditions and includes approximate energy values (work functions) of the faces (orbitals) forming the identified metal-active layer junctions and the polymer-fullerene (donor-acceptor) interfaces identified from Figure 4.10.

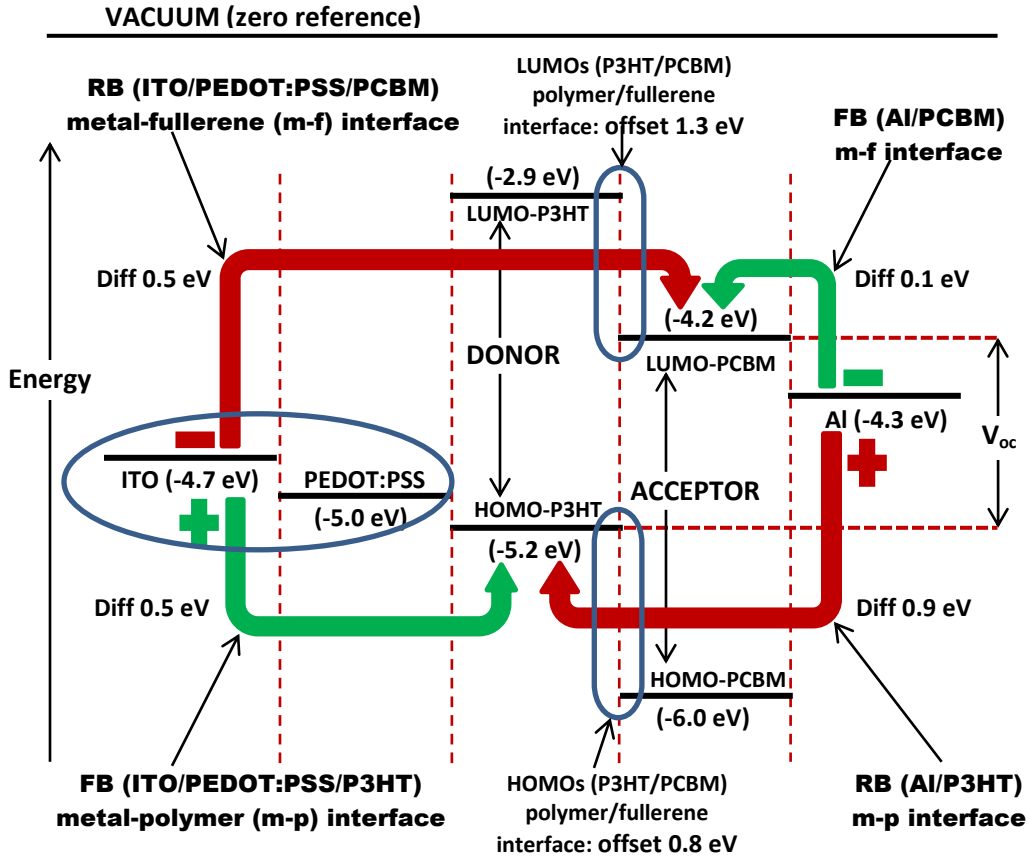

Figure 4.11 *Energy level diagram of the ITO/PEDOT:PSS/P3HT:PCBM/Al device under non-equilibrium conditions as well as the associated metal-active layer interfaces, donor polymer-acceptor fullerene interfaces and biases*

From the energy level diagram of the P3HT:PCBM based device shown in Figure 4.11, we identify 8 metal-polymer interfaces (or electrical contacts). The four which are making significant contributions to the performance of the device, namely Al/PCBM-LUMO, ITO/PEDOT:PSS/P3HT-HOMO, Al/P3HT-HOMO and ITO/PEDOT:PSS/PCBM-LUMO are shown. The approximate work function ϕ of each of the materials forming the m-p contact is shown, for example, in the case of the Al/PCBM-LUMO interface, $\phi_m = \phi_{Al} = 4.3$ eV and $\phi_s = \phi_{PCBM} = 4.2$ eV.

We remind that **only magnitudes of the work functions are compared**, because the negative sign on each of the given work functions is **solely** to emphasise the position of the energy level

relative to the assigned zero potential at infinity (vacuum). Since the work functions of the constituent materials (metal and semiconductor) forming each of the junctions are different, it implies that any of the junctions is either Schottky (rectifying) or ohmic. A rectifying contact is characterised by the formation of a potential barrier ϕ_B which bars the corresponding charge carrier in the metal from entering the semiconductor. This means that an electron blocking interface (contact) is marked by the build-up of an electron blocking potential barrier ϕ_{Be}.

We investigated the nature of the significant four interfaces (that is, electrical contacts) using the criteria explained in earlier sections, which we here summarise as:

- For n-type semiconductor (in contact with a metal): if $\phi_m > \phi_s$, it implies electron blocking Schottky (rectifying) interface and therefore an electron blocking potential barrier ϕ_{Be} formed.
- For n-type semiconductor: if $\phi_m < \phi_s$, it implies ohmic interface, which implies no blocking potential barrier.
- For p-type semiconductor: if $\phi_m < \phi_s$, it implies a hole blocking Schottky interface and therefore a hole blocking potential barrier ϕ_{Bh} present.
- For p-type semiconductor: if $\phi_m > \phi_s$, it implies ohmic contact and therefore no blocking potential barrier.

Since P3HT is a hole conducting polymer, it merits fall under p-type organic semiconductors while PCBM, an electron conducting fullerene, is therefore an n-type semiconductor fullerene. Application of the outlined criteria in determining (for example) the nature of the Al/PCBM-LUMO interface gives that the Al/PCBM-LUMO interface is an electron blocking Schottky contact, since $\phi_{Al} > \phi_{PCBM-LUMO} \equiv \phi_m > \phi_s$.

We similarly determined the nature of each of the other interfaces and obtained the findings given in Table 4.1.

Table 4.*1 Summary findings of the nature of each of the significant metal-polymer interfaces of the fabricated bulk heterojunction ITO/PEDOT:PSS/P3HT:PCBM/Al solar cell*

Metal-polymer interface description	**Work functions ϕ_m vs ϕ_s relation**	**Nature of interface**	**Nature of Potential barrier ϕ_B**
Al/PCBM-LUMO	$\phi_{Al} > \phi_{PCBM-LUMO}$	Schottky (rectifying), electron blocking	Schottky barrier ϕ_{Be}, Electron blocking
ITO/PEDOT:PSS/P3HT -HOMO	$\phi_{ITO/PEDOT:PSS} < \phi_{P3HT-HOMO}$	Schottky, hole blocking	Schottky barrier ϕ_{Bh}, hole blocking
Al/P3HT-HOMO	$\phi_{Al} < \phi_{P3HT-HOMO}$	Schottky, hole blocking	Schottky barrier ϕ_{Bh}, hole blocking
ITO/PEDOT:PSS/PCBM -LUMO	$\phi_{ITO/PEDOT:PSS} > \phi_{PCBM-LUMO}$	Schottky, electron blocking	Schottky barrier ϕ_{Be}, electron blocking

Table 4.1 shows that all the four metal-polymer interfaces are rectifying contacts. Each Schottky interface is manned by the associated potential barrier, which hinders like charge carriers (electrons) from the metal side from crossing the interface into the semiconductor.

To aid understanding, we explain the electronic interactions at the Al/PCBM-LUMO interface, the understanding of which can be applied in explaining encounters at other interfaces. An electron in Al, which approaches the Al/PCBM-LUMO interface with the 'intention' of crossing the interface and be in the PCBM (a semiconductor), finds itself confronted (at the junction) by an electron barring potential barrier ϕ_{Be} of the form shown in Figure 2.4.

This potential barrier will be in the PCBM (a fullerene semiconductor) region adjacent (next) to the interface. It impedes the electron from entering the PCBM. For the electron to enter the PCBM, it has to overcome this potential barrier ϕ_{Be}. Depending on the height, width and other barrier determinant parameters as well as the electron kinetic energy, temperature, bias electric field, etc., the electron may cross the interface either by thermionic emission or by quantum mechanical tunneling. The other four metal-polymer interfaces not yet discussed have very large work function offsets, which result in the formation of too large potential barriers that stifle any significant thermionic emission or quantum tunneling. For example, in the case of the ITO/PEDOT:PSS/PCBM-HOMO interface, the ITO electrode alone has a work function of approximately 4.7 eV and the PCBM-HOMO's work function is approximated at 6.0 eV (Figure 4.11). This gives an energy difference of 1.3 eV, which is too large for any significant charge (hole in this case) injection, either thermionically or quantum mechanically. Other metal-semiconductor interfaces (in our device depicted by Figures 4.9 → 4.11) with too large potential barriers are Al/PCBM-HOMO {(6.0-4.3) eV = 1.7 eV}, Al/P3HT-LUMO {(4.3-2.9) eV = 1.4 eV} and ITO/PEDOT:PSS/P3HT-LUMO {(4.7-2.9) eV = 1.8 eV}.

Biasing configurations are also shown in Figure 4.11. We note that under forward bias (FB) (green colour coded), the Al electrode is negative, and injects electrons into LUMO of PCBM, while the ITO/PEDOT:PSS electrode is positive, injecting holes into HOMO of P3HT. Under reverse bias (RB) (red colour coded), the Al electrode is positive, injecting holes into HOMO of P3HT, while ITO/PEDOT:PSS electrode is negative, injecting electrons into the LUMO of PCBM. Charge is always injected into transport level with smallest barrier height for the charge. For both, FB and RB we expect electron injection into PCBM-LUMO to dominate when compared with injection into P3HT-LUMO, because (as can be deduced from Figure 4.11) the barrier is smaller with PCBM. Based on similar analysis, but applied to hole flow into either P3HT-HOMO or PCBM-HOMO, we expect hole injection into P3HT-HOMO to overwhelm that into PCBM-HOMO since the barrier is smaller with P3HT.

The PCBM fullerene has many encouraging properties as an electron acceptor. First, it has an energetically deep lying LUMO[128] which by nature makes it possess high electron affinity relative many potential organic donors. Furthermore, it has a triply degenerate LUMO, which allows the molecule to be reversibly reduced with six electrons. As a result, it is capable of

accepting six electrons in its structure, which shows its ability to stabilize negative charge. The P3HT:PCBM conjugated polymer-fullerene blend exhibits ultrafast {~ 45 fs, (that is ~ 45×10^{-15} s)}[10], [128] photoinduced charge transfer (CT), in which an electron from P3HT exciton is transferred to PCBM at the donor LUMO to acceptor LUMO level. The back transfer is of orders of magnitude slower.[128] Furthermore, PCBM has been shown to have very high electron mobility (up to 1 $cm^2 V^{-1}s^{-1}$ in field effect transistors (FETs)[129] The two materials are capable of packing effectively in crystalline structures conducive to charge transport[130] The electronic structure of PCBM, like many fullerenes, remains constant throughout the fabrication. Comparative analysis of the empirical energy level values given in Figure 4.11 for the P3HT and PCBM LUMOs, together with the photon-to-charge carrier conversion process illustrated in Figure 4.12, expose that the P3HT:PCBM LUMO interface produces a downhill energetic driving force which exceeds the exciton binding energy.

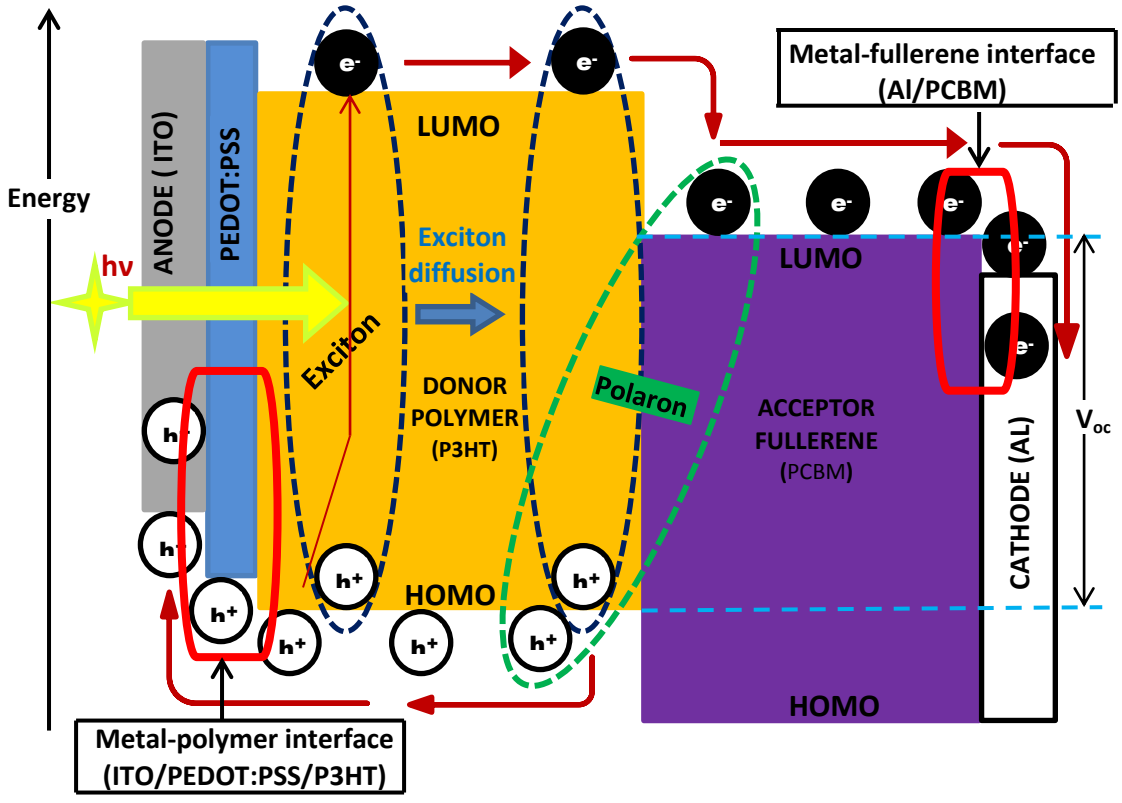

Figure 4.12 *Charge carrier transport levels* (*not to scale*) *and elementary energetic mechanisms of the photon-to-electron conversion process in the fabricated bulk heterojunction solar cell incorporating a conjugated polymer (P3HT) as the photon absorber material and a fullerene (PCBM) as the acceptor material*

In this way, this P3HT conjugated polymer:PCBM fullerene polymer interface facilitates exciton dissociation. The overall of this energetic driving force for a forward electron transfer from the donor to the acceptor is represented by the energy difference (offset) between the LUMOs of the donor and the acceptor. Literature[128], [131-133] gives that a minimum energy difference (offset) of 0.3 eV is required to effect the exciton splitting and charge dissociation. LUMOs' offset for our device has been found to be 1.3 eV. This is far much greater than the minimum required and unfortunately results in excess energy waste, $\{i.e.(1.3-0.3=1.0)eV\ waste\}$. The ideal polymer would be one having minimum threshold energy difference between the LUMOs, so that wasted energy upon exciton splitting would be avoided.[134-136] Optimisation would therefore be required. This calls for methods that result in fine tuning the bandgap for maximum absorption of light and for achievement of the maximum attainable open circuit voltage V_{oc}.[137-140]

In Figure 4.12, we also show the charge carrier transport levels and note that, in either case (FB or RB) of the bulk heterojunction ITO/PEDOT:PSS/ P3HT:PCBM/Al solar cell, holes are always transported along the HOMO of P3HT and electrons are propagated along the LUMO of PCBM. The difference between these two energy levels gives the open circuit voltage V_{oc}.

4.2.5 Comparative optical responses of active ingredients with the AM1.5 solar spectrum and establishment of the contribution of unabsorbed radiation to the limiting efficiency

We conducted absorption measurements of the active experimental materials, P3HT, PCBM and P3HT:PCBM blend, firstly for purposes of getting information on how much of the AM1.5 solar spectrum the materials absorb for charge carrier generation and secondly, in order to determine the contribution of the optical behaviour of the active materials to the limiting efficiency. For comparative purposes, we were able to obtain AM1.5 solar spectral irradiance[141-142] (that is, terrestrial irradiance) and corresponding wavelength distribution data through the University of Oldenburg's Renewable Energy (Photovoltaic) Division, Germany.

4.3 Results and Discussion

The optical data were used to plot comparative graphs (shown in Figure 4.13) of AM 1.5 spectral irradiance and the superimposed absorptivities of the active materials against wavelength

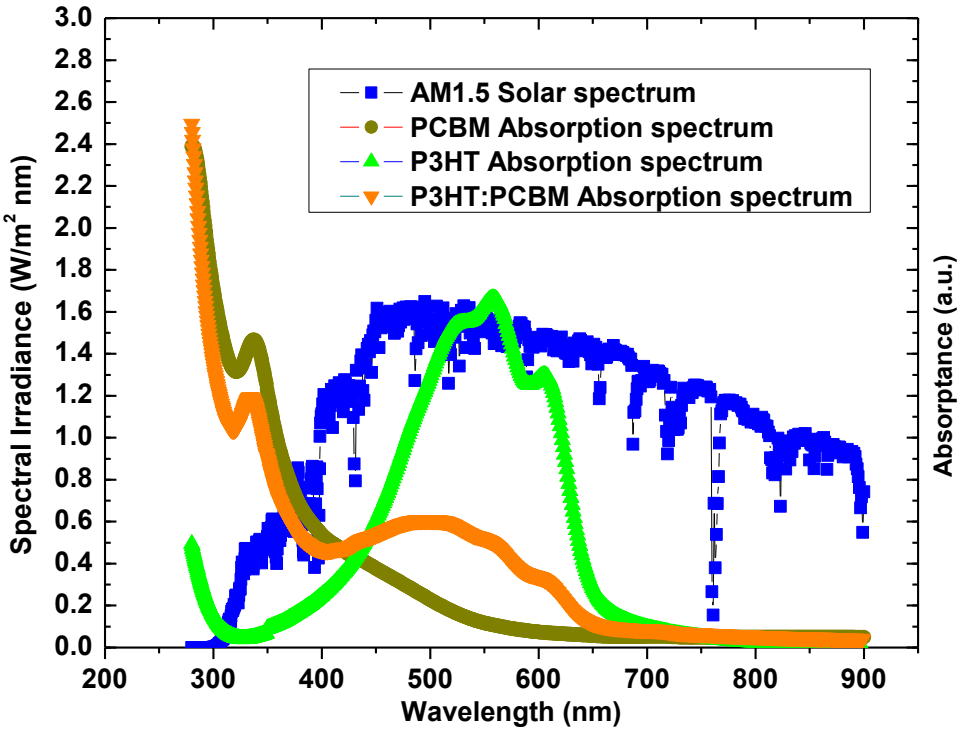

Figure 4.13 *Extractable portion of AM1.5 solar spectrum as defined by the experimental materials*

These plots enabled us to determine the following attributes of the materials (which in turn contribute to the behaviour of the solar cells made out of them):

- the utilisable range of the AM1.5 (terrestrial) solar spectrum for photovoltaic effect due to the P3HT:PCBM composite (which for our case was in the ratio 1:1) and also due to the individual active materials (P3HT (donor) and PCBM (acceptor))
- the optical properties of the active materials in the generation of charge carrier pairs (electron–hole)
- the theoretical limiting efficiency as based only on the radiation which cannot be absorbed by the active materials

Theory has already advanced that the performance of a given solar cell very much depends on the amount of solar radiation absorbed by the active material(s). This sets a limit of efficiency right from the onset, because in practice, not all the incident flux is absorbed. Only photons possessing energy greater than or equal to the band gap of the material are absorbed and may or may not contribute to electron-hole pair generation. A photon of energy greater than the

material's band gap is still capable of producing only one electron-hole pair. In theory, it could have been possible for one photon to produce two, three or four, etc., electron-hole pairs if its energy was respectively double, triple or quadruple, etc., that of the absorbing material's band gap. Such multiple energy photons are negligibly available in nature. Excess energy is mostly dissipated as heat in the lattice. For argument's sake, if such multiple energy photons were of an appreciable fraction in nature, their absorption would result in large amounts of excess energy being dispersed in the lattice, which would in turn increase the temperature of the cells of the material to unbearable levels. Too much temperature generates too much heat, which may detriment the cells. Based on this, we can therefore fall back on the assertion that an absorbed photon can generate only one electron-hole pair.

The fraction $f_{0-\lambda}$ of the of the blackbody energy between zero and λT has been shown (Section 3.4) to be given by

$$f_{0-\lambda} = \int_0^{\lambda T} \frac{C_1 d(\lambda T)}{\sigma(\lambda T)^5 \left[\exp\left(C_2 / \lambda T\right) - 1\right]} \tag{4.1}$$

The red edge of the visible spectrum is at about 770 nm (or 0.77 μm). If the sun is assumed to be a blackbody at 5777 K, the fraction of energy between zero and the red edge of the visible spectrum is obtained by first integrating Eq. (4.1) and then substituting λT with, $\lambda T = 0.77\,\mu m \times 5777\,K = 4448\,\mu m\,K$, which gives about 56%.

For P3HT (electron donor), the absorption edge is at approximately 670 nm. Using equation (4.1), the fraction $f_{0-\lambda}$ of energy from zero to λT is therefore about 46%. The absorption edge for PCBM (an electron acceptor) is at about 560 nm, which gives a fraction $f_{0-\lambda}$ of about 32%, being the one capable of generating electron-hole pairs. As for P3HT:PCBM, the absorption edge is at approximately 630 nm, but with a much smaller absorption peak (at about 500 nm wavelength) compared to that of P3HT alone. The composite (that is, P3HT:PCBM) cannot therefore give a fraction $f_{0-\lambda}$ which is higher than 46%. This sets a limiting efficiency of 46%, based only on radiation that inherently cannot be absorbed by the materials under consideration.

It is of interest to note that 46% efficiency would only be possible if the two materials absorbed like blackbodies; in which case, each of them would be absorbing all radiation of all wavelengths

that fall on it. Such 100% absorption, which is independent of wavelength, is characteristic of the ideal and does not hold for real materials like the P3HT and PCBM. The 46% efficiency is also based on the assumption that every absorbed photon generates an electron-hole pair that dissociates successfully and is finally collected. Furthermore, reflection and transmission losses cannot be ruled out for such thin film castings. The limiting efficiency is therefore bound to decrease to a much lower value when other loss mechanisms are factored in.

This analysis has revealed that many factors have to be considered in the choice of materials for organic photovoltaic effect. For example, the thickness of the active materials' layer is a very crucial factor, because too small a thickness is prone to large transmission losses and too large a thickness suffers numerous recombination losses among many others. It is also important to choose materials which exhibit optical responses that are significantly favourable. The band gaps of the materials are particularly crucial. However, there is hope in that the address of this demand seems to lie in conjugated polymers which avail many different band gaps suitable for absorption within the UV and the visible ranges of the AM1.5 solar spectrum.

References: Chapters 1 – 4

[1] Marcel, V. *Energy, Environment and Resources Department, New Petroleum Producers Discussion Group*. Associate Fellow, Energy, Environment and Resources, 2016. https://www.chathamhouse.org/publication/cost-emerging-national-oil-company?gclid=CMaA86yHqdICFQtAGwod-B4Hng; 2016.

[2] https://www.studentenergy.org/topics/fossil-fuels?gclid=CPSB-d6IqdICFSEW0wodVV819g; 2016.

[3] https://www.reference.com/science/long-fossil-fuels-last-76ee451cf8641391; 2016.

[4] Makomva, A.C.B. *Z. Electrical Supply Authority (ZESA) Country Perspective on Rural Electrification*. Village Power 1998, Scalling up Electricity Access for Sustainable Rural Development, 6-8 October 1998 WASHINGTON DC,USA; 1998.

[5] Dennler, G.; Scharber, M.C. and Brabec, C.J. *Polymer-fullerene bulk-heterojunction solar cells*. Adv. Mater, 21, 1323-1338; 2009.

[6] Roth, S.; Blumentritt, S.; Burghard, M.T.; Cammi, E.; Carrol, D.; Curran, S.; Düsberg, G.; Liu, K.; Muster, J.; Philipp, G. and Rabenau. *Molecular rectifiers and transistors based on π-conjugated materials*. Synth. Met, 94, 105; 1998.

[7] Sargent, E.H. *Infrared photovoltaics made by solution processing*. Nat. Photonics, 3, 325-331; 2009.

[8] Liao, K.S.; Yambem, S.D.; Halder, A.; Alley, N.J. and Curran, S.A. *Designs and Architectures for the Next Generation of Organic Solar Cells*. Energies, 3, 1212-1250, doi: 10.3390/en3061212; 2010.

[9] Krebs. F.C. *Polymeric Solar Cells: Materials, Design, Manufacture*. DEStech Publications, Inc., Lancaster, Pennsylvania; 2010.

[10] Chiguvare, Z. *Electrical and Optical Characterization of Bulk Heterojunction Polymer-Fullerene Solar Cells*. PhD thesis, Oldenburg University, Germany, 2005

[11] Zhang, Z. and Yates, Jr*. J.T. *Band Bending in Semiconductors: Chemical and Physical Consequences at Surfaces and Interfaces*. Chem. Rev., 112 (10), pp 5520–5551; 2012.

[12] (a) https://en.wikipedia.org/wiki/Band_bending; 2016.
(b) *www.iapp.de/orgword/?Basics:What_are _organic_semiconductors*

[13] Heeger, A.J.; Sariciftci, N.S. and Namdas, E.B. *Semiconducting and Metallic Polymers*, OUP Oxford, 2010.

[14] Serway, R.A. and Jewett, J.W. *Principles of Physics, 5th ed*. BROOKS COLE Publishing Company; 2012.

[15] Geoghegan, M. and Hadziioannou, G. *Polymer Electronics*, OUP Oxford, 2013.

[16] Kao, K.C. and Hwang, W. *Electrical Transport in Solids, with particular reference to organic semiconductors*, volume 14 of *International Series in the Science of the solid State*. Pergamon Press, Oxford; 1981.

[17] Warren, Z. *The Hall effect in metals and semiconductors*. 2014. https://www.academia.edu/10461272/The_Hall_effect_in_metals_and_semiconductors?auto=download

[18] Peter, Y.Y. and Cardona, M. *Fundamentals of Semiconductors-Physics of Materials Properties*. Fourth Edition, Springer-Verlag Berlin Heidelberg; 2010.

[19] Simmons, J.G. *Theory of metallic contacts on high resistivity solids. I: Shallow traps*. J. Phys. Chem. Solids, **32**, 2587-99; 1971.

[20] Simmons, J.G. *Theory of metallic contacts on high resistivity solids. II: Deep traps*. J. Phys. Chem. Solids **32**, 2581-91; 1971.

[21] Shockley, W. and Pearson, G.L. *Modulation of conductance of thin films of semiconductors by surface charges*. Phys. Rev., **74**, 232-3; 1948.

[22] Tamm, I. *A possible kind of electron binding on crystal surfaces*. Phys. Z. Sowjetunion **1**, 733-746; 1932 and Z. Phys. **76**, 849-50; 1932.

[23] Shockley, W. *On the surface states associated with a periodic potential*. Phys. Rev., **56**, 317-23; 1939.

[24] Helfrich, W. *Space-charge-limited and volume controlled currents in organic solids, in Physics and Chemistry of the Organic Solid State*. Wiley Interscience (New York), 3, 1-65; 1967.

[25] Bendersk II, V.A. and Lavrushko, A.G. *Reabsorption of light and photoconductivity of anthracene crystals*. Soviet Phys. – Solid State, **13**, 1072-76; 1971.

[26] Bendersk II, V.A. and Lavrushko, A.G. *Investigations of pulsed photocurrents in anthracene crystals*. Soviet Phys. – Solid State, **13**, 1280-3; 1971.

[27] Rose, A. *Recombination processes in insulators and semiconductors*. Phys. Rev., 97, 322-333; 1955.

[28] Rose, A. *Comparative anatomy of models for double injection of electrons and holes into solids*. J. Appl. Phys., 35, 2664-78; 1964.

[29] Rose, A. *The role of space-limited currents in photoconductivity controlled devices*. IEEE Trans. Electron Devices ED 19 430-3; 1972.

[30] Gadisa, G. *Studies of Charge Transport and Energy Level in Solar Cells Based on Polymer/Fullerene*. LiU-Tryck, Linköping, Sweden, Dissertation No. 1056; 2006.

[31] Salaneck, W.R.; Friend, R.H. and Brédas, J.L. *Electronic structure of conjugated polymers: Consequences of electron-lattice coupling*. Phys, Rep.-Rev. Sec. Phys Lett., 319, 231-251; 1999.

[32] Oriou, J. *Synthesis and structure-properties relationship of alternated π-conjugated copolymers*. 2014 https://tel.archives-ouvertes.fr / tel-01070649v1

[33] Boman, M. *Electronic Structure Calculations of Conjugated Polymers. Metal/Polymer Interfaces, and Fulleride Polymers*. Linköping; 1995.

[34] Zumdahl, Z. *Chemistry*. Houghton Mifflin; 2003.

[35] Pope, M. and Swenberg, C.E. *Electronic Processes in Organic Crystals and Polymers*. 2nd edn, New York: Oxford University Press; 1999.

[36] Deibel, C. and Dyakonov, V. Polymer – fullerene bulk heterojunction solar cells. IOP Publishing Ltd, Rep. Prog. **73**; 2010.

[37] Heeger, A.J. Nobel lecture: *Semiconducting and metallic polymers. The fourth generation of polymeric materials*. Rev. Mod. Phys.,**73**, 681-700; 2001.

[38] Akamatsu, H.; Inokuchi, H. and Matsunaga, Y. Electrical conductivity of the perylene-bromine complex. Nature, **173**, 168; 1954.

[39] Shirakawa, H.; Louis, E.J.; MacDiarmid, A.J.; Chiang, C.K. and Heeger, A.J. *Synthesis of electrically conducting organic polymers: halogen derivatives of polyacetylene.* $(CH)_x$ J. Chem. Soc. Chem. Commun., 579; 1977.

[40] Hertel, D. and Baesslar, H. *Photoconduction in amorphous organic solids*. ChemPhysChem, **9**, 666; 2008.

[41] Lund, J.; Røge, R.; Peterson, R and Larsen, T. *Polymer solar cells*. Aalborg University, Faculty of Physics and Technology- Project Group: N44OB; 2006.

[42] Heeger, A. J.; Kivelson, S; Schrieffer, J.R. and Su, W.-P. *Silitons in conducting polymers*. Rev. Mod.Phys., **60**, 781-850; 1988.

[43] Carlberg, C. *Electrochemistry of Conjugated Polymers*. Linköping; 1996.

[44] Kline, R.J. and McGehee, M.D. *Morphology and Charge Transport in Conjugated Polymers*. Journal of Macromolecular Science[w], Part C: Polymer Reviews, **46**, 27–45; 2006.

[45] Schwartz, B.J. *Conjugated polymers as molecular materials: How chain conformation and film morphology influence energy transfer and interchain interactions*. Annu, Rev. Phys. Chem., 54, 141-172; 2003.

[46] Chen, T.A. and Rieke, R.D. *The 1st regioregular head-to-tail poly(3-hexylthiophene-2,5 diyl) and a regiorandom isopolymer-ni vs. pd catalysis of 2(5)-bromo-5(2)-(bromozincio)-3-hexylthiophene polymerization*. J. Am. Chem. S., 114 (25), 10087–10088; 1992.

[47] Mccullough, R.D.and Lowe, R.D. *Enhanced electrical-conductivity in regioselectively synthesized poly(3-alkythiophenes)*. J. Chem. Soc.-Chem. Commun., **1**, 70–72; 1992.

[48] -Osteritz, E.M.; Meyer, A.; Langeveld-Voss, Bea M.W.; René Janssen, A.J.; Meijer, E. W. and Bäuerle, P. *Two-dimensional crystals of poly(3-Alkylthiophene)s: Direct visualization of polymer folds in sub-molecular resolution*. Angew. Chem. Int. Ed. **39**, 2679-2684; 2000.

[49] Brown, P.J.; Sirringhaus, H.; Harrison, M.; Shkunov, M. and Friend, R.H. *Optical spectroscopy of field-induced charge in self-organized high mobility poly(3-hexylthiophene)*, Phys. Rev. B **63**, 125204(1)- 125204 (11); 2001.

[50] Hugger, S.; Thomann, R.; Heinzel, T. and Thurn-Albrecht, T. *Semicrystalline morphology in thin films of poly(3-hexylthiophene)*. Colloid Polym. Sci. **282** , 932–938; 2004.

[51] Bao, Z.; Dodabalapur, A. and Lovinger, A.J. *Soluble and processable regioregular*

poly(3-hexylthiphene) for thin film field-effect transistor applications with high mobility. Appl. Phys. Lett. **69**, 4108-4110; 1996.

[52] Osterbacka, R.; An, C.P.; Jiang, X.M.; et al. *Two-dimensional electronic excitations in self-assembled conjugated polymer nano-crystals*. Science, 287 (5454), 839–842; 2000.

[53] Sirringhaus, H.; Tessler, N. and Friend, R.H. *Integrated optoelectronic devices based on conjugated polymers*. Science **280** , 1741-1744. 1998.

[54] Arias, A.C. Corcoran, N.; Banach, M.; Friend, R. H. and MacKenzie, J.D. *Vertically segregated polymer-blend photovoltaic thin -film structures through surface-mediated solution processing*, Appl. Phys. Lett. **80**, 1695-1697; 2002.

[55] Thompson, B.C. and Fréchet, J.M.J. *Polymer–Fullerene Composite Solar Cells.* Angew. Chem. Int. Ed. 47, 58 – 77; 2008.

[56] Zhang, F.; Jespersen, K.G.; Björström, C.; Svensson, M.; Andersson, M.R.; Sundström, V.; Magnusson, K.; Moons, E.; Yartsev, A. and Inganäs, O. *Influence of solvent mixing on the morphology and performance of solar cells based on polyfluorene copolymer/fullerene blends*. Adv. Funct. Mater. **16**, 667–674; 2006.

[57] Geens, W.; Shaheen, S.E.; Wessling, B.; Brabec, C.J.; Poortmans, J. and Sariciftci, N. S. *Dependence of field -effect hole mobility of PPV-based polymer films on the spin-casting solvent*. Org. Electron. **3**, 105–110; 2002.

[58] Shi, Y.; Liu, J. and Yang, Y. *Device performance and polymer morphology in polymer light emitting diodes: The control of thin film morphology and device quantum efficiency*. J. Appl. Phys., **87**, 4254-4263; 2000.

[59] Nguyen, T.-Q.; Kwong, R.C.; Thompson, M.E. and Schwartz, B.J. *Improving the performance of conjugated polymer-based devices by control of interchain interactions and polymer film morphology*, Appl. Phys. Lett. **76**, 2454-2456; 2000.

[60] Xu, B. and Holdcroft, S. *Molecular control of luminescence from poly(3-hexy1thiophenes)*. Macromolecules **26**, 4457-4460; 1993.

[61] Rose, A. *Concepts in Photoconductivity and Allied Problems*. Wiley Interscience (New York); 1963.

[62] Williams E.W. *Solar Cells*. IEE Special Publication, Institution of Electrical Engineers (UK); 1978.

[63] Chiang, C.K.; Fincher, C. R.; Jr., Park, Y.W.; Heeger, A.J.; Shirakawa, H.; Louis, E J.; Gau, S.C. and MacDiarmid, A.G. *Physical Review Letters, 39*, 1098-1101, 1977.

[64] Nelson, J. *The Physics of Solar Cells*. Imperial College Press; 2003.

[65] Feller, F.; Rothe, M.; Tammer, M.; Geshke, D. and Monkman, A.P. *Temperature dependence of the space charge distribution in injection limited conjugated polymer structures*. J.Appl.Phys., 91, 9225; 2002.

[66] Calvet, L.E. *Electrical Transport in Schottky Barrier MOSFETs*. PhD Dissertation,Yale University; 2001

[67] Sze, S.M. *Semiconductor device*. Wiley, New York; 1998.

[68] Koehler, M. and Hummelgen, I.A. *Temperature dependent tunneling current at metal/polymer interfaces – potential height determination*. Appl. Phys.Lett., 70, 3254; 1997.

[69] Campbell, A.J.; Bradley, D.D.C. and Lidzey, *Space conduction with traps in poly(phynlene vinylene) light emitting diodes*. J. Appl. Phys., 82, 6326; 1997.

[70] Das, R.R.; Battacharya, P.; Perez, W.; Katiyar, R.S. and Bhalla, A.S. *Leakage current characteristics of laser-ablated srbi2nb2o9 thin films*. Appl. Phys. Lett., 81:880; 2002.

[71] Henisch, H.K. *Semiconductor Contacts, An approach to ideas and models*. International Series of Monographs on Physics No.70. Clarendon Press, Oxford; 1984.

[72] Braun, D. *Electronic injection and conduction processes for polymer devices*. J. Polymer Science B, 41:2622; 2003.

[73] https://www.hyperphysics.educ; 2014.

[74] Frenkel, J. *On pre-breakdown phenomena in insulators and electronic semiconductors*. Phys. Rev., **54**, 647-648; 1938.

[75] Bässler, H. *Charge transport in disordered photoconductors a Monte Carlo simulation study*. Phys. Status Solidi (b), **175,** 15-56; 1993.

[76] Gartstein, Y.N. and Conwell, E.M. *High-field hopping mobility in molecular systems with spatially correlated energetic disorder*. Chem. Phys. Lett., **245,** 351-358; 1995.

[77] Novikov, S.V.; Dunlap, D.H.; Kenkre, V.M.; Parris, P.E. and Vannikov, A.V. *Essential role of correlations in governing charge transport in disordered organic Materials*. Phys. Rev. Lett., **81**. 4472-4475; 1998.

[78] Brutting, W.; Berleb, S. and M¨uckl. A. *Device physics of organic light-emitting diodes based on molecular materials*. Organic Electronics, 2:1; 2001.

[79] Lampert, M.A. and Mark, P. *Current Injection in Solids*. Academic, New York; 1970.

[80] Abkowitz, M.; Facci, J.S. and Rehm, J. *Direct evaluation of contact injection efficiency into small molecule based transport layers: Influence of extrinsic factors*. *J. Appl. Phys.*, 83:2670; 1998.

[81] Helfrich, W. and Mark, P. *A proof for space charge in space-charge-limited hole currents in anthracene*. Z. Phys., 168, 495-503; 1962.

[82] Pacios, R. Nelson, J.; Bradley, D.D.C. and Brabec, C.J. *Composition dependence of electron and hole transport in polyfluorene:[6,6]-phenyl C61-butyric acid methyl ester blend films*. Appl. Phys. Lett., **83**, 4764-4766; 2003.

[83] Shaheen, Sean E.; Kopidakis, Nikos; Ginley, David S.; White, Matthew S. and Oslon, Dana C. *Inverted bulk-heterojunction plastic solar cells*. SPIE; 2007.

[84] deBoisblanc, Jenna. *Synthesis and Characterization of P3HT:PCBM Organic Solar Cells*. Senior Thesis; 2010. http://physastro.pomona.edu/wpcontent/uploads/2012/09/thesis_debois.pdf

[85] Krebs, Frederik C. *Roll-to-roll fabrication of monolithic large-area polymer solar cells free from indium-tin-oxide*. Solar Energy Materials and Solar Cells, 93(9): 1636 – 1641; 2009.

[86] Sigma-Aldrich, C. 2006. Sigma-aldrich. http://www.sigmaaldrich.com.

[87] Nelson, J. *The Physics of Solar Cells*. Imperial College Press; 2003.

[88] Krebs, F.C.; Alstrup, J.; Spanggaard, H.; Larsen, K. and Kold, E. *Production of large-area polymer solar cells by industrial silk screen printing, lifetime considerations and lamination with polyethyleneterephthalate*. Solar Energy Materials ans Solar Cells; 2004.

[89] Archer, M.D. and Hill, R. *Clean Electricity From Photovoltaics*. Imperial College Press, 2001.

[90] Yadav B.C. and Kumar R. *Structure, properties and applications of fullerenes*. International Journal of Nanotechnology and Applications ISSN 0973-631X Volume 2, Number 1, pp 15–24; 2008.
© Research India Publications. http://www.ripublication.com/ijna.htm

[91] Hoppe, H.; Arnold, N.; Sariciftci, N.S. and Meissner, D. *Modeling the optical absorption within conjugated polymer/fullerene-based bulk-heterojunction organic solar cells.* Sol. Energy Mater.Sol. Cells **80**, 105; 2003.

[92] Lioudakis, E.; Othonos, A.; Alexandrou, I. and Hayashi, Y. *Optical properties in conjugated poly(3-hexyl thiophene):[6,6]-phenyl-c61 butyric acid methyl ester composites*. J. Appl. Phys., 102, 083104; 2007.

[93] Gavrilenko, A.V.; Matos, T.D. Bonner, C.E.; Sun, S.-S.; Zhang, C. and Gavrilenko, V.I. *Optical absorption of poly(thienylene vinylene)-conjugated polymers: experiment and first principle theory*. J. Phys. Chem. C 112, 7908; 2008.

[94] Schueppel, R. et al *Optimizing Organic Photovoltaics using tailored heterojunctions: a photoinduced absorption study of oligothiophenes with low band gaps*. Phys.Rev. B,77, 085311; 2008.

[95] Beenken,W.J.D. Excitons in conjugated polymers: do we need a paradgma change? Phys. Status Solidi A, **206**, 2750; 2009.

[96] Bredas, J-L.; Beljonne, D.; Coropceanu, V. and Cornil, J. *Charge-transfer and energy-transfer processes in π-conjugated oligomers and polymers: a molecular picture*. Chem. Rev., **104** 4971; 2004.

[97] Kohler, A. and Beljonne, D. *The singlet-triplet exchange energy in conjugated polymers*. Adv.Funct. Mater., **14**, 11; 2004.

[98] van der Horst, J.-W.; Bobbert, P.A.; Michels, M.A.J. and Bässler, H. *Calculation of excitonic properties of conjugated polymers using the Bethe–Salpeter equation* , J. Chem. Phys., **114**, 6950-6957; 2001.

[99] Scholes, G.D. and Rumbles, G. *Excitons in nanoscale systems*. Nature Mater., **5**, 683; 2006.

[100] Forrest, S.R. Nature, 428, (6986), 911; 2004.

[101] Su, Y.-W.; Lan, S.-C. and Wei, K.-H. Organic Photovoltaics. Materials Today, Vol. 15, No. 12; 2012.

[102] Huang, Y.; Westnhoff, S.; Screearunothai, P.; Hodgkiss, J.M.; Dellener, C.; Friend, R.H. and Beljonne, D. *Electronic structures of interfacial states formed at polymeric semiconductor heterojunctions*. Nature Mater., 7, 483; 2008.

[103] Zhou, Y.; Pei, J.; Dong, Q.; Sun, X.; Liu, Y. and Tian, W. *Donor-Acceptor molecule as the acceptor for polymer-based bulk heterojunction solar cells*. J. Phys. Chem., C **113**, 7882; 2009.

[104] Barbour, L.W.; Pensack, R.D.; Hegadorn, M.; Arzhantsev, S and Asbury, J.B. *Excitation transport and charge separation in an organic photovoltaic material: watching excitons diffuse to interfaces*. J. Phys. Chem. C112, 3926; 2008.

[105] Collini, E. and Scholes, G.D. *Coherent interchain energy migration in conjugated polymer at room temperature*. Science **323**, 369; 2009.

[106] Markov, D. E. and Tanase, C. Blom, P.W.M. and Wildeman, J. *Simultaneous enhancement of charge transport and exciton diffusion in poly(p-phenylene vinylene) derivatives*. Phys. Rev. B **72,** 045217 8 (1)-045217 (6); 2005.

[107] Meijer, E.J.; De Leeuw, D.M.; Setayesh, S.; Van Veenendaal, E.; Huisman, B.-H.; Blom, P.W.M.; Hummelen, J.C.; Scherf, U.; Kadom, J. and Klapwijk, T.M. *Solution -processed ambipolar organic field-effect transistors and inverters*. Nat. Mater. **2,** 678-682; 2003.

[108] Lorentzo, E. Solar Electricity: *Engineering of Photovoltaic Systems. Institute of Solar Energy*, Polytechnic University of Madrid; 1994.

[109] www.renewableenergyworld.com/articles/2010/07/instrumentation-for-quantum-efficiency; 2010.

[110] PVEDUCATION.ORG: www.pveducation.org/pvcdrom/quantum-efficiency; 2015.

[111] Pub Chem: https://pubchem.ncbi.nlm.nih.gov/compound/16217324#section=2D-Structure and http://www.fis.unical.it/files/fl178/6726noteXRD.pdf

[112] Chemical Information Profile for Indium Tin Oxide [CAS No. 50926-11-9] - National Institute of Environmental Health Sciences U.S. Department of Health and Human Services Research Triangle Park, NC http://ntp.niehs.nih.gov/ Data Availability Checklist for Indium Tin Oxide [50926-11-9]; 2009.

[113] https://www.indiamart.com/techinstroexhaustcontrol/indium-tin-oxide-glass.html

[114] Jiao Li, Juncheng Liu, Congjie Gao, Jinling Zhang and Hanbin Sun. *Influence of MWCNTs Doping on the Structure and Properties of PEDOT:PSS Films*. International Journal of Photoenergy, Volume 2009; 2009.

[115] Leslie, H. Jimison. Dion Khodagholy, Thomas Doublet, Christophe Bernard, George G. Malliaras and Róisín M. Owens *Applications of Conducting Polymer Devices in Life Sciences*. France **(www.bel.emse.fr**); 2017.

[116] Mao, H.Y.; Xu, B. and Holdcroft, S. Synthesis and structure-property relationships of regioirregular poly(3-hexylthiophenes). *Macromolecules*, 26:1163, 1993.

[117] Sirringhaus, H.; Tessler, N. and Friend, R. *Integrated optoelectronic devices based on conjugated polymers*. Science, **280**:1741; 1998.

[118] Tremel,K. and Ludwigs, S. *Morphology of P3HT in thin films in relation to optical and electrical properties*. Adv. Polym. Sci., **265**, 39-82; 2014.

[119] Chen, T. A.; Reuben, X. W. and Riecke, D. *Regiocontrolled synthesis of poly(3alkylthiophenes) mediated by rieke zinc*: *Their characterization and solid-state properties*. J. Am. Chem. Soc., 117:233; 1995.

[120] Lu, J. P.; Li, X. P. and Martin, R. M. *Ground state and phase transitions in solid c60*. Phys.Rev. Lett., 68:1551; 1992.

[121] Kandjani, S.A. Mirershadi, S. and Nikniaz, A. *Inorganic–Organic Perovskite Solar Cells*. DOI: 10.5772/58970, under CC by 3.0 licence; 2015.

[122] Andersson, P.D.; Nilsson, D.; Svensson, P.O.; Chen, M.; Malmström, A.; Remonen, T.; Kugler, T. and Berggren, M. *Active matrix displays based on all-organic electrochemical smart pixels printed on paper*. Adv. Mater., 14:1460, 2002

[123] Wong, K.W.; Yip, H.L.; Luo, Y.; Yong, K.Y.; Lau, W.M.; Low, K.H.; Chow, H.F.; Gao, Z. Q.; Yeung, W.L. and Chang, C.C. *Blocking reactions between indium-tin oxide and poly (3,4-ethylene dioxythiophene):poly(styrene sulphonate) with a self-assembly monolayer*. Appl. Phys. Lett, 80:2788, 2002.

[124] Crispin, X.; Crispin, A.; de Jong, M.P.; Marciniack, S.; Osikowicz,W.; Jönsson, S.; Fahlman, M.; Kluger, T. van IJzendoorn, L.J.; de Voigt, M.J.A. and Salaneck, W.R. *Stability of indium tin oxide/polymer interfaces*. Mat. Res. Soc. Symp.Proc., 747:V5.5.1; 2002.

[125] Kim, J.S.; Ho, P.K.H.; Thomas, P.D.S.; Friend, R.H.; Cacialli, F.; Bao, G.W. and Li, S.F.Y. X-ray photoelectron spectroscopy of surface treated indium-tin oxide thin films. Chem. Phys. Lett. 315:307; 1999.

[126] Chiguvare, Z. *Electrical and Optical Characterisation of Bulk Heterojunction Polymer – Fullerene Solar Cells*. *PhD Thesis* 26; 2004.

[127] Frechet, J.M.J. and Thompson, B.C. *Polymer-Fullerene Composite Solar Cells*. Wiley-VCH-Vrlag GmbH & Co. KGaA, Weinheim Angew. Chem. Int Ed. 47, 58-77; 2008.

[128] Gunnes, S.; Neugebauer, H. and Sariciftci, N.S. *Chem. Rev*, 107, 1324-1338; 2007.

[129] Singh, T.B.; Marjonovic, N.; Matt, G.J.; Gunes, S.; Sariciftci, N.S.; Montaigne Ramil, A,; Andreev, A.; Sitter, H.; Schwodiauer, R. and Bauer, S. *Org. Electron*, 6, 105-110; 2005.

[130] Rispens, M.T.; Meetsma, A.; Rittberger, R.; Brabec, C.J.; Sariciftci, N.S. and Hummelen, J.C. *Chem. Commun*., 2116-2118; 2003.

[131] Brabec, C.J.; Winder, C.; Sariciftci, N.S.; Hummelen, J.C.; Dhanabalan, A.; van Hal, P.A. and Janssen, R.A.J. *Adv. Funct. Mater*., 12, 709-712; 2002.

[132] Winder, C.; Matt, G.; Hummelen, J.C.; Janssen, R.A.J; Sariciftci, N.S.; Brabec, C.J. Thin Solid Films. 403-404, 373-379; 2002.

[133] Hwang, J.D. and Lee, K.S. *J. Electrochem. Soc*. 155, H259; 2008.

[134] Ahmad, Z.; Sayyad, M.H.; Saleem, M.; Kamirov, Khasan S. and Shah, M. Physica E **41**, 18; 2008.

[135] van Duren, J.K.J.; Yang, X.; Loose, J.; Bulle-Lieuwma, C.W.T.; Sieval, A.B.; Hummelen, J.C. and Lanssen, A.J. *Relating the morphology of poly(p-phenylene vinylene)/methanofullerene blends to solar cell performance*, Adv.Funct.Mater. **14**,425-434; 2004.

[136] Gadisa, A. *Studies of Charge Transport and Energy Level in Solar Cells Based on olymer/Fullerene Bulk Heterojunction*. Linköping Studies in Sciece and Technology – Dissertation No. 1056 Linköping University, SE-581 83 Linköping, Sweden; 2006.

[137] El-Nahass, M.M.; Abd-El-Rahman, K.F.; Farag, A.A.M. and Darwish, A.A.A. *Org. Electron*. **6**, 129; 2005.

[138] Duffie J.A. and W.A. Beckman. *Solar Engineering of Thermal Processes*. J.Wiley, New York, 1991

[139] Chiguvare, Z.; Parisi, J. and Dyakonov V. *Current limiting mechanisms in indium-tin-oxide/poly3-hexylthiophene/aluminium thin film devices*. J. Appl. Phys. 94:2440; 2003.

[140] Ahmad, Z. and Sayyad, M.H. *Electrical characteristics of a high rectification ratio organic Schottky diode based on methyl red*, Optoelectronics and advanced materials-Rapid Communications Vol.3,No 5, p.509-512; 2009.

[141] Gueymard, C.; Myers, D. and Emery, K. *Proposed reference irradiance spectra for solar energy systems testing, Solar Energy*, Volume 73, Issue 6, 443-467; 2002.

[142] Gueymard, C. *The sun's total and spectral irradiance for solar energy applications and solar radiation models*. Solar Energy, Volume 76, Issue 4, 423-453; 2004.

Chapter 5

Effect of charge injection mechanisms at metal-active layer interfaces on the efficiency of thin-film photoactive P3HT: PCBM composite device under increasing incident light intensity

5.1 Introduction

One of the challenge gaps in organic solar cells is to account for the observed decrease in the device's efficiency with effect from a characteristic threshold open circuit voltage as the intensity of the incident light is increased. Revelation of the underpinning physics compelling such behaviour awakens insight into informed pathways of improving the performances of these excitonic solar cells.[1-6] Since this decay behaviour surfaces during the device's operation under illumination when the photogenerated current is at play, it is logical to link the cause of the decay in efficiency to the photogenerated current flow through the cell,[7-8] because it is the only new parameter plying across the cell. Current conduction in such organic semiconductor assemblies is characterised by the motion of both charge carriers (electrons and holes) in opposite directions. This current increases with increase in incident light intensity.[7-8], [10] A bulk heterojunction (BHJ) organic photovoltaic device of the metal/organic active layer/metal assembly has the structural presence of metal-active layer junctions sandwiching a polymer-fullerene blend. This means that charge carriers diffusing[9] or drifting (by hopping or percolation, etc. mechanisms) inside the composite towards the electrodes, have to overcome potential barriers[10-12] at metal-active layer junctions in order for them to cross over to or from the respective electrodes. Metal-active layer junctions therefore play critical roles in regulating charge conduction mechanisms as the incident light intensity changes in metal/active layer/metal devices.[13-14] In so doing, they impact on the power conversion efficiencies[15] of the devices, the improvements of which rest upon a clearer understanding of the devices' voltage regimes, comprised of electric charge conduction processes at metal-active layer junctions and space charge limited current (SCLC) conduction[6], [16-21] in the bulk material(s) or their blends. Call is also for a deeper understanding of the devices' optical and thermal behaviour, which in coupling with a clear understanding of the electrical behaviour, would give impetus to optimisation endeavours. In light of this, we focus this chapter on the problem statement, 'effect of charge injection mechanisms at metal-

polymer interfaces on the efficiency of conjugated polymer-fullerene blend solar cells'. Specifically, we seek to make a contribution in bringing to light, fundamental interface physics accounting for the observed decrease in the efficiency of organic solar cells at high incident light intensity and extend our investigations to finding out how the observed $V_{oc\ thresh\ eff\ decay}$ is quantitatively linked to the device's voltage regimes at the metal-active layer junctions.

We advance the following hypotheses:

- Electrical conduction and the coupled power conversion efficiency in photoactive metal/polymer/metal devices are to a large extent influenced by the photogenerated voltage, which drives an increased dark (opposing) current within the organic solar cell that impacts negatively on the efficiency of the device.
- The experimentally observed threshold open circuit voltage ($V_{oc\ thresh\ eff\ decay}$) corresponds to the threshold voltage ($V_{thresh\ tunn}$) for tunneling regime commencement in such optoelectronic devices of organic descent.

To test these hypotheses, the effect of external voltage bias on charge injection across electrical contacts formed as thin films of each of the organic semiconductors P3HT or PCBM (in the P3HT:PCBM blend) contacts with the metal electrodes ITO (enhanced with PEDOT:PSS) and Al respectively of the ITO/PEDOT:PSS/P3HT:PCBM/Al solar cells. The solar cells were fabricated as described in Chapter 4. We restricted our investigations to the problematic metal-polymer interface regions.

5.2 Results and Discussion

Figures 5.1 (a) and (b) show the obtained current density *J* and semi-logarithmic *J* versus voltage *V* curves of the representative as cast bulk heterojunction (BHJ) ITO/PEDOT:PSS/P3HT:PCBM/Al solar cell, in the dark (0 mW/cm^2) and under differing light illumination intensities (0.27 mW/cm^2 to 100 mW/cm^2). Each of the fabricated experimental devices displayed electrical characteristics similar to those in Figure 5.1. The asymmetrical nature of the curves in Figure 5.1 (b), is ascribed to the difference between the work functions of the electrodes (ITO/PEDOT:PSS and Al) and the active blend materials (P3HT and PCBM) in electrical contact with the electrodes. This indicates the existence of Schottky junctions and therefore different potential barriers at the electrode (a metal)-polymer interfaces.

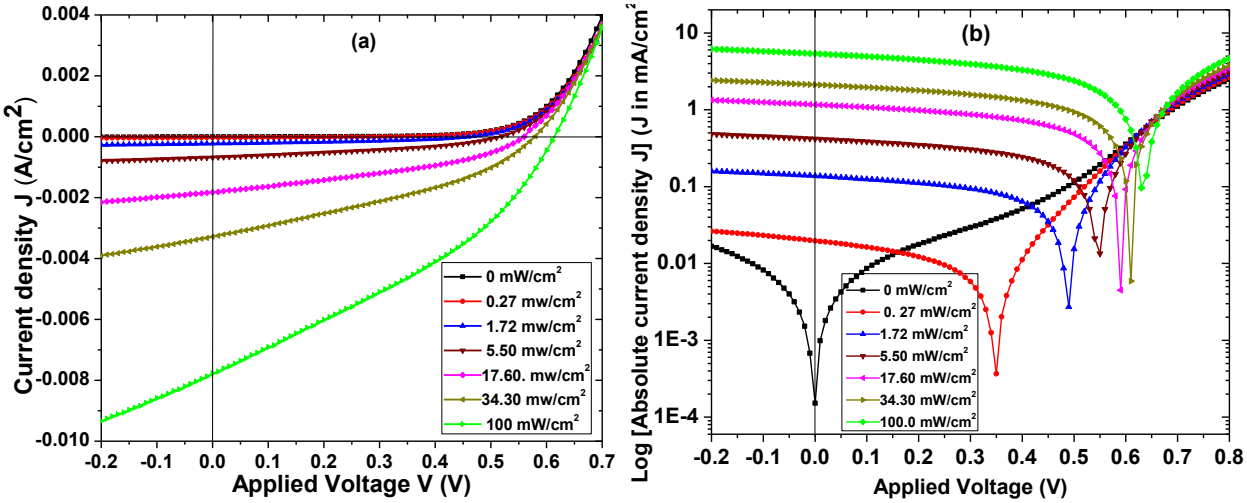

Figure 5.1 (*a*) *Linear scale and* (*b*) *semi-logarithmic family plots of current density variation with applied voltage for the as cast bulk heterojunction ITO/PEDOT:PSS/P3HT:PCBM/Al solar cell, in the dark* (*0 mW/cm*^{2}) *and under differing illumination intensities* (*0.27→100 mW/cm*^{2})

In order to gain more insight into the fundamental electrical behaviour of the device, we isolated for study, its dark J(V) curve from Figure 5.1 (a) and its corresponding dark semi-logarithmic scale curve from Figure 5.1 (b), the display of which is presented in Figure 5.2.

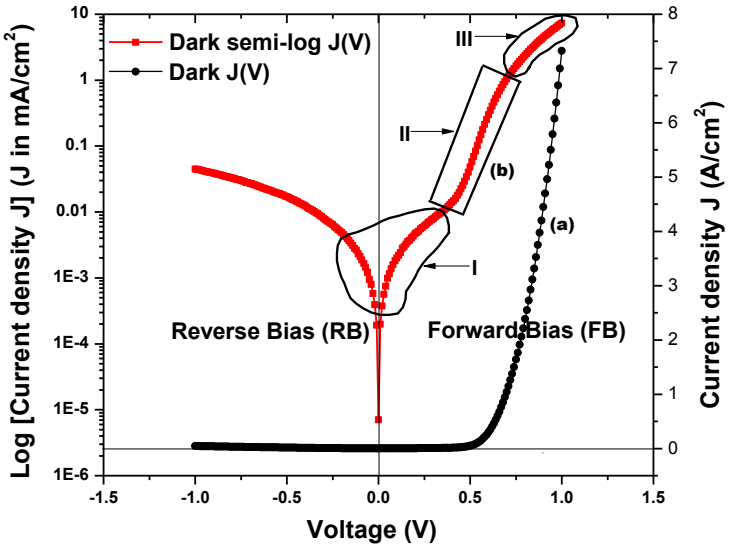

Figure 5.2 (a) *Dark current density and* (b) *corresponding log current density versus voltage characteristics for the Schottky barrier junction type ITO/PEDOT:PSS/P3HT:PCBM/Al device*

The dark forward and reverse bias current-voltage characteristics of the ITO/PEDOT:PSS/P3HT:PCBM/Al device shown in Figure 5.2(a) are characteristic of a diode and show rectification behaviour as well as non-linearity, with very small leakage current under reverse bias. This indicates the formation of depletion regions at the metal-active layer interfaces of the device. Forward bias corresponds to positive (+ve) potential on the ITO/PEDOT:PSS electrode and negative (-ve) potential on the Al electrode. We investigated the rectification phenomena of the device by calculating RFs at different applied bias voltages and used the values in plotting the graph for the variation of rectification factor with absolute values of applied voltage. The obtained graph is shown in Figure 5.3. The rectification factor/ratio (RF or RR) is determined as the ratio of the forward current I_F to the reverse current I_R at a certain applied voltage V. Mathematically:

$$\left|RF\right|_V = \left|\left(\frac{I_F}{I_R}\right)\right|_V \tag{5.1}$$

RF is therefore subject to the applied voltage.

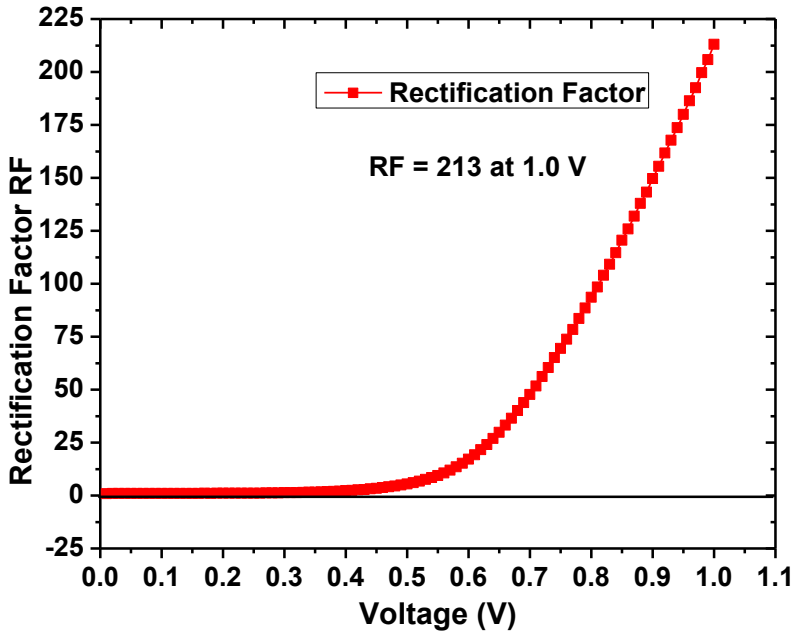

Figure 5.3 *RF vs voltage of the ITO/PEDOT:PSS/P3HT/PCBM/Al Schottky junction*

As the graph shows, the device was found to be having rectification factors of ~ 213 at 1.0 V. In general, high rectification factors at different bias voltages are evident from the graph. The incidence of high RF is attributed to the fact that under reverse bias, large potential energy

barriers exist at the metal-active layer interfaces of ITO/PEDOT:PSS/P3HT:PCBM/Al devices. Such high values of RF are typical of polymer based diodes with asymmetric electrodes.[6], [22-24] ITO/PEDOT:PSS/P3HT:PCBM/Al devices therefore generally exhibit very high rectification behaviour. This behaviour is mainly due to the formation of space charge layer at the ITO/PEDOT:PSS/P3HT:PCBM/Al interfaces.

The discussed diode I-V characteristics of the fabricated ITO/PEDOT:PSS/P3HT:PCBM/Al solar cell in the dark have several features that correspond to various types of charge transport within the device. In Figure 5.2 (b), we identify three corresponding, typical charge transport regions labelled I, II and III revealed by the device in semi-logarithmic representation of the dark current density-voltage characteristics. The low bias voltage regime, represented by region I in Figure 5.2 (b) is characterised by an ohmic flow of charges expressed clearly and exactly as $J \propto V/d$, where J is the current density, V is the applied bias voltage and d (~ 100 nm) is the thickness of the active P3HT:PCBM (polymer-fullerene) blend film. The current is limited mainly by shunt (parallel) resistance (R_{sh}) emanating from the P3HT:PCBM film. In this regime, injection of charge carriers from the electrodes into the polymer material is considerably reduced due to the low bias voltage which cannot compensate for the internal (built in) field.[25] Under forward bias conditions in region I, the depletion layer is minimised at the interfaces and current flow originates mainly from extrinsic effects that give leakage currents.[13], [25]

Region II is the intermediate positive voltage bias regime, which results from increasing the bias voltage. This increase further decreases the internal electric field and enhances the injection of charge carriers from the electrodes into the bulk P3HT:PCBM composite. Charge conduction (injection) in this region is therefore across the metal-active layer interfaces, in which for our devices, the electrodes were ITO/PEDOT:PSS and Al and the active materials were P3HT and PCBM. The sharp J(V) slope and exponential increase in current with bias voltage (shown in Figure 5.2 (b) II) characterise injection limited (IL) behaviour of charge flow in this region. The current increase should be due to decrease in the depletion layer width at the interfaces. The mathematical formulation of conduction across this Schottky junction region is $J \propto \exp(qV/k_BT)$, where k_B is the Boltzmann constant. In reverse bias, the depletion layer increases and almost all the current is due to the minority carriers of P3HT:PCBM.

All this shows that in region II, current is controlled by the diode characteristics of the device, which in effect are factors attributed to the device's metal-active layer interface(s). The main junction factor that controls the injection process is the potential barrier, which in turn is often mainly controlled by the interface dipoles, Fermi level alignments, defects,[25] energetic disorder introduced by the roughness at metal-organic semiconductor interface[26] and impurities. In certain situations, image force also plays a role by giving rise to current backflow.[27]

The high bias regime (which accounts for charge transport in the bulk/blend material(s)) is shown by region III of plot (b) in Figure 5.2. This is the region corresponding to space charge limited region $\left(J \propto V^2/d^3\right)$, in which the bias voltage has been increased beyond the flat band condition. At flat band operation, the bias voltage will be high enough to compensate for the built-in potential of the diode. Immense current injection is therefore expected in this region. However, due to low charge carrier mobility, compounded by the presence of impurities, traps and current limitation by series resistance (R_s), the transportation rate of the injected charge carriers is greatly reduced and charges accumulate in the bulk of the active organic material(s). Hence the dominant controller of the transport flow is now space charge limited current (SCLC), which results in saturation of current.[28-29]

Further analysis of the dark $J(V)$ curves in Figure 5.2 produced the following parameter values, (which we ascribe to the diode behaviour of our ITO/PEDOT:PSS/ P3HT:PCBM/Al device of cell area 0.08 cm^2, active layer thickness $d \sim 100$ nm and fabrication thermodynamic temperature $T \sim 300$ K): reverse saturation current density $J_0 \sim 10^{-4}$ mA/cm^2, reverse saturation current $I_0 \sim 8 \times 10^{-9}$ A = 8 nA, Ideality factor $n \sim 1.73$ and dark barrier potential height $\phi_{B-dark} \sim 0.452$ V.

The reverse saturation current density was determined by interpolation of the exponential slope of $J(V)$ at $V = 0$. The dark reverse saturation current I_0 is the maximum leakage current in the absence of light. It is an extremely important parameter which differentiates one diode (organic solar cell) from another. It is a measure of the recombination in a device. A device (for example, organic solar cell) with larger recombination will have a larger I_0 ($\Rightarrow$ larger J_0). I_0 increases as T increases and decreases as the material quality increases.

The value of the ideality factor *n* greater than unity can be attributed to the recombination of electrons and holes in the depletion region of the interface. It is also associated with the Fermi level pinning at the interface or with relatively large voltage drops in the interface region.[24] The ideality factor of the device was estimated by use of the slope of the linear section of region II (the exponential region of the forward bias of the semi-logarithmic J(V) characteristics. The slope which is equal to $\left(\frac{dV}{d(\ln J)}\right)$, was then used in equation (5.2) to determine *n*.

$$n = \left(\frac{q}{kT}\right)\left(\frac{dV}{d(\ln J)}\right) \tag{5.2}$$

The value of the barrier potential height ϕ_B was estimated from the forward bias current-voltage characteristics by use of equation (5.3), in which *A** is the Richardson constant.

$$\phi_B = \frac{kT}{q}\ln\left(\frac{A^*T}{J_0}\right) \tag{5.3}$$

In the case of the fabricated device under examination, the more relevant equation describing current as a function of applied voltage is the modified Schottky equation (5.4), because the device is a non-ideal diode. This practical (real-diode) equation is[30-32]

$$I = I_{01}\left[\exp\left(\frac{qV - IR_s}{n_1 kT}\right) - 1\right] + I_{02}\left[\exp\left(\frac{qV - IR_s}{n_2 kT}\right) - 1\right] + \left(\frac{V - IR_s}{R_{sh}}\right) \tag{5.4}$$

where the symbols carry their usual meanings. Comparative output parameters obtained for the fabricated ITO/PEDOT:PSS/P3HT:PCBM/Al device in the dark and under 100 mW/cm^2 white light illumination are shown in Figure 5.4. As can be seen in Figure 5.4, the maximum current is not always reached at 0 Volts (when device is under short circuit conditions), but at times it is achieved at more negative bias, corresponding to a higher internal field. This conveys information that the polaron pair dissociation in the device is more difficult. One of the reasons could be that the active layer is thicker than the optimal thickness for optimum polaron dissociation. If the active layer is thicker, it means that at the same external voltage, the internal field at zero bias is lower, hence the need for thickness optimisation. However, mechanisms of exciton-polaron pair dissociation are still not clearly understood.

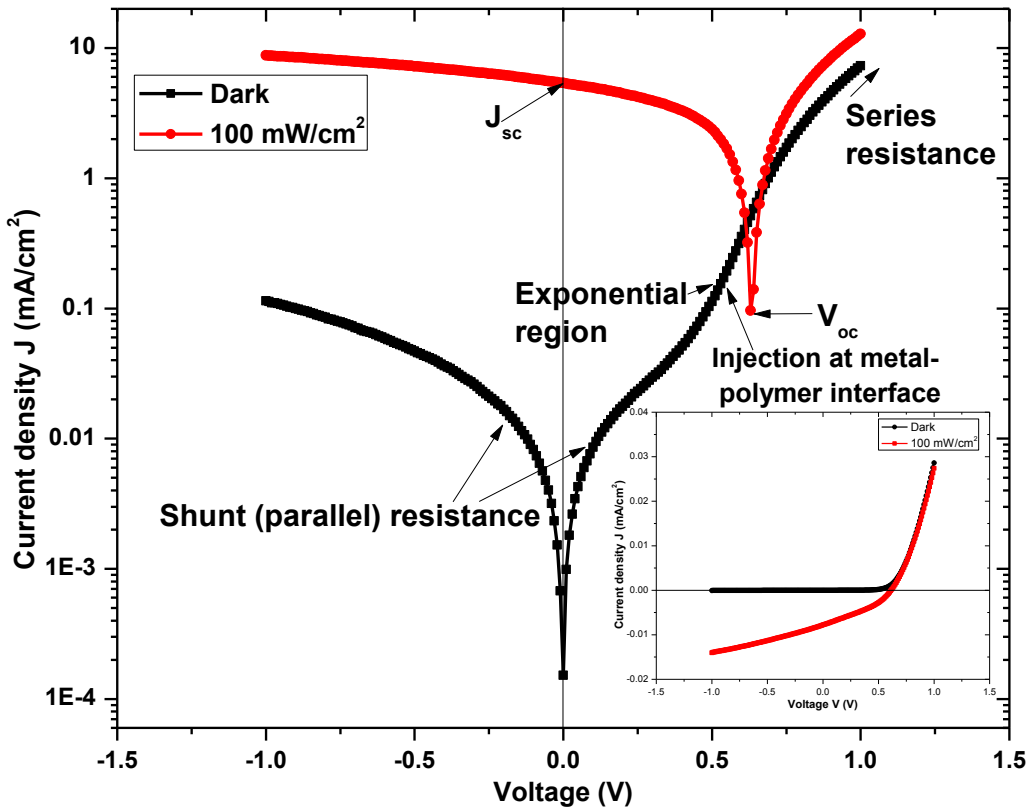

Figure 5.4 *Comparative semi-logarithmic representation of the dark and illuminated (100 mW/cm^2) J(V) characteristics for the fabricated ITO/PEDOT:PSS/P3HT:PCBM/Al solar cell. The inset is for the corresponding dark and 100 mW/cm^2 raw J(V) plots for the device.*

Under solar simulated white light illumination intensity ranging from dark (0 mW/cm^2) to 100 mW/cm^2, the device gave the output parameters shown in Table 5.1.

Table 5.1 *Output photovoltaic parameters obtained for the ITO/PEDOT:PSS/P3HT:PCBM/Al solar cell in the dark and under different solar simulated white light illumination intensities*.

Light Intensity (mW/cm^2)	V_{oc} (V)	J_{sc} (mA/cm^2)	P_{max} (mW/cm^2)	FF	Efficiency (%)	Series Resistance (Ω)	Shunt Resistance (Ω)
0	0	0.0002	0.000			12021.94	12021.94
0.27	0.35	0.02	0.002	0.3570	0.91	6169.50	28828.83
1.72	0.49	0.14	0.029	0.4280	1.68	878.83	7804.88
5.5	0.55	0.42	0.099	0.4256	1.79	288.86	3200.00
17.6	0.59	1.17	0.289	0.4205	1.64	124.86	1151.08
34.3	0.61	2.11	0.530	0.4115	1.55	80.57	800.00
100	0.64	5.39	1.323	0.3837	1.32	42.45	266.67

5.2.1 Efficiency decay with increase in light intensity versus metal-active layer interface contributions

In most applications, the solar cell operates under approximately AM1.5 white light illumination, which is equivalent to 100 mW/cm^2 simulated white light intensity. Table 5.1 shows the open circuit voltage V_{oc} for the ~100 nm thick experimental device under 100 mW/cm^2 white light illumination to be 0.64 V. The magnitude of the electric field F produced by this V_{oc} is given by: $F = (V_{oc}/d) = (0.64V/100\,nm) = 6.4\times10^4$ V/cm. This shows that the bias V_{oc} of magnitude 0.64 V is enough to bias the device externally with an electric field of ~ 6.4×10^4 V/cm. Such high bias electric fields, though produced by the photogenerated V_{oc}, must be impacting on the photogenerated current, (responsible for its creation) in a negative way which decreases the efficiency of the organic solar cell.

We built up this hypothesis from empirical observations of the decrease in the device's efficiency, shown in Figure 5.5 with effect from a characteristic threshold open circuit voltage ($V_{oc\ thresh\ eff\ decay}$) as the light intensity (I) incident on it was increased. As can be read from Figure 5.5, $V_{oc\ thresh\ eff\ decay}$ for the device was found to be ~ 0.53 V. Below this threshold V_{oc}, efficiency was observed to increase.

To verify the hypothesis, we set to study these empirical observations of the performance behaviour of our ITO/PEDOT:PSS/P3HT:PCBM/Al device under differing illumination intensities shown in Figure 5.5, in order to find explanation to the evolution of this threshold open circuit voltage at which efficiency of the P3HT:PCBM based device starts to decay ($V_{thresh\ eff\ decay}$). Models explaining conduction mechanisms at metal-polymer junctions are examined. We also seek to find out whether the observed $V_{thresh\ eff\ decay}$ is correlated to certain fundamental voltages marking the onset or transition of elementary electrical behaviours in the device and obtain comparative values of the thresholds. The findings are used to formulate generalisations explaining the origin (or cause) of the observed decrease in efficiency as light intensity increases. This knowledge provides a sound base for improved architecture of ITO/PEDOT:PSS/P3HT:PCBM/Al solar cells and the generality of organic solar cells, in that it will enable us to identify specific domains and attributes of the cell to improve.

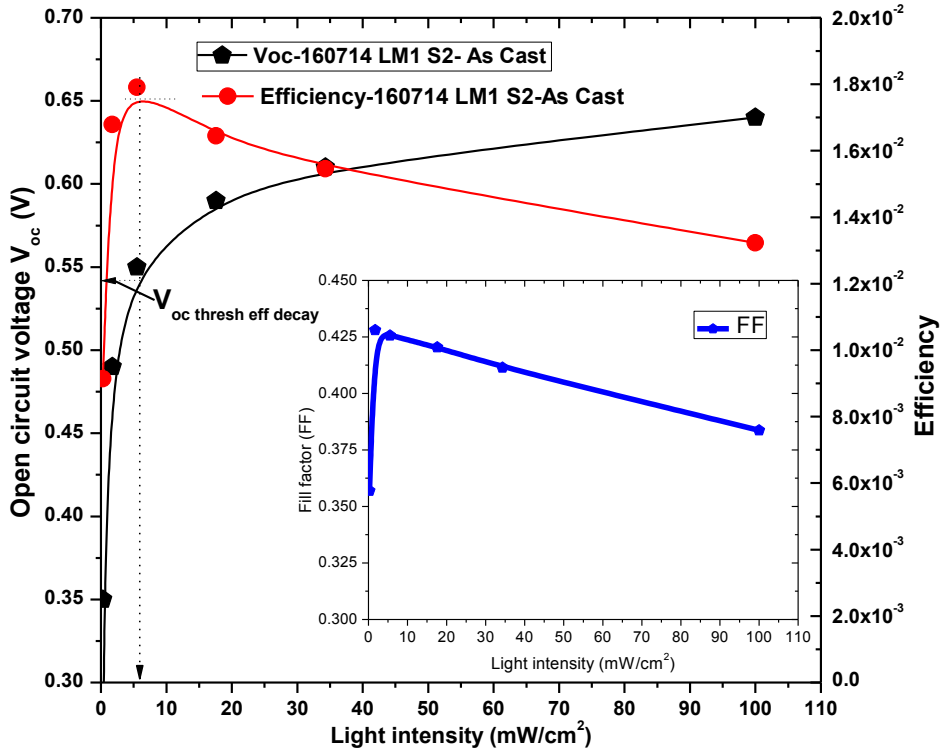

Figure 5.5 *Variation of efficiency η and open circuit voltage V_{oc} with light intensity. The smooth curves are lines of best fit to the respective data points. Inset is for the variation of the corresponding fill factor with light intensity.*

For the fabricated device, Figure 5.5 shows that at very low white light illumination intensity in the approximate range $0 < I < 5.5$ mW/cm^2 corresponding to V_{oc}s less than 0.53 V, the efficiency of the device increases sharply in similar manner to V_{oc} and peaks at $V_{oc} \sim 0.53$ V (the alluded $V_{thresh\ eff\ decay}$), corresponding to I ~ 5.5 mW/cm^2. Further increase in incident light intensity is seen (Figure 5.5) to induce a significant fall in the rate of increase of V_{oc} and simultaneously triggers a rapid decrease in the (performance) efficiency of the device.

It is the explanation of this observed turning point in the performance behaviour of polymer-fullerene devices that is central to this investigation. Specifically, we investigate the contributions of metal-active layer interfaces to this retrogressive behaviour, by finding out how charge injection mechanisms/processes at metal-active layer interfaces aggravate the behaviour.

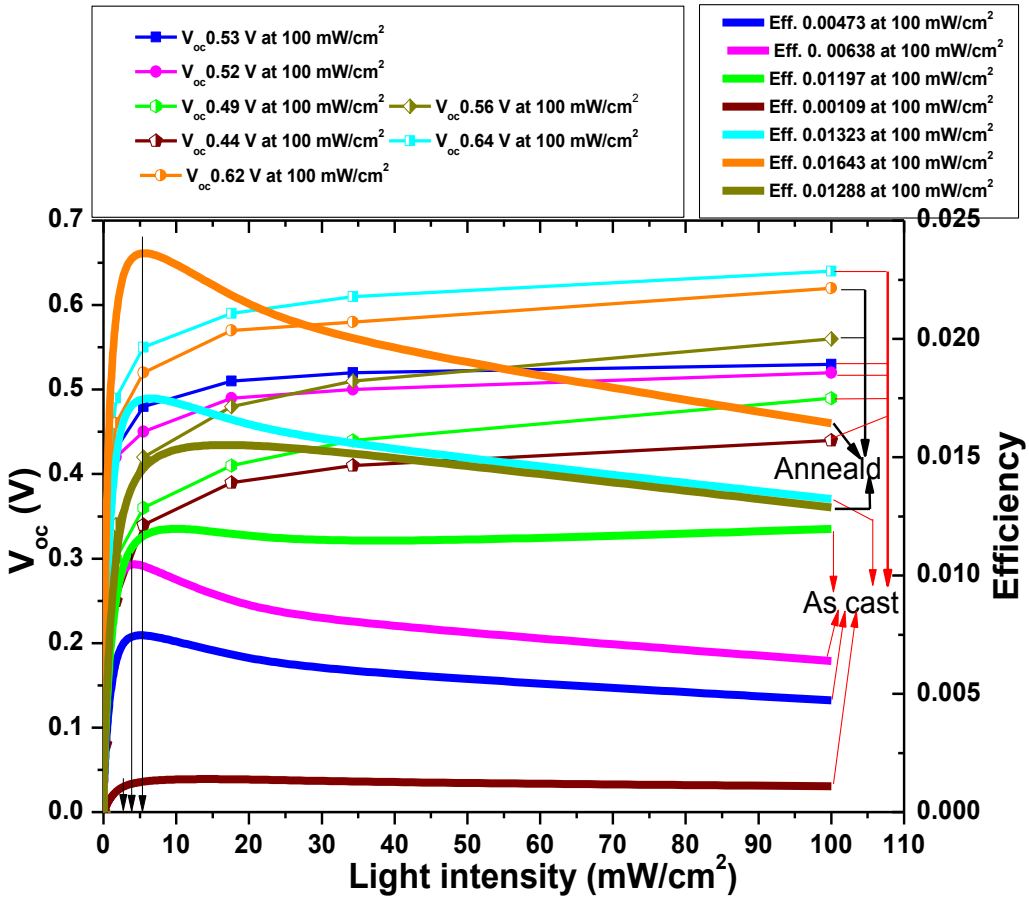

Figure 5.6 *Family of open circuit voltage V_{oc} and efficiency η against light intensity I incident on ITO/PEDOT:PSS/P3HT:PCBM/Al devices from different batches. The smooth η vs I curves are lines of best fit to the data points.*

For reliability check, we experimented with several ITO/PEDOT:PSS/P3HT:PCBM/Al solar cells and for each case plotted variations of V_{oc} and efficiency η with incident light intensity *I* and noted $V_{\text{thresh eff decay}}$. The resulting family of curves for a few representative devices from different batches is shown in Figure 5.6.

In all plots we witness sharp increases in efficiency at low incident light intensity (~ $0 < I < 6.5$ mW/cm^2), up to peak values (thresholds) which mark the onset of efficiency decay for any beyond illumination intensity. We note the general efficiency peak shifts towards increasing incident light intensity (that is, the right hand side (RHS)) for devices with higher operational power conversion efficiencies at 100 mW/cm^2 incident intensity. Therefore, the higher the operational efficiency at 1.5AM illumination intensity, the greater is the peak shift to the RHS.

This is the expected behaviour, because by so doing, the device delays the onset of efficiency peaking, which means delayed decrease in efficiency and therefore larger increase range. This information is useful in unfolding the behaviour pattern we want in the organic solar cell. As such, we need to identify sites within the cell which contribute towards the unwanted turning point from increase to decrease behaviour in efficiency and be able to explain how the behaviour occurs at these sites. This discussion has already singled out metal-active layer interface sites, which are under present investigation.

To aid analysis of the plots in Figure 5.6, we present in Table 5.2, approximate values of the parameters having a bearing on the peaking of the device efficiency at low incident light intensity and the marking of the onset shown. All the values are extractions from the figure.

Table 5.2 *Approximate values of the parameters associated with onset of decrease (decay) in the power conversion efficiency of the ITO/PEDOT:PSS/ P3HT:PCBM/Al solar cell as incident light illumination intensity increases*

*Threshold Light Intensity I (mW/cm^2)	Device state	$V_{thr\ eff\ dec}$	V_{oc} at 100 mW/cm^2 (V)	Efficiency η at $V_{thr\ eff\ dec}$ %	*η at 100 mW/cm^2	% fall in η	Bias E-field due to $V_{thr\ eff\ dec}$ (V/cm)	Bias E-field due to V_{oc} at 100 mW/cm^2 (V/cm)
5.3	As Cast	**0.54**	0.64	**1.805**	**1.323**	**26.7**	5.4×10^4	$\mathbf{6.4\times10^4}$
3.0	As Cast	**0.47**	0.53	**0.750**	**0.473**	**36.9**	4.7×10^4	$\mathbf{5.3\times10^4}$
2.0	As Cast	**0.42**	0.52	**1.083**	**0.638**	**41.1**	4.2×10^4	$\mathbf{5.2\times10^4}$
5.5	As Cast	**0.36**	0.49	**1.200**	**1.197**	**0.3**	3.6×10^4	$\mathbf{4.9\times10^4}$
1.8	As Cast	**0.33**	0.44	**0.167**	**0.109**	**34.7**	3.3×10^4	$\mathbf{4.4\times10^4}$
5.5	Annealed	**0.43**	0.56	**1.583**	**1.288**	**18.6**	4.3×10^4	$\mathbf{5.6\times10^4}$
6.5	Annealed	**0.52**	0.62	**2.375**	**1.643**	**30.8**	5.2×10^4	$\mathbf{6.2\times10^4}$

In Figure 5.7, we use data from the asterisked columns in Table 5.2 to show in scatter plot the positive correlation between the threshold incident light intensity and the operational power conversion efficiency under solar simulated white light intensity of 100 mW/cm^2. The percentage fall in power conversion efficiencies from those at the decay thresholds to those for the devices under 100 mW/cm^2 illumination is generally very high. This is a setback. Good device architecture is one that works towards minimising and delaying such falls so that the

increase is extended over most of the illumination intensity range. We also note the generally high bias electric fields which seem characteristic of the P3HT:PCBM based assemblies.

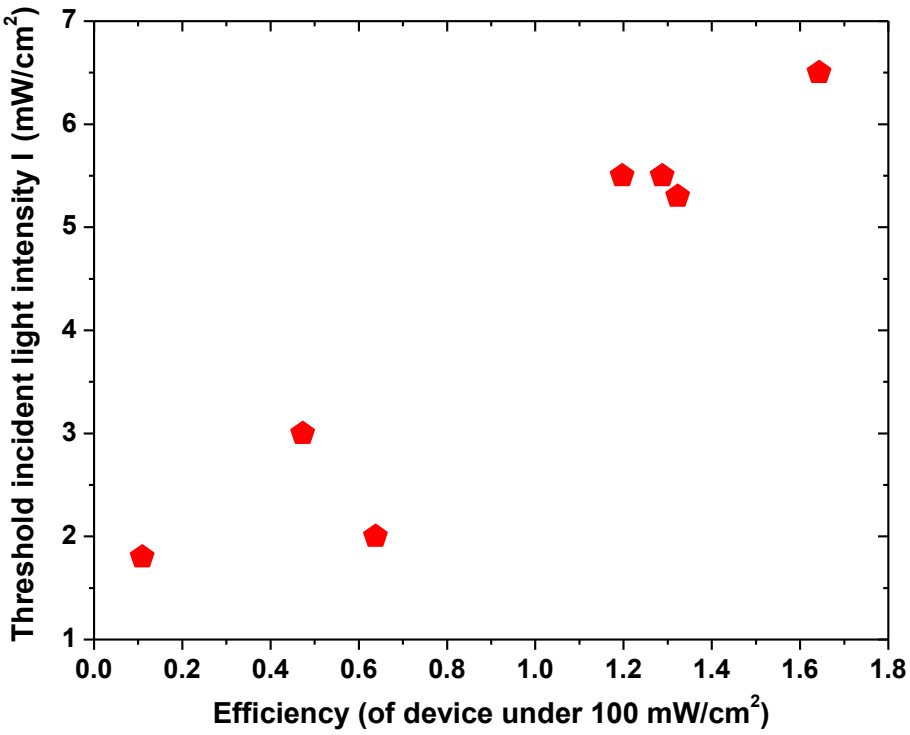

Figure 5.7 *Scatter plot revealing positive correlation between the efficiency under100 mW/cm^2 illumination of the P3HT:PCBM based device and the threshold incident light intensity at which efficiency starts to decrease.* (*Note that efficiency is the independent variable in this case.*)

We present Table 5.3 for purposes of giving an overview of the values of parameters of merit describing the average experimental ITO/PEDOT:PSS/P3HT:PCBM/Al solar cell that was fabricated and studied. Attention is drawn to the $V_{oc\ \text{thresh eff decay}}$ values which seem to suggest the existence of a unique threshold open circuit voltage ($V_{\text{oc unique thresh}}$) which triggers ohmic behaviour in the device when the device is operating under AM1.5 incident white light intensity. The value of this $V_{\text{oc unique thresh}}$ for a well fabricated device, could be around 0.46 V order of magnitude, as deduced from the averages in Tables 5.3 (a) and (b). Annealing at 60^{o}C for 15 minutes was done on a few devices whose figures of merit and graph profiles are respectively shown in Table 5.3 (b) and Figure 5.6, solely for the purpose of ascertaining whether there is a

significant difference in values of $V_{\text{thresh eff decay}}$ between those of well done 'as cast' and those of well done 'annealed' devices.

Table 5.3: *Parameters of merit for the 'as cast' and 'annealed ITO/PEDOT:PSS/P3HT:PCBM/Al solar cell subjected to 100 mW/cm^2 (AM 1.5) solar simulated white light illumination*

(a) As Cast

Device/Cluster Description		110714 H2 M	160714 LM1 M	160714 LM1 S2	200714 LM2 M	210714 LM3 M	160814 U2 M	**Average Performance**
Device/Cluster State		As Cast	As Cast	As Cast	As Cast	As Cast	As Cast	**As Cast ± 0.03**
100 mW/cm^2 (AM 1.5)	V_{oc} (V)	0.53	0.63	0.64	0.58	0.56	0.49	**0.57**
	Abs. I_{Sc} (mA)	0.219	0.313	0.431	0.377	0.217	0.461	**0.34**
	Abs. J_{Sc} (mA cm^{-2})	2.7375	3.9125	5.3875	4.7125	2.7125	5.7625	**4.20**
	P_{max} (mW cm^{-2})	0.4725	0.9943	1.3230	1.0735	0.6753	1.1974	**0.96**
	Fill Factor	0.3257	0.4034	0.3837	0.3928	0.4445	0.4241	**0.40**
	PC Efficiency (%)	0.47	0.99	1.32	1.07	0.68	1.20	**0.96**
	Series Res. (Ω)	43.1	40.5	42.4	46.9	54.5	31.1	**43.10**
	Parallel Res. (Ω)	320.0	320.0	266.7	266.7	533.3	228.6	**322.60**
0 < *I* < 7.0 mW/cm^2	**$V_{\text{thresh. eff decay.}}$ (V)**	0.47	0.53	0.53	0.46	0.44	0.36	**~ 0.47**

Key: Cluster comprises 3 'neighbour' solar cells fabricated on same 1.25 cm x 1.25 cm substrate

(b) Annealed

Device/Cluster Description		110714 H2 M	160714 LM1 M	200714 LM2 M	**Average Performance**
Device/Cluster State		Annealed	Annealed	Annealed	**Annealed ± 0.03**
100 mW/cm^2 (AM 1.5)	V_{oc} (V)	0.58	0.64	0.60	**0.61**
	Abs. I_{Sc} (mA)	0.454	0.430	0.340	**0.41**
	Abs. J_{Sc} (mA cm^{-2})	5.675	5.375	4.2625	**5.10**
	P_{max} (mW cm^{-2})	1.207	1.233	1.155	**1.20**
	Fill Factor	0.4013	0.3701	0.4516	**0.41**
	PC Efficiency (%)	1.21	1.23	1.155	**1.20**
	Series Res. (Ω)	43.6	41.4	36.2	**40.40**
	Parallel Res. (Ω)	177.8	228.6	400.0	**268.80**
0 < *I* < 7.0 mW/cm^2	**$V_{\text{thresh eff. decay}}$ (V)**	0.44	0.48	0.45	**~ 0.46**

5.2.2 Link of $V_{oc\ thresh\ eff\ decay}$ to charge flow (injection) mechanisms at metal-active layer interfaces

We set to find out whether the $V_{thresh\ eff\ decay}$ manifestation could be originating from elementary (fundamental) charge flow (injection) processes at metal-active layer interfaces of P3HT:PCBM devices. To determine the charge injection mechanisms in these devices the Fowler-Nordheim (FN) quantum mechanical tunneling theory as well as the Richardson-Schottky (RS) thermionic emission theory were invoked and used in the analysis of J(V) data obtained (in the dark and at different light intensities) from the several (alluded) experiments with the P3HT:PCBM based devices. The choice of the two theoretical models was based on descriptions (presented in Section 2.2.1) of how charge carriers cross such devices' metal-active layer junctions during current conduction.

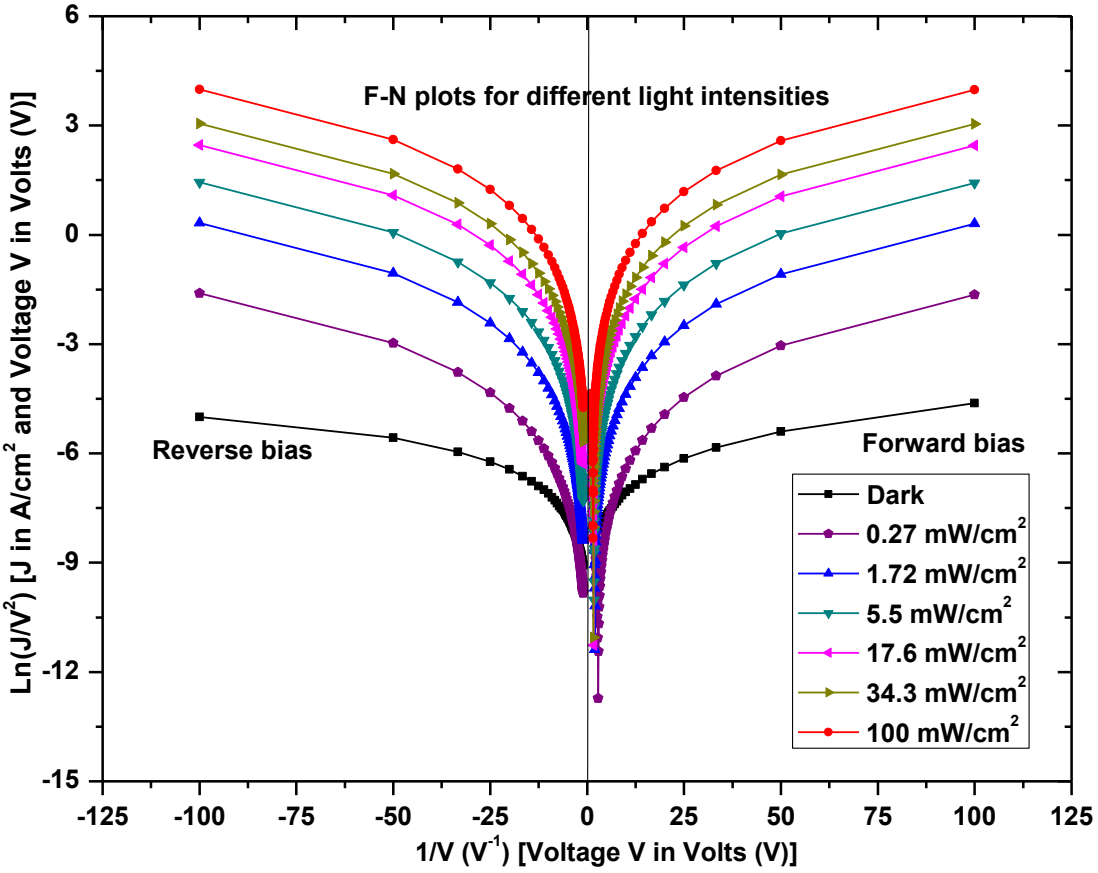

Figure 5.8 *FN plots for the ITO/PEDOT:PSS/P3HT:PCBM/Al photoactive device in the dark and under different white light illumination intensities*

Figure 5.8 shows two distinct families of FN curves for the device, each of which is composed of a dark curve and six other curves plotted using J(V) data belonging to the device illuminated at different intensities ranging from 0.27 mW/cm^2 to 100 mW/cm^2. Each curve is a plot of $Ln\left(J/V^2\right)$ versus $1/V$, the type of which can be deduced from equation (2.31), which in effect is the FN theory asserting the way in which electric charge can flow at metal-polymer junctions. We remind that this theory can be expressed in terms of the electric field *F* as presented in equation (2.29). We note the asymmetric nature of the curves, which indicates the existence of different potential barriers at the junctions. The curves in Figure 5.9 have been isolated from the family in Figure 5.8, mainly for purposes of distinct demonstration of the asymmetric property.

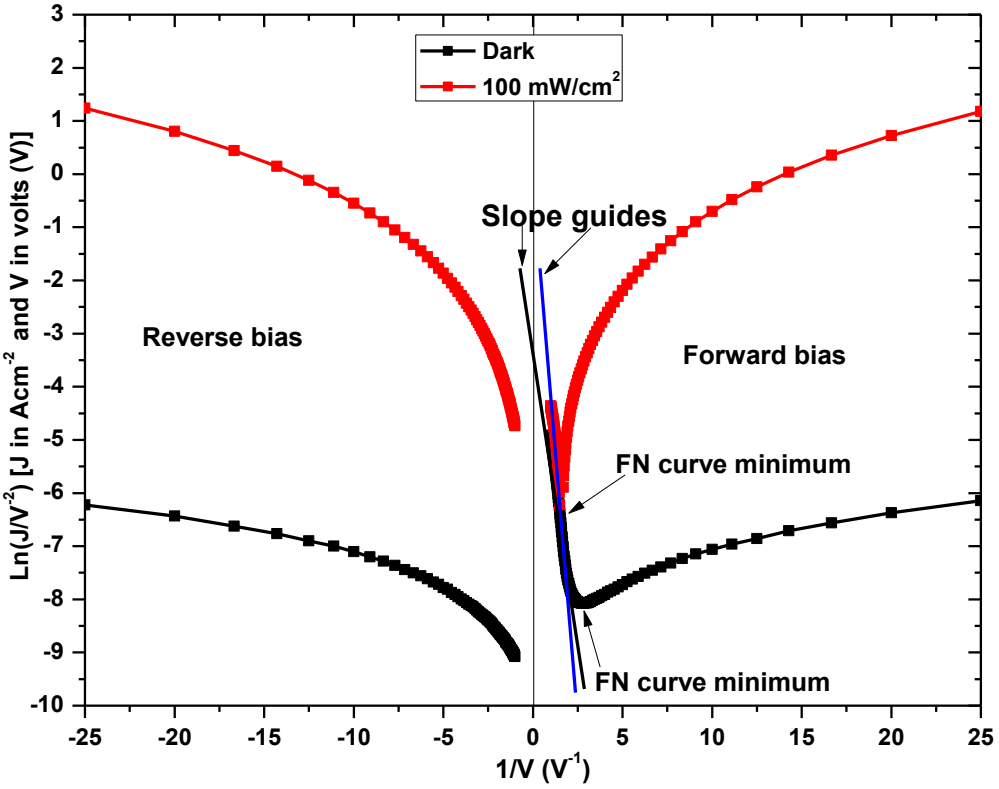

Figure 5.9 *Non–symmetry between corresponding FN curves for forward and reverse bias in ITO/PEDOT:PSS/P3HT:PCBM/Al devices*

For identification of regions of merit and comparison of injection processes at metal-active layer interfaces of ITO/PEDOT:PSS/P3HT:PCBM/Al solar cells in the dark and under 100mW/cm^2 white light illumination, we plotted the FN curves shown in Figure 5.10.

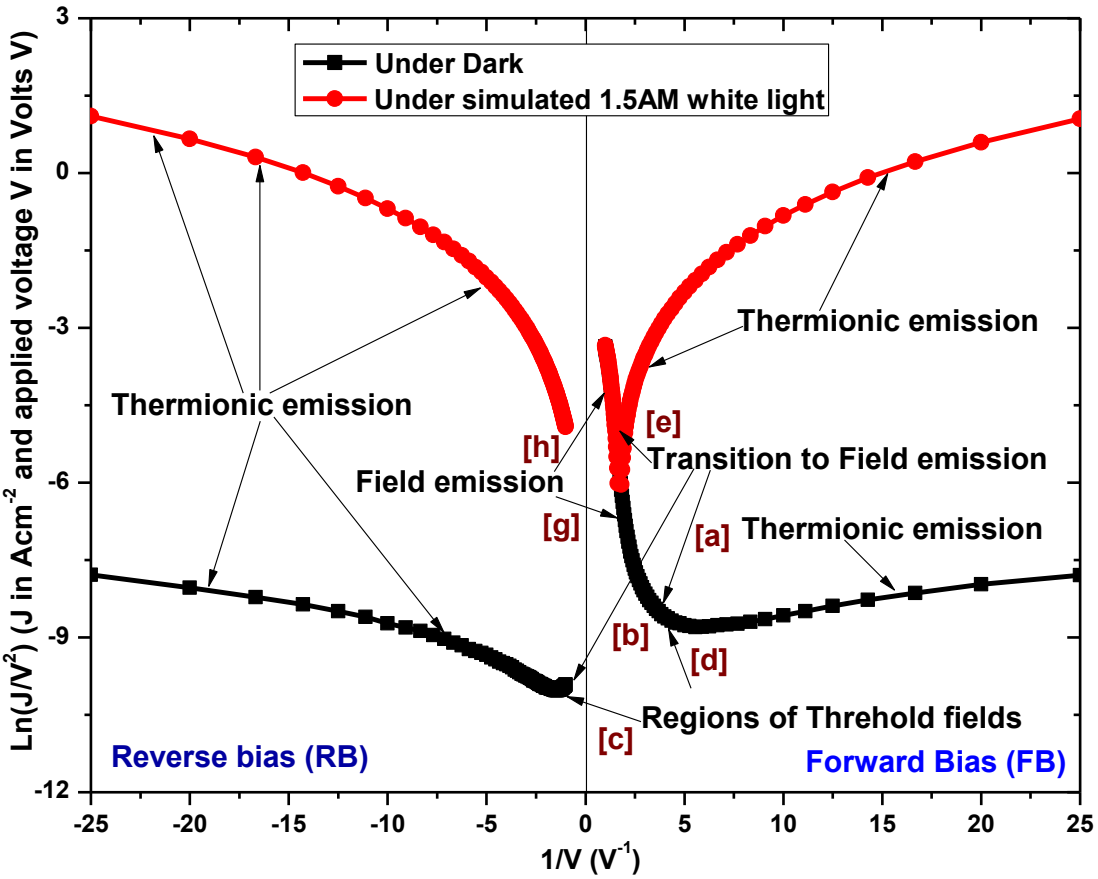

Figure 5.10 *Regions associated with thermionic and field emissions at metal-active layer interface*

The plots are for another identical device, which interestingly is beginning to tunnel under dark. Regions [a], [b] an [e] are associated with transition from RS thermionic emission regime to FN quantum mechanical tunneling (field emission) regime identified by regions [g] and [h]. We note that under forward bias (FB), transition from thermionic emission to field emission occurs much earlier under dark than under illumination. This lead in transition to tunneling by 'under dark' than by 'under illumination' in FB, is explicitly demonstrated in Figure 5.11 through comparative plots of the same data in absolute value representation under the same scale. This is explained by the existence of barriers of different heights. In FB, charge carriers under 100 mW/cm^2 illumination intensity must be encountering a much greater barrier height than under dark, because (as shown in Figure 5.11) tunneling starts at a much higher bias electric field under FB 100 mW/cm^2 illumination (green) than under FB dark (red). Barrier height therefore increases as illumination intensity increases. Under reverse bias, transition from thermionic

emission regime to tunneling regime is hardly taking place for most of the bias voltage ranges shown in Figures 5.9 – 11.

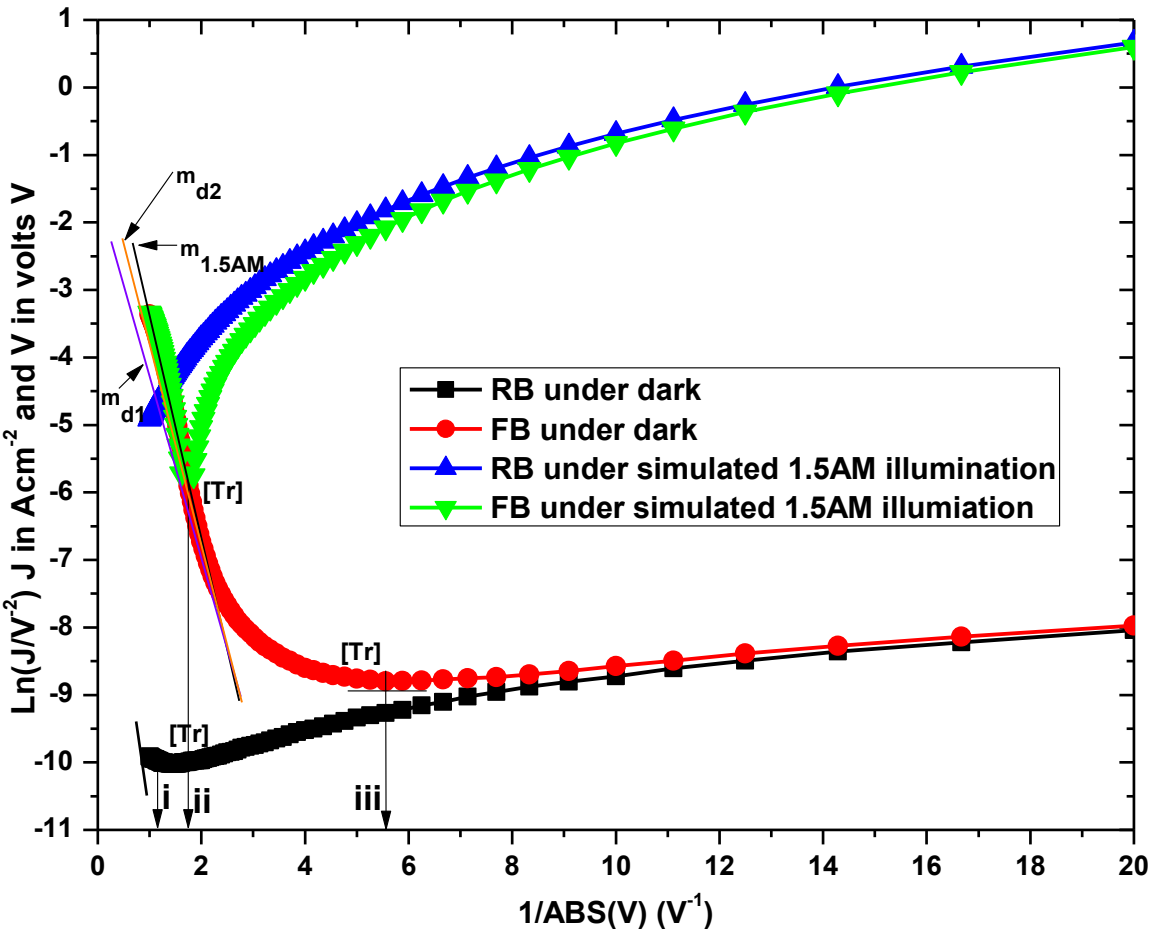

Figure 5.11 *Lead in transition from thermionic behaviour to tunneling characteristic by dark forward bias (FB) than by illuminated FB (AM 1.5) of an organic solar cell*

Only at very high electric fields (for example, ~ 8.33 × 10^4 V/cm in Figure 5.11) is transition to tunneling starting to manifest itself under dark. No likelihood of transition shows for the same magnitude of bias voltage under AM 1.5 (100 mW/cm^2) illumination. This is clear evidence for the existence of very large barriers at metal-active layer interfaces under reverse bias.

For broadened insight into the more intricate elementary processes at the metal-active layer interfaces of the ITO/PEDOT:PSS/P3HT:PCBM/Al devices, we comparatively studied charge injection mechanisms in the dark, under forward bias (FB) and under reverse bias (RB) using Figure 5.12, which was produced from the experimental ITO/PEDOT:PSS/P3HT:PCBM/Al

device J(V) data in Fowler-Nordheim (FN) formulation [Ln(J/V^2) versus 1/V]. Such broadening helps in making correct identification of the charge flow constraints at the interfaces, which in turn enables informed corrective measures and contribution to the device's performance improvement endeavours.

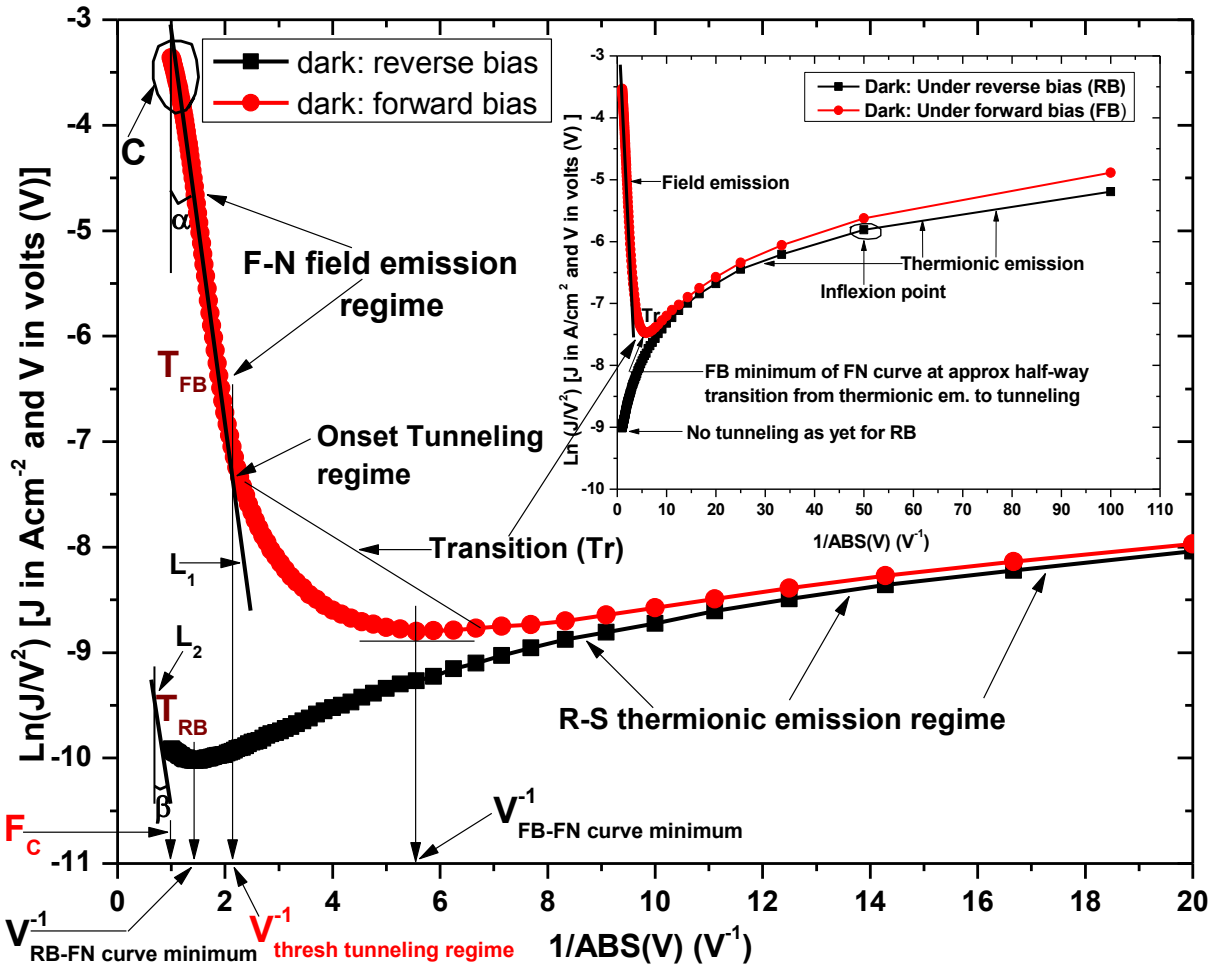

Figure 5.12 *Comparative configuration of the truncated Fowler-Nordheim (FN) plots for our ITO/PEDOT:PSS/P3HT:PCBM/Al solar cell in the dark under forward bias and reverse bias. Inset displays profile for wider bias voltage range and the proliferation of inflexion points*

In Figure 5.12, the dark reverse bias (+ve Al and –ve ITO/PEDOT:PSS) FN Ln (J/V^2) vs 1/V plot corresponds to electron injection through the negative ITO/PEDOT:PSS electrode into the LUMO of PCBM and hole injection through the positive Al electrode into the HOMO of P3HT. As for the forward bias (-ve Al and +ve ITO/PEDOT:PSS), the FN Ln (J/V) vs 1/V plot

corresponds to electron injection through the negative Al electrode into the LUMO of PCBM and hole injection through the positive ITO/PEDOT:PSS electrode into the HOMO of P3HT (see Figure 4.11). The Fowler-Nordheim quantum mechanical tunneling theory asserts that the curves plotted out of Ln (J/V^2) against $1/V$ {or Ln (J/F^2) vs $1/V$, where F is the associated electric field} are linear with negative slope if charge injection (flow) through the junction potential barrier is by tunneling. The theory assumes that the tunneling is through a triangular potential barrier (see Figure 2.24) in a Wentzel, Kramers and Brillouin (WKB) approximation.[33-34]

In Figure 5.12, curves whose lines of best fit are straight lines with negative slope can be observed at high applied voltages (thus high applied electric fields). Since this observation is in conformity with FN theory, the physics being conveyed is that under the given parameter settings, charge is penetrating the potential barriers at the metal-active layer interfaces of the device by FN quantum tunneling (field emission) mechanism. Metal-active layer interfaces characteristic of our device have already been identified in Chapter 4. For our device, no certainty on whether the tunneling charge carriers are electrons or holes can be made. However, based on the higher tunneling fields needed for the injection of holes into the HOMO of P3HT than for the injection of electrons into the LUMO of PCBM (Figure 4.11), we put forward the tunneling superiority of holes.

For the forward bias curve in Figure 5.12, field emission regime is evident in the region corresponding to T_{FB} (for Tunneling under Forward Bias) and as expected, shows occurrence at high voltages. The steepness (slope) of the straight line of best fit is directly proportional to the barrier height ϕ_B. This implies that, the greater the slope of the FN best fit, the higher is the associated potential barrier. In Figure 5.11, for example, the respective slopes m_{d1}, m_{d2} and $m_{1.5AM}$ for the FN fits shown, are related in magnitude by the inequality $m_{d1} > m_{d2} > m_{1.5AM}$. This means that their associated potential barriers are such that

$\phi_{B(m_{d1})} > \phi_{B(m_{d2})} > \phi_{B(m_{1.5AM})}$, where, *d* is for under dark and 1.5AM is for under 1.5AM illumination.

The mathematical representation of the magnitude of the potential barrier under tunneling regime is given by Eq. (2.26) or practically by Eq. (2.33). If the FN plots {Ln (J/V) vs $1/V$} are nonlinear, it indicates non-compliance with FN theory (that is, no tunneling) under the given configuration values, in which case, the charge injection would be by Richardson-Schottky (RS)

thermionic emission, in conformity with the proposed sum of the two (FN tunneling and RS thermionic emission) contributions to current[10] at metal-active layer junction.

In the device, tunneling under FB starts at a threshold voltage which is comparatively lower than the one under reverse bias. The existence of threshold voltages for tunneling is evident in both biases (RB and FB), but the difference is in the magnitudes of the thresholds. Tunneling under Reverse Bias (T_{RB}) is shown to occur much latter than under FB. This is attributed to a higher potential barrier to be surmounted under RB than under FB. The transition stage of the dark RB curve of Figure 5.12 is showing that the onset of tunneling is imminent in the reverse biased device and a steeper tunneling (T_{RB}) slope of the curve is predicted by the gradient angle β, which is visibly smaller than the counterpart angle α for T_{FB}. This is in conformity with the attribution of a steeper slope of the FN curve to a higher blocking potential at the metal-active layer interface of the device.

As Figure 5.12 shows, more thermionic emission current is evident under forward bias than under reverse bias. We explain this behaviour by propounding that this suggests the existence of a smaller potential barrier $(\phi_B \leq k_B T)$ under forward bias, which should be overcome easily by many charge carriers whose thermal energy will be greater than its (that is, ϕ_B) height. Reverse bias (RB) has much larger barriers, hence much smaller thermionic emission current. Conversely, the tunneling currents achieved under FB (for injection of holes through ITO/PEDOT:PSS and electrons through the Al electrode) are much lower than those for injection under reverse bias. This is so, because of the existence of higher potential barriers under RB, which makes surmounting of them by thermionic emission difficult, but favours tunneling if the bias voltage (hence electric field) is high enough. As Figure 4.11 illustrates, under RB, (with the ITO electrode biased negative and the Al one biased positive), electrons from ITO have to overcome a much larger barrier into LUMO of P3HT. Likewise, holes from Al have to overcome a larger barrier into HOMO of PCBM, thus smaller net current as is evident from Figure 5.12.

In the encircled region C (of Figure 5.12) corresponding to much higher electric fields (F_C) ($F_C \geq 1\times10^5$ V/cm for our device), the FN curve shows a bowing inclination suggestive of it tending to level off from the straight line ascribed to quantum tunneling. This points to a reduction in conductivity when compared to the straight line segment attributed to the field

emission regime. The likely explanation (based on the suggestion in reference[6]) for this behaviour is that all possible traps in the region have now been filled through tunneling and space charge is building up close to the injecting electrodes (Al and ITO/PEDOT:PSS for our double carrier device).

The non-linear region to the right in Figure 5.12 FN curves depicts thermionic emission. This implies that at low voltages, at the same temperature (300K), charge carriers with thermal energy $\left(300k_B/e\right) \approx 2.585\times10^{-2}$ J being greater than the barrier height (~ 0.67 eV) are able to pass above the barrier. The RS thermionic emission is verified by the production of straight lines of positive slope upon plotting Ln J vs $\sqrt{V}$ or Ln J vs $\sqrt{F}$ in application of the RS model, which in experimental representation is given by Eq. (2.11) or (2.15). The RS plots for our device are shown in Figure 5.13. Higher voltages show non-linearity of the RS curves, especially under forward bias, which subscribes to field emission under such conditions.

The dark curves of Figure 5.12 reveal the characteristics of the solar cell corresponding to room temperature (~300 K). The principal curves have been truncated at about 20 mW/cm^2 in order to make the minimum turning points of the curves explicit. As labelled in the figure (5.12), negative slope indicates tunneling, whereas positive slope shows the field independent thermionic emission. Inflexion points, as shown for dark in the insert, appear along the thermionic regime section of the curves and lead to steep descents in the curving until a minimum turning point corresponding to some high bias voltage is reached for each curve. In other words, we can say that an obstruction of thermionic emission is witnessed in this region. This blockage of thermionic emission suggests that there must be an additional counter internal electric field, which surfaces in the device and suppresses thermionic emission process from claiming a contribution to charge flow across the metal-active layer interface. At the observed FN curve minima (regions Tr-FN curve minima in Figure 5.12 and Tr-i to iii in Figure 5.11), it should be that this internal field completely obliterates the dominance of thermionic emission. The fall and rise section of the curve corresponds to the transition (Tr) region (conspicuously showing under FB in Figures 5.9 to 5.12) which encompasses the minimum and adjacent limbs of the FN curve, the assembly of which forms an asymmetrical open letter U. The observed minimum therefore demarcates the transition from thermionic emission dominated charge injection to field emission dominated conduction across barriers at the electrical contacts of such devices. The non-

symmetric characteristic indicates the existence of different barriers at the associated metal-active layer interfaces. More evidence for the existence of an additional internal electric field in such organic solar cells emanate from the observation of positive currents even when negative bias is still applied.[6]

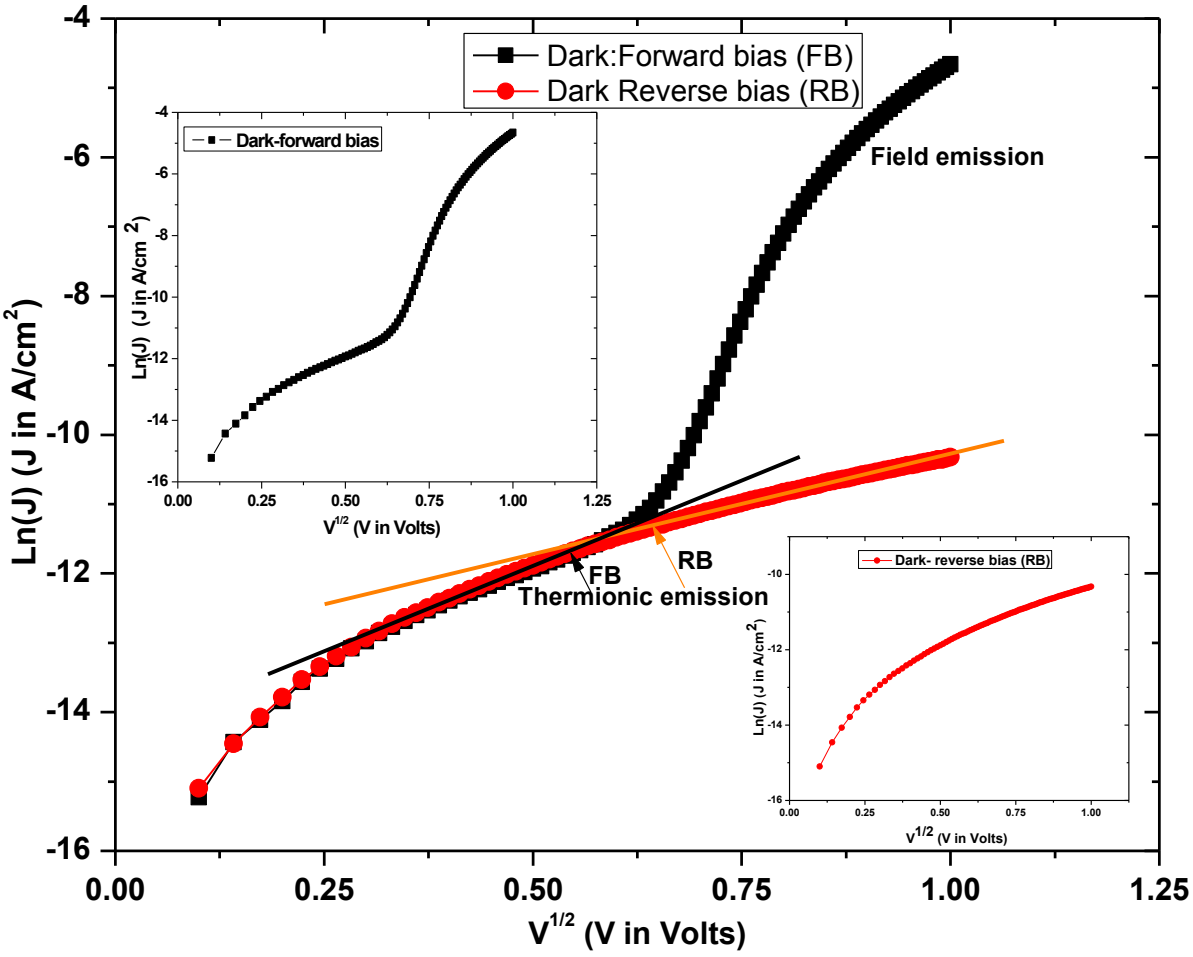

Figure 5.13 *Richard-Schottky* (*RS*) *thermionic emission curves for the experimental ITO/PEDOT:PSS/P3HT:PCBM/Al device*

When the applied field is high, the internal field may be overwhelmed by the quantum mechanical tunneling which dominates with increase in the applied (bias) voltage. As a result, the influence of the internal (built in) field will be overshadowed. However, at low applied fields, this field becomes significant and its influence cannot be assumed trivial. In fact, under certain cases of low bias voltage (that is, applied field), this internal field can even become greater than the applied electric field, to the extent of changing the direction of flow of the current. This

internal field stops all the thermionically generated charge until a certain field overcomes it. Its magnitude may be visualized at the (minimum) turning points of the FN curve.[6] The magnitude of this internal field was determined at the shown minima in the transition regions of Figure 5.12. These are the points corresponding to the labels $\mathbf{V^{-1}}_{\text{RB-FN curve minimum}}$ and $\mathbf{V^{-1}}_{\text{FB-FN curve minimum}}$ on the $\mathbf{V^{-1}}$ axis. In reverse bias (RB), the internal field corresponding to the minimum of the FN curve for the device under dark was found to be 7.14×10^4 Vcm^{-1} and in forward bias (FB), the obtained internal field was 2.13×10^4 Vcm^{-1}. The results show that the internal field corresponding to the dark RB minimum value is significantly higher than that corresponding to dark FB minimum. This supports the observation that transition from thermionic emission to field emission occurs earlier under FB than under RB.

From the FN minimum in Figure 5.12, build ups towards the alluded linear steep ascents of negative slope are observed, especially under forward bias. Ibid[6] suggested that this observed minimum of the dark FN curve is related to the open circuit voltage of the device. In addition to this, we advance the hypothesis that this minimum of the FN curve is approximated in magnitude by the experimentally observed threshold open circuit voltage at which efficiency starts to decay ($V_{oc\ thresh\ eff\ decay}$). In order to verify this, we compared the found voltage of 0.1818 V corresponding to the FB minimum of the dark FN curve in Figure 5.12, with the observed $V_{oc\ thresh\ eff\ decay}$ value of ~ 0.461 V obtained for the same device. Though different, their corresponding electric fields are of the same order of magnitude. We conducted reliability checks through repeated experimentation with several such devices and obtained similar approximations. Following on this, we determined the value of the voltage corresponding to the onset of strict quantum tunneling (field emission regime), which begins at the end of the transition region and is labelled 'onset of tunneling regime' in Figure 5.12. We found the magnitude of this voltage (at the point labelled $V^{-1}_{thresh\ tunneling\ regime}$ on the V^{-1} axis) to be ~ 0.4598 V and noticed that its value is approximately equal to the observed value of $V_{oc\ thresh\ eff\ decay}$ for the same device. This seemed to confirm the suggestion by[35] and[6] that the observed FN curve minimum is related to the open circuit voltage of the device.

We mounted several replica method experiments with many identical devices and to avoid over-crowdedness of the curves (which diminishes clarity) we present in Figure 5.14, the obtained FN curves for a small sample. For comparative purposes, voltage values which we obtained through

analysis of the shown FN curves for the sample are displayed in Table 5.4 together with those of the corresponding observed $V_{oc\ thresh\ eff\ decay}$.

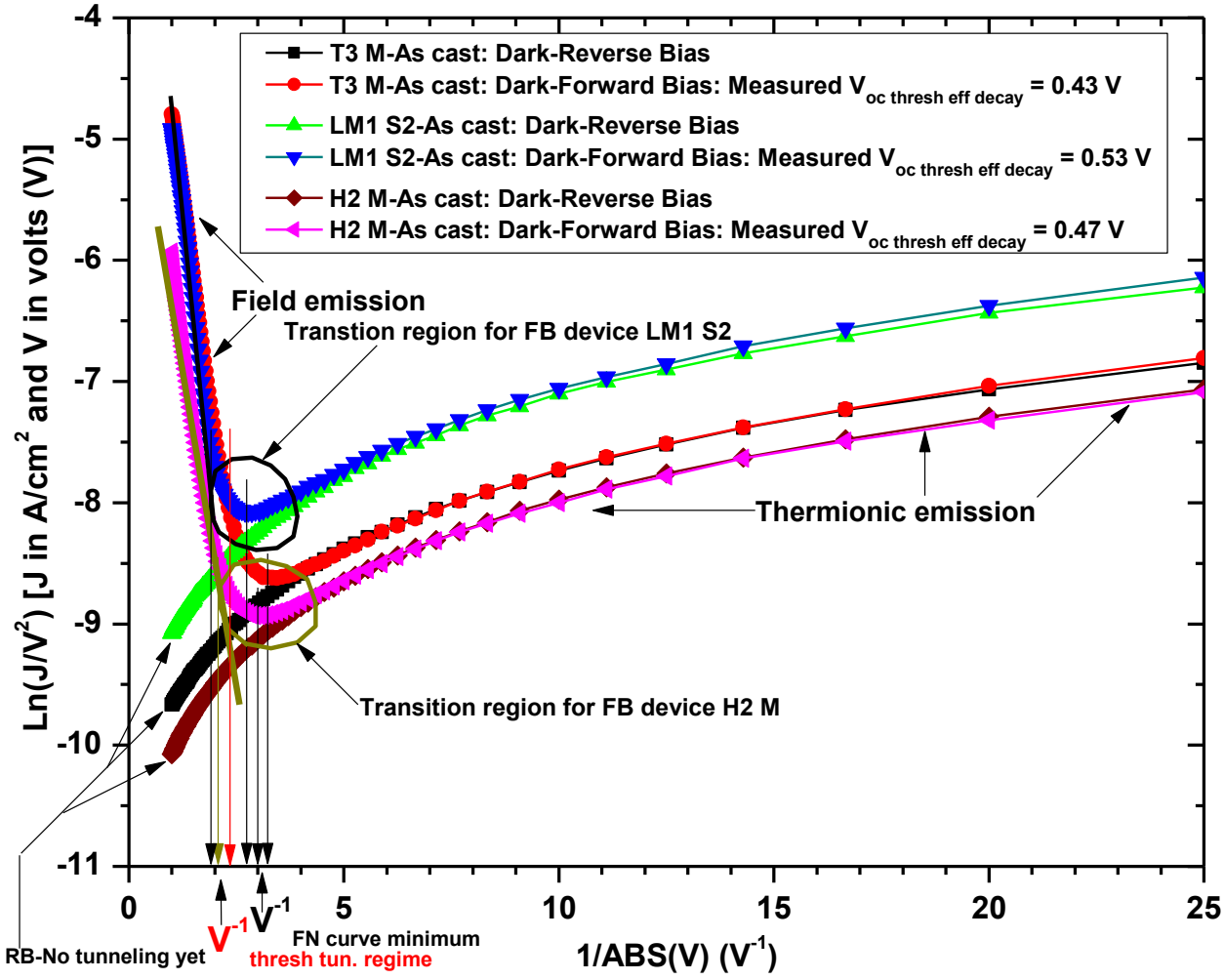

Figure 5.14 *FN curves for sample ITO/PEDOT:PSS/P3HT:PCBM/Al devices used in determining magnitudes of* $V_{thresh\ tunneling\ regime}$ *marking onset of field emission regime and* $V_{FN\ curve\ minimum}$ *associated with curve minimum in the transition region from thermionic to field emission*

The preceding analysis and findings displayed in Table 5.4 show that (in allowance of experimental error) $V_{thresh\ tunneling\ regime}$ values are equal to $V_{oc\ thresh\ eff\ decay}$ values. In light of this, we contribute that the observed threshold open circuit voltage from which efficiency starts to decrease indicates the value of the internal voltage within the device corresponding to the onset of field emission (FN quantum mechanical tunneling) injection of charge through the potential barrier at the metal-active layer interface. Based on our presented results and analysis, we not

only confirm the proposal by[35] that the internal (built in) voltage is related to the open circuit voltage, but also add that the observed FN internal voltage suppressing thermionic emission is actually the open circuit voltage built within the device. In the case of our ITO/PEDOT:PSS/P3HT:PCBM/Al device, this is the electromotive force between the PCBM LUMO and the P3HT HOMO.

Table 5.4 *Approximate values of* $V_{oc\ thresh\ eff\ decay}$ *compared with FN* $V_{thresh\ tunneling}$ *and* $V_{curve\ minimum}$ *for the sample, where* η *and* I *are device efficiency and incident light intensity respectively*

Device Identity (Under FB)	$V_{oc\ thresh\ eff.\ decay}$ from V_{oc} and η Vs I plot (V) ± 0.02	FN Formulation $V_{thresh\ tunneling\ regime}$ (V) ± 0.001	FN Formulation $V_{curve\ minimum}$ (V) ± 0.001	FN Thresh Electric Field $F_{thresh\ tun.\ regime}$ (V/cm) ± 0.001×10^4
LM1 S2-as cast	0.53	0.526	0.370	5.263×10^4
T3 M-as cast	0.43	0.426	0.303	4.255×10^4
H2 M-as cast	0.47	0.465	0.323	4.651×10^4

The observed minimum in each of the FN plots corresponds to the V_{oc} which is linked to the changeover within the transition zone from thermionic emission superiority flow to field emission dominated conduction of charge in such devices. The transition from thermionic to field emission is not an instantaneous event, but is rather a gradual process, although the time it takes is still very small. The location of the minimum of the FN curve is about half-way of the transition zone and it signals the end of thermionic emission dominance as well as the start of the superiority of quantum mechanical tunneling (field emission).

To aid understanding of the charge injection processes at the electrical contacts of our device, we present in Figure 5.15, the non-scaled energy diagram which shows locations of the FN curve minimum, the FN $V_{thresh\ tunneling}$ and $V_{oc\ thresh\ efficiency\ decay}$.

Also as Figure 5.15 shows, the transition region (which houses the minimum on the FN curve) is characterised by hybrid operations of thermionic and field emission processes, which for purposes of exposing the gradual nature of the takeover of each of the processes, are discretely presented in the figure as field assisted thermionic and thermally assisted field emission processes. The model enabling explanation of this change from thermionic to field emission at the metal-active layer interfaces of such organic devices under isothermal confinements is:[6], [35]

$$F_{th} = \frac{2\sqrt{2m}\, k_B T \phi_B^{(3/2)}}{q\hbar\left(\phi_B - k_B T\right)} \tag{5.5}$$

where F_{th} is the threshold field for change over from RS thermionic emission to FN field emission and the other symbols carry their usual meanings.

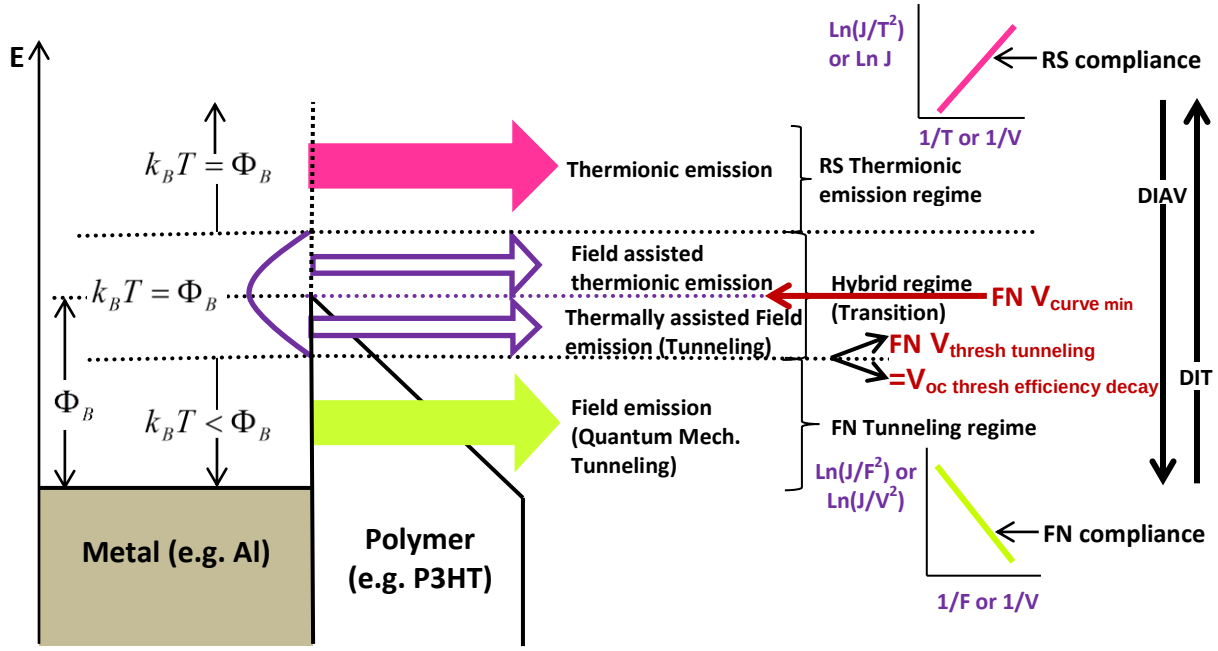

Figure 5.15 *Charge Injection mechanisms through and above a triangular potential barrier at a metal-active layer interface, where Φ_B is the potential barrier height, DIAV implies Direction of Increase of Applied Voltage and DIT implies Direction of Increase of Temperature*

Analysis of equation (5.5) gives that the electric field F increases with increase in temperature. When $\phi_B \leq k_B T$, the field is not defined, which means that all the charges have thermal energy equal to or greater than that needed to surmount the barrier.[6] Therefore, only thermionic emission takes place in this case.

5.2.2.1 Accounting for the decrease in efficiency as incident light intensity increases

Since $V_{\text{thresh tunneling}}$ has been found to be equal to $V_{\text{oc thresh efficiency decay}}$, it implies that the values of the observed $V_{\text{oc thresh efficiency decay}}$ parameters in the J(V) curves of metal-organic active layer - metal solar cell devices, indicate the magnitudes of the internal electric fields which trigger quantum mechanical tunneling within the devices' metal-active layer interfaces. The finding also

confirms that the internal voltages generating these electric fields are the open circuit voltages. Figure 5.12 shows that for our device in the dark and under reverse bias (RB), tunneling (which corresponds to T_{RB} in the figure) starts at $V^{-1} \approx 0.7\ V^{-1}$, which gives the threshold internal voltage ($V_{thresh\ tun}$) of approximately 1.4286 V in magnitude. We have found out that this voltage is the built in (internal) open circuit voltage and it generates an internal threshold electric field for onset of tunneling ($F_{\text{thresh tun}}$) which is ~ 1.428×10^5 V/cm. This threshold field is much higher than ~ 4.5454×10^4 V/cm found for the corresponding forward bias configuration. The disparity in the field magnitudes further confirms that the barrier to be overcome under reverse bias is larger than that under forward bias, a case which also accounts for the witnessed threshold for the onset of field emission (quantum mechanical tunneling) occurring at much smaller threshold internal electric fields under forward bias than under reverse bias.

The threshold voltage at which efficiency starts to decrease ($V_{\text{oc thresh eff decay}}$) is a member of the open circuit voltages corresponding to different illumination intensities (see Figures 5.11 and 5.12), of which we deliberately pick the 1.5AM (100mW/cm^2) incident white light intensity since solar cells mostly operate under this intensity. For ease of comparison in the analysis, we display in Table 5.5 typical forward bias values of the sample's threshold open circuit voltages (as well as the associated threshold fields) and compare these with their counterparts when the same devices are subjected to 100mW/cm^2 incident white light illumination.

Table 5.5 *Comparison of values of threshold open circuit voltages and associated electric field parameters for start of decrease in device efficiency and onset of quantum tunneling, to the corresponding operational parameter values at 100mW/cm^2 illumination intensity for different ITO/PEDOT:PSS/P3HT:PCBM/Al devices under forward bias*

Device Identity (Under FB)	**$V_{oc\ thresh\ eff\ decay}$ from V_{oc} and η Vs I plot (V)**	**FN Formulation $V_{thresh\ tunneling\ regime}$ (V)**	**FN Formulation $V_{curve\ minimum}$ (V)**	**FN-Thresh Tunn Electric Field $F_{thresh\ tun.\ regime}$ (V/cm)**	**V_{oc} at 100 mW/cm^2 (1.5AM Solar simulated)/V**	**Elect Field due to V_{oc} at 100 mW/cm^2 illum F_{100} (V/cm)**
LM1 S2-as Cast - FB	0.53	0.5263 ~ **0.53**	0.3704	5.263×10^4	0.64	6.4×10^4
T3 M-as cast - FB	0.43	0.4255 ~ **0.43**	0.3030	4.255×10^4	0.52	5.2×10^4
H2 M-as cast - FB	0.47	0.4651 ~ **0.47**	0.3226	4.651×10^4	0.53	5.3×10^4

We note (from Table 5.5) that when the devices are illuminated, the thresholds for tunneling under forward bias occur at electric fields smaller than those generated by the open circuit voltages corresponding to 100 mW/cm^2 illumination intensity. For example, the shown threshold V_{oc} for the onset of tunneling in device LM1 S2 under forward bias is ~ 0.53 V, which generates an associated internal threshold field ($F_{\text{thresh tun}}$) approximately equal to 5.3×10^4 V/cm. Based on the preceding discussion, it means that once this threshold has been reached, two simultaneous mechanisms are triggered within the device and these are: FN quantum mechanical tunneling (field emission) of charge through the potential barrier at the metal-active layer interface of the device and decrease in the power conversion efficiency η of the device. It is the tunneling which on the other hand is responsible for the decrease in the efficiency, because it increases the dark current. To mimic the opto-electrical mechanisms which come into play within our ITO/PEDOT:PSS/P3HT:PCBM/Al device under different illumination intensities, we developed Figure 5.16, which we refer to in the explanation. When the polymer-fullerene based device is illuminated and the pathway is conducive, the generated excitons ultimately dissociate into electrons and holes, which under drive by the electric field due to the built in voltage V_{bi}, migrate to their respective metal electrodes - (electrons to Al and holes to ITO/PEDOT:PSS). We expect a sea of electrons and holes (as in Figure 5.16) with net negative charge in the P3HT:PCBM blend to be prevalent. This charge migration within the device constitutes the photogenerated current I_{ph} through the device, which results in charge accumulating on the electrodes, thus the formation of the photogenerated voltage V_{ph} responsible for driving current through the external circuit and doing work. The downside of this mechanism is that the accumulating charge also biases the same device with the same voltage V_{ph} (shown in Figure 5.16), which then drives the

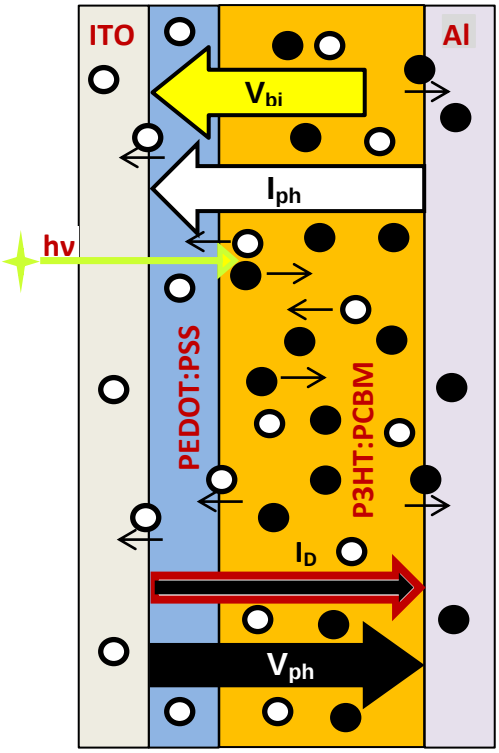

Figure 5.16 *Opto-electrical mechanisms at play within our illuminated polymer-fullerene based device. White circles denote holes and black circles denote electrons*

problematic dark current I_D through the device. The nature of the bias is similar to the forward bias case analysed. Since the dark current I_D (or dark current density J_D) acts in opposite direction to the photogenerated current I_{ph} (or photogenerated current density J_{ph}) it brings in the negative effect of reducing the short circuit current density J_{SC} (because $J_{SC} = J_{ph} - J_D$). As a result, the power conversion efficiency η of the solar cell device is reduced, since η directly depends on J_{SC} as given by $\eta = \frac{J_{sc}V_{oc}}{P_{light}} FF$, where FF is the fill factor and P_{light} is the incident light power. If the photogenerated voltage V_{ph} increases, the dark current also increases since it is driven by V_{ph}. FN tunneling is characterised by a tremendous increase in current, which starts once the threshold field for onset of the tunneling has been reached. Electric fields higher than the threshold result in even more tunneling current through the device, which means higher V_{ph} and I_D, the net effect of which is further decrease in η as I_D increases after $V_{thresh\ tun}$ or ($V_{oc\ thresh\ eff\ decay}$). We therefore surmise that the sudden decrease in device efficiency must be due to the unexpectedly large increase in the dark current density J_D caused by the avalanche of tunneling current which takes centre stage from the advent of the threshold tunneling electric field and throughout the field emission regime. This dark current density J_D acts against the photogenerated current density and since it becomes boosted upon arrival at the thresholds and increases drastically for V_{oc} (or V_{ph}) greater than tunneling threshold, it significantly reduces the photogenerated current density J_{ph}, hence the device efficiency η, which is directly proportional to the photogenerated current density. Voc which follows Vph is proportional to light intensity.

The photogenerated voltage Vph is equal to the open circuit voltage Voc corresponding to the illumination intensity at hand. Solar cells mostly operate under subjection to 1.5AM incident white light illumination intensity (100 mW/cm^2), which generates within the device, open circuit voltages (V_{oc}s) far much greater than the threshold voltages ($\Rightarrow$ threshold fields) for start of tunneling. Therefore much further decrease in efficiency is witnessed. For example, when our LMI S2 device was under 100 mW/cm^2 incident white light intensity, the corresponding V_{oc} was found to be 0.64 V (see Table 5.5), which is much greater than the shown corresponding efficiency decay threshold of 0.53 V. This 0.64 V generates an internal field of 6.4×10^4 V/cm, which is far much greater than the threshold field of 5.3×10^4 V/cm under FB, which leads to the

creation of larger dark current density J_D and the ultimate further lowering of the device efficiency.

5.3 Conclusions

Increasing white light intensity incident on bulk heterojunction P3HT:PCBM composite devices increases the photogenerated current density (J_{ph}), which simultaneously inflicts (causes) increase in the photogenerated voltage (V_{ph}), due to increased accumulation of charge carriers on the electrodes. Whilst V_{ph} is responsible for driving current through the external circuit and doing work, it unfortunately biases its parent device (which produced it) with the same voltage V_{ph} and drives dark current density (J_D) through the device. Since J_D acts in opposite direction to the photogenerated current density, it implies that as it (J_D) increases with increase in V_{ph}, it significantly reduces the photogenerated current density. The short circuit current density (J_{SC}), being the maximum photogenerated current density, is therefore significantly decreased, hence the decrease in device efficiency η, since η is directly proportional to the short circuit current density. At light intensities lower than the threshold light intensity (that is, those light intensities corresponding to voltages lower than the threshold open circuit voltages at which the device efficiency starts to decay), polymer-fullerene solar cells exhibit increase in efficiency.

5.4 References

[1] Dimitrov, S.D.; Schroeder, B.C.; Nielsen, C.B.; Bronstein, H.; Fei, Z.; McCulloch, I.; Heeney, M. and Durrant, J.R. *Singlet Exciton Lifetimes in Conjugated Films for Organic Solar Cells*. MDPI Polymers; 2016.

[2] Tang, C.W. *Two-layer organic photovoltaic cell*. Appl. Phys. Lett., 48, 183-185; 1986.

[3] Hu, H.; Jiang, J.; Yang, G.; Liu, J.; Li, Z.; Lin, H.; Liu, Y.; Zhao, J.; Huang, F.; et al. *Terthiophene-based D-A polymer with asymmetric arrangement of alkyl chains that enables efficient polymer solar cells*. J. Am. Chem.Soc. 137, 14149-14157; 2015.

[4] Liu, Y.; Zhao, J.; Li, Z.; Mu, C.; Ma, W.; Hu, H.; Jiang K.; Lin, H.; Ade, H. and Yan, H. *Aggregation and morphology control enables multiple cases of high-efficiency polymer solar cells*. Nat. Commun. 5293; 2014.

[5] Kao, K.C. and Hwang, W. *Electrical Transport in Solids, with particular reference to organic semiconductors*, volume 14 of *International Series in the Science of the solid State*. Pergamon Press, Oxford; 1981.

[6] Chiguvare, Z. *Electrical and Optical Characterization of Bulk Heterojunction Polymer-Fullerene Solar Cells*. PhD thesis, Oldenburg University, Germany; 2005.

[7] Rose, A. *Concepts in Photoconductivity and Allied Problems*. Wiley Interscience (New York); 1963.

[8] Williams E.W. *Solar Cells*. IEE Special Publication, Institution of Electrical Engineers (UK); 1978.

[9] Feller, F.; Rothe, C.; Tammer, M.; Geshke, D. and Monkman, A.P. *Temperature dependence of the space charge distribution in injection limited conjugated polymer structures*. J. Appl. Phys., 91: 9225; 2002.

[10] Sze, S.M. *Semiconductor device*. Wiley, New York; 1998.

[11] Calvet, L.E. *Electrical Transport in Schottky Barrier MOSFETs*. PhD Dissertation,Yale University; 2001

[12] Henisch, H.K. *Semiconductor Contacts, An approach to ideas and models*. International Series of Monographs on Physics No.70. Clarendon Press, Oxford; 1984.

[13] Das, R.R.; Battacharya, P.; Perez, W.; Katiyar, R.S. and Bhalla, A.S. *Leakage current characteristics of laser-ablated srbi*2*nb*2o9 *thin films*. Appl. Phys. Lett., 81:880; 2002.

[14] Braun, D. *Electronic injection and conduction processes for polymer devices*. J. Polymer Science B, 41:2622; 2003

[15] Lorentzo, E.; et al. *Solar Electricity Engineering of Photovoltaic Systems*. Institute of Solar Energy Polytechnic University of Madrid; 1994.

[16] Fu-Chien Chiu and Chun-Hsing Shih. *A Review on Conduction Mechanisms in Dielectric Films*. Advances in Materials Science and Engineering, Volume 2014 (2014), Article ID 578168; 2014 http://dx.doi.org/10.1155/2014/578168 Review Article

[17] Frechet, J.M.J. and Thompson, B.C. *Polymer-Fullerene Composite Solar Cells*. Wiley VCH-Vrlag GmbH & Co. KGaA, Weinheim Angew. Chem. Int Ed. 47, 58-77; 2008.

[18] Sirringhaus, H.; Tessler, N. and Friend, R. *Integrated optoelectronic devices based on conjugated polymers*. Science, 280:1741; 1998.

[19] Gunnes, S.; Neugebauer, H. and Sariciftci, N.S. *Chem. Rev*, 107, 1324-1338; 2007.

[20] Singh, T.B.; Marjonovic, N.; Matt, G.J.; Gunes, S.; Sariciftci, N.S.; Montaigne Ramil, A,; Andreev, A.; Sitter, H.; Schwodiauer, R. and Bauer, S. *Org. Electron*, 6, 105-110; 2005.

[21] Winder, C.; Matt, G.; Hummelen, J.C.; Janssen, R.A.J; Sariciftci, N.S.; Brabec, C.J. *Thin Solid Films*. 403-404, 373-379; 2002.

[22] Hwang, J.D. and Lee, K.S. *J. Electrochem. Soc*. 155, H259; 2008.

[23] Mahapatro, A.K. and Ghosh, S. IEEE *Transactions on electron devices*. 48, 1911; 2001.

[24] Ahmad, Z.; Sayyad, M.H.; Saleem, M.; Kamirov, Khasan S. and Shah, M. Physica E **41**, 18; 2008.

[25] Gadisa, A. *Studies of Charge Transport and Energy Level in Solar Cells Based on Polymer/Fullerene Bulk Heterojunction*. Linköping Studies in Sciece and Technology – Dissertation No. 1056 Linköping University, SE-581 83 Linköping, Sweden; 2006.

[26] van Duren, J.K.J.; Yang, X.; Loose, J.; Bulle-Lieuwma, C.W.T.; Sieval, A.B.; Hummelen, J.C. and Lanssen, A.J. *Relating the morphology of poly(p-phenylene vinylene)/methanofullerene blends to solar cell performance*, Adv.Funct.Mater. **14**,425-434; 2004.

[27] Gartstein, Yu N. and Conwell, E.M. *Field-dependent thermal injection into a disordered molecular insulator*. Chem. Phys. Lett. **255**, 93-98; 1996.

[28] Martens, H.C.F.; Blom, P.W.M. and Schoo, H.F.M. *Comparative study of hole transport in poly(p-phenylene vinylene derivatives*. Phys. Rev. B **61,** 7489-7493; 2000.

[29] Lampert, M.A. and Mark, P. *Current Injection in Solids*, Academic, New York; 1970.

[30] Rhoderick, E.H. *Metal Semiconductors Contacts*, Oxford University Press; 1978.

[31] El-Nahass, M.M.; Abd-El-Rahman, K.F.; Farag, A.A.M. and Darwish, A.A.A. *Org. Electron*. **6**, 129; 2005.

[32] Ahmad, Z. and Sayyad, M.H. *Electrical characteristics of a high rectification ratio organic Schottky diode based on methyl red*, Optoelectronics and advanced materials-Rapid Communications Vol.3,No 5, p.509-512; 2009.

[33] Griffiths, D.J. Introduction to Quantum Mechanics. 2nd Edition, Pearson Education; 2005.

[34] Springer link: link.springer.com/content/pdf/10.1007%2F978-3-642-31558-9_1.pdf

[35] Chiguvare, Z.; Parisi, J. and Dyakonov V. *Current limiting mechanisms in indium-tin-oxide/poly3-hexylthiophene/aluminium thin film devices*. J. Appl. Phys. 94:2440; 2003.

Chapter 6

Opto-electrical performance analysis of nanocomposited P3HT:PCBM bulk heterojunction excitonic devices for varying active film thicknesses

6.1 Introduction

In a composite, the performance of P3HT and PCBM as a thin film heterojunction depends on many parameters such as techniques by which the thin films are grown,[1] processing conditions,[2] morphology of the deposited photoactive thin film,[3] thickness of the active layer, heat treatment[4] and many others. Whilst organic descent devices based on the bulk heterojunction (BHJ) concept in which a semiconducting conjugated polymer is intimately mixed with a fullerene derivative (generating a nanometer phase separation) seems the most promising,[5] finding the active layer thickness which is commensurate with the mix still remains a challenge. Two of the major factors limiting the power conversion efficiency of the BHJ solar cell are low carrier mobility inside the photoactive layer and incomplete absorption of the incident light.[6-8] These parameters (like many others) both depend directly on the thickness L of the active film. Increase in the thickness lengthens the optical path of incident light. This allows for greater absorption A as given by:[6], [9-10]

$$A = -Log\left(I_0\, e^{-4\pi k L/\lambda}\right) \tag{6.1}$$

where, A is the measured absorbance, I_0 is the incident irradiance and k is the extinction coefficient of the material.

However, while the total number of charges created in the active layer increases, due to higher absorption as L is increased; there arises the unwanted downside that the photogenerated electrons and holes must now travel, on average, a greater distance through the active layer before they can reach their respective electrodes. This exposes the charges to a higher probability of recombination before reaching the respective electrodes.[11-14] Therefore, the anticipated increase in the photogenerated current is unlikely, because the higher recombination will now further curtail the current. This calls for active layer thickness (ALT) optimization.

Along this, we studied the characteristic changes in the opto-electrical properties of the 1:1 blend of P3HT:PCBM with thickness of the active layer in ITO/PEDOT:PSS/P3HT:PCBM/Al solar

cells, with intentions of finding out their effect on the threshold voltage at which efficiency starts to decrease ($V_{threshold\ eff\ decay}$) and also for purposes of optimizing the thickness of the active layer. To obtain different active layer thicknesses (ALTs), each sample was cast at different spin-coat speeds. The spin-coat speeds used were 1000, 2000, 3000 and 4000 revolutions per minute (rpm). This technique produced four different active film thickness samples, in which all same sample devices had their photoactive P3HT:PCBM blends spin-coated at the same speed, for example, 1000 rpm. Each deposition was done at room temperature, under normal atmospheric pressure and was accorded a 1 minute spin-coating period. A sample consisted of three batches of devices, with each batch being made up of 4 clusters and each cluster having 3 devices on it. This made up a total of 36 devices per sample. For clarity, each cluster was a 1.25 cm × 1.25 cm glass/ITO/PEDOT:PSS substrate base, on which three 1:1 ratio P3HT:PCBM blend devices were ultimately mounted. Table 6.1 gives a detailed description of the samples.

Table 6.1 *Description of the samples*

Sample name	**Spin-coating speed (rpm)**	**Active layer thickness (nm)**
S_1	**1000**	**84.5**
S_2	**2000**	**77.1**
S_3	**3000**	**69.4**
S_4	**4000**	**61.5**

Thicknesses of the active layers were measured by surface profilometer, which in another way confirmed the achievement of different active layer thicknesses through different casting speeds. We considered the active film thickness to be a crucial parameter in determining the efficiency of our nanocomposited P3HT:PCBM based solar cell, because it has a bearing on almost all parameters contributing to the performance of the organic solar cell. Some of the effects may, for example, aggravate recombination. In the following sections, we present a summarised report of our findings on the studies of active (that is, 1:1 bulk heterojunction blend of P3HT:PCBM) layer thickness variation effect on the performance of ITO/PEDOT:PSS/P3HT:PCBM/Al configured device.

6.2 Results and discussion

6.2.1 Influence of active layer thickness on optical characteristics of spin-coated polymer-fullerene based BHJ solar cells of ITO/PEDOT:PSS/P3HT:PCBM/Al configuration

The absorbance data used to produce the absorption spectra displayed in Figure 6.1 were obtained through the use of a Varian Cary 500 - Scan UV-Visible spectrophotometer.

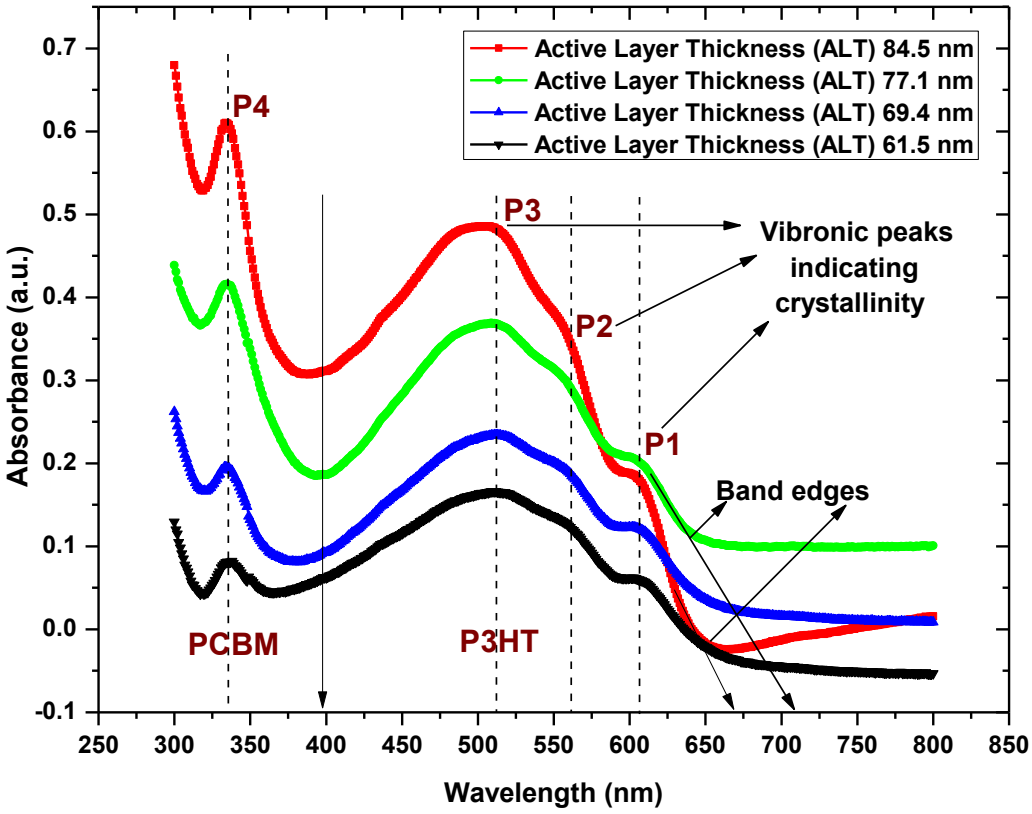

Figure 6.1 *Ultraviolet-visible absorbance spectra due to photoactive P3HT:PCBM blend layers of differing thicknesses*

The spectra are due to the alluded experimental 1:1 P3HT:PCBM composite layers of thicknesses 84.5 nm, 77.1 nm, 69.4 nm and 61.5 nm. As the figure shows, the absorption characteristics of the composite films were investigated in the wavelength range 300 – 800 nm. All the spin-coated films with different thicknesses showed their main peaks around 512 nm. Furthermore, a significant increase in absorbance with increase in active layer thickness is evident. This is expected, because in our case, greater thickness nears the recommended order of

the absorption length (approximately 100 nm) for conjugated polymers. In addition, increased layer thickness increases the number of active molecules which have the potential to capture more incoming incident photons. However, the setback is that for active layer thickness larger than the diffusion length of the excitons (about10 nm in disordered and semi-crystalline polymers) recombination increases.[15] This fuels increased recombination inside the conjugated P3HT polymer. However, loss compensation may be enhanced to a small extent by those few photons with wavelengths in the weakly absorbing region, which may penetrate further into the active film and reach those domains with favourably high densities of P3HT:PCBM interfaces for optimum dissociation of the excitons. All four absorption spectra (Figure 6.1) of the P3HT:PCBM active layers display typical absorption characteristics that are divided into two main regions labelled P3HT and PCBM in Figure 6.1. The P3HT region which spans from approximately 650 – 400 nm is attributed to absorption by the main absorber polymer (the electron donor P3HT). The second region corresponding to wavelengths below 400 nm is due to absorption by the PCBM molecules.[14], [16]

The spectral region corresponding to P3HT absorption exhibited three different bands. The main peak P3 was around 512 nm and is attributed to the $\pi - \pi^*$ electronic transition within the P3HT main polymer.[17-18] This peak showed a small blue shift with increase in the thickness of the active layer. This behaviour could be ascribed to the interruption of the structure and orientation for P3HT chain ordering[14], [19] due to more thickening of the active layer. The blue shift could as well be due to phonon generation or vibronic interaction with the exciton. P1 peaks ~~is~~ are attributed to the absorption of the inter-chain stacking which suggests an improvement in the chain ordering and band P2 is attributed to the extended absorption of the conjugated polymer.[14], [20] The absorption band below 400 nm (P4 region) is due to absorbance associated with PCBM. No peak shift showed in P4 region. However there was delayed transition from P3HT dominated absorbance to that due to PCBM, as shown by the blue shift of other troughs relative to the 77.1 nm thick layer, which showed no shift from the usual. The non-shift of the 77.1 nm layer trough might indicate nearness of its thickness to the optimal thickness under the given fabrication settings.

While the absorbance curves help in giving idea about the proportion of light absorbed by the thin films, they also provide qualitative information about the crystalline vibration as well as the

band gap energy of the polymer.[21] In Figure 6.1 curves of the optical absorbance of the P3HT polymer region, we identify the vibronic progression which is characterised by vibronic peaks. The appearance of vibronic progression means that there is a coupling vibrational mode in the conjugated polymer P3HT, which results in excitation from the ground state to the excited state or emission from the excited state down to the ground state.[21] The vibronic peaks indicate the dominant optical absorption and their corresponding transition. These peaks depend on the crystalline property of the polymer. The sharper the vibronic peak, the greater is the crystallinity of the polymer. With amorphous phase, these signature vibronic peaks disappear from the absorption spectrum. Our results show diminished P2 vibronic peaks, which suggest less crystallinity of the polymer in the region. P1 and P3 regions show sharper vibronic peaks indicative of comparatively higher crystallinity. P3HT chains usually exhibit highly crystalline features facilitated by their self-orientation into two dimensional sheets.[22] The degree of P3HT crystallinity could be explained by the Head-Tail orientation as opposed to Head-Head orientation. The higher degree of crystallinity is attributed to the ordered packing of P3HT stacks in the chains.[23] P3HT crystallinity can improve the performance of the solar cell by enhancing the charge carrier transport through the formation of percolation pathways leading to higher charge carrier mobility and resulting in enhancement of device efficiency.[24]

6.2.1.1 Photoluminescence analysis

We analysed photoluminescence behaviour of our samples. Photoluminescence is light emission from any matter after absorption of photon(s). As such, it is a loss mechanism which may proliferate in a polymer-fullerene device and therefore needs minimization. Based on the optical behaviour exhibited by our sample devices in Figure 6.1, we expect increase in photoluminescence with increase in active layer thickness as approximated in Figure 6.2, because as more light absorbing molecules are made available by the greater thickness, the concentration of the luminescent species also rises. With this assumption, we add that photoluminescence quenching (which is a counter process to minimise photoluminescence) should therefore increase with more thinning of the active layer. Such behaviour demonstrates the existence of well-mixed states of electron donor (P3HT) and acceptor (PCBM) that in turn facilitate rapid transfer of charges.[25-26] In Figure 6.2, we approximate the assumed photoluminescence quenching behaviour for our devices by noting that in the plot (Figure 6.2),

lower values of photoluminescence, which are associated with thinner active film thicknesses, are indicative of higher luminescent quenching as film thickness decreases.

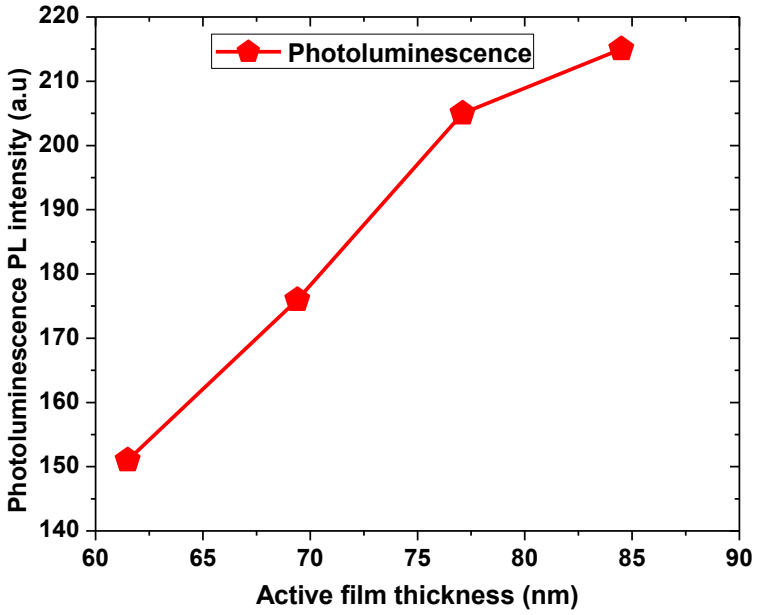

Figure 6.2 *Photoluminescence quenching approximations for different active layer thicknesses*

We add that photoluminescence vis-à-vis photoluminescence quenching should be related to the reduction in internal quantum efficiency as the incident light intensity becomes large and should therefore be crucial determinant of the threshold open circuit voltage at which efficiency starts to decrease ($V_{thresh\ eff,\ decay}$) in polymer-fullerene devices.

As the active film thickness reaches 84.5 nm, about half the incident light between 350 and 610 nm is absorbed in one optical path. This spectral response is not that favourable, because of significant non-absorption losses (50%), which we ascribe to imperfections associated with device architecture in ambient.

6.2.1.2 Extinction coefficient investigation

From Beer's law, the absorbance α of incident light by a sample depends on the concentration *c* of the absorbers, the optical path length *L* of the light through the sample and the extinction coefficient ε. The extinction coefficient (or molar absorptivity) is a parameter defining how

strongly a substance absorbs light at a given wavelength per molar concentration (or mass density). Therefore mathematically

$$\alpha = cL\varepsilon \qquad \text{from which} \qquad \varepsilon = \frac{\alpha}{cL} \tag{6.2}$$

A high value of the extinction coefficient ε means that the substance absorbs light strongly at the particular wavelength.

In light of this, we investigated the variation of extinction coefficient with wavelength λ of the incident light (300 – 650 nm) for the different active layer thicknesses and obtained the absorption spectra shown in Figure 6.3.

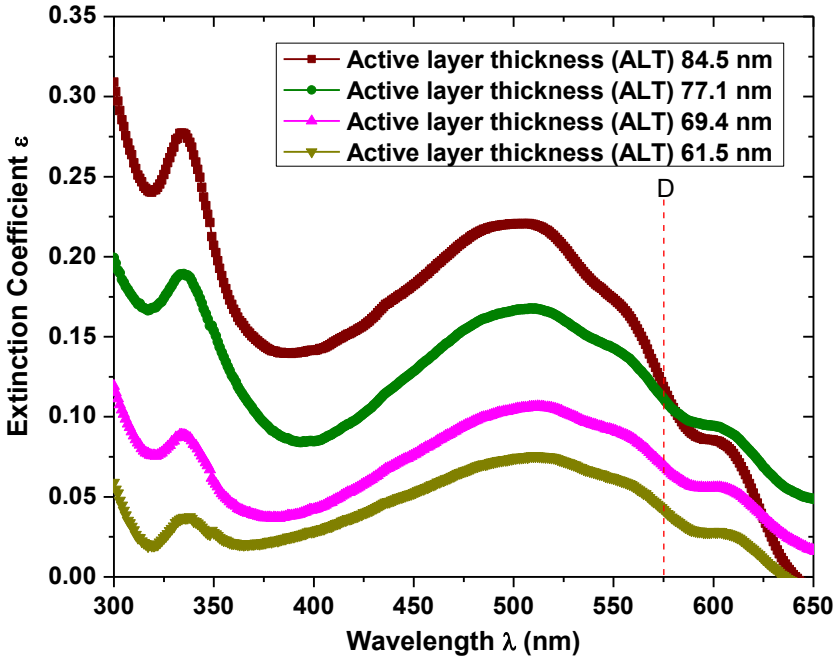

Figure 6.3 *Variation of extinction coefficient ε with 1:1 P3HT:PCBM blend (active) layer thicknesses in ITO/PEDOT:PSS/P3HT:PCBM/Al devices*

The extinction coefficients were calculated using equation (6.2) and assuming a typical absorption length (optical path length) *L* of conjugated polymers equal to 100 nm and concentration of 2.2% of P3HT:PCBM blend.[27] We note from Figure 6.3 that the extinction coefficients are generally low for all the devices. The highest, corresponding to the 84.5 nm active film device, is only of peak value of about 0.225 at ~ 510 nm wavelength. Such low ε values suggest weak absorbing profiles attributed to short-comings in the manufacturing processes. Comparatively, we observe that higher values of ε are correspondingly associated

with thicker active layer. This is due to the increased number of P3HT molecules available in the active layer to undertake photo-absorption. Furthermore, we found the value of the extinction coefficient to increase with active layer thickness in the wavelength range 300 – 575 nm. This is the region corresponding to the left of the demarcation line D in Figure 6.3. The high value of extinction coefficient in the absorption band is due to the crystallization of the polymer material leading to more $\pi - \pi^*$ absorption.[26]

In Figure 6.4, we display the variation of maximum (peak) values of extinction coefficient (extracted from Figure 6.3 in the principal absorber P3HT region) with active layer thickness and pose the need to optimize the active layer thickness vis-à-vis recombination losses to high extinction coefficients.

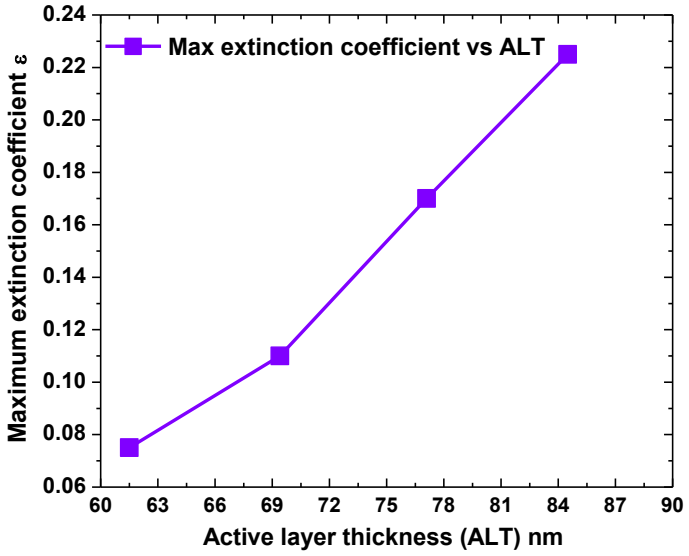

Figure 6.4 *Maximum values of extinction coefficients for different active layer thicknesses*

However, while the importance of optimization of active film thickness needs no over-emphasis, it currently appears difficult to establish universally optimum thickness values, because of the various competitive processes which come into play in coupling with variations in the construction settings, constraints and circumstances.

6.2.2 An analysis of transformations in the surface morphology of P3HT:PCBM film blend for differing film thicknesses (2D – treatment)

The performance of organic solar cells based on the blend of regioregular poly(3-hexylthiophene) (P3HT) and phenyl-C61-butyric acid methyl ester (PCBM) is strongly influenced by the morphology of the active layer on the nanoscale level. [28-31] As such an insight into the surface and internal structures of the photoactive blend layers incorporated in the organic solar cells is crucial, because information on lateral, vertical or three-dimensional morphology changes and contributions to the performance of the devices can be provided. Morphology generally refers to the packing (for example, crystalline packing configuration) of polymer domains, which encompass the spatial dimensions of the donor acceptor phases. The challenge in bulk heterojunction solar cells is to arrive at an optimal tradeoff in the active blend, between exciton dissociation (where a fine-grained phase segregation is perfect) and charge transport (where a bilayer configuration is optimum).[28-30] This implies that the ideal is a bicontinuous composite of donor and acceptor with maximum interfacial area for exciton dissociation and a mean domain size commensurate with the exciton diffusion length (5 – 10 nm).

It is for this stringent requirement that we studied the surface morphology of the experimental 1:1 P3HT:PCBM composite films of different thicknesses in bulk heterojunction ITO/PEDOT:PSS/P3HT:PCBM/Al devices using the Veeco Dimension 3100 Atomic Force Microscope (AFM) in the tapping mode. We delimited our study to the lateral perspective and produced the images shown in Figure 6.5. No obvious changes were observed in film morphology as a result of change in active layer thickness. All the samples show varied topological features appearing as white enclaves in the figure. The 84.5 nm active layer thickness seems to possess large deviation of height variations on a lateral scale. In the 77.1 nm and 69.4 nm samples, the density of height variations is reduced. It is the 77.1 nm thick blend layer which shows the least roughness variations as well as the comparatively improved crystallization of P3HT together with seemingly conducive PCBM phase aggregation. Also, of the samples investigated, it is this 77.1 nm active layer thickness which exhibited comparatively optimum values of parameters of merit.

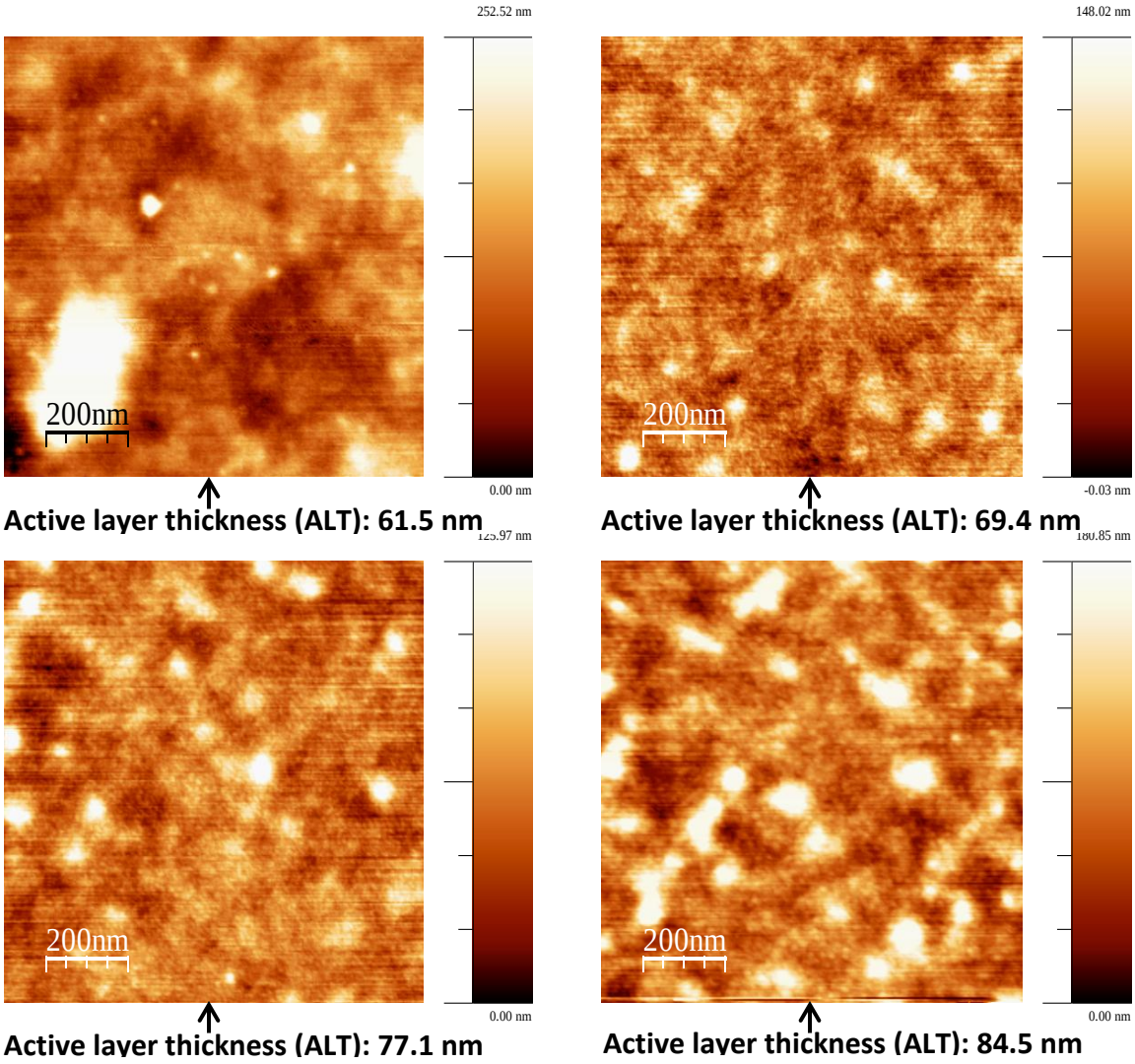

Figure 6.5 *AFM images of P3HT:PCBM active layers for different thicknesses*

P3HT:PCBM crystallinity improves the solar cell performance by assisting charge carrier transport through the forming of percolation pathways which lead to higher charge carrier mobility and thus enhanced device efficiency.[31-34] A good interfacial morphology can prevent current leakage and surface recombination.

6.2.3 Electrical behaviour analysis of P3HT:PCBM blend devices for varying active film thicknesses

6.2.3.1 Characteristic parameters of merit ascribed to the cells

In Figures 6.6 (a) and (b), we respectively show our obtained J(V) and output power versus voltage behaviour characteristics of the experimental ITO/PEDOT:PSS/P3HT:PCBM/Al solar cells of the different active layer thicknesses (ALTs) displayed in the plot legends.

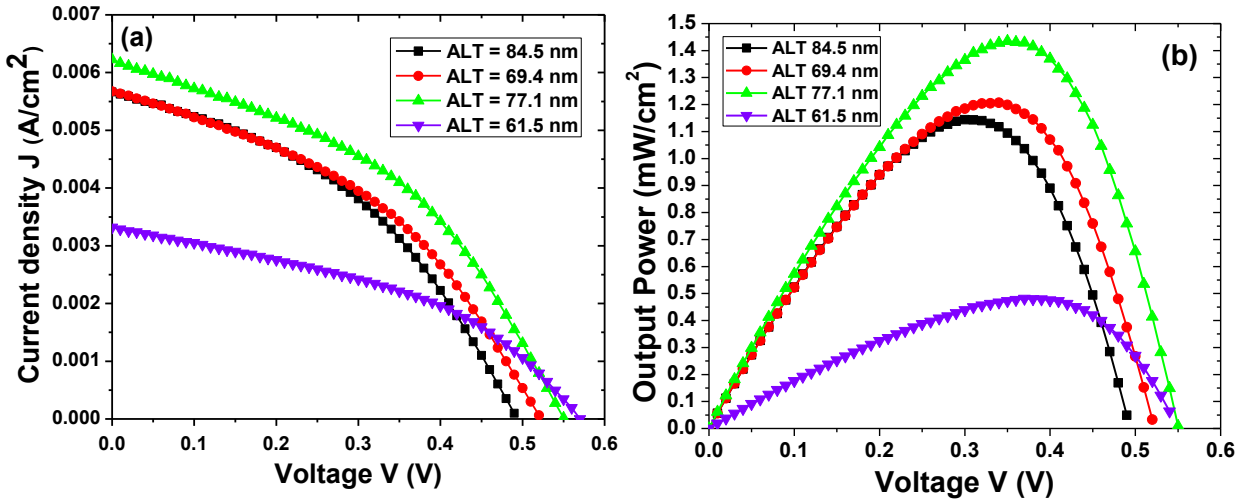

Figure 6.6 (a) ***J(V)*** *and* (b) ***output power*** *characteristics for different active layer thicknesses (ALTs) under solar simulated white light illumination intensity of 100 mW/cm^2 incident on the ITO/PEDOT:PSS/P3HT:PCBM/Al devices*

The photovoltaic (PV) measurements were carried out under AM1.5 solar simulator source of intensity 100 mW/cm^2. Figure 6.6 measurements are from **'as cast'** devices belonging to batches different from those of Table 6.2, which have also been analysed and included for reliability check. With reference to Figure 6.6 (a) measurements, the highest short circuit current density J_{sc} of approximately 0.0063 A/cm^2 is that due to the 77.1 nm active layer thickness device. The peculiarity may partly be attributed to the lowering of interfacial barriers.[14] This high J_{sc} value is also consistent with the comparatively improved morphology shown for the device. Such morphology minimises charge carrier recombination. On the downside, the lowest J_{sc} value of about 0.0034 A/cm^2 belongs to the device with the thinnest active layer thickness of 61.5 nm. The low current density measurement should partly be due to the comparatively high series

resistance (R_s) evident in the corresponding 'as cast' device in Table 6.2. High series resistance is a problematic characteristic for thinner active layers.

Figure 6.6 (b) shows the highest output power to be emanating from the 77.1 nm thick active layer. As Table 6.2 also exhibits, the best PV performance is from the 77.1 nm active layer thickness device. For comparison, as cast performances are displayed adjacent to the corresponding annealed devices with the same active layer thickness. As expected, parameter values for the as cast devices, are generally lower than those of their annealed counterparts.

Table 6.2 *Characteristic output values of ITO/PEDOT:PSS/P3HT:PCBM/Al solar cell devices of differing thicknesses at 300 K under shown white light illumination*

Active Layer Thickness (nm)		84.5		77.1		69.4		61.5	
Device State		As Cast	Anld	As Cast	Anld	As Cast	Anld	As Cast	Anld
100 mW/cm^2 (AM 1.5)	V_{oc} (V) ± 0.02	0.49	0.50	0.55	0.56	0.53	0.53	0.55	0.59
	Abs. I_{Sc} (mA) ± 0.02	0.40	0.45	0.34	0.50	0.22	0.45	0.17	0.38
	Abs. J_{Sc} (mA cm^{-2}) ± 0.02	5.04	5.67	4.19	6.23	2.74	5.68	2.11	4.74
	P_{max} (mW cm^{-2}) ± 0.004	0.813	1.144	0.750	1.435	0.473	1.207	0.379	1.097
	Fill Factor ± 0.0003	0.3292	0.4040	0.3258	0.4116	0.3257	0.4013	0.3260	0.3924
	PC Efficiency (%) ± 0.05	0.81	1.14	0.75	1.44	0.47	1.21	0.38	1.10
	Series Res. (Ω) ± 7	75	40	112	41	43	44	215	52
	Parallel Res. (Ω) ± 7	229	229	229	200	320	178	533	267
0 < I < 7.5 mW/cm^2	$V_{oc\ thresh\ eff\ decay}$ (V) ± 0.02	0.41	0.40	0.45	0.46	0.48	0.44	0.49	0.55

In addition, we investigated the variation of V_{oc} and efficiency with incident light intensity for different active layer thicknesses (ALTs) and obtained the results shown in Figure 6.7. The display enabled us to note the threshold open circuit voltages ($V_{oc\ thresh\ eff\ decay}$) at which

efficiency corresponding to each active layer thickness starts to decrease. Such threshold values are shown for a different batch of experimental devices in Table 6.2.

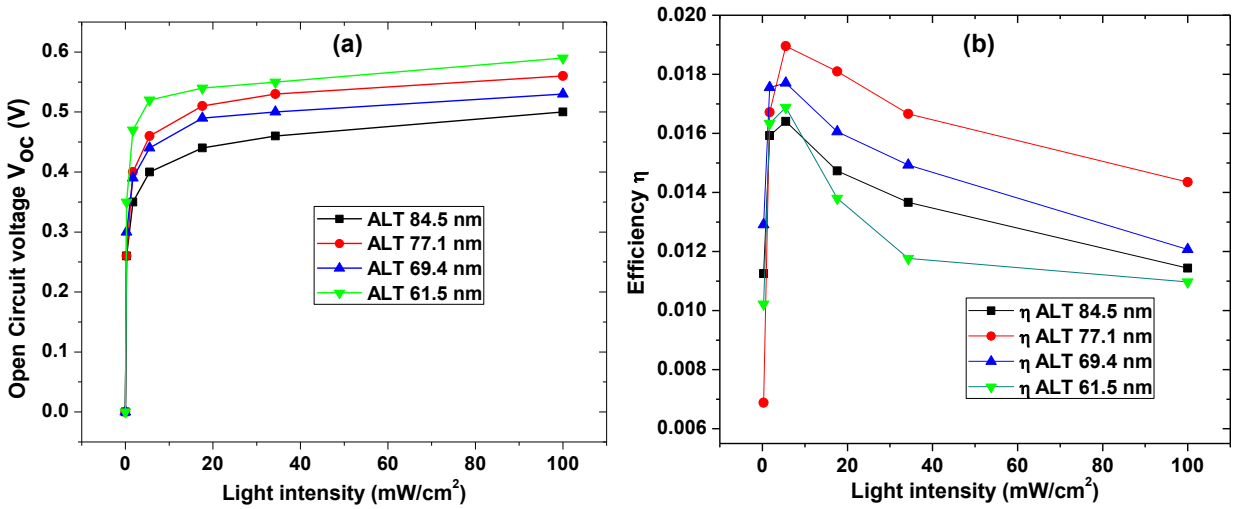

Figure 6.7 *Variation of* (*a*) V_{oc} *and* (*b*) *efficiency with incident light intensity for different active (thin) layer thicknesses (ALTs)*

The superiority of the ALT 77.1 nm device is spotted in Figure 6.7, in that it shows the greatest rise in efficiency before the threshold voltage for onset of its decrease is reached. Furthermore, the 77.1 nm film thick device exhibits the highest efficiency under the commonly employed operational intensity of 100 mW/cm^2. The sharp drop in the efficiency of the 61.5 nm ALT device must be due to several factors whose drawback effects become more pronounced with decrease in thinness. Among the main contributors is the acute rise in series resistance due to the unavoidable presence of pinholes associated with fabrication in ambient. Other contributors should include shunt (parallel) resistance (due to large leakage across the junction) and probably morphology. It is the morphology that mainly determines the severity of recombination current in the space charge region of the cell and the reverse saturation current of the junction. All such activities also impact negatively on the fill factor *(FF)* and hence the efficiency.

6.2.3.2 Parasitic resistances in sandwiched P3HT:PCBM nanocomposited photoactive films of different thicknesses in solar cell devices

In Figure 6.8 we show how the parasitic resistances (namely, series resistance R_s and shunt/parallel resistance R_{sh}) and maximum power vary for different active layer thicknesses of

1:1 P3HT:PCBM blends in our *ITO/PEDOT:PSS/P3HT:PCBM/Al solar cells*. We note that the optimum power output (of ~1.4 mW/cm^2) is associated with the 77.1 nm thick active layer device, which displays R_s and R_{sh} values of 40.9 Ω and 200.0 Ω respectively.

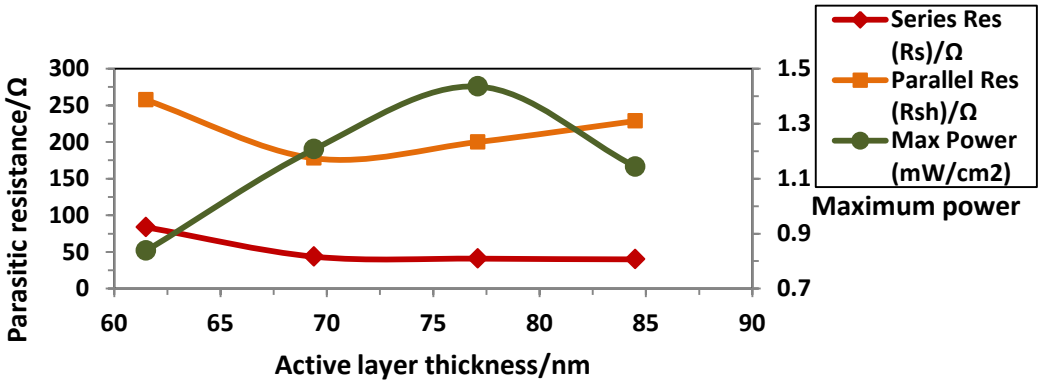

Figure 6.8 *Variation of parasitic resistances and maximum power output with differing active layer thicknesses of the ITO/PEDOT:PSS/P3HT:PCBM/Al solar cells*

The competitive interaction among R_s, R_{sh} and the diode (characteristics) P3HT:PCBM blend solar cell plays an important role in determining how current flows in the device. Since R_s induces a voltage drop on itself, it means that it in a way regulates the voltage drop on the diode. The desire is to have a very large (if not all) voltage drop on the diode. Therefore, the larger the series resistance R_s is, the higher is the potential drop across it and the less is the potential drop on the diode. This results in slower increase in current density J with applied voltage V and a show of less square-ness of the J(V) curve, which implies lower fill factor (FF) and (hence) efficiency η, because $\eta = \frac{J_{sc} V_{oc} FF}{P_{in}}$, where, P_{in} is the incident irradiance.

R_s should therefore be very small.[35-40]

By ratio dividing the photogenerated voltage V, R_s basically determines where the photogenerated current principally flows, to the diode or to the external load. In Figures 6.9 (a) and (b) we present sketches of the ideal and practical solar cells to help deduce the effect of R_s.

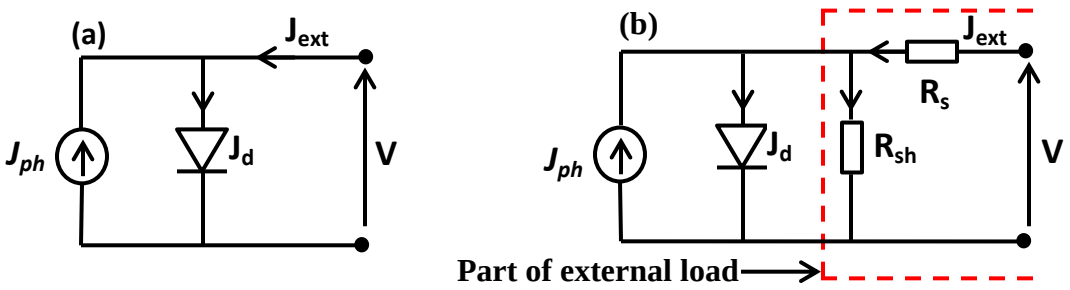

Figure 6.9 *Equivalent circuits for (a) an ideal and (b) a real (practical) solar cell. J_{ph} is the photogenerated current density, J is the current density flow in the external load, R_s and R_{sh} are the series and shunt resistances respectively, J_d is the current density through the diode and V is the applied voltage*

If *V* is the photogenerated voltage, the smaller R_s becomes, the more is the potential drop on the diode (that is, the organic solar cell in this case) and therefore the greater is the portion of the photogenerated current J_{ph} flowing into the diode, which is what we want. The counter side is that if R_s is large, the current through the diode would be very small and this would imply a small potential drop on the diode. The ideal R_s would be an infinitesimally small (zero) R_s, which is a requirement not met by our samples due to numerous drawback factors, some of which are, imperfections associated with ambient fabrication and un-optimized solvent evaporation rate. However, while we acknowledge series resistances R_s in our devices to be contributions of the following four parts: (1) bulk resistance of the active layer and functional layers in the film, (2) bulk resistance of the electrodes, (3) contact resistance of every interface in the device and (4) probe resistance;[40] we however assume the dominant contribution to be that due to (1), the P3HT:PCBM blend active layer.

Shunt resistance R_{sh} corresponds to parallel resistance shown in the equivalent circuit of the solar cell in Figure 6.9. It indicates current losses in the cell. Some of such losses are: current leakage from the edge of the cell, current leakage from the pinholes in the active film [40] or current leakage due to charge carrier flow into traps. Therefore, R_{sh} has the effect of 'thieving' a portion of the photogenerated current by way of dividing and sharing the photogenerated current with the diode. Ideally, R_{sh} should be infinitely large in order for it to effectively block any of the photogenerated current from flowing into it and be lost, for example, as heat. If the shunt resistance was to exhibit this perfect behaviour practically, then it would be assisting in ensuring

that all the photogenerated current passes through the preferred diode, but the problem is that it does not do so in reality. Practically, R_{sh} is not large enough to warrant neglect of current through it. A case in-point is of our devices (in Figure 6.9), which show shunt resistances of 228.6 Ω, 200.0 Ω, 177.8 Ω and 257.3 Ω for the active layer thicknesses 84.5 nm, 77.1 nm, 69.4 nm and 61.5 nm respectively under 100 mW/cm^2 white light illumination. These are small R_{sh} values when compared with the threshold R_{sh} of 6×10^3 Ω/cm^2 found elsewhere[40] and above which the current through such R_{sh} can be considered negligible. As a result, the current flowing through each of the shunt resistances cannot be ignored and the associated $J(V)$ curves deviate from squareness to show low *FF* values (which imply low efficiencies in general). Also, if R_{sh} is small, the current under reverse bias will then flow into R_{sh} and current flow in the external load will increase linearly with increasing reverse voltage. Referring to Figure 6.8, it is also interesting to note that optimum power output is shown by the device configured with the 77.1 nm active layer thickness.

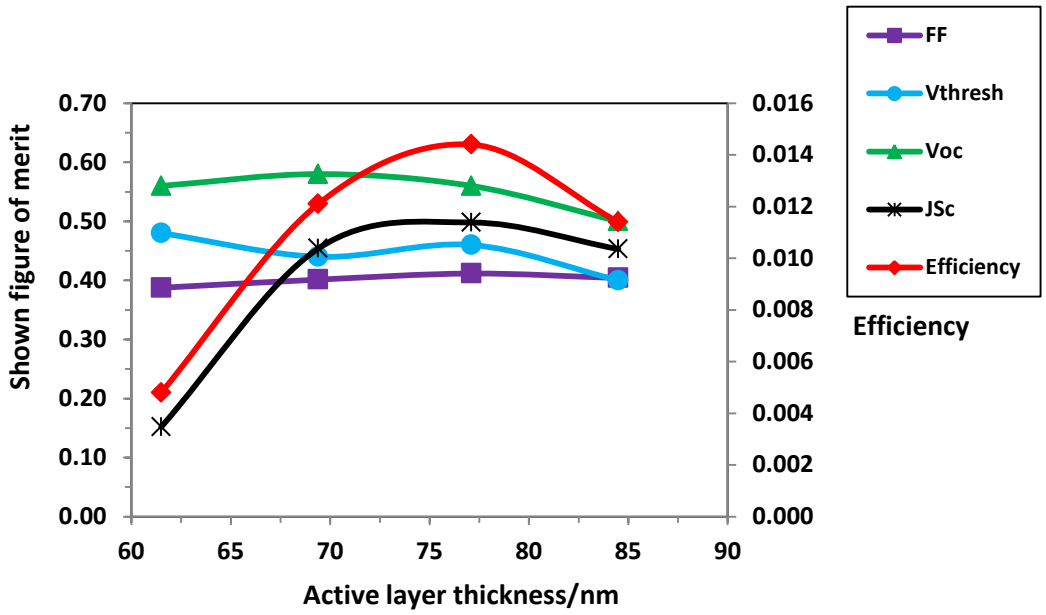

Figure 6.10 *Variations of parameters of merit – V_{oc}, J_{sc}, efficiency η, fill factor (FF) and $V_{thresh\ eff\ decay}$ with active layer thickness for the P3HT:PCBM blend based solar cell*

In Figures 6.10 and 6.11 we present graphical and pictorial summaries of the values of parameters of merit ascribed to the nanoscale composite devices constituting our sample. The parameters are: open circuit voltage (V_{oc}), short circuit current (J_{sc}), efficiency (η) and fill factor

(*FF*). Optimal parameter value measurements have been found to favour the 77.1 nm active layer thickness devices, which on average have displayed significantly better photovoltaic performance that is supported by the relatively higher efficiency and fill factor. The better performance could mainly be due to improved morphology.

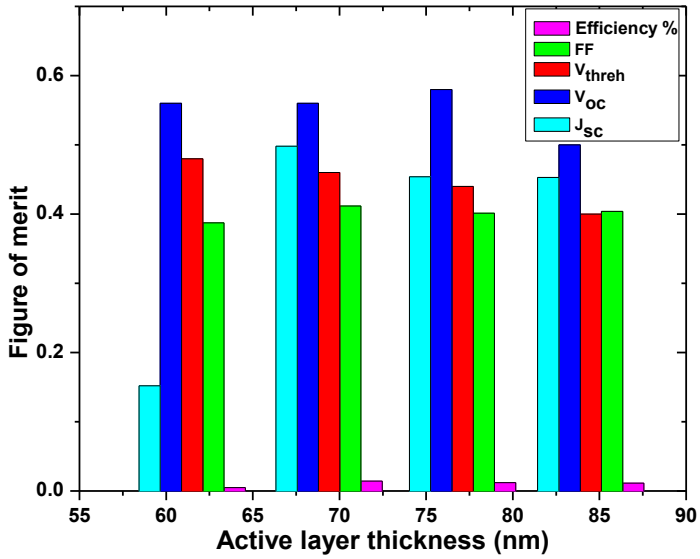

Figure 6.11 *Pictorial representations of figures of merit summarising the electrical performance of the devices with differently thickened active layers*

In view of the values of the opto-electrical properties displayed by the various active excitonic films, we assert that under the same settings, the optimal active layer thickness in bulk heterojunction 1:1 P3HT:PCBM blend devices of the configuration ITO/PEDOT:PSS/P3HT:PCBM/Al, is of the order 77.1 nm.

6.2.3.3 Dark Characteristics

6.2.3.3.1 Dark current density-voltage characteristics of the different ALT devices

Figure 6.12 shows the dark J(V) characteristics of our ITO/PEDOT:PSS/P3HT:PCBM/Al solar cell with different thicknesses of the active layers.

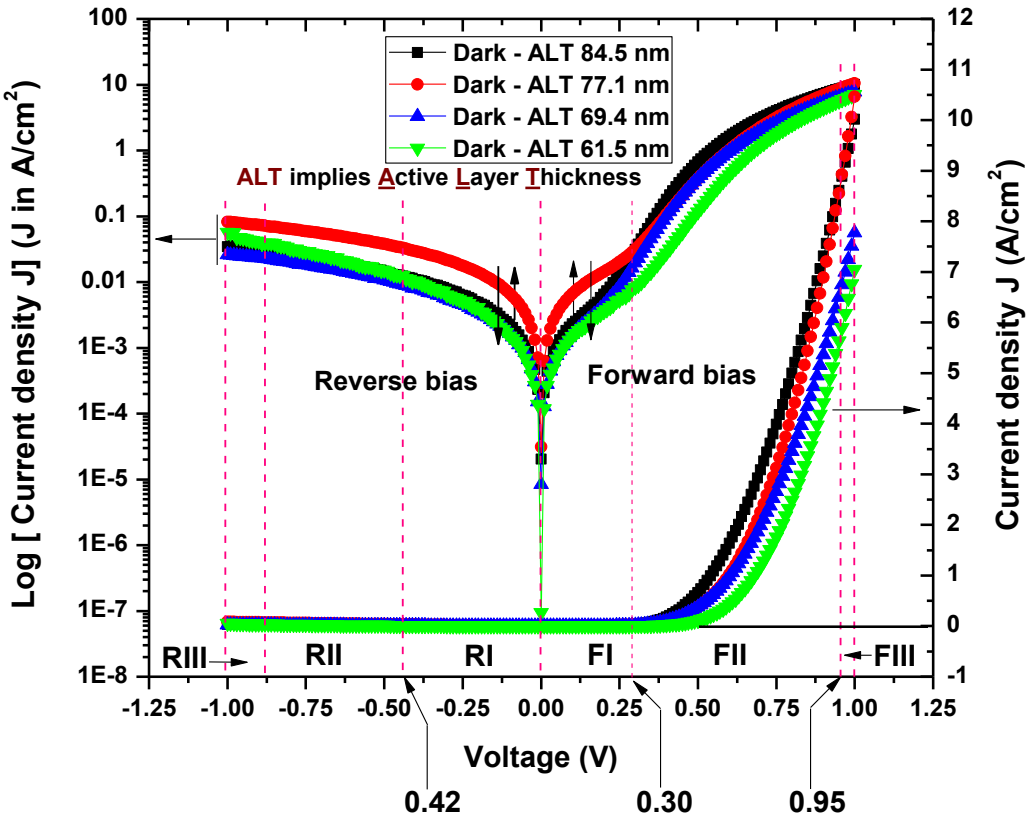

Figure 6.12 *Dark J(V) characteristics of 1:1 P3HT:PCBM composite devices with different active layer thicknesses in the range 61.5 nm to 84.5 nm, where J (or J_D) is the dark current density, V is the bias voltage, FI, FII and FIII identify regions under forward bias which exhibit peculiar current density behaviour characteristics, wherein RI, RII and RIII relate to the reverse bias counterparts*

We identify five regions (FI, FII, FIII, RI, RII and RIII) which exhibit peculiar current behaviour characteristics. The dashed red lines mark approximate boundaries for the corresponding regions under dark J–V curves and the dark semi-logarithmic plots. The surfacing of many peculiar regions shows that there are many competing processes within the active P3HT:PCBM films. In

each of the identified regions, the dark current density, J (or J_{dark}), at a given voltage increases for the different thicknesses according to the following order:

Region FI → $\mathbf{J_{(ALT\ 61.5\ nm)} < J_{(ALT\ 69.4\ nm)} < J_{(ALT\ 84.5\ nm)} < J_{(ALT\ 77.1\ nm)}}$

Region FII → $\mathbf{J_{(ALT\ 61.5\ nm)} < J_{(ALT\ 69.4\ nm)} < J_{(ALT\ 77.1\ nm)} < J_{(ALT\ 84.5\ nm)}}$

Region FIII → $\mathbf{J_{(ALT\ 61.5\ nm)} < J_{(ALT\ 69.4\ nm)} < J_{(ALT\ 84.1\ nm)} < J_{(ALT\ 77.1\ nm)}}$

Region RI → $\mathbf{J_{(ALT\ 61.5\ nm)} \approx J_{(ALT\ 69.4\ nm)} < J_{(ALT\ 84.1\ nm)} < J_{(ALT\ 77.1\ nm)}}$

Region RII → $\mathbf{J_{(ALT\ 69.4\ nm)} < J_{(ALT\ 61.5\ nm)} \approx J_{(ALT\ 84.1\ nm)} < J_{(ALT\ 77.1\ nm)}}$

Region RIII → $\mathbf{J_{(ALT\ 69.4\ nm)} < J_{(ALT\ 84.1\ nm)} < J_{(ALT\ 61.5\ nm)} < J_{(ALT\ 77.1\ nm)}}$

These results can be explained in terms of the modifications of the charge carrier injection barriers as well as changes in the morphology instigated by the different thicknesses of the active layers.

All the dark J-V curves for the different active layer thicknesses in Figure 6.12 are non-symmetric and characteristic of diodes with different rectification factors/ratios. Rectification factor RF (or rectification ratio RR) of a diode **at a given voltage** refers to the ratio of the forward bias current (or current density) to the reverse bias current (or current density) measured at the same absolute bias voltage. We determined the respective rectification ratios at 1.00 V and found them to be: ~291 for the 84.5 nm ALT, ~304 for the 77.1 nm ALT, ~297 for the 69.4 nm ALT and ~124 for the 61.5 nm ALT. This confirms the existence of large and different potential energy barriers at the metal-active layer interfaces of the devices under reverse bias.

The J_{dark} – V characteristics can be described by the equation

$$J_{dark} = J_0\left\{\exp\left(\frac{qV}{nk_BT}\right)\right\} \text{ for case } \frac{V}{T} >> 0 \qquad (6.3)$$

where V is the applied voltage, n is the ideality factor of the diode, k_B is the Boltzmann constant, J_0 is the reverse saturation density, T is the absolute temperature and q is the elementary charge. We note that the optimum J_{dark} values in the identified forward and reverse bias regions prevail

more in the 77.1 nm active layer thickness devices, which should therefore be having comparatively smaller barrier heights in the dark than others.

In Figure 6.13 (a) we used the dark and 100 mW/cm^2 illumination curves for the 77.1 nm ALT device to show the different current behaviour regions for our devices. The devices show compliance with the practical solar cell behaviour predicted by the equivalent circuit equation (6.4), which takes parasitic resistances R_s and R_{sh} into consideration.

$$J = J_0\left[\exp\left(\frac{q(V - JR_s)}{nk_BT}\right) - 1\right] + \frac{V - JR_s}{R_{sh}} - J_{ph} \qquad (6.4)$$

In Eq. (6.4), J is the recorded current density on the external load, J_{ph} is the photogenerated current density and k_B is the Boltzmann constant.

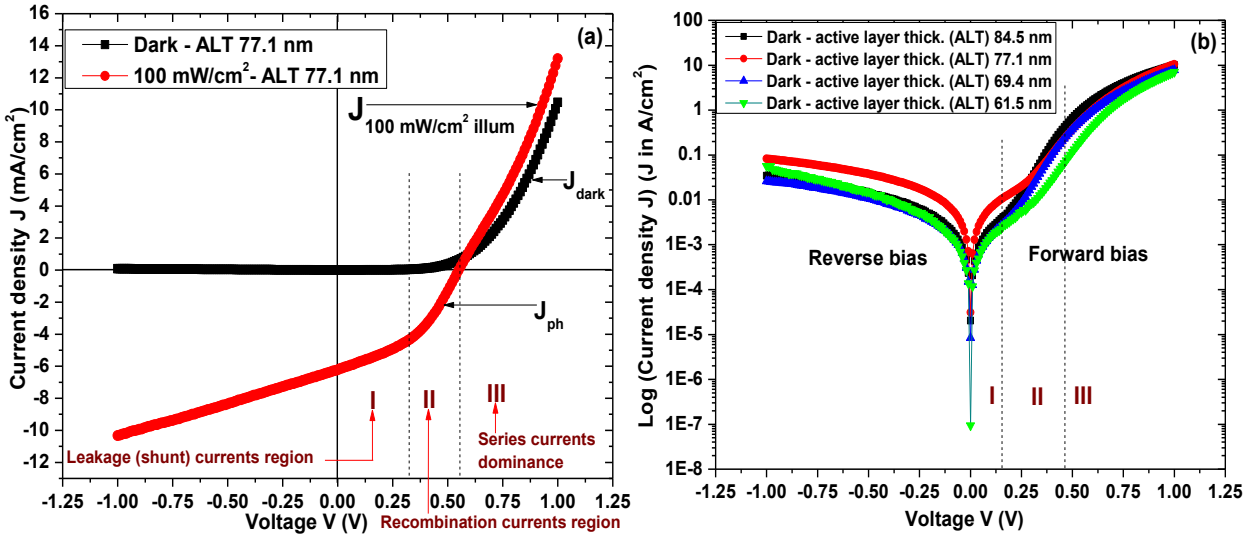

Figure 6.13 *(a) Typical J vs V plot for the ALT 77.1 nm device under dark and simulated 100mW/cm^2 (b) Regions of merit for the different ALTs in semi-logarithmic representation*

According to Eq. (6.4), the J(V) curve of the solar cell is divided into three regions, both in the dark and under illumination.[41-42] The equivalent regions for the different thicknesses in semi-logarithmic representation under dark are shown in Figure 6.13 (b). At low positive voltages (corresponding to Region I in Figures 6.13 (a) and (b)) the J(V) curves are straight lines with slopes determined by the $1/R_{sh}$. If R_{sh} decreases, the slope of the J(V) curve increases. This makes the *J(V)* curve around J_{sc} become less parallel to the *x*-axis, thus reducing the squareness,

hence the fill factor and efficiency of the device. At intermediate positive voltages corresponding to Region II, the J(V) curves for the different thicknesses are exponential lines in which the J(V) characteristics are limited (or determined) by the diodes whose practical representations are described by the equation

$$J = J_0\left[\exp\left(\frac{qV}{nk_BT}\right)-1\right] \qquad (6.5)$$

If the flow of currents in junctions is by diffusion only, then n = 1. If currents in the device are dominated by recombination, then n = 2 and where diffusion current and recombination currents both exist, n is in the range 1 – 2.[43] At room temperature, there are only two variables in equation (6.5), n and J_0. The ideality factor n is dominated by exciton dissociation and recombination in the device and J_0 is reported to be related to the difference between the donor HOMO and the acceptor LUMO (ΔE_{DA}) of the materials.[40] At high voltages, which correspond to Region III, the *J(V)* curve is a second straight line, with the slope controlled by 1/*Rs* (where $1/R_s$ is equal to dJ/dV).

6.2.3.3.2 Space charge limited conduction (SCLC) for different active layer thickness devices

We studied the bulk transport mechanisms in ITO/PEDOT:PSS/P3HT:PCBM/Al photoactive devices through analysis of the space charge limited conduction (SCLC) processes for charge transport in the devices formed of the differently thickened nanoscale 1:1 P3HT:PCBM active layers. To this effect, we plotted the dark J(V) characteristics in double logarithmic scale under forward bias for the different active layer thicknesses and produced the family of curves shown in Figure 6.14, which we then used to investigate the diode behaviour of the devices.

All the obtained curves subscribe to a power law dependence of the proportionality form $J \propto V^m$ (that is, $J = cV^m \Rightarrow Log\,J = m\,Log\,V + Log\,c$), where m is the gradient that takes different values over different applied voltage regions and c is a constant. We identified three peculiar bulk transport (electrical) behaviour regions labelled I, II and III in Figure 6.14. Region I is the low voltage region, located between 0 and approximately 0.18 V for the devices formed of active layer thicknesses 61.5 nm, 69.4 nm and 84.5 nm. The 77.1 nm active layer thickness (ALT)

device exhibits an extension of the region (that is, region I) to approximately 0.24 V. This is the region corresponding to i → e for the 77.1 nm ALT in Figure 6.14. We found *m* for each of the thicknesses in this linear region to be about 1.3. This value can be approximated to *m* = 1, which shows that charge transport in this region conforms to ohmic behaviour and can be represented by the equation[14], [44]

$$J = qn\mu V/d \tag{6.6}$$

where *n* is the hole concentration, μ is the charge mobility and *d* is the active film thickness.

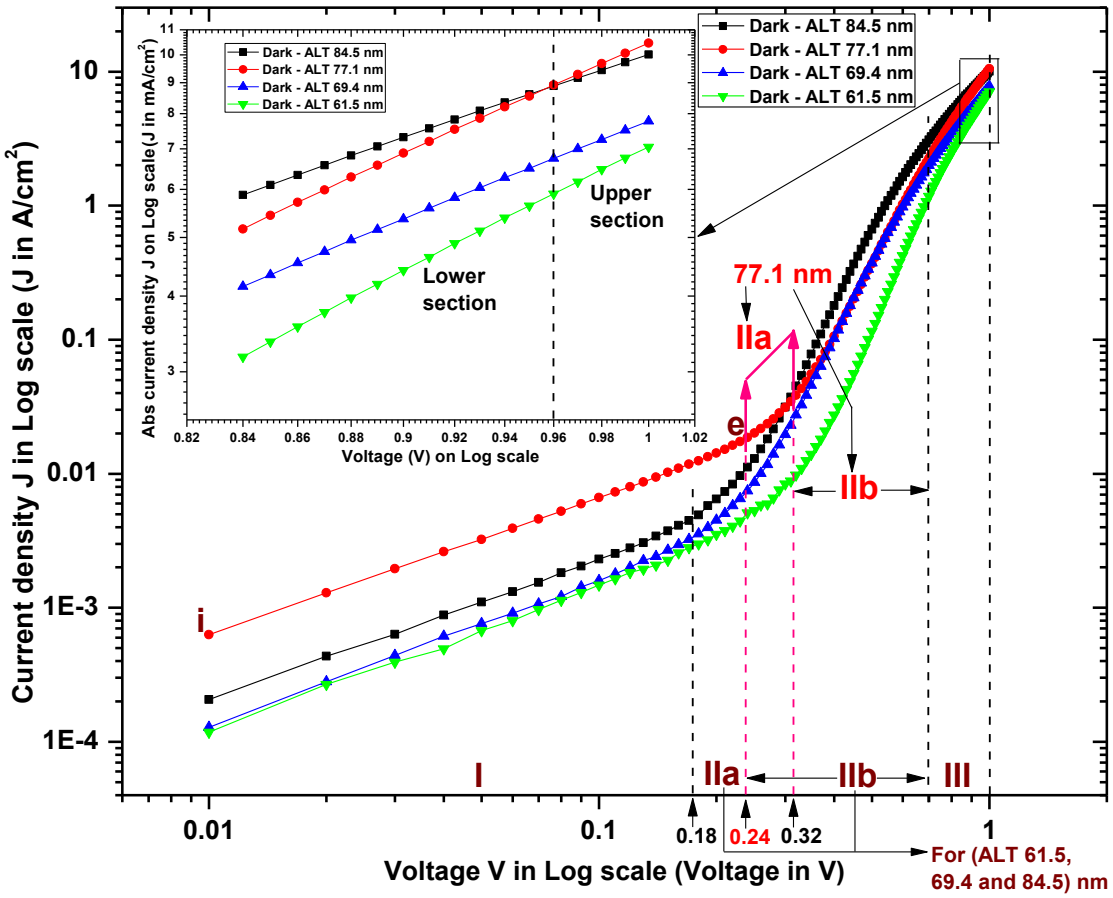

Figure 6.14 *Dark J(V) characteristics in double logarithmic (J-V) scale representation for ITO/PEDOT:PSS/P3HT:PCBM/Al solar cells with different 1:1 P3HT:PCBM active layer thicknesses*

The extension of the ohmic characteristic for the 77.1 nm ALT device suggests a relatively more improved morphology to be associated with its active layer than others. Furthermore, the 77.1

nm ALT device exhibits the highest current density in the region. All these electrical property exhibitions in favour of the 77.1 nm thick active layer are supportive of the premise that this thickness could be the optimum ALT under the given settings.

In region II we identified two sub-regions, IIa and IIb. Sub-region IIa lies between ~ 0.18 V and ~ 0.24 V for the 61.5, 69.4 and 84.5 nm active film thick devices and between ~ 0.24 V and ~ 0.32 V for the 77.1 nm counterpart device. The generally higher gradients (steepness) of curves in region IIa when compared with those of region I show the non-ohmic nature of region IIa. In this region, the gradients on average take *m* values in the approximate range 2.1 ± 0.2 and charge transport is attributed to trap-controlled SCLC with traps located at a single energy level inside the band gap.[14] The equation describing this mechanism is[45]

$$J = \frac{9}{8}\varepsilon\varepsilon_0\,\theta\mu\frac{V^2}{d^3} \tag{6.7}$$

where ε is the dielectric constant of the polymer, which is obtained from capacitance-voltage (C–V) measurements and has been found to be ≈ 3.5 for P3HT:PCBM [14], ε_0 is the permittivity of free space = 8.854×10^{-12} Fm^{-1}, θ is the trap limiting factor, which refers to the ratio of free to trapped charges and is given by[46]

$$\theta = \left(\frac{N_v}{N_t}\right)\exp\left(\frac{E_t}{kT}\right) \tag{6.8}$$

where N_v refers to the effective density of states in the valence band, N_t is the trap concentration at the energy level E_t, k is the Boltzmann's constant and T is the absolute temperature.

Region IIb corresponds to the region between the voltages ~ 0.24 V and ~ 0.70 V for the 61.5, 69.4 and 84.5 nm active film thick devices and between ~ 0.32 V and ~ 0.70 V for the 77.1 nm ALT device. In this region, the gradients for the differently thickened active layer devices become so highly steep that the respective *m* values take to the tune of the order of 10 – 13. The J(V) characteristics in this region are associated with the filling of traps (or trap filling limit).[14] All the four ALTs show the presence of traps. Interestingly, from approximately 0.7 V applied voltage through to 1.0 V, the curves start to exhibit bowing, in a way suggestive of quadratic

increase with higher applied voltages. We assigned label III to this bowing region in Figure 6.14. The bowing behaviour should be indicating that almost all the traps have been filled and therefore marks the onset of trap-free space charge limited conductivity (TFSCLC). When in trap-filled SCLC, the current density associated with each ALT increases quadratically with increasing applied voltage[14], [45] (thus, in conformity with the exhibited bowing of Figure 6.14 J–V curves at higher applied voltages) because there will be no current shunting (a loss mechanism) into traps. Minimal losses if still evident would then be due to other competing mechanisms. The J–V dependence in the TFSCLC region (III) is described by Child's law[14], [47]

$$J = \frac{9}{8} \varepsilon_0 \mu \frac{V^2}{d^3} \qquad (6.9)$$

with *m* taking the value of 2 when strictly TFSCLC, otherwise *m* can take values in the range 2 – 3 for the rest of region III. Bulk transport conforms to Child's law when the injected charge carriers from the electrodes numerically surpass the thermally generated carriers and all traps are filled.[14], [45]

In each of the identified regions, the dark current density, J (or J_{dark}), at a given voltage increases for the different ALTs according to the following order:

Region I (Ohmic) → $\mathbf{J_{(ALT\ 61.5\ nm)} < J_{(ALT\ 69.4\ nm)} < J_{(ALT\ 84.5\ nm)} < J_{(ALT\ 77.1\ nm)}}$

Region IIa → $\mathbf{J_{(ALT\ 61.5\ nm)} < J_{(ALT\ 69.4\ nm)} < J_{(ALT\ 84.5\ nm)} < J_{(ALT\ 77.1\ nm)}}$

Region IIb → $\mathbf{J_{(ALT\ 61.5\ nm)} < J_{(ALT\ 69.4\ nm)} \approx J_{(ALT\ 77.1\ nm)} < J_{(ALT\ 84.5\ nm)}}$

Region FIII (lower section) → $\mathbf{J_{(ALT\ 61.5\ nm)} < J_{(ALT\ 69.4\ nm)} < J_{(ALT\ 77.1\ nm)} < J_{(ALT\ 84.5\ nm)}}$

Region FIII (upper section) → $\mathbf{J_{(ALT\ 61.5\ nm)} < J_{(ALT\ 69.4\ nm)} < J_{(ALT\ 84.5\ nm)} < J_{(ALT\ 77.1\ nm)}}$

These results show that there is no universal order of increase of current density with ALT. As results show, different ALTs respond differently to different applied voltages. Charge carrier mobilities (μ values) are therefore dependent upon region. In determining the charge mobility μ in the active layer of a given device, it is necessary to first of all establish the region of location of the charge whose mobility is being sought. This can be done through plotting log *J* vs log *V* corresponding to the section under study and determining the slope (gradient) of the resultant curve. If the gradient of the log *J* against log *V* curve is 1, it implies that the region is ohmic and the characteristic ohmic equation has to be used to find the associated mobility. In this case, use

is then made of the equation (6.6) by plotting $J\,vs\frac{V}{d}$ using data corresponding to the region, (that is, ohmic region for now). The slope of the obtained curve is then equated to $nq\mu$. This is done so, because according to equation (6.6), the plot of $J\,vs\frac{V}{d}$ in ohmic region should be a straight line of gradient $nq\mu$. As such, $\mu_{in\ low voltage\ Ohmic\ region} = \frac{slope}{nq}$. Determination of the mobility μ in other identified regions (for example, SCLC) can be done in a similar way. In Figure 6.15, we show plots of $J\,vs\frac{V}{d}$ in the ohmic region for our different active layer thickness devices.

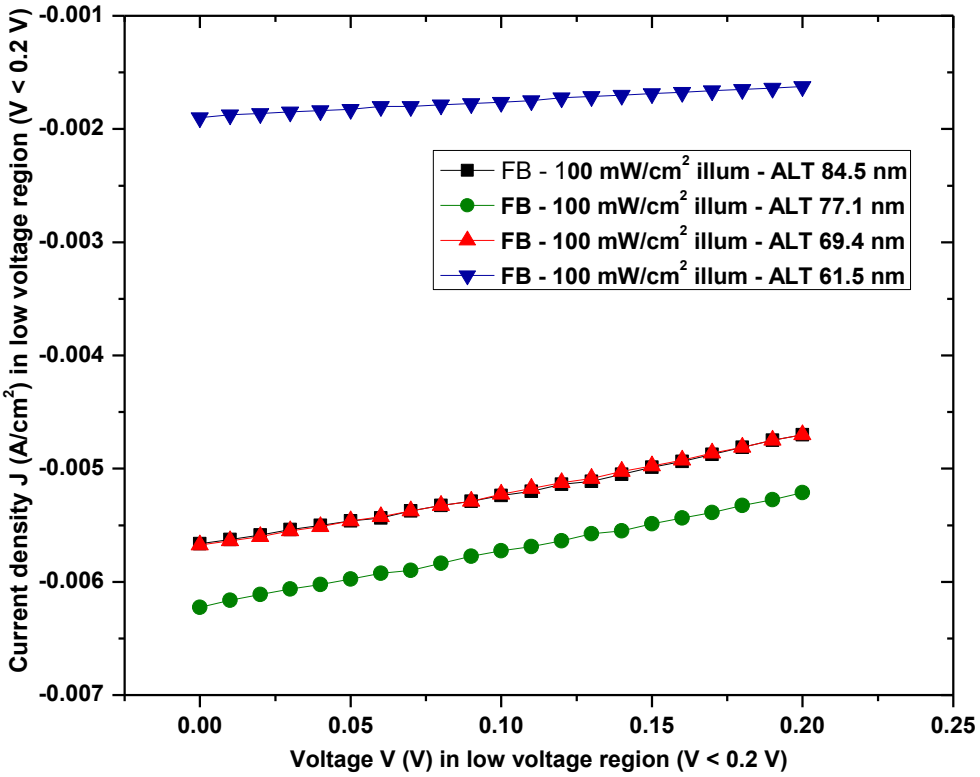

Figure 6.15 *J–V/d in low voltage ohmic region for the differently thickened active film devices*

Based on the visual difference in the slopes and the exhibited corresponding current density magnitudes, we surmise that the highest (ohmic region) mobility is associated with the 77.1 nm active layer thick device and the lowest is ascribed to the 61.5 nm ALT, which is the thinnest. In application of the outlined procedure for determining the mobility, we determined the dark

charge mobilities for the different active layer thicknesses in the upper section of the TFSCLC region (that is, region III) of our experimental devices. To this effect, we re-plotted in the inset of Figure 6.14, the log *J* vs log *V* dependence of the upper section of region III whose parts of the curves are included within the shown rectangle and are redrawn for clarity in Figure 6.16.

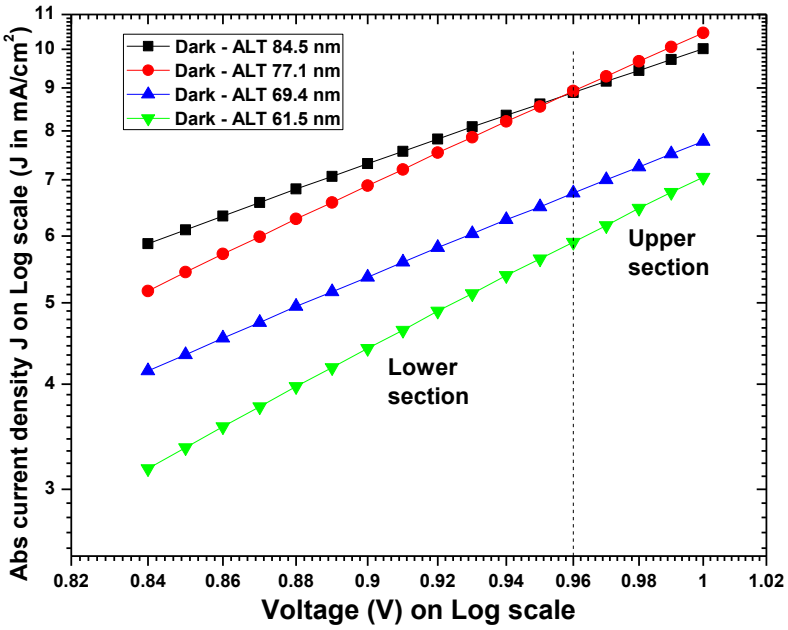

Figure 6.16 *Absolute current density J vs applied voltage V on double logarithmic scale for the trap free space charge limited current/conduction (TFSCLC) region in the applied voltage range 0.84 – 1.00 V for the different active layer thicknesses (ALTs)*

We used the J(V) data in this region to estimate the charge carrier mobilities in the active layers by plotting $J\ vs \frac{V^2}{d^3}$ for each active layer thickness. In Figure 6.17, we show the obtained graphs for the different ALTs. The slope of each of the $J\ versus \frac{V^2}{d^3}$ curves was obtained and used simultaneously with Eq. (6.9) to determine the associated mobility μ as follows:

Based on equation (6.9), the slope of the $J\ versus \frac{V^2}{d^3}$ curve equals $\frac{9}{8}\varepsilon\varepsilon_0\mu$. From this,

$$\mu_{in\ the\ TFSCLC\ region)} = \frac{8}{9} \times \frac{1}{\varepsilon\varepsilon_0} \times slope \qquad (6.10)$$

where the relative permittivity ε for P3HT:PCBM has been estimated to be ~ 3.5 [14] and $\varepsilon_0 = 8.854 \times 10^{-12} Fm^{-1}$.

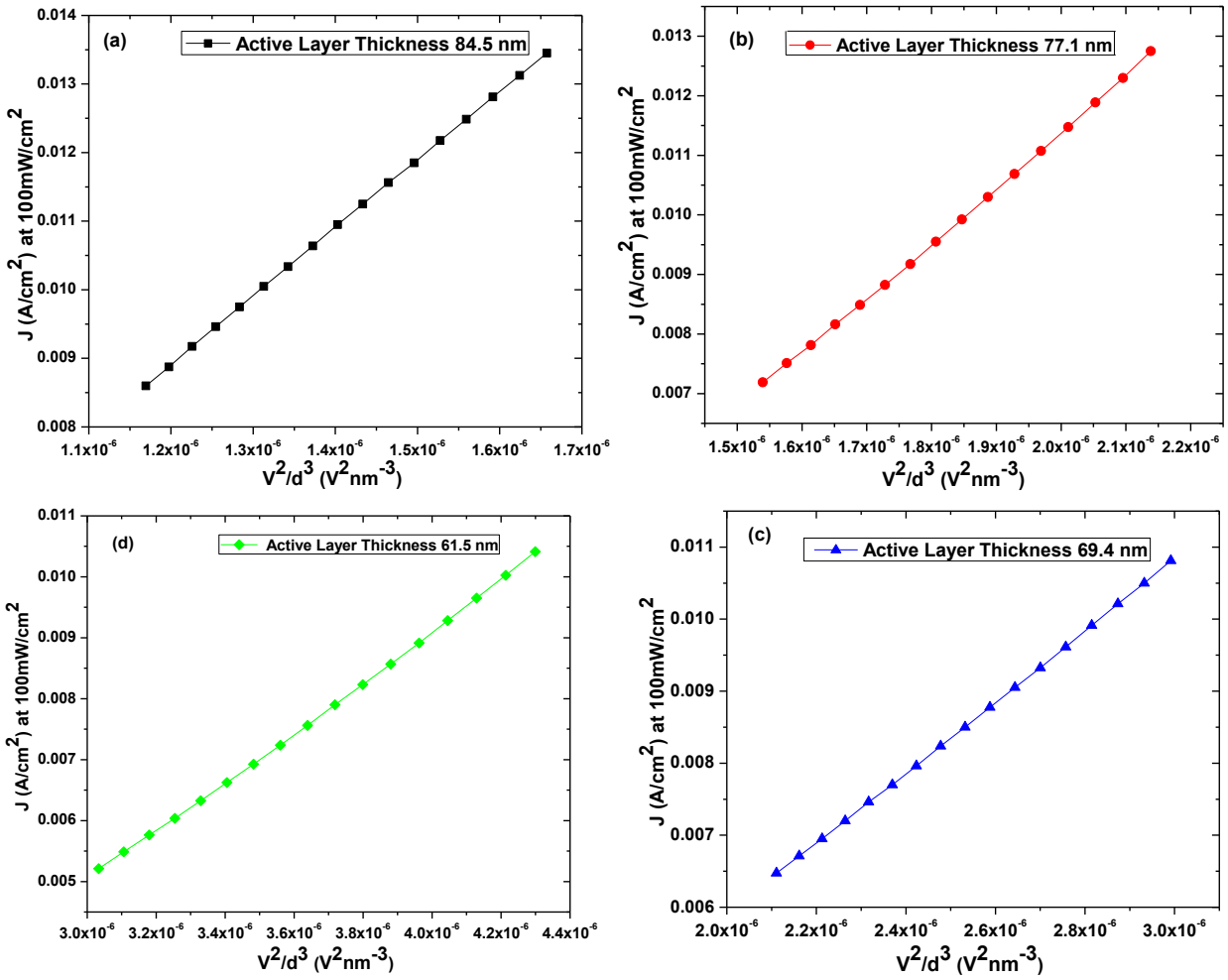

Figure 6.17 *J versus* $\frac{V^2}{d^3}$ *curves for upper section in TFSCLC region (III) for different ALTs*

In Table 6.3 we present the obtained dark charge carrier mobilities in the different active layer thicknesses corresponding to the upper section of region III, the TFSCLC region.

Table 6.3 *Approximate values of charge carrier mobilities in the different active layer thicknesses for the upper section of the trap free space charge limited current (TFSCLC) region*

Active layer thickness (ALT) / nm ± 0.1	**~ (Dark) Charge carrier mobility μ ($cm^2V^{-1}s^{-1}$) in TFSCLC region ± 0.005 × 10^{-6}**
61.5	1.263 ×10^{-6}
69.4	1.481 ×10^{-6}
77.1	2.463 ×10^{-6}
84.5	2.317 ×10^{-6}

Although the mobilities lie in the low 10^{-6} – 10^{-4} range, the Langevin recombination constant $(\gamma = (q/\varepsilon)\bar{\mu})$ was not considered in the analysis, because we assumed Schottky contacts existence, which eliminate dark recombination due to presence of large potential barriers.

While the results show that the dark charge carrier mobility is very low, they also predict similar order and pattern of magnitude under illumination. In conformity with literature,[14], [48] the charge carrier mobility in the P3HT:PCBM composite (as in organic thin films) is very low. This is mainly attributed to the structural disorder in the films[48] and presence of trap states. The charge carrier mobility was found to increase with increase in film thickness up to the 77.1 nm ALT, at which the maximum μ value is recorded. Thereafter, the mobility decreases with increase in film thickness, as shown by the lower μ value of the 84.5 nm ALT in comparison with the one in the 77.1 nm ALT. The minimum mobility is shown to be in the 61.5 nm ALT. This could be due to a significant drop in the active layer morphology, which increases the phase separation in a way that adversely distorts the percolation pathways and therefore result in decreased charge carrier mobility.

6.2.3.3.3 Effect of different active layer thicknesses on charge injection mechanisms at electrical contacts in the dark in ITO/PEDOT:PSS/P3HT:PCBM/Al devices

Although it currently appears difficult to establish a universal optimum active layer thickness (ALT) in excitonic devices, due to 'variations in polymer structure (regioregularity, molecular weight, poly-dispersity, etc.) and processing conditions'],[49 optimization of the active film

thickness for given settings still remains crucially important. In this regard, we studied the charge injection processes at electrical contacts of the experimental ITO/PEDOT:PSS/P3HT:PCBM/Al devices formed of nanoscale thin 1:1 P3HT:PCBM active layers of thicknesses 61.5 nm, 69.4 nm, 77.1 nm and 84.5 nm, with the objectives of optimizing the thickness of the active layer and also determine the effect of film thickness on the electrical characteristics of the devices, in particular the threshold open circuit voltage for onset of quantum tunneling regime. Furthermore, determination of the modifications due to ALT on the charge carrier (electron or hole) injection barriers is made. To gain insight into the modifications and charge injection mechanisms in the mentioned devices, we analysed the J(V) data using the Fowler-Nordheim (FN) field emission theory and the Richardson-Schottky (RS) thermionic emission theory, both of which have been described in Chapters 4 and 5.

6.2.3.3.3.1 Fowler-Nordheim field emission analysis

FN theory asserts that if charge injection from the electrodes is overwhelmingly of quantum mechanical tunneling through a triangular interface barrier, then a plot of $Ln\left(J/V^2\right) against \left(1/V\right)$ yields a straight line whose slope is directly proportional to $\phi^{(3/2)}$, where ϕ is the potential barrier at the metal-polymer junction.[50] In Chapter 5 we showed that for the FN case in which the variable (V/d) is used in place of the applied electric field F, $Ln\left(J/V^2\right) vs \left(1/V\right)$ plot then gives:

$$slope\left(or\ gradient\right) = -k\,d \tag{6.11}$$

where

$$k = \frac{8\pi\left(2m*\right)^{(1/2)}\phi^{(3/2)}}{3hq} \tag{6.12}$$

and d is the active layer thickness, q is the elementary charge $=1.602\times10^{-19}C$, h is Planck's constant $=6.626\times10^{-10}\,m^2kg/s$ and m^* is the effective charge carrier mass.

Substitution of k in Eq. (6.12) into Eq. (6.11) and rearrangement gives

$$slope = -\left[\frac{8\pi\left(2m*\right)^{(1/2)}\phi^{(3/2)}}{3hq}\right]d, \qquad \Rightarrow\ \phi = \left[\frac{-3hq\left(slope\right)}{8\pi d\left(2m^*\right)^{(1/2)}}\right]^{(2/3)} \tag{6.13}$$

Figure 6.18 shows our obtained FN tunneling curves for the devices under reverse bias (RB) and forward bias (FB), which are clearly identifiable by use of the insert legend key.

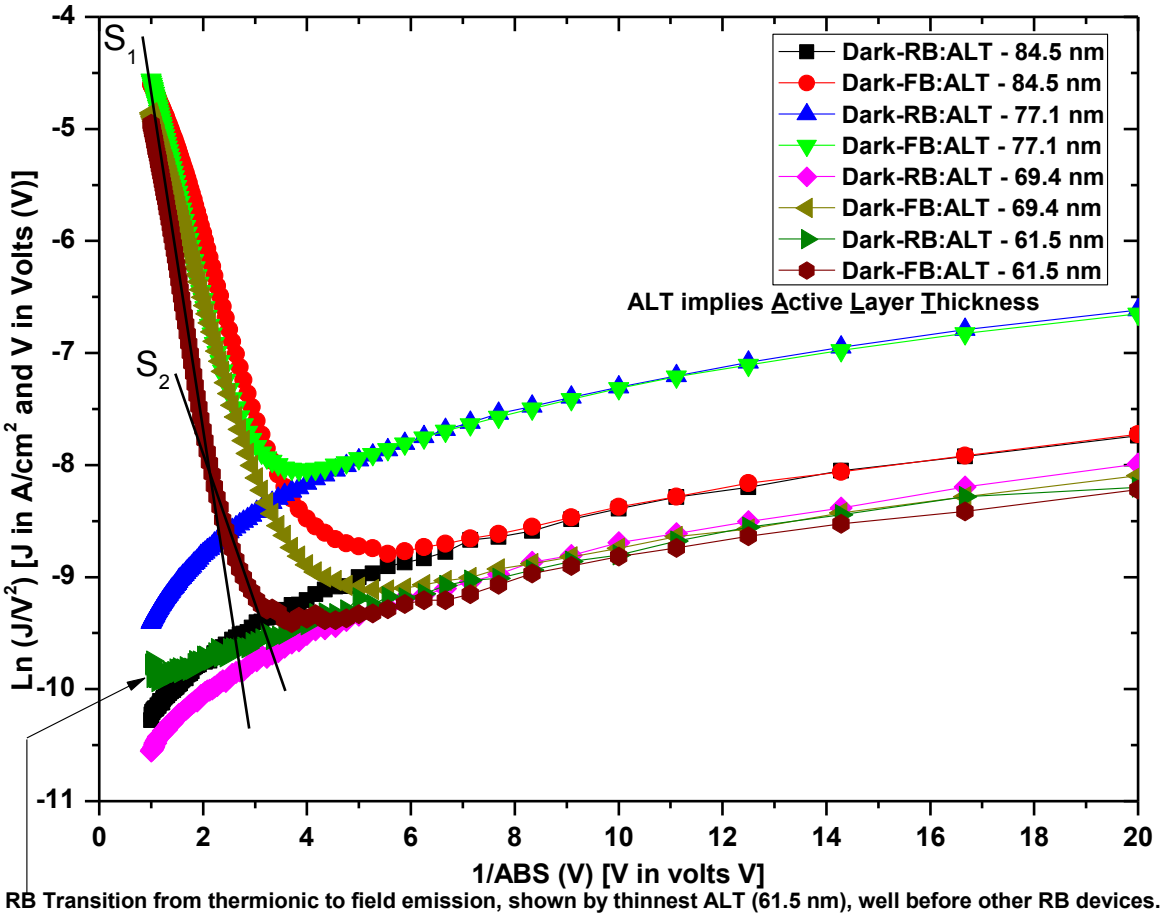

Figure 6.18 *Dark reverse bias (RB) and forward bias (FB) Fowler–Nordheim (FN) plots for ITO/PEDOT:PSS/P3HT:PCBM/Al devices with different active 1:1 P3HT:PCBM blend layer thicknesses*

In each of the devices, reverse bias corresponds to electron injection through the ITO/PEDOT:PSS electrode and to hole injection through the Al electrode. Forward bias ascribes to electron injection through the Al electrode and hole injection through the ITO/PEDOT:PSS electrode.

Under forward bias, $\ln\left(J/V^2\right)$ vs $\left(1/V\right)$ plots are linear with a negative slope at relatively high voltages ($\Rightarrow$ high electric fields) indicating that charge flow through the respective interfacial barriers is by quantum mechanical tunneling of predominantly holes. In conformity with the proposed sum of the two contributions to the current density (Chapter 5), through each of the

metal-polymer junctions (a consideration which imposes a minimum in the *FN* plots at room temperature) the nonlinear forward bias *FN* curves indicate no *FN* tunneling and should therefore be ascribed to field independent thermionic emission contribution to the current density. The slope of each of the linear fits in the tunneling regime is proportional to the corresponding barrier height. The presence of more than one slope, for example, *S*1 and *S*2 in the tunneling regime of the 61.5 nm *ALT* device indicates that more than one barrier exists in this region. The minimum in each of the forward bias *FN* plots signifies transition from thermionic emission to field emission conduction dominance. We note that under *FB*, the minima marking the conduction transitions from thermionic to field emission at the electrical contacts of the experimental devices do not coincide. This shows that different potential barriers exist in the different devices.

Since *RS* thermionic contribution predominates at high temperatures (and low applied electric fields),[50] but in our case the temperature remained within ambient confinements, which are of low temperature range, we therefore consider the thermionic contribution to be quasi constant. The *FN* tunneling process exhibits superiority at low temperatures and high electric fields ($\Rightarrow$ high applied voltages). Under FB in the field emission regime of Figure 6.18, the slopes of the linear sections of the plots show increase as the active layer thicknesses decrease (which implies negative correlation between slope and ALT). Support of this characteristic can easily be picked from observing that the plot due to the thinnest ALT of 61.5 nm exhibits the greatest tunneling slope. In a nutshell, the slopes show the magnitude relation:

$$\left|ALT\,61.5\,nm\ slope\right| > \left|ALT\,69.4\,nm\ \ slope\right| > \left|ALT\,77.1\,nm\ \ slope\right| > \left|ALT\,84.5\,nm\ \ slope\right|$$

This means that the tunneling regime potential barrier height ϕ increases as the thickness of the active layer decreases, a behaviour characteristic, which is in conformity with Eq. (6.13).

Also of interest is the 77.1 nm ALT device which exhibits the highest magnitude of the thermionic current density when compared with devices of other ALTs. Infact, the order of magnitude of the thermionic current density when incorporating other thicknesses is shown to be: $\mathbf{J_{77.1\ nm\ ALT} > J_{84.5\ nm\ ALT} > J_{69.4\ nm\ ALT} > J_{61.5\ nm\ ALT}}$

This adds onto other optimal characteristics already shown by the 77.1 nm ALT. Such behaviour may indicate the presence of the least pinhole (trap) density in the active layer of the device

when compared with other active layer thicknesses. It might also be that the associated traps (in the 77.1 nm ALT) may have been the shallowest.

Another peculiar characteristic is that at very high fields (~ 0.6 V) under *FB*, the curves tend to deviate from the FN straight lines. This behaviour is most likely caused by the very high increase in injected charge carriers (both electrons and holes, since the devices are double charge carriers) which outweigh what the bulk is able to transport and as a result builds up space charge that acts against more charge injection or the behaviour might be due to Poole Frenkel emission. We further note (in Figure 6.18) that at very high electric fields, the curves coincide. This means that in this region, the current density is now independent of the different active layer thickness attributes.

Under reverse bias (RB), it is only the 61.5 nm ALT device that shows onset of transition from thermionic emission to field emission and this occurs at a much higher field (~ 0.98 V applied voltage). Other thicknesses show neither onset of transition nor tunneling. This shows that RB barrier heights are much greater than those of their FB counterparts. Many competitive factors should be contributing to the resultant RB barrier heights.

6.2.3.3.3.2 Richardson-Schottky (RS) dark thermionic emission analysis

Figure 6.19 displays the dark J-V dependence of the studied devices having the differently thickened 1:1 P3HT:PCBM active layers. Forward bias in Figure 6.19 corresponds to electron injection into LUMO of PCBM from the negatively biased AL electrode and hole injection into HOMO of P3HT through ITO/PEDOT:PSS electrode. Reverse bias corresponds to electron injection into LUMO of P3HT and hole injection into HOMO of PCBM. The inset in Figure 6.19 (a), which is separately presented for clarity in Figure 6.19 (b) helps in illustrating the forward and reverse biases. Straight lines in the RS plots indicate that charge flow through the interface is by thermionic emission and the nonlinear sections show that the injection of charge is by FN tunneling.

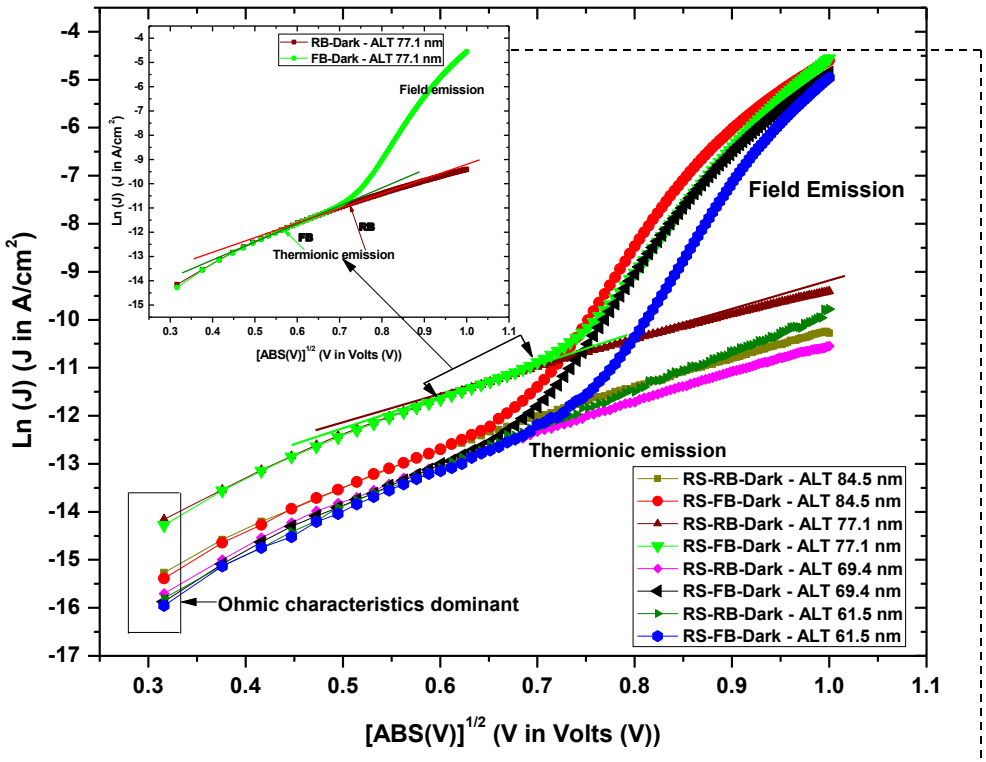

Figure 6.19 (a) *Dark RS thermionic emission plots for ITO/PEDOT:PSS/P3HT:PCBM/Al devices with* ***different active 1:1 P3HT:PCBM blend layer thicknesses under reverse bias (RB) and forward bias (FB)***

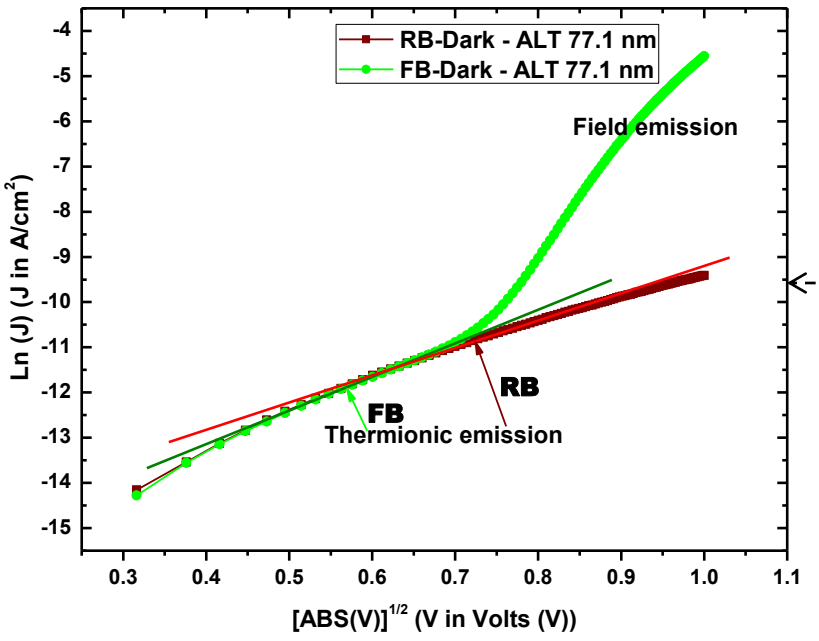

Figure 6.19 (b) *Dark RS thermionic emission plot {inset in Fig 6.19 (a) above} for the 77.1 nm 1:1 P3HT:PCBM blend ALT device under reverse and forward bias*

6.2.3.4 J(V) characteristics of different active layer thickness solar cells under solar simulated white light illumination intensity of 100 mW/cm^2 in ambient

Figure 6.20 shows the J–V characteristics whose photovoltaic (PV) measurements were conducted under AM 1.5 solar simulator source of 100 mWcm^{-2} for the different 1:1 P3HT:PCBM based devices formed of the displayed active layer thicknesses.

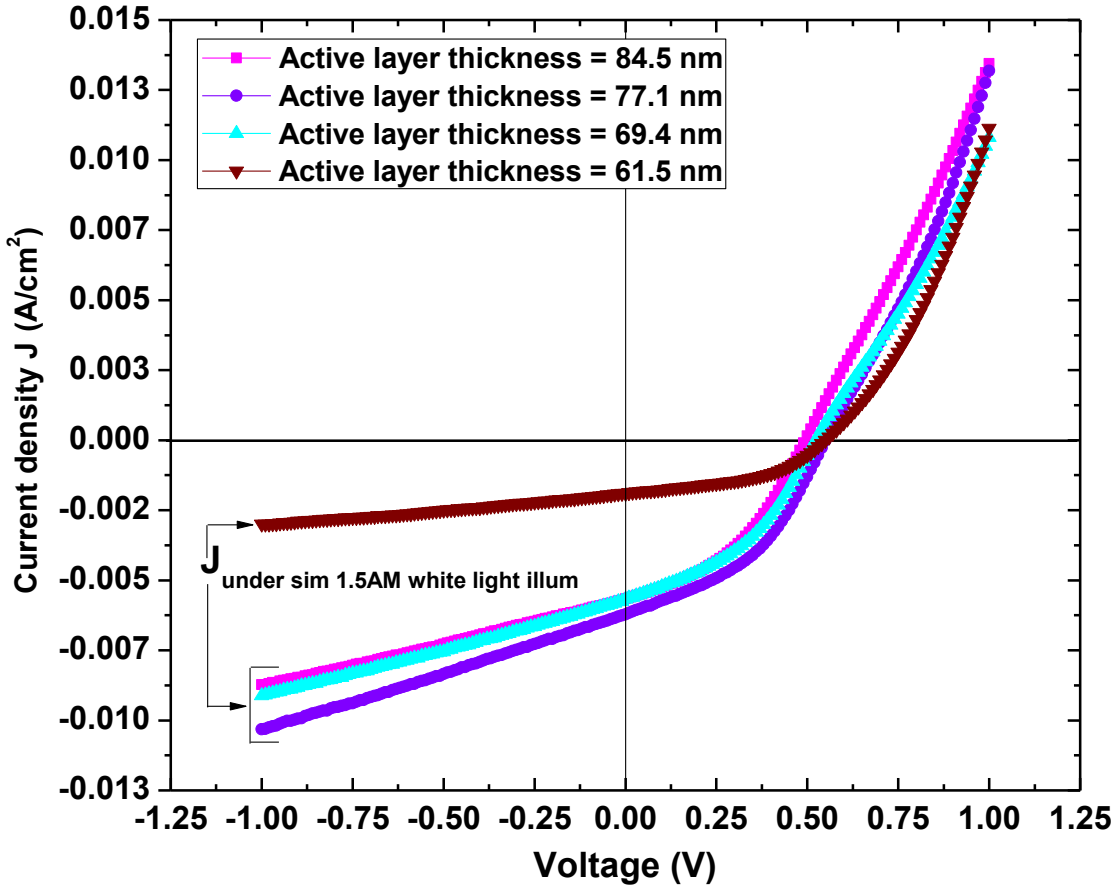

Figure 6.20 *Linear scale J(V) characteristic curves of the differently thickened 1:1 P3HT:PCBM composite films in ITO/PEDOT:PSS/P3HT:PCBM/Al solar cells under solar simulated white light illumination intensity of 100 mW/cm^2 in ambient*

In Figure 6.20 we show the corresponding J(V) characteristic curves plotted in semi-logarithmic scale. Analysis based on Figures 6.20 and 6.21 plots in conjunction with the obtained performance vales shown in Table 6.2 lead to the overall finding of the optimum device performance being associated with the 77.1 nm active layer thickness.

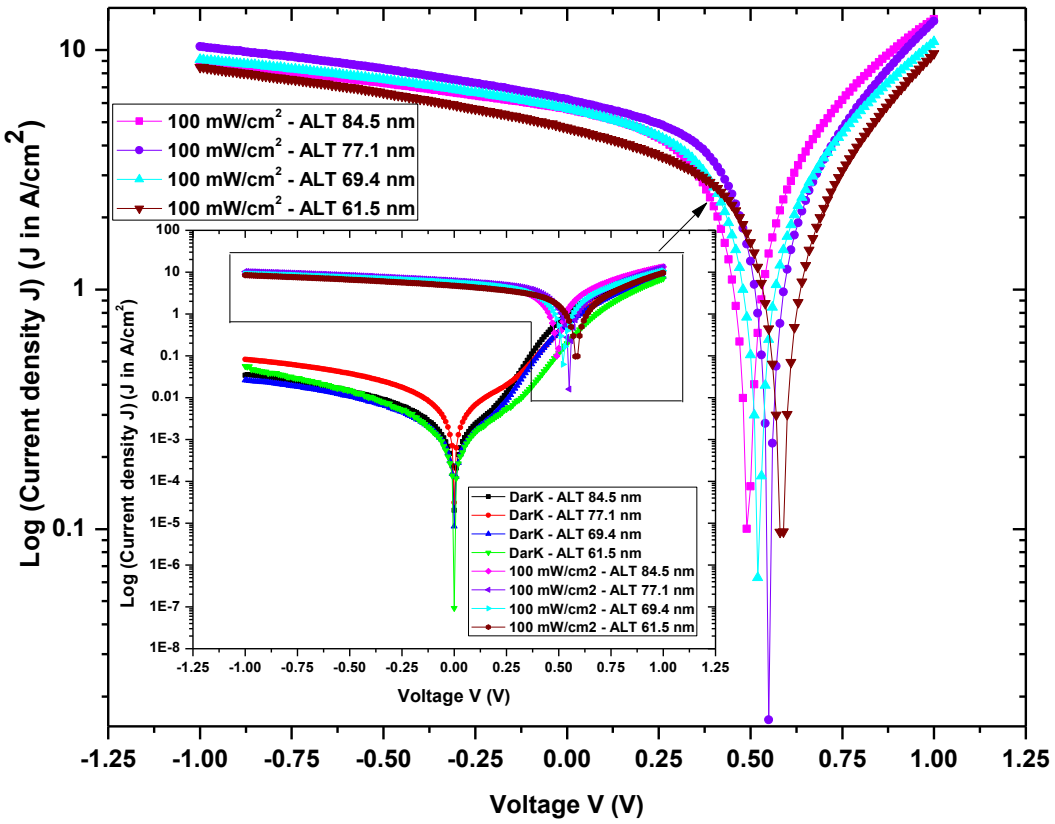

Figure 6.21 *The corresponding J(V) characteristic plots in semi-logarithmic scale for the differently thickened 1:1 P3HT:PCBM composite films in ITO/PEDOT:PSS/P3HT:PCBM/Al solar cells under solar simulated white light illumination intensity of 100 mW/cm^2 in ambient*

Under 100 mW/cm illumination (Figure 6.20) the magnitudes of the open circuit voltages for the different active layer thicknesses follow the order: V_{oc} (61.5 nm) > V_{oc} (77.1 nm) > V_{oc} (69.4 nm) > V_{oc} (84.5nm). The differences should mainly be due to changes in morphology, caused by the different ALTs.[51-53] The highest annealed power conversion efficiency (PC) of 1.44% was found for the 77.1 nm ALT. This thickness was also comparatively found to provide the best optical absorption, the highest maximum output power, highest fill factor of 0.4116 and current density (J_{sc}) of 6.2250 mA/cm^2. This, for example, is significantly higher than the J_{sc} value of 4.7375 mA/cm^2 belonging to the 61.5 nm thick active layer. The J(V) behaviour of the 77.1 nm thick active layer shows that in comparison with other ALTs, it should be having favourable charge carrier pathways and does not lose much in terms of bulk recombination.

6.2.3.4.1 $V_{oc\ thresh\ eff\ decay}$ versus $V_{oc\ thresh\ onset\ of\ FN\ field\ emission}$ in the different active layer thicknesses

We investigated the effect of active layer thickness on the prediction of V_{oc} for onset of Fowler–Nordheim (FN) quantum tunneling (field emission) by the observed threshold open circuit voltage for onset of decrease in efficiency in organic solar cells. Use was made of differently thickened 1:1 P3HT:PCBM composite thin film based organic solar cells of the structural fabrication ITO/PEDOT:PSS/P3HT:PCBM/Al. Table 6.4 displays the obtained results.

Table 6.4 *Threshold open circuit voltages (and corresponding electric fields F_s) for onset of decrease in efficiency versus FN voltage (and field F) minima for transition from TE to FE as well as threshold open circuit voltages (and corresponding fields) for onset of field emission*

Active Layer Thickness (ALT) (nm)	84.5	77.1	69.4	61.5
#Observed $V_{oc\ thresh\ eff\ decay}$ /V	0.41	**0.450**	0.48	0.49
$V_{oc\ FN\ min\ (Approx.\ Median\text{-}Transition\text{-}TE\ to\ FE)}$ /V	0.18	0.27	0.19	0.25
***$V_{oc\ FN\ thresh\ onset\ of\ field\ emission}$ /V**	0.33	**0.454**	0.33	0.43
#Corresponding $F_{thresh\ eff\ decay}$ (N/C)	4.852×10^6	$\mathbf{5.837 \times 10^6}$	6.916×10^6	7.967×10^6
$F_{FN\ min\ (Approx.\ Median\text{-}Transition\text{-}TE\ to\ FE)}$ (N/C)	2.113×10^6	3.505×10^6	2.668×10^6	4.065×10^6
***$F_{FN\ thresh\ onset\ of\ field\ emission}$ (N/C)**	3.945×10^6	$\mathbf{5.889 \times 10^6}$	4.803×10^6	7.070×10^6

We note that the correct prediction of the FN threshold voltage (or field) for onset field emission regime holds only for the optimal 77.1 nm active layer thickness whose $V_{oc\ \text{thresh eff decay}} \approx 0.450$ V and $V_{\text{oc FN thresh onset of field emission}} \approx 0.454$ V.

6.3 Conclusions

The study has shown that the opto-electrical performance of organic solar cells whose active nanoscale blend of conjugated polymers is of the bulk heterojunction make, strongly depends on the active layer thickness. Whilst this study's empirical results demonstrated optimal performance at approximately 77.1 nm active layer thickness, the overall findings have been that the existence of a static universal optimum active layer thickness is not practical. Such an

optimum rather exhibits contextual dependence. Fabrication settings like thin filming techniques, mixing ratio of donor and acceptor materials, solvent used, solvent evaporation technique and nature of environment have a bearing on the associated maximum film thickness. Morphological outcomes are also film thickness dependent. Device efficiency determinant parameters found to be directly affected by the active layer thickness are charge carrier mobility (which is generally low inside the photoactive film) and incomplete absorption of the incident light.

6.4 References

[1] Zhou, J.P.; Chen, X.H. and Xu, Z. *Influence of P3HT:PCBM Film Formation Process on the Performance of Polymer Solar Cells.* Spectroscopy and Spectral Analysis, Vol. 31, No. 10, pp. 2684-2687; 2011.

[2] Ng, A.; Sun, Y.C.; Fung, M.K.; Ng, A.M.C.; Leung, A.B.; Djurišić A.B. and Chan, W.K. *Influence of the Polymer Processing Conditions on the Performance of Bulk Heterojunction Solar Cells.* SPIE Proceedings, Organic Photonic and Devices XIV, Vol. 8258; 2012.

[3] Balderrama, V.S.; et al. *Influence and Relationship of Film Morphology on Organic Solar Cells Manufactured with Different P3HT:PC[70]BM Blend Solutions.* 8th International Conference on Electrical Engineering Computing Science and Automatic Control, Vol. 1, No. 5, pp. 26-28; 2011.

[4] Kumer, P. *Effect of thermal Treatment on the Performance of Organic Bulk-Heterojunction Photovoltaic Devices,* Physics of Semiconductor Devices. International Workshop on IWPSD, Mumbai, 16-20 December, pp16-20; 2007.

[5] Morvillo, P.; Bobeico, E.; Esposito, S. and Diana, R. *Effect of the active layer thickness on the device performance of polymer solar cells having [60] PCBM and [70] PCBM as electron acceptor.* ELSEVIER Energy Procedia 31, 69-73; 2012.

[6] Moule, A.J.; Bonekamp, J. B. and Meerholz, K. *The effect of active layer thickness and composition on the performance of bulk-heterojunction solar cells.* Journal of Applied Physics, 100, 0945503; 2006.

[7] Yu, G.; Gao, J.; Hummelen, J.C.; Wudl, F. and Heeger, A.J. *Polymer Photovoltaic Cells: Enhanced Efficiencies via a Network of Internal Donor-Acceptor Heterojunctions.* Science **270**, 1789; 1995

[8] Shaheen, S.E.; Brabec, C.J.; Sariciftci, N.S.; Padinger, F.; Fromherz, T. and Hummelen, J.C. *Fullerenes: From Synthesis to Optoelectronic Properties.* Appl. Phys. Lett. 78, 841; 2001.

[9] Padinger, F.; Rittberger, R.S. and Sariciftci, N.S. *Effects of Postproduction Treatment on Plastic Solar Cells.* Advanced Functional Materials, Vol. 13, Issue 1, 85–88; 2003.

[10] Coakley, K.M. and McGehee, M.D. *Conjugated Polymer Photovoltaic Cells*. Chem. Mater. **16**, 4533-4542; 2004.

[11] Schilinsky, P.; Waldauf, C. and Brabec, C.J. *Recombination and loss analysis in polythiophene based bulk heterojunction photodetectors.* Appl. Phys. Lett. **81**, 3885; 2002.

[12] Nogueira, A.F.; Montanari, I.; Nelson, J.; Durrant, J.R.; Winder, C. and Sariciftci, N.S. *Charge Recombination in Conjugated Polymer/Fullerene Blended Films Studied by Transient Absorption Spectroscopy*. J. Phys. Chem. B, **107**, 1567; 2003.

[13] Hoppe, H.; Arnold, N.; Sariciftci, N.S. and Meissner, D. *Modeling the optical absorption within conjugated polymer/fullerene-based bulk-heterojunction organic solar cells.* Sol. Energy Mater.Sol. Cells **80**, 105; 2003.

[14] Kadem, B.; Hassan, A.K. and Cranton, W.M. *Efficient P3HT:PCBM bulk heterojunction organic solar cells; effect of post deposition thermal treatment.* Springer Science+Business Media New York; 2016.

[15] Drees, M.; Davis, R.M. and Heflin, J.R. *Thickness dependence, in situ measurements and morphology of thermally-controlled inter-diffusion in poly-C60 photovoltaic devices.* Physical Review B, Vol. 69, No. 16, Article ID: 165320; 2004.

[16] Ramani, R.; Alam, S. *A comparative study of thje influence of alkl thios on the structural transformations in P3HT/PCBM and P3OT/PCBM blends.* Polymer, **54**(25), 6785-6792; 2013.

[17] Ryu, M.S.; Hyuk, J.C. and Jin, J. *Effects of thermal annealing of polymer-fullerene photovoltaic solar cells for high efficiency.* Curr. Appl. Phys., **10**(2), S206–S209; 2010.

[18] Erb, T.; Zhokhavets, U.; Hoppe, H.; Gobsch, G.; Al-Ibrahim, M. and Ambcher, O. *Thin solid films, absorption and crystallinity of poly(3-hexylthiophene)/fullerene blends in dependence on annealing temperature.* Thin Solid Films, **511**, 483–485; 2006.

[19] Al-Ibrahim, M. and Ambacher, O. *Effects of solvent and annealing on the improved performance of solar cells based on poly.3-hexylthiophene:fullerene.* Appl. Phys. Lett., **86**, 201120; 2005.

[20] Sun, Y.; Liu, J.-g.; Ding, Y. and Han, Y.-c. *Controlling the surface composition of P3HT/PCBM blend films by using miced solvents with different evaporation rates.* Chin. J. Polym. Sci., **31**(7), 1029–1037; 2013.

[21] Bhattacharya, J. *Understanding the physics of degradation of polymer solar cells.* Graduate Theses and Dissertations, Paper 13475; 2013. http//lib.dr.iastate.edu/etd.

[22] Kim, Y.S.; Lee, Y.; Kim, J.K.; Seo, E.O.; Lee, E.W.; Lee, W.; Han. S.H. and Lee, S.H. *Effects of solvents on the performance and morphology of polymer photovoltaic devices.* Curr. Appl. Phys., **10**, 985–989; 2010.

[23] Chuang, S.-Y.; Chen, H.-L.; Lee, W.-H.; Huang, Y.-C.; Wei-Fang, S.; Jen, W.-M. and Chen, C.-W. *Regioregularity effects in the chain orientation and optical anisotropy of composite polymer/fullerene films for high-efficiency, large-area organic solar cells.* J. Mater. Chem., 19, 5554–5560; 2009.

[24] Zhokhavets, U.; Erb, T.; Hoppe, H.; Gobsch, G. and Sariciftci, N.S. *Effect of annealing of poly (3-hexylthiophene)/fullerene bulk heterojunction composites on structural and optical properties.* Thin Solid Films, 496, 679–682; 2006.

[25] Kuila, B,K. and Nandi, A.K. *Physical, Mechanical and Conductivity properties of poly(3-hexylthiophene-montmorrilonite clay nanoparticles produced by the solvent casting method.* Macromolecules, Vol.37, No. 23, 8577–8584; 2004.

[26] Islam, Md.S.; Islam, Md.E.; Ismail, A.B.Md. and Baerwolff, H. *Influence of Thickness and Annealing Temperature on the Optical Properties of Spin-Coated Photoactive P3HT:PCBM Blend.* Optics and Photonics Journal, 3, 28–32; 2013.

[27] Ohkita, H and Ito, S. *Transient absorption spectroscopy of polymer-based thin-film solar cells.* Polymer, Vol. 52, No. 20, 4397 – 4417; 2011.

[28] Chen, L-M.; Hong, Z.; Li, G. and Yang, Y. *Recent progress in polymer solar cells: Manipulation of polymer:fullerene morphology and the formation of efficient inverted polymer solar cells.* Adv. Mater. **21**, 1434; 2009.

[29] Moule, A.J. and Meerholz, K. *Morphology control in solution-processed bulk-heterojunction, solar cell mixture.* Adv. Funct. Mater. **19**, 3028; 2009.

[30] Deibel, C. and Dyakonov, V. *Polymer–fullerene bulk heterojunction solar cells.* IOP Publishing – Rep. Prog. Phys. **73**, 096401 (39pp); 2010.

[31] Hoppe, H.; Niggemann, M.; Winder, C.; Kraut, J.; Hiesgen, R.; Hinsch, A.; Meissner, D. and Sariciftci, N.S. *Nanoscale Morphology of Conjugated Polymer/Fullerene-Based Bulk- Heterojunction Solar Cells.* Adv. Funct. Mater. **14**, 1005-1011; 2004.

[32] Ma, W.; Yang, C.; Gong, X.; Lee, K. and Heeger. A. J. *Thermally Stable, Efficient Polymer Solar Cells with Nanoscale Control of the Interpenetrating Network Morphology.* Adv. Funct. Mater. **15**, 1617; 2005.

[33] Reisdorffer, F.; Haas, O.; Le Rendu, P. and Nguyen, T.P. *Co-solvent effects on the morphology of P3HT:PCBM thin films.* Synth.Met. **161**, 2544 – 2548 ; 2012.

[34] Nam, Y.M.; Huh, J. and Jo, W.H. *Optimization of thickness and morphology of active layer for high performance of bulk-heterojunction organic solar cells.* Eleservier: Solar Energy Materials and Solar Cells, **94**, 1118–1124; 2010.

[35] Rau, U.; Grabitz, P.O. and Werner, J.H. *Resistive limitations to spatially inhomogeneous electronic losses in solar cells.* Appl. Phys. Lett., Volume 85, Issue 24, id 6010; 2004.

[36] Kim, M.S.; Kim, B.G. and Kim, K. *Effective variables to control the fill factor of organic photovoltaic cells.* ACS Appl. Mater Interfaces, 1(6), 1264–9; 2009.

[37] Xue, J.; Uchida, S.; Rand, B.P. and Forrest, S.R. *Semiconductor materials for solar photovoltaic cells.* Appl. Phys. Lett., 84, 3031; 2013.

[38] Seok, J.; Yun, J.-M.; Kim, S.-S.; Kim, D.-Y.; Kim J. and Na, S.-I. *Variations of cell performance in ITO-free organic solar cells with increasing cell areas.* IOP Publishing Semicond. Scie. Techno., Vol. 26, No. 3: 2011.

[39] Street, R.A.; Song, K.W. and Cowan, S. *Band tail recombination in polymer:fullerene organic solar cells*. Org. Eletron. 12, 244; 2011.

[40] Qi, B. and Wang, J. *Fill factor in organic solar cells.* Phys. Chem. Chem. Phys., **15**, 8972–8982; 2013.

[41] Servaites, J.D.; Ratner, M.A. and Marks, R.J. *Organic solar cells: A new look at traditional models*. Energy Environ. Sci., **4**, 4410; 2011.

[42] Stevens, D.M.; Qin, Y.; Hillmyer, M.A. and Frisbie, D. *Enhancement of the Morphology and Open Circuit Voltage in Bilayer Polymer/Fullerene Solar Cells.* J. Phys. Chem. C, 113, 11408–11415; 2009.

[43] Sze, S.M.; *Physics of Semiconductor Devices.* Wiley, New York; 1981.

[44] Kadem, B.Y.; Hassan, A.K. and Cranton, W. *Enhancement of power conversion efficiency of P3HT:PCBM solar cell using solution processed Alq3 film as electron transport layer*. J. Mater. Sci. Mater. Electron. **26**(6), 3976–3983; 2015.

[45] Gunduz, B.; Yahia, I.S. and Yakuphanoglu, F. *Electrical and photoconductivity properties of p-Si/P3HT/Al and p-Si/P3HT/MEH-PPV/Al organic devices: comparison study*. Microelectron. Eng. **98**, 41–57; 2012.

[46] El-Nahass, M.M.; Abd, K.F. and El-Rahman, *Nickel phthalocyanine thin films.* J Alloys Compd. **430**, 194 – 199; 2007.

[47] Apaydin, D.H.; Yildiz, D.E.; Cirpan, A. and Toppare, L. *Optimizing the organic solar cell efficiency: the role of the active layer thickness.* Sol. Energy Mater. Sol. Cells **113**, 100–105; 2013.

[48] Shen, Y.; Li, K.; Majumdar, N.; Campbell, J.C. and Gupta, M.C. *Bulk and contact resistance in P3HT:PCBM heterojunction solar cells.* Sol. Energy Mater. Sol.Cells 95, 2314–2317; 2011.

[49] Thompson, B.C. and Fréchet, J.M.J. *Polymer–Fullerene Composite Solar Cells.* Angew. Chem. Int. Ed. 47, 58 – 77; 2008.

[50] Chiguvare, Z. *Electrical and Optical Characterisation of Bulk Heterojunction Polymer – Fullerene Solar Cells*. *PhD Thesis* 26; 2004.

[51] Gang, L.; Shrotriya, V.; Yao, Y. and Yang, Y. *Investigating the annealing effects and film thickness dependence of polymer solar cells based on poly,,(3-hexylthiophene).* Journal of Applied Physics, 98; 2005.

[52] G. Li, Shrotriya, V. Huang, J.; Yao, Y.; Moriarty, T.; Emery, K. and Yang. Y. *High-efficiency solution processable polymer photovoltaic cells by self-organization of polymer blends.* Nat. Mater. **4**, 864; 2005.

[53] Kumar, P.; Kumar, H.; Jain, S.C.; Venkatesu, P.; Chand, S. and Kumar, V. *Effect of active layer thickness on open circuit voltage in organic photovoltaic devices.* Jpn. J Appl. Phys. 48: 121501; 2009.

Chapter 7

Influence of post-fabrication thermal annealing on the opto-electrical characteristics of P3HT:PCBM based solar cells

7.1 Introduction

Although polymer photovoltaic solar cells offer many amenities such as mechanical flexibility and durability, large area devices, lightweight cells, material diversity and low-cost fabrication, [1-8] their performance is still low. Empirical observations reveal that P3HT:PCBM based solar cell performance greatly depends upon thermal annealing processes employed. Of significant peculiarity are the annealing temperatures and durations, since these are inherent to the annealing process (whether pre or post-annealing). The parameters greatly determine the energetics and kinetics of the blending process or morphology. Disappointingly, the associated physics is still barely understood, despite numerous endeavours.[9-13]

It is against this background that we undertook the study we here report on. The study focuses on clarifying the thermal annealing mechanisms in organic semiconductor material-based devices and the influence of post-fabrication thermal annealing temperature on the optical and electrical performances of bulk heterojunction ITO/PEDOT:PSS/P3HT:PCBM/Al photoactive devices. Included in the study is an insight into the morphological changes within the P3HT:PCBM blends due to the annealing and how the resultant changes impacted on the opto-electrical characteristics of the devices.[14-18] The annealing treatment was confined to the 65 – 180 °C temperature range. Charge transport in the bulk is estimated using the space charge limited current (SCLC) conduction model. Furthermore, use is made of the Richardson–Schottky (RS) thermionic emission and Fowler–Nordheim (FN) quantum mechanical tunneling models to investigate barrier potential modifications at the metal-active layer interfaces of the devices due to heat treatment at different temperatures.

7.2 Methodologies

The experimental methodologies were conducted as described in Chapter 4, Section 4.2.3. In all the experimental devices, the active layer thickness was kept constant at the optimized value of

77.1 nm found in the optimum thickness search of Chapter 6 investigations. Upon completion of the fabrication, the devices were left to cool down for 30 minutes, after which the non-control devices were annealed at different temperatures in the range 50 °C to 180 °C before being subjected to opto-electrical characterisation techniques described in Section 4.2.3.

7.3 Results and Discussion

7.3.1 Optical absorption spectra characteristics of annealed P3HT:PCBM photoactive cells

Figure 7.1 shows the optical absorption spectra of the one nano layer constant thickness of 1:1 P3HT:PCBM blend in each of the fabricated devices, comprising the control (as-cast) and others thermally annealed at the different temperatures indicated. All spectra of the P3HT:PCBM active layers show typical absorption spectra that are divided into two main regions. The major region, spanning from 650 – 400 nm is due to optical absorption by the principal conjugated polymer (P3HT), while the minor region (below 400 nm) is due to absorption by the fullerene (PCBM) molecules.

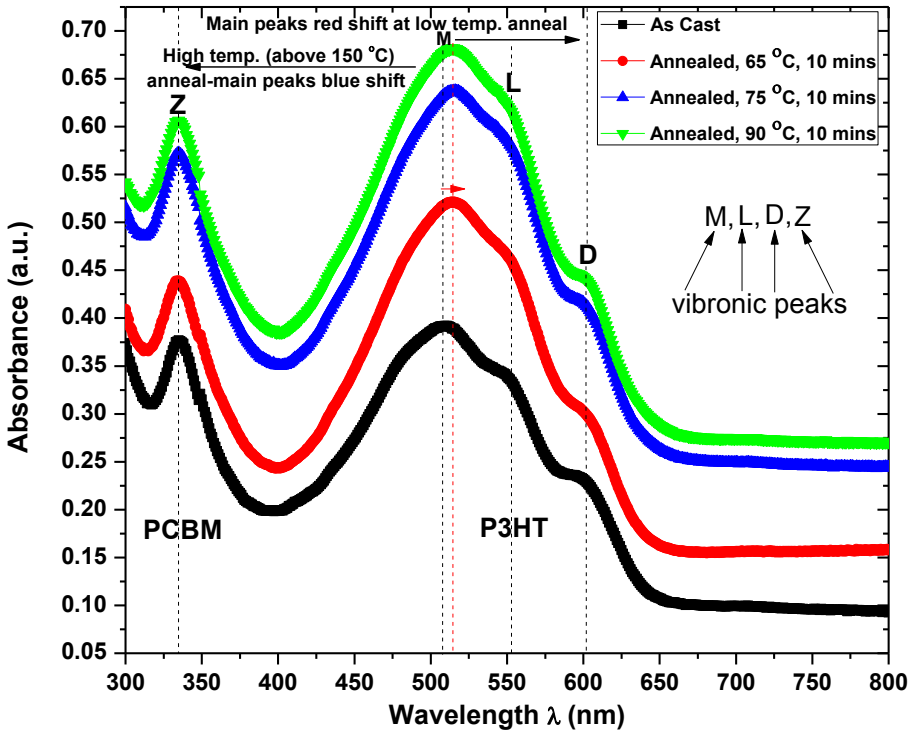

Figure 7.1 *Ultraviolet-visible (UV-Vis) absorption spectra due to thin films of 1:1 P3HT:PCBM before and after annealing at different temperatures in the low temperature range (65 – 90 °C)*

The peak absorption wavelength λ_{max} for the untreated film is ~ 510 nm, with shoulders at ~ 545 nm and ~ 595 nm. We note that the absorbance of the active film increased with increase in the thermal annealing temperature and that this effect is apparent (clearly seen) even if the films are subjected to such low treatment temperatures as 65 °C or a few degrees Celsius above room temperature (≈ 30 °C). All the annealing processes were administered for 10 minutes. For the temperature range 65 °C to 90 °C shown in Figure 7.1, the highest increase in absorbance was found to be at the annealing temperature of 90 °C. An increase in the absorption band after annealing generally indicates increased packing of the P3HT domains.[19] Three different bands, D, L and M are exhibited by the P3HT spectral region. The main absorption peak band (region M) around 510 nm) generally indicates the π–π* electronic transition within the P3HT backbone polymer.[6], [20] As Figure 7.1 shows, a 65 °C annealing treatment resulted in the principal (main) peak wavelength red-shifting to ~ 515 nm, but the two shoulder peaks at ~ 553 and 602 nm showed no change in position. Curves of the other active films annealed at 75 °C and 90 °C (as well as 100 °C, 130 °C and 140 °C not shown) also exhibited similar behaviour. Then main peak and shoulder peaks collectively form the set of vibronic peaks. When the annealing temperature was in turn increased to 150 °C, 160 °C and 180 °C (which correspond to high temperature annealing), the result (not shown) was a blue-shift of the main peak wavelength (λ_{max}). This behaviour could be due to the interruption of the structure and orientation for the P3HT chain ordering as a result of too much heat treatment.[21-22] As Figure 7.1 shows, the peaks at ~ 333 nm, which correspond to PCBM (region Z) showed no spectral shift at any of the treatment temperatures. Infact the PCBM nano-scale thin films showed no significant change in the optical behaviour when the annealing temperature was varied. This shows that although the absorption spectra of the blend layers are contributions of the two spectra, one from P3HT and the other from PCBM, the optical changes in the P3HT:PCBM films are attributed to changes in the P3HT polymer. The observed red-peaking of the main peak absorption wavelength λ_{max} during low temperature annealing may be attributed to an increased interchain interaction among P3HT chains, which results in more delocalized conjugated π electrons and the lowering of the band gap between π and π* that leads to increase of the alluded optical π–π* transition.[2]

Thermal annealing has an important impact on the crystallinity of P3HT. The annealing enhances the crystallinity of P3HT instigated by the diffusion of PCBM molecules into aggregates causing the P3HT molecules to be crystallized in the free region of PCBM that leads to more π–π*

absorption.[23] The increased absorption after annealing is likely to be due to the ordering P3HT domains induced by heat treatment, which causes the development of bigger aggregates or more condensed moieties that are composed of multiple inter-chain species of P3HT, packing of the P3HT domains and reduced torsion of the P3HT.[23] The movement of the main absorption peak towards longer wavelength with increasing temperature may be due to the characteristic behaviour of polymers with shorter conjugation length which absorb higher energy photons.[19] The clearly distinguishable and sharper vibronic peaks with increasing annealing temperature up to 140 °C, point towards increased P3HT crystallinity. The highest optical absorbance was found at the annealing temperature of ~ 140 °C (not shown in Figure 7.1 for simplicity and clarity of presentation sequence in the shown low annealing temperature range of 65 – 90 °C). The finding is supported by literature.[6], [19], [23] It is most likely that when the active composite is treated at the optimal 140 °C annealing temperature, the conjugated P3HT chain becomes fully self-assembled to orderly structure, with conjugated bond length and thermal diffusion of PCBM molecules into larger PCBM aggregates increased.[24] This motion (promoted by the raised annealing temperature) creates regions with low PCBM concentration. It is in these PCBM free regions that the P3HT aggregates can become converted into P3HT crystallites.[19] Further increase of the annealing temperature beyond 140 °C leads to a decrease of the P3HT crystallinity, which causes the P3HT crystallites to become unstable due to over-enhanced thermal motion of the P3HT molecules at too high temperatures. Such excessive heat treatment temperatures result in a melting down (that is, destruction) of P3HT crystallites, hence a reduction of the P3HT crystallinity.[24] Band D in Figure 7.1 is attributed to the absorption of the inter-chain stacking of P3HT, which suggests an improvement in the chain ordering, while band L is attributed to the extended conjugated polymer.[22], [25]

7.3.2 Morphological analysis

We studied the AFM images of the P3HT:PCBM active blend layer in order to understand the morphological changes that take place in the blend layer as a result of thermal annealing . Figure 7.2 shows the obtained AFM images for the samples comprised of the control (as-cast film with no thermal treatment) and those heat treated at different temperatures. For the as-cast film, the surface is very smooth, with root mean square (rms) surface roughness of 0.325 ± 0.003 nm. No distinct phase segregation is observed.

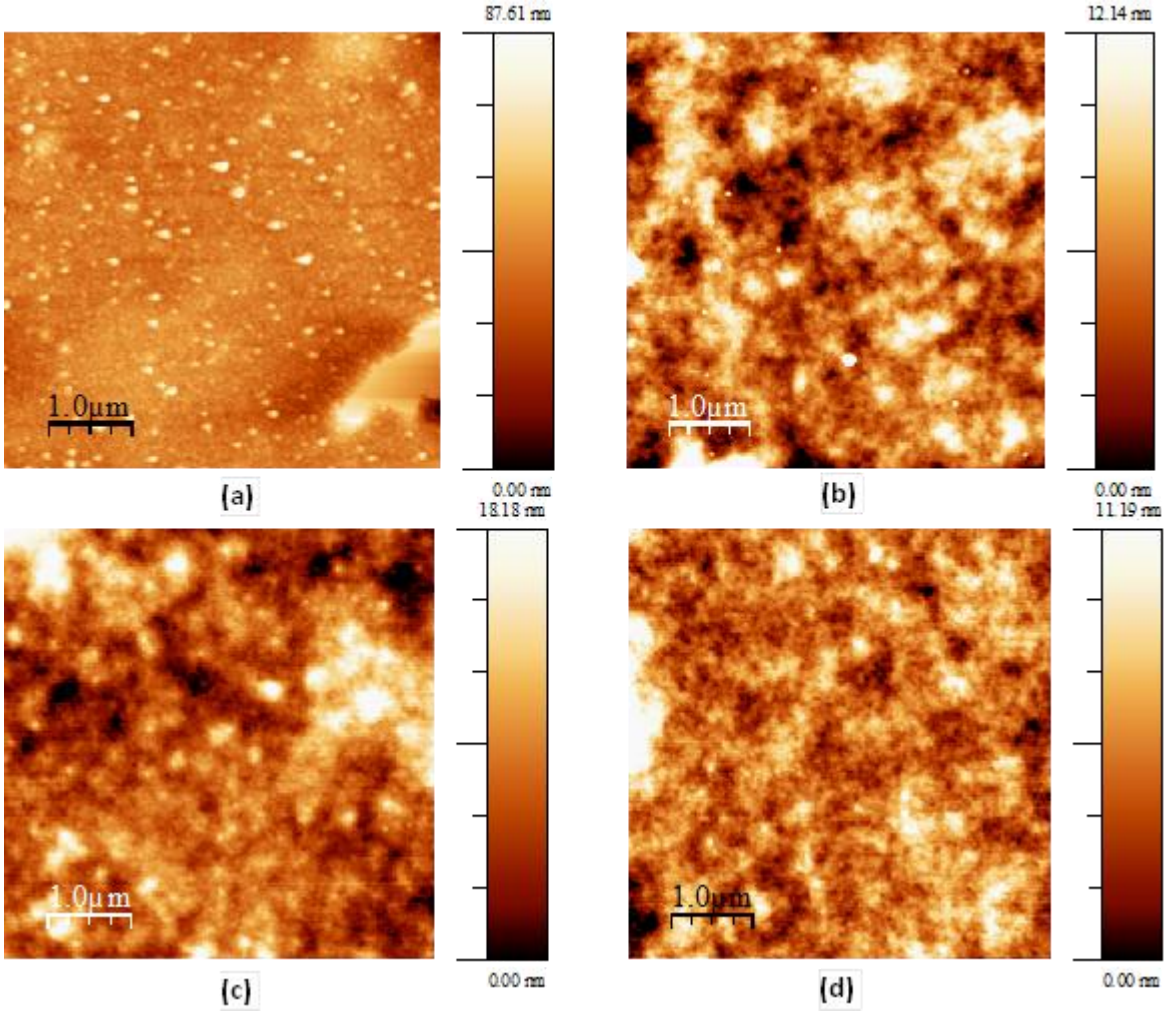

Figure 7.2 *AFM images of the surface of the 1:1 P3HT:PCBM active films (a) before annealing and after annealing at (b) 65 °C, (c) 75 °C and (d) 90 °C. The annealing duration for the films was 10 mins.*

The other experimental devices (b), (c) and (d) were subjected to different thermal annealing temperatures of magnitudes 65 °C, 75 °C and 90 °C respectively for 10 minutes each. This resulted in the surface roughness becoming 0.537 nm for (b), 0.694 nm for (c) and 0.721 nm for (d). Figure 7.2 shows the changes in the texture of the active layers due to annealing at different temperatures. We note the vast difference in surface roughness between the as-cast film and the annealed layers. Within the shown temperature range, (65 – 90 °C) the degree of roughness increases with annealing temperature. Also within the same experimental temperatures of 65 – 90 °C, the comparatively outstanding device performance with high power conversion efficiency was obtained with the active layer thermally annealed at 90 °C. This shows that for annealing in the temperature range 65 °C to 90 °C, a positive correlation exists between device performance

and surface roughness of the film. The more the roughness of the film, the higher is the efficiency of the device. The increased surface roughness is believed to be advantageous in increasing the contact area between the active layer and the top metal contact, which should therefore enhance charge collection at the electrode as well as the short circuit current.[26]
Increase in the thermal annealing temperature generates clear phase segregation corresponding to rougher surface of P3HT:PCBM in which the brighter regions are likely to represent PCBM rich domains[27] and the brown hill-like elongations (see Figures 7.3 (b), (c) and (d)) most likely represent P3HT rich domains. The black invasions may be associated with impurities due to fabrication in air. Etxebarria et al[28] demonstrated that in general, three different nano-morphological domains could be formed in polymer:fullerene blends and these are: small, intermediate and large nano-morphology domains. Results obtained in this study suggest that intermediate domains are revealed when films are heat-treated at temperatures up to 140 °C. This temperature range has been found to enhance the interface area, which improves charge generation (implying larger current density J_{sc}) and transport (larger fill factor FF).[22]

Studies have shown that the diffusion length of excitons (and also of charge carriers) in organic materials is often only a few nanometers (4 to 10 nm for exciton in P3HT:PCBM).[2] Therefore only those excitons generated near enough to the polymer-fullerene interfaces will have greater likelihood of successful charge carrier dissociation and transfer. Also, only those charge carriers generated near the electrodes will mainly be collected and contribute to photocurrent. As such, the increased contact area brought about by the favourable thermal annealing enhances charge carrier transfer and efficiency of charge collection at the metal polymer interface. The increased surface roughness might also enhance total internal reflection and improve light collection.[2]
Ibid[2] integrated the surface area of their roughest film and found that the surface area was only 0.1 % more than that of a completely flat surface. This shows that such mechanisms only play a minor role in device efficiency enhancement. Instead, the annealing enhances ordered (crystalline) structure formation, which is indicated by the appearance of vibronic peaks in the absorption spectra.[2] Crystallinity leads to increase in absorption and charge carrier mobility. It is these two processes which most likely account for the significant increase in the power conversion efficiency of annealed P3HT:PCBM based solar cells. Actually, it is mainly the crystallinity of P3HT facilitated by the alluded diffusion of PCBM molecules in aggregates,

which is enhanced by the administration of the tolerable heat treatment. The P3HT molecules are promoted to crystallize in the free region of PCBM that leads to more π–π* absorption.[23]

It has been demonstrated elsewhere[29] that the crystallization-induced structure formation is beneficial for photovoltaic device operation in that the lamellar crystal has an intrinsic size at the 10-nm length scale, which is within the size optimal for exciton dissociation. Whilst PCBM aggregation and crystallization could facilitate electron transport, it is still not clear where exactly the PCBM aggregation takes place. Dang, et al.[29] suggested that it may occur in the inter-lamellar amorphous layer or at the inter-spherulitic grain boundaries and went on to propose that a hierarchical PCBM structure is formed in the blend connecting the 10 nm lamellae to the inter-spherulitic network. In addition, Ibid[29] poses that in combination to the edge-on orientation of P3HT crystals, such self-assembly morphology closely approximates the optimal BJH.

Many studies[2], [19], [22-23] have shown that when the thermal annealing treatment is conducted at temperatures above 140 °C, the devices degrade worse and worse with temperature increase, because the too high annealing temperature generates too large domain sizes with lower interface area between the donor and acceptor.[22] The exaggerated phase segregation between P3HT and PCBM is likely to be the main cause of the deterioration of P3HT:PCBM-based solar cell performance[30-31] at high treatment temperatures like 150 °C and above. Table 7.1 results also help in confirming the deterioration in the performance of such devices at high annealing temperatures through the shown outcome performance of the investigated 160 °C treatment temperature. Charge carrier recombination has also been found to increase at excessive annealing temperatures, because the too high annealing temperature reduces the connected domains and proliferates isolated spherical-like nanoscale PCBM aggregates,[22] which in the main are neither linked to electrodes nor located within the diffusion length of the exciton from its creation site in P3HT. The composite morphology therefore manifests the physical interaction of the donor and acceptor components of BHJ solar cells, which can be optimized by administering thermal annealing at the optimum temperature for optimal duration. This will result in the establishment of the optimized BHJ solar cell that is defined by a deeply quenched bicontinuous composite network of donor and acceptor with maximum interfacial area commensurate with the exciton diffusion length (~ 4 – 10 nm in P3HT:PCBM composite).[32] The poor performance of as-cast nanoscale films is generally attributed to a poorly grown morphology that consists of an

intimately mixed composite of donor and acceptor instead of the bicontinuous network with well-developed and ordered pathways for efficient transport of charge.[32] Good thermal annealing (characterised by optimum temperature and duration) initiates phase-segregation of the two active components (P3HT:PCBM) on a suitable length scale, which allows for maximum ordering (crystallinity) within each phase.[33] This ensures effective charge transport in continuous pathways to the electrodes and minimises recombination of free charges.[32]

7.3.3 Dark and illuminated J(V) characteristics of ITO/PEDOT:PSS/P3HT:PCBM/Al devices due to thermal annealing at different temperatures

7.3.3.1 Dark J(V) output behaviour due to annealing

Figure 7.3 shows the current density versus voltage (J–V) curves in semi-logarithmic representation due ITO/PEDOT:PSS/P3HT:PCBM/Al devices in which, one was the as-cast (control – without post-fabrication thermal treatment) while others were heat treated (thermally annealed) at different temperatures for the same duration after fabrication. All the curves are asymmetric and exhibit diode characteristics, with rectification factors of ~ 7.5×10^2 at 1.0 V. Since the results are due to the same cluster devices, which underwent the same fabrication treatments, using the same active blend, we assume equality of their as-cast states before others were subjected to different heat treatments. From the curves, we note that the response of a given device to thermal annealing over the same duration depends on the treatment temperature. We identify three possible current behaviours attributed to annealing temperature: an increase, decrease or no change in conductivity. Under reverse bias in the low voltage range (0 to ~ – 0.30 V) and the ohmic (linear) as well as the lower section of the exponential region (up to point I) under forward bias, higher values of current density than those of the corresponding as-cast device are displayed by all the annealed devices. The behaviour is according to expectation, because thermal annealing is likely to induce more cemented interchain interactions, which can be conducive to film reordering that result in crystallization of the polymers (P3HT and PCBM) and increased mobility of charge carriers. Film ordering is generally weak in as-cast films. One of the main reasons for this is that the relatively high spin-coating and centrifugal based evaporation speed tends to leave the polymer chains lying in the plain of the film.[34-35] Therefore in most such cases, negligible polymer chains bridge the as-cast electrodes.[13] The 75 °C

annealing temperature manifested high conductivity through production of the highest current density for the entire reverse bias as well as the ohmic and exponential regions under forward bias, a behaviour suggestive of dependence of optimal heat treatment temperature on region of the active nanoscale film.

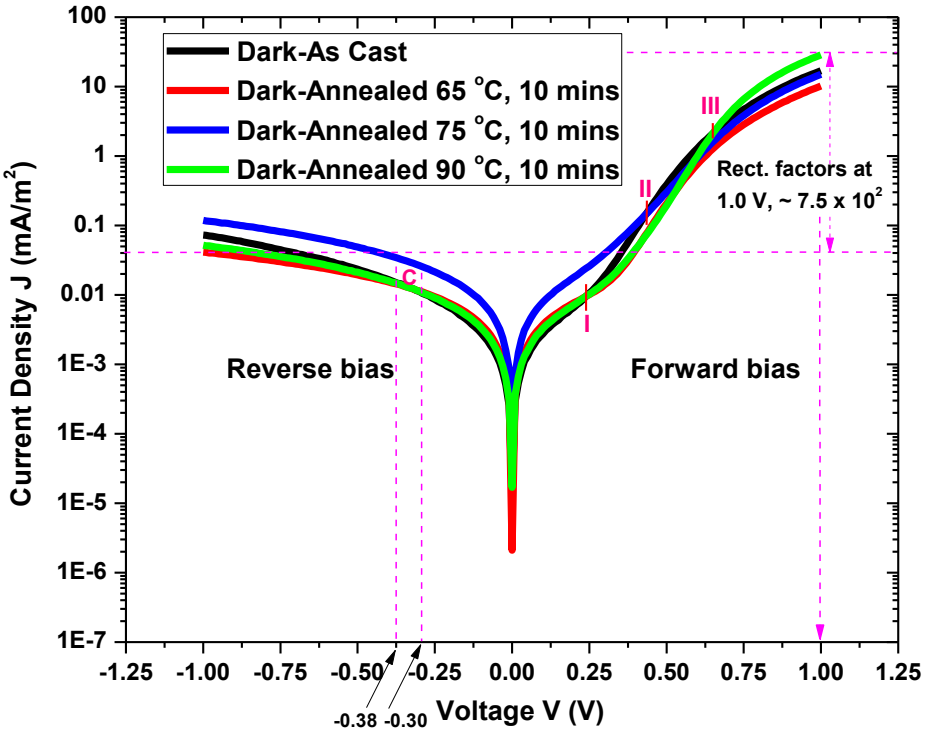

Figure 7.3 *Dark semi-logarithmic scale J–V characteristic curves of ITO/PEDOT:PSS/P3HT:PCBM/Al devices before and after thermally annealing the devices at different temperatures*

In region C between 0.30 V and 0.38 V under reverse bias, the J–V curves for the devices annealed at 65 °C and 90 °C merge with that due to the as-cast, because of the drop in the rate of increase of their plot values. The coincidence of the curves in the identified region shows that the magnitudes of the current densities due to the two annealed devices become equal to their as-cast counterpart in the interval. The explanation for the displayed behaviour in the region by the 65 °C annealed device may be that; although thermal annealing frees the polymers (especially P3HT) of impurities like remnant solvent, water and oxygen, the annealing temperature for the given duration must be below some threshold keep up value of supplied energy,[13] which also depends on the applied (bias) voltage, hence the polymer chains may resort to their as-cast configuration. It also means that the reduction of free volume[13] and consequent increase in

interchain interaction, which usually accompanies low temperature annealing over short periods, should be negligible for the 65 °C annealed device during alignment of its curve with the as-cast.

As for the 90 °C annealed device under reverse bias, the observed decrease in the rate of increase of the current density or conductivity (starting from about middle of the low voltage region (0 to ~ – 0.30 V)) and subsequent alignment with the as-cast in region C may be attributed to greater increase in the potential barrier height at the metal polymer interfaces (due to the relatively higher 90 °C annealing temperature), which limit charge flow and suppress current increase. Furthermore, we also assume that the surface of the blend is made up of P3HT as well as PCBM domains as illustrated in Kadem, et al.[22] Therefore the nature of metal–polymer (Al/P3HT) or metal-fullerene (Al/PCBM) interface varies so as to have a varying energy level alignment across the surface[22] which brings in the existence of potential barriers of different types and magnitudes across the Al/P3HT and Al/PCBM junctions spread.

In the voltage range – 0.38 to ~ – 1.00 V under reverse bias, as well as regions defined by the exponential stretch above point I and the space charge limited current (SCLC) division (II → III) under forward bias, the J–V curves due to devices annealed at 65 °C and 90 °C appear lower than those for their respective as-cast counterparts. Similar behaviour is also witnessed for the 75 °C annealed device from the SCLC division to the entire trap free space charge limited current (TFSCLC) domain in which the 65 °C annealed's curve also stretches below that due to the corresponding as-cast. The curves portray values of current density which magnitude-wise became surprisingly lower than those for the as-cast in the identified regions, because of annealing. This reduction in current density after the annealing exercise may be emanating from dedoping the polymer blend of impurities such as oxygen, remnant solvent and water. The dedoping is likely to have been more rigorous on the 65 °C annealed device under reverse bias in the voltage range – 0.38 to ~ – 1.00 V, since it exhibits the lowest current density values in the region. An impurity like oxygen is likely to have been absorbed from the environment during fabrication in atmospheric air (since the annealing was not conducted under inert surroundings) and also during conduction of the electrical characterisation measurements. As such, a significant amount of oxygen (O_2) molecules is likely to be embedded in the nanoscale thin P3HT:PCBM active blend films. The oxygen dopant has been found to enhance the conductivity of P3HT through the production of localised states within the $\pi - \pi^*$ gap.[18], [36] Low temperature (< 100

°C) annealing over short durations (< 5 minutes) frees the polymer of trapped impurities (ZC), like the alluded remnant solvent, water and oxygen. Oxygen dedoping has been found to lead to a decrease in conductivity.[13] A number of studies have shown that oxygen is one of the substances given off when P3HT based thin film devices are heated[36-37] and also that the density of charge carriers induced by the structural defects and moisture or oxygen may decrease upon heat treatment and lead to drop in conductivity.[13], [37-38] Distinguished scholars[13], [38] explain that due to many traps, especially in n-channel semiconductor devices (like P3HT:PCBM devices), when annealing is conducted, oxygen (enough to act as an electron trap) is easily reduced if the treatment is in air. As a result, oxygen captures the electrons and retains them, thereby making available a higher number of holes in the HOMO of P3HT to contribute to current. Ibid[13] conclude that the observed reduction in conductivity (upon low temperature annealing) may therefore be interpreted as the reduction in electron trapping centres (for example, reduction of oxygen electro-negativity) and hence reduction of trap induced hole density.

Optimum crystallinity in the active layer of the 90 °C annealed device is evident in the TFSCLC division (of Figure 7.3) under forward bias, where it picks up and maintains optimum conductivity (shown by maximum current density display) in comparison to the others. The optimal conductivity exhibited by the 90 °C annealing temperature in the TFSCLC region under forward bias further confirms the dependence of optimum annealing temperature on the region of the active film under consideration. As such, the establishment of a universal optimal annealing temperature that holds for all regions of an organic semiconductor or blend still remains a challenge. The decrease in the rate of increase (slope) of current density in each of the active layers in the TFSCLC region (evidenced by the bowing tendency of each curve) shows that the maximum forward bias current density has not yet been reached (see Figures 7.3 above point III and 7.5 in same TFSCLC region). Such behaviour is likely to be indicating that polymer ordering temperatures may not have been reached by administering low temperature annealing (for example, 65 – 90 °C) on P3HT:PCBM based solar cells. Based on the annealing analysis advanced in this section, we confirm the finding[13] that annealing is a two stage process resulting in a decrease and/or increase in conductivity. In our case, the findings have been based on analysis of experimental results for post-deposition annealing at different temperatures, whereas ibid[13] was based on results from annealing the same device several times. We contribute that

processes which lead to current density either increasing and surpassing the as-cast counterpart value (note intersection III) or decreasing and falling below the as-cast value (note intersections I, II and C) strengthen the premise[13] that both impurity dedoping and film ordering effects may take place simultaneously all the time, with one effect being more effective than the other. We also remind that excessively high temperatures may either degrade/lower the device performance, due to conformational changes[13], [39] within the active blend materials or may permanently destroy it.

We also investigated annealing mechanisms associated with heat treatment of P3HT:PCBM-based solar cells at different intermediately high temperatures, in the range 100 to 140 °C.

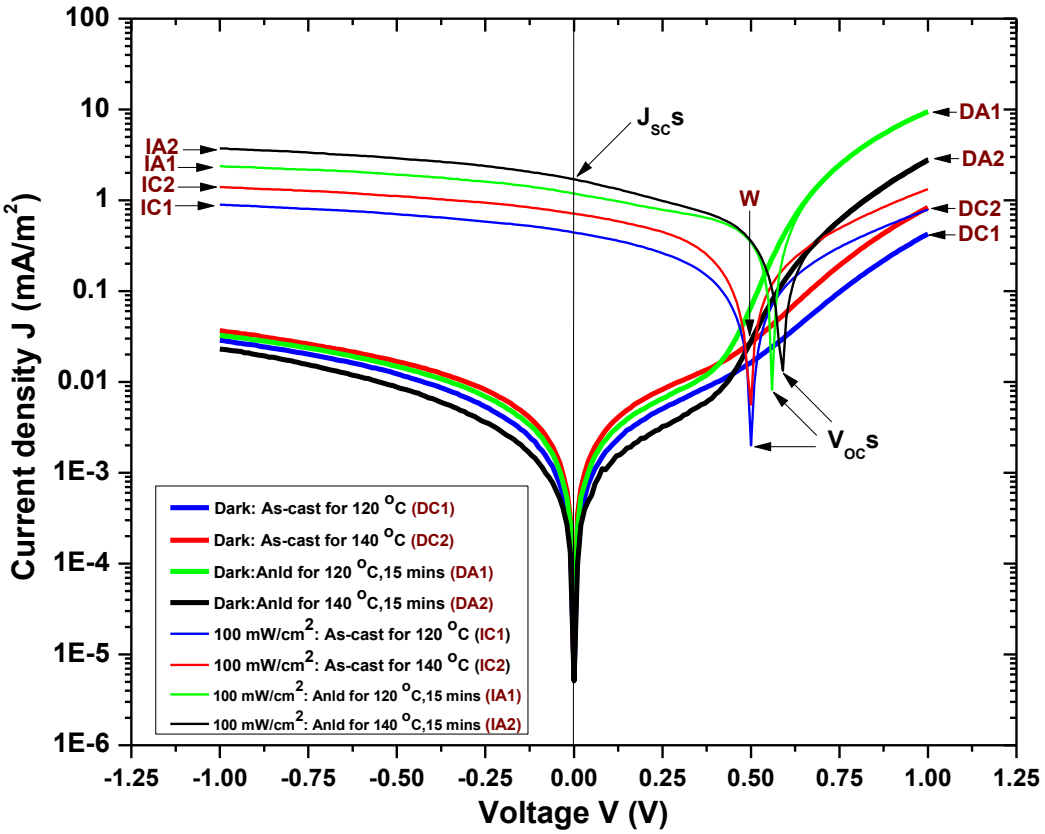

Figure 7.4 *Comparative dark and 100 mW/cm^2 illuminated J-V curves of the as-cast and heat-treated (120 °C and 140 °C) P3HTPCBM-based solar cells in semi-logarithmic representation. The key for the abbreviations is: DC1→under Dark Control curve 1 (implying curve is from the control (that is, as-cast or reference) cell* 1)). Likewise, DC2→*Dark Control curve 2, DA1→Dark Annealed curve 1, DA2→Dark Annealed curve 2, IC1→Illuminated Control curve 1, IA1→Illuminated Annealed plot 1, etc.*

The resultant behaviour of the annealed devices and their as-cast counterparts are summarised by the J(V) characteristics which emanated from devices annealed at 120 and 140 °C and are here exhibited in semi-logarithmic representation by Figure 7.4.

The curves DC1, DC2, DA1 and DA2 show the dark J–V characteristics before and after annealing the solar cells. Abbreviations have been explained in the Figure's foot-note. We note that the dark current density for the 140 °C annealed device DA2 decreased significantly to values lower than those due to the as-cast counterpart DC2 for the entire reverse bias connection and up to about half-way up the exponential domain under forward bias. From then on (about midway up the exponential territory at intersection W) under forward bias, the DA2 current density surpasses that due to its corresponding as-cast and becomes much higher. This behaviour substantiates the assertion put forward earlier in this section that annealing of polymers is a two-step process which first causes a decrease in conductivity, followed by its increase. As explained under the 65 – 90 °C annealing, the process is also here confirmed by this under dark J(V) analysis of the 140 °C annealing. The decrease in the current density to below the as-cast counterpart is mainly due to impurity dedoping and the subsequent increase in conductivity should be due to reordering of polymer chains and crystallization which assume at higher applied voltages corresponding to the exponential region and above.

Upon illumination, higher J_{sc} (which is now photogenerated short circuit current density corresponding to curve IA2 in Figure 7.4) is witnessed in the device which had been annealed at a higher temperature (140 °C).This suggests that more reordering and crystallization must have taken place during annealing. Both J_{sc} and V_{oc} increase with increase in post-fabrication annealing temperature and also exhibit higher magnitudes than their as-cast counterparts.

7.3.3.1.1 Conduction manifestations in ITO/PEDOT:PSS/P3HT:PCBM/Al devices due to annealing

In this sub-section we undertake an exploratory interpretation of the dark forward bias (FB) J–V characteristic curves of as-cast and annealed ITO/PEDOT:PSS/P3HT:PCBM/Al devices in double-logarithmic representation in order to gain insight into the conduction behaviour of the active layers heat-treated at different temperatures. In Figure 7.4 we show the obtained J–V curves due to the

devices comprised of the as-cast and those thermally annealed at different temperatures, in double logarithmic scale under forward bias.

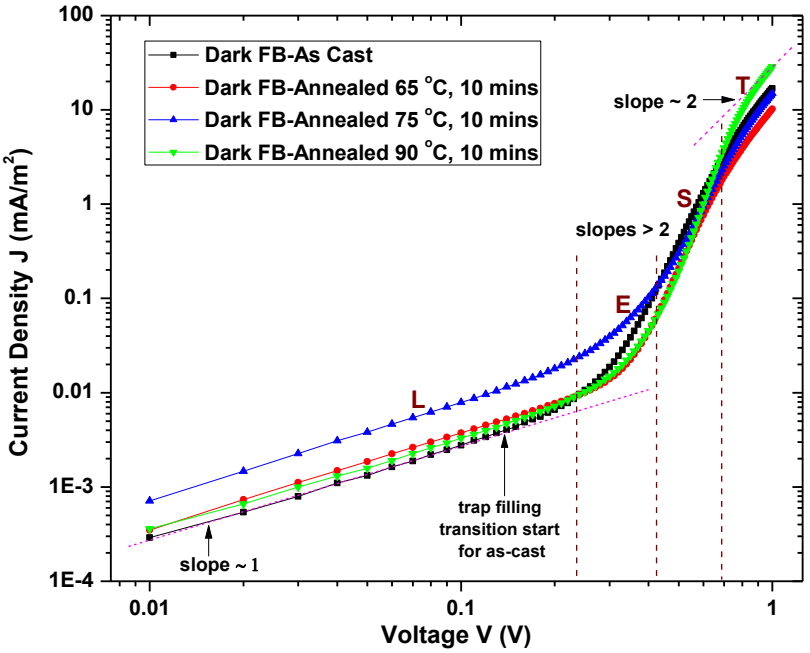

Figure 7.5 *Dark forward bias (FB) J–V characteristic curves of ITO/PEDOT:PSS/P3HT:PCBM/Al devices in double-logarithmic scale before and after being thermally annealed at different temperatures*

The conduction behaviour in each of the devices is sourced from the slope of the curve. At low voltages (region L) the slopes of the J–V curves are approximately equal to 1 for both as-cast and all the annealed devices, which indicate compliance with Ohm's law. J therefore linearly depends on voltage V in this region. The slope associated with each of the curves in region T is about 2, and it indicates trap-free space charge limited current (TFSCLC) conduction. The steepest slopes (> 2) characteristic of the exponential (E) and space charge limited current (SCLC) conduction (S) regions indicate charge flow impregnated with the filling of traps distributed exponentially or Gaussianly within the π–π* gap.[40-41] On a related side note, if a J–V curve in double-logarithmic scale is parallel to the J axis, it indicates that the traps are distributed in a discrete energy level within the π–π* gap.[13]

The slopes of the family of curves in Figure 7.4 are seen to increase from about 1 in the ohmic region to values greater than 2 in region E as well as S and finally fall back to about 2 in region T. The transition from a gentle slope in linear (ohmic) region L to a steep slope in regions E and

S takes place slowly for the as-cast device. This gradual increase of slope behaviour by the as-cast device means that traps of continuous distribution in energy (which are in the as-cast active thin film) are now being filled. Furthermore, we note that this trap filling regime (accompanying the transition process and continuing in regions E and S) commences at much lower voltages (see Figure 7.4) for the as-cast device than for the annealed sample. Since the traps seem easier to fill (assuming such to be the well based interpretation of the observed leading start) it becomes most likely that they are shallow traps, which dominate the as-cast device.

For the annealed devices, the start of trap filling in each device occurs at a comparatively higher starting voltage, which is commensurate with the annealing temperature. The lagged trap filling start in the annealed devices (interpreted from the delayed transition (Figure 7.4) from gentle to steep slopes for the annealed devices) suggests that most of the shallow traps have vanished in the annealed devices as a result of the annealing. This confirms the claim that the density of shallow traps dwindles with thermal annealing temperature. Though delayed, the sudden transition from gentle slope in ohmic region to sharp steepness in exponential and SCLC regions, (which is characteristic of annealed devices) is suggestive of the filling of traps located in discrete energy levels.

7.3.3.1.1.1 Space charge limited current (SCLC) model for charge carrier mobility (μ)

The J(V) characteristics (shown in Figure 7.4) which we plotted for each sample device in double-logarithmic representation under forward bias, is based on the SCLC model for charge transport. We used these established characteristics to estimate the charge carrier mobility μ in the TFSCLC region of the (P3HT:PCBM) active layer of each experimental device. For ease of understanding, we remind that the J–V measurements were carried out in the dark in order to focus the investigation on the diode behaviour of the solar cells under study. In the TFSCLC region, the space charge limited current conduction theory is described by Child's law[42]

$$J = \frac{9}{8}\varepsilon\,\varepsilon_0\,\mu\frac{V^2}{d^3} \qquad (7.1)$$

where, *d* is the active layer thickness, which we assumed constant at 77.1 nm.

Using data in this region, the charge carrier mobility ascribed to the active layer of each device in this region was estimated by plotting J vs V^2/d^3. The obtained variation of charge carrier

mobility μ with thermal annealing temperature is included in Table 7.1. The charge carrier mobilities are very low. This is likely to be due to structural disorder and (the under dark detected) impurity dedoping in the active layer, which immobilizes electrons. The results also substantiate the findings that charge carrier mobility increases with post-fabrication annealing temperature. Literature[22] has found that above 140 °C charge mobility decreases, as results for the 160 °C annealed device show in Table 7.1. We attribute this to the exaggerated increase in the phase separation describing the downwardly changed film morphology, caused by the intolerably high heat treatment temperature, which degrades or even destroys the percolation pathways.

7.3.3.1.1.2 Richardson–Schottky (RS) thermionic emission model and barrier potential (ϕ_B)

The Richardson–Schottky (RS) thermionic emission model was invoked for use in determining the barrier potential (ϕ_B) dependence on the annealing temperature in the studied polymer-fullerene solar cells. These are the potential barriers which build up at the metal-polymer interfaces of the metal electrodes and the active organic materials forming the device (for example, Al/PCBM, Al/P3HT, ITO/PEDOT:PSS/P3HT interfaces in our case). The physics of the formation of such barriers was presented in chapters 1 to 3 of this thesis. J–V characteristics can be described by the equation.[43]

$$J = J_0 \exp\left(\frac{qV}{n\,k\,T}\right) \tag{7.2}$$

where J_0 is the reverse saturation current density, n is the ideality factor, T is the thermodynamic temperature, k is Boltzmann constant and q is the elementary charge. Above the ohmic region, the current voltage characteristics may be fitted to the Richardson–Schottky model

$$J = A^{*}T^{2} \exp\left(\frac{-\phi_B}{kT}\right) \exp\left[\left(\frac{q^3 V}{4\pi\varepsilon_0\varepsilon_r d}\right)^{\frac{1}{2}} \div kT\right] \tag{7.3}$$

where A^{*} is the effective Richardson constant, ε_0 is the permittivity of free space = 8.854×10^{-12} Fm^{-1} and ε_r is the relative permittivity ≈ 3.5 for 1:1 P3HT:PCBM.[22] Assuming no image force

lowering effect, the reverse saturation current density J_0 can be described by the RS thermionic emission model, from which equations (7.2) and (7.3) give

$$J_0 = A^* T^2 \exp\left(\frac{-\phi_B}{kT}\right). \tag{7.4}$$

From equation (7.4), the potential barrier height ϕ_B is then given by

$$\phi_B = \frac{kT}{q} \ln\left(\frac{A^* T^2}{J_0}\right) \tag{7.5}$$

To find J_0, use is made of equation (7.2), from which

$$\ln J = \ln J_0 + \left(\frac{qV}{nkT}\right) \tag{7.6}$$

Therefore the graph of $\ln J$ versus V should be a straight line of slope = $\frac{d \ln J}{dV} = \frac{q}{nkT}$, from

which $$n = \frac{q}{kT}\left(\frac{dV}{d \ln J}\right) \tag{7.7}$$

and $\ln J_0$ = *intercept of graph on ln J axis*, which gives: $J_0 = e^{\text{intercept}}$ (7.8)

Use of equations (7.5), (7.6) and (7.8) was then made to determine the variation of the potential barrier height ϕ_B with thermal annealing temperature for each experimental device. The findings are summarised in Table 7.1.

The results show that the potential barrier height increases with increase in post-fabrication annealing temperature for low temperature annealing, but decreases at overly high temperatures exemplified by the included 160 °C result. It has been shown elsewhere[22] that the ϕ_B increase with heat treatment temperature relationship holds for up to approximately 140 °C. The variation in the barrier height with post-fabrication thermal annealing at different temperatures could be attributed to recombination[22, 44] since the ideality factor *n*, was found to decrease with heat treatment (see Table 7.1) up to about 135 °C (not shown in Table 7.1). The ideality factor is a figure of merit for charge carrier recombination mechanism in a semiconductor diode, like our experimental organic solar cell. Charge carrier recombination may take place at the metal-polymer interface as charge attempts to cross the depletion region adjacent to the junction or it may occur in the bulk. The ideality factor is more on happenings at the metal-polymer junction

where the potential barrier is encountered by the charge. A diode ideality factor of 1 means direct recombination of electrons and holes across the bandgap (bimolecular recombination). We spin coated a layer of PEDOT:PSS to form the ITO/PEDOT:PSS electrode, partly in order to block the flow of electrons to the ITO electrode. An ideality factor of 2 is interpreted as recombination through defect states, that is, recombination centres.[45]

Increase of potential barrier height with treatment temperature is also evidenced by the obtained Fowler-Nordheim (FN) plots of Figure 7.6, which show increasing steepness of the straight sections of the plots at high voltages as the annealing temperature increases. In conformity with expectation, the steepest plot at relatively high applied voltages of about 0.5 V (which implies highest potential barrier of the sample) is that due to the device annealed at 90 °C.

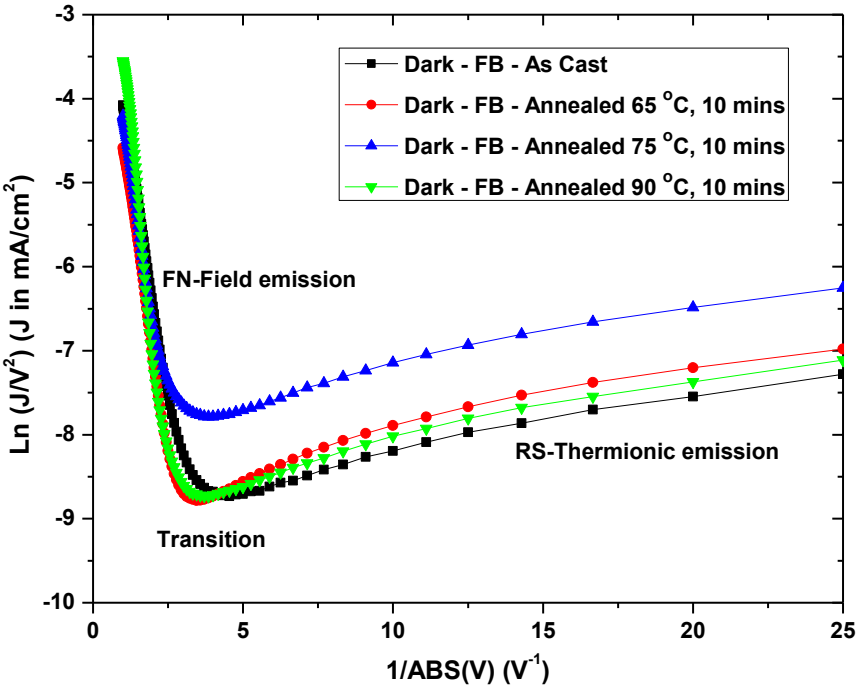

Figure 7.6 *Fowler-Nordheim plots for charge carrier injection into potential barriers at metal-polymer interfaces of ITO/PEDOT:PSS/P3HT:PCBM/Al devices, composed of one as-cast and others heat-treated at different temperatures*

The FN plots show that at high forward bias voltages, the curves due to as-cast and annealed devices coincide, a behaviour which is likely to be expressing that at such high voltages, space charge in the annealed devices limits the current in the same way as in the as-cast devices,

although most of the shallow traps must have vanished in the annealed. Both impurity dedoping and thermally induced chain reordering may be taking place at the same time in the active layers of the devices annealed at such temperatures.

7.3.3.2 J(V) output characteristics of illuminated P3HT:PCBM based solar cells subjected to different annealing temperatures

J–V measurements of the sample P3HT:PCBM based photoactive devices were conducted under AM1.5 solar simulator source of varying illumination intensity from 0.1 to 100 mW/cm^2 for the control device and each of the experimental devices heat treated at different temperatures after fabrication. Table 7.1 presents a comparative summary of the quantitatively exhibited photovoltaic performance, under 100 mW/cm^2 illumination, of the alluded experimental devices comprising the control (untreated) and the heat treated batch.

Table 7.1 *Typical output values of parameters of merit summarising the electrical characteristics of the (double carrier) ITO/PEDOT:PSS/P3HT:PCBM/Al devices at 100 mW/cm^2 incident white light* illu*mination before and after thermal annealing at different temperatures, for the same time duration of 10 minutes*

Device Descript.	**J_{sc} (mA/cm^2)**	**V_{oc} (V)**	**Fill Factor FF**	**Mobility μ $\times 10^{-6}$ (cm^{2}V^{-1}s^{-1})**	**Ideality factor *n***	**Barrier Pot. ϕ_B (eV)**	**Efficiency η (%)**	**η % increase/ decrease**	**Series Res. R_s (Ω)**	**Shunt Res. R_{sh} (Ω)**
As-cast	3.9625	0.48	0.3584	1.83	2.73	0.64	0.68	–	70.7	228.57
Annealed at 65 °C (for 10 mins)	5.1625	0.53	0.3596	1.91	2.45	0.73	0.98	+ 44.12	55.3	177.78
Annealed at 75 °C (for 10 mins)	5.4250	0.58	0.3768	1.94	2.43	0.77	1.19	+ 75.00	41.1	228.57
Annealed at 90 °C (for 10 mins)	7.7750	0.62	0.4108	2.16	2.33	0.81	1.64	+ 141.18	29.2	264.08
Annealed at 160 °C (for 10 mins)	0.8137	0.44	0.3041	1.37	2.81	0.74	0.11	– 83.82 **decrease**	383.0	765.55
% change: As-cast vs Annealed 90°C	**+ 96.21 increase**	**+ 29.17 increase**	**+ 14.62 increase**	**+ 18.03 increase**	**– 14.65 decrease**	**+ 26.56 increase**	**+ 141.18 increase**		**– 58.70 decrease**	**+ 15.54 increase**

The performance is described by the organic solar cell parameters of merit as a function of different heat-treatment temperatures. Of the shown treatment temperatures, the best

photovoltaic performance was demonstrated by the device heat treated at 90 °C, which produced power conversion efficiency PCE (η) = 1.64 %, V_{oc} = 0.62 V, J_{sc} = 7.78 mA cm^{-2} and FF = 0.4108, whereas the as-cast device had PCE = 0.68 %, V_{oc} = 0.48 V, J_{sc} = 3.96 mA cm^{-2} and FF = 0.3584. The increase in power conversion efficiency is over 2.4 times the value of the as cast. The value of the short circuit current density almost doubled upon annealing. This improvement can be attributed to increased charge mobility[46-47] in the active layer, because of the improved crystallinity of the active composite and the reduced charge carrier recombinations for the annealed device, shown by the decreased ideality factor *n*. Increases in the open circuit voltage and fill factor can be attributed to the burning of shunts. Upon thermal treatment at 160 °C, the values of the figures of merit fell to PCE = 0.11 %, V_{oc} = 0.44 V, J_{sc} = 8137 mA cm^{-2} and FF = 0.3041. This substantiates the degradation of polymer-fullerene solar cells upon heat treatment at intolerably high temperatures. Series resistance (R_s) is seen (in Table 7.1) to have decreased with increase in annealing temperature, with the 90 °C annealed device exhibiting a 58.70 % decrease in series resistance when compared with its as-cast counterpart. This welcome decrease in R_s contributes to improvement in the performance of the favourably annealed device.

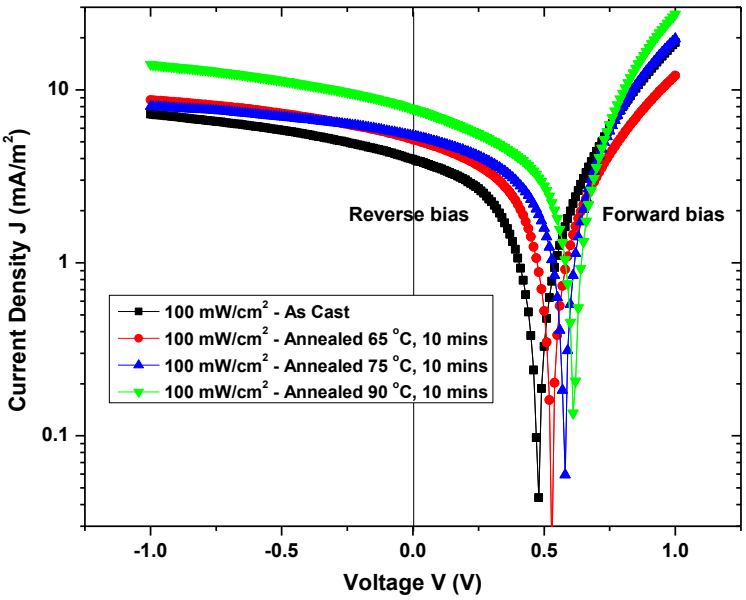

Figure 7.7 *Semi-logarithmic scale representation of the output J(V) characteristic curves of ITO/PEDOT:PSS/P3HT:PCBM/Al devices at 100 mW/cm^2 incident white light illumination before and after thermal annealing at different temperatures*

In Figure 7.6 we present comparative semi-logarithmic representation of the as-cast (control) and the post-treatment output J(V) curves of the sample devices under 100 mW/cm^2 white light illumination. The magnitudes of both the short circuit current density J_{sc} and the open circuit voltage V_{oc} show increase with thermal annealing temperature.

7.4 Conclusions

This investigation revolved around attempts to empirically broaden and deepen the presently scarce understanding of the fundamental mechanisms defining thermal annealing process in conjugated polymers. To achieve this, we studied the opto-electrical effects of post-fabrication thermal annealing of bulk heterojunction ITO/PEDOT:PSS/P3HT:PCBM/AL solar cells at different heat treatment temperatures in the range 65 – 160 °C. The photoactive P3HT:PCBM layer was cast in air. The effect of air exposure has been found to chemically dope the polymer, creating conducive pathways within the blend. Furthermore, this doping has been found to be responsible for the comparatively superior photovoltaic performances of as-cast devices when compared to their annealed counterparts in certain regions of the active films. As for the annealed devices, dedoping brought in by thermal annealing has been demonstrated to be responsible for the aggravated drop of efficiency. The given summary findings lead to the generalisation that annealing of polymers is a two-step process, which first causes a decrease in conductivity, followed by its increase.

Although impurity dedoping decreases 'under dark' current density in certain regions of the active P3HT:PCBM composite layer during annealing, it has beneficial aftermaths, some of which surface upon illumination of the P3HT:PCBM-based solar cell. When illuminated, photogenerated current density in the illuminated device immediately increases. This happens so, because of less electron capture and immobilization during illumination of the annealed device, since such mechanisms were minimised upon impurity dedoping during annealing. Therefore more electrons and holes take part in photocurrent generation. The photo-induced electron transfer at the P3HT:PCBM interface should be almost 100 % efficient after annealing (especially if the annealing is executed at optimum temperature and duration) because the annealing must have closed the traps which had been created by air-borne impurity doping.

Morphologically, thermal annealing has been found to enhance the formation of the deeply quenched bicontinuous network at the nanoscale between P3HT and PCBM, leading to high efficiency devices. We propose that the beneficial structure formation in P3HT:PCBM blends which is initiated by the crystallization of P3HT as it segregates PCBM, possibly to the amorphous P3HT phase (as the solvent rapidly evaporates during active layer casting by spin coating, followed by the slow shelf drying) is more promoted by post-fabrication thermal annealing.

It has been demonstrated elsewhere[29] that the crystallization-induced structure formation is beneficial for photovoltaic device operation in that the lamellar crystal has an intrinsic size at the 10-nm length scale, which is within the size optimal for exciton dissociation. Whilst PCBM aggregation and crystallization could facilitate electron transport, it is still not clear where exactly the PCBM aggregation takes place. Dang, et al.,[29] suggested that it may occur in the inter-lamellar amorphous layer or at the inter-spherulitic grain boundaries and went on to propose that a hierarchical PCBM structure is formed in the blend connecting the 10 nm lamellae to the inter-spherulitic network. In addition, ibid[29] poses that in combination to the edge-on orientation of P3HT crystals, such self-assembly morphology closely approximates the optimal BJH.

Thermal annealing renders significant enhancement in J_{sc}, V_{oc} and *FF* of the annealed device. The optical absorbance was found to increase with increase in annealing temperature and the thermal annealing temperature of ~ 140 °C seems to be indicative of the required optimal annealing temperature for optimum power conversion efficiency of the bulk heterojunction 1:1 P3HT:PCBM based solar cells.

7.5 References

[1] Huang, H.-T; Lee, C.-T. and Lee, H.-Y. *Performance improvement mechanisms of P3HT:PCBM inverted polymer solar cells using extra PCBM extra P3HT interfacial layers.* Org. Electron. 21; 2015.

[2] Gang, L.; Shrotriya, V.; Yao, Y. and Yang, Y. *Investigating the annealing effects and film thickness dependence of polymer solar cells based on poly,,(3-hexylthiophene).* Journal of Applied Physics 98; 2005.

[3] Brabec, C.J.; Sariciftci, N.S. and Hummelen, J.C. *Plastic Solar Cells. Advanced* Functional Materials, 11 No. 1; 2001.

[4] Brabec, C.J.; Dyakonov, V.; Parisi, J. and Sariciftci, N.S. *Organic Photovoltaics: Concepts and Realizations.* Springer, Heidelberg; 2003.

[5] Chen, Fang-Chung; Xu, Qianfei and Yanga, Yang. *Enhanced efficiency of plastic photovoltaic devices by blending with ionic solid electrolytes.* Applied Physics Letters Volume 84, No. 16; 2004.

[6] Sirringhaus, H.; Brown, P.J.; Friend, R.H.; Nielsen, M.M.; Bechgaard, K.; Langeveld, B.M.W.; Spiering, A.J.H.; Janssen, R.A.J.; Meijer, E.W.; Herwig, P. and de Leeuw, D.M. *Two-Dimensional Charge Transport in Self-Organized, High-Mobility Conjugated Plymers.* Nature, Vol. 401; 1999.

[7] Mihailetchi, V.D.; Xie, H.X.; de Boer, B,; Koster, L.J.A. and Blom, P.W.M. *Charge transport and photocurrent generation in poly (3-hexylthiophene): methanofullerene bulk-heterojunction solar cells.* Advanced Functional Materials, 16: 2006.

[8] Schilinsky, P.; Waldauf, C and Brabec, J. *Recombination and loss analysis in polythiophene based bulk heterojunction photodetectors.* Applied Physics Letters, Vol. 81, No. 20; 2002.

[9] Dimitrov, S.D.; Schroeder, B.C.; Nielsen, C.B.; Bronstein, H.; Fei, Z.; McCulloch, I.; Heeney, M. and Durrant, J.R. *Singlet Exciton Lifetimes in Conjugated Films for Organic Solar Cells*. MDPI Polymers; 2016.

[10] Zen, A.; Pflaum, J.; Hirschmann, S., Zhuang, W.; Jaiser, F.; Asawapirom, U.; Rabe, J.P.; Scherf, U. and Neher, D. *Effect of Molecular Weight and Annealing of Poly(3-hexylthiophene)s on the Performance of Organic Field-Effect Transistors.* Advanced Functional Materials, Vol. 14, No. 8; 2004.

[11] Al-Ibrahim, M.; Ambacher, O.; Sensfuss, S. and Gobsch, G. *Effects of Solvent Annealing on the Improved Performance of Solar Cells based on Poly(3-Hexylthiophene):Fullerene.* Applied Physics Letters, Vol. 86, No. **20**; 2005.

[12] Kim, Y.; Stelios, A.C.; Nelson, J.; Cook, D.D.C.B.S. and Durrant, J.R. *Device Annealing Effect in Organic Solar Cells with Blends of Regioregular Poly(3-Hexylthiophene) and Soluble Fullerene.* Applied Physics Letters, Vol. 86, No. **6**; 2005.

[13] Chiguvare, Z; Parisi, J. and Dyakonov, V. *Influence of Thermal Annealing on the Electrical Properties of Poly(3-hexylthiophene)-Based Thin Film Diodes.* Z Naturforsch **62a**, 609 – 619; 2007.

[14] Burroughes, J.H.; Bradley, D.D.C.; Brown, A.R.; Marks, R.N.; Mackay, K.; Friend, R.H.; Burn, P.L. and Holmes, A.B. *Light-emitting diodes based on conjugated polymers*. Nature, 347:539; 1990.

[15] Ho, P.K.H.; Granström, M.; Friend, R.H. and Greenham, N.C. *Ultrathin self-assembled layers at the ito surface to control charge injection and electroluminescence efficiency in polymer light-emitting diodes made from soluble conducting polymers*. Nature, 357:477; 1992.

[16] Gustafsson, G.; Cao, Y.; Treacy, G.M.; Klavetter, F.; Colaneri, N. and Heeger, A.J. *Flexible light emitting diodes made from soluble conducting polymers*. Nature, 357:477; 1992.

[17] Davids, P.S.; Campbell, I.H. and Smith, D. L.; Device model for single carrier organic diodes. *J. Appl. Phys.*, 82:6319, 1997.

[18] Chiguvare, Z. *Electrical and Optical Characterisation of Bulk Heterojunction Polymer – Fullerene Solar Cells*. *PhD Thesis* 26; 2004.

[19] Hamad, M. K.; Al-luaiby, H.F.; Hussain, W.A. and Hassan, A.K. *Post-fabrication annealing effects on the performance of polymer:Fullerene solar cells with ZnO nanoparticles.* Chemistry and Materials Research Vol. 6 No. 6; 2014.

[20] Erb, T.; Zhokhavets, U.; Hoppe, H.; Gobsch, G.; Al-Ibrahim, M. and Ambacher, O. *Thin solid films, absorption and crystallinity of poly(3-hexylthiophene)/fullerene blends in dependence on annealing temperature.* Thin Solid Films, **511**, (483 – 485); 2006.

[21] Al-Ibrahim, M.; Ambacher, O. *Effects of solvent annealing on the improved performance of solar cells based on poly(3-hexylthiophene):fullerene.* Applied Physics Letters, Vol. **86**, 201120; 2005.

[22] Kadem, B.; Hassan, A.K. and Cranton, W.M. *Efficient P3HT:PCBM bulk heterojunction organic solar cells; effect of post deposition thermal treatment.* Journal of Materials Science Materials in Electronics, Springer Science+Business Media New York; 2016

[23] Islam, Md. S.; Islam, Md. E.; Ismail, A.B.Md. and Baerwolff, H. *Influence of Thickness and Annealing Temperature on the Optical Properties of Spin-Coated Photoactive P3HT:PCBM Blend.* Optics and Photonics Journal, 3, 28 – 32; 2013.

[24] Yu Xuan; Yu Xiao-ming; Hu Zi-yang; Zhang Jian-jun; Zhao, G. and Zhao, Y. *Efficiency enhancement of polymer solar cells by post-additonal annealing treatment.* Springer Link – optoelectronics Letters, Volume 9, Issue 4; 2013.

[25] Sun, Y.; Liu, J.-g.; Ding, Y. and Han, Y. c. *Controlling the surface composition of P3HT/PCBM blend film by using mixed solvents with different evaporation rates.* Chin.J. Polym. Sc. **31**(7) 1029–1037; 2013.

[26] Ma, W.; Yang, C.; Gong, X.; Lee, K. and Heeger, A.J. *Thermally stable, efficient power solar cells with nanoscale control of the interpenetrating network morphology.* Adv. Funct. Mater. **15**, 1617 – 1622; 2005.

[27] Parlak, E.A. *The blend ratio effect on the photovoltaic performance and stability of poly (3-hexylthiophene):[6, 6]-phenyl-C61 butyric acid methyl ester (PCBM)and poly(3-octylthiophene):PCBM solar cells.* Sol. Energy Mater. Sol. Cells **100**, 174 – 184; 2012.

[28] Etxebarria, I.; Ajuria, J. and Pacios, R. *Solution-processable polymeric solar cells: a review on materials, strategies and cell architectures to overcome 10* %. Org. Electron. **19**, 34 – 60; 2015.

[29] Dang, M.T.; Wantz, G.; Hirsch, L. and Parneix, J. *Solution processing of polymer photoactive solar cells in air and under inert atmosphere.* The Electrochemical Society (ECS) Transactions 23 (1); 2009.

[30] Watts, B.; Belcher, W.J.; Thomsen, L.; Ade, H. and Dastoor, P.C. *A quantitative study of PCBM diffusion during annealing of P3HT:PCBM blend films.* Macromolecules **42**(21), 8392 – 8397; 2009.

[31] Lee, J.U.; Jung, J.W.; Emrick, T.; Rusell, T.P. and Jo, W.H. *Morphology control of a Polythiophene-fullerene bulk heterojunction for enhancement of the high-temperature stability of solar cell performance by a new donor-acceptor diblock copolymer.* Nanotechnology **21**, 105201; 2010.

[32] Thompson, B.C. and Fréchet, J.M.J. *Polymer–Fullerene Composite Solar Cells.* Angew. Chem. Int. Ed. 47, 58 – 77; 2008.

[33] Chu, C-W.; Yang, H.; Hou, W-J.; Huang, J.; Li, G. and Yang, Y. *Control of the nanoscale crystallinity and phase separation in polymer solar cells.* Appl. Phys. Lett., Volume 92, Issue 10, Online: https://dx.doi.org/10.1063/1.2891884; 2008.

[34] McBranch, D.; Campbell, I.H.; Smith, D.L. and Ferraris, J.P. *Optical determination of chain orientation in electroluminescent polymer films.* Appl. Phys. Lett. **66**, 1175; 1995

[35] Schaller, R,D.; Snee, P.T.; Johnson, J.C.; Lee, L.F.; Wilson, K.R.; Haber, L.H.; Saykally Thuc-Quyen Nguyen, R.J. and Schwartz, B.J. *Nanoscopic interchain aggregate domain formation in conjugated polymer films studied by third harmonic generation near-field scanning optical microscopy.* The Journal of Chemical Physics, Volume 117, Issue 14, Online: https://doi.org/10.1063/1.1499479; 2002.

[36] Mattis, B.A.; Chang, P.C. and Subramanian, V. Effect of thermal cycling on performance of poly(3-hexylthiophene) transistors. Mat. Res. Soc. Symp. Proc.,771:L10.35.1; 2003.

[37] Nakazono, M.; Kawai, T. and Yoshino, K. *Effects of heat treatment on properties of poly(3-alkylthiophene).* Chem. Mater.,6:864, 1994.

[38] Horowitz, G. *Organic field-effect transistors.* Adv. Mater., 10:365, 1998.

[39] Kim, J.; Lee, J.; Han, C.W.; Lee, N.Y. and Chung, I.-J. *Effect of thermal annealing on the lifetime of polymer light-emitting diodes.* Appl. Phys. Lett. 82, 4238; 2003.

[40] Lampert, M.A. and Mark, P. *Current Injection into Solids.* Academic Press, New York; 1970.

[41] Kao, K.C. and Hwang, W. *Electrical Transport in Solids, with particular reference to organic semiconductors*. Vol. 14 of International Series in the Science of the Solid State, Pergamon Press, Oxford 1981.

[42] Apaydin, D.H.; Yildiz, D.E.; Cirpin, A. and Toppare, L. *Optimizing the organic solar cell efficiency: roll of the active layer thickness.* Sol. Energy Mater. Sol. Cells 113, 100–105; 2013.

[43] Güllü, Ö.; Aydoğan, Ş. and Türüt, A. *High barrier Schottky diode with organic interlayer*. Solid State Commun. **152** (5), 381–385; 2012.

[44] Shrotriya, V. and Yang, Y. *Capacitance–voltage characterization of polymer light-emitting diodes.* Journ. Appl. Phys. **97**, 054504; 2005.

[45] Deibel: https://blog.disorderedmatter.eu/2016/05/14/the-diode-ideality-factor-in-organic-solar-cells- recombination

[46] Sarah, M.S.P.; Zahid, F.S.S. and Rusop, M. *Investigation on I-V Different Heating Temperatures of nanocomposited MEH-PPV:CNTs Organic Solar Cells.* Hindawi Publishing Corporation International Journal of Photoenergy, Volume 2012, Article ID 872324, 6 pages doi: 10.1155/ 2012/872324; 2012.

[47] Reyes-Reyes, M.; Kim, K. and Carroll. D.L. *High-efficiency photovoltaic devices based on annealed poly(3-hexylthiophene) and 1-(3-methoxycarbonyl)-propyl-1- phenyl-(6,6)C61(6,6)C61 blends.* Appl. Phys. Lett. **87**, 083506; 2005.

Chapter 8

Conclusions and recommendations

8.1 Conclusions

To broaden and deepen our understanding of opto-electrical characteristics of bulk heterojunction polymer-fullerene solar cells (for cell performance improvement), we studied the structure formation and opto-electronic behaviour manifestations of 1:1 regioregular poly (3-hexylthiophene 2,5 diyl) (P3HT):[6,6] phenyl-C61 butyric acid methyl ester (PCBM) blend based devices and arrived at the following conclusions:

- The observed threshold open circuit voltage at which efficiency (that is, external quantum efficiency (EQE)) starts to decrease ($V_{oc\ threshold\ efficiency\ decrease}$) in conjugated polymer-fullerene based solar cells, indicates the value of $V_{oc\ threshold\ tunneling\ onset}$, which is the threshold internal open circuit voltage within the organic solar cell device, corresponding to the onset of field emission (FN quantum mechanical tunneling) injection of charge through the potential barrier at the metal-polymer interface.

- Under good device architecture, $V_{oc\ threshold\ efficiency\ decrease} \approx V_{oc\ threshold\ tunneling\ onset} \approx 0.46$ V.

- Transition from thermionic to field emission is not an instantaneous event, but is rather a gradual process, although the time it takes is still very small.

- The minimum of the FN curve indicates the end of thermionic emission dominance as well as the start of the superiority of quantum mechanical tunneling (field emission).

- The FN internal voltage suppressing thermionic emission is actually the open circuit voltage built within the device. In the case of our ITO/PEDOT:PSS/P3HT:PCBM/Al device, this is the electromotive force between the PCBM LUMO and the P3HT HOMO.

- The total current in an ***electrode/organic semiconductor/metal*** photoactive device is the superposition of the thermionic emission and the quantum tunneling currents.

- Based on our findings, we have explained the electrical behaviour of decrease in efficiency as incident light intensity increases by generalising that as the incident white light intensity increases, it also increases the photogenerated open circuit voltage, which increasingly biases the device with voltages that are sufficient to greatly increase the dark current. Since dark current counteracts the photogenerated current (or current density), it now progressively reduces the net photogenerated current as it (the dark current) increases. As a result, the efficiency (that is, the external quantum efficiency) of the solar cell decreases with increase in incident light intensity, because efficiency is current dependent.

- Our study has concluded that no universal optimum active layer thickness exists for nanoscale bulk heterojunction polymer-fullerene based solar cells, but propose that such optimal ALT is rather contextual to the fabrication settings like thin filming techniques, mixing ratio of donor and acceptor materials, type of solvent used, evaporation/drying techniques, nature of environment, as well as the generated film morphology and outcome competing processes. For our 1:1 ITO/PEDOT:PSS/P3HT:PCBM/Al devices the optimum performance active blend layer thickness was found to be 77.1 nm.

- Post fabrication thermal annealing of our 'air borne' ITO/PEDOT:PSS/P3HT:PCBM/Al devices was generally found to take place via two mechanisms in some of the regions of the device: The first process is that of decrease in the conductivity of the device as a result of heat driven dedoping (removal) of impurities like water vapour, oxygen and remnant solvent, which had gained occupancy in device imperfections dating back to the fabrication era. In the second stage, conductivity increases due to reordering and densification of the polymer chains.
- For optimisation purposes, it is important to establish control of the morphology of the organic photoactive nanoscale layers. Crystallization-induced phase separation, for example, by thermal annealing, has been found to direct the formation of a nanostructure

in the blends. Morphology studies elsewhere have shown that P3HT crystallization expels PCBM into the spherulitic interlamellar amorphous layers, where it encroaches to its miscibility limit. Above the solubility limit, PCBM aggregates start to form. The studies suggest that the crystallization of P3HT and encroachment of PCBM in interlamellar give rise to inter-connected donor and acceptor phases close to optimal bulk heterojunction structure. This suggests that the nanostructure formation in P3HT:PCBM blends is determined by the crystallization of P3HT. The fundamental mechanisms amounting to the origin of the morphology in P3HT:PCBM blends involve crystallization induced phase separation followed by the aggregation/crystallization of the second component.

8.2 Recommendations

- There is a need to find ways of lengthening the lifetimes of the excitons under conditions of study.
- C – V measurements could be taken to identify the role of traps and density of carrier.
- There is a need for interdisciplinary teamwork by both research scientists and architectural engineers in order to come up with new multifunctional active materials with higher photo-response and wider absorption band.
- Due to the need to gain deeper understanding of effects of barrier potentials and ideality factor on the performance of organic solar cells, we recommend investigations into the impact of processes such as annealing and active layer thickness variation on potential barrier and ideality factor in BHJ organic solar cells. This could include actual determination of the HOMO and LUMO of Donor/Acceptor (D/A) after annealing treatment at various temperatures.
- 3D determination of the D/A domains in the interconnected network
- Pump probe measurements could be taken to measure electron mobility (μ_e) and hole mobility (μ_h) for use in determining the type and nature of recombination mechanisms.
- Determination of the crystallization and diffusion processes during bicontinuous network formation
- Scanning tunneling microscopy measurements to map the 2D distribution of P3HT and PCBM domains on the aluminium (Al) and PEDOT:PSS interfaces to find out if it is the same or different and determine the different interfacial energies.

- Effects of imperfections, impurities and traps, for example, on charge injection at metal-polymer junctions of organic solar cell devices are suggested as further research candidates.
- We recommend the use of work from this study to establish a thorough understanding of the physics and operation of organic solar cells. The gained knowledge is recommended for use in ongoing research and in improving the architecture and performance (for example, power conversion efficiency) of the device.

9 Appendices

9.1 Appendix I

Excimer: In the main text, it has been given that excimers can form in polymer materials used in the making of solar cells and these are unwanted. An excimer is a short-lived dimeric or heterodimeric molecule formed from two monomers, at least one of which has the valence shell completely filled by electrons and the other is in an excited state. Excimers are often diatomic and are composed of two atoms or molecules that would not bond if both were in the ground state. The excited state may have been triggered by the dimer molecule absorbing light whose energy is equal to its HOMO-LUMO gap, which causes an electron in its HOMO to be excited to the LUMO. It is during this momentary excited state configuration that the dimer is referred to as an excimer. When the excimer returns to the ground state, its components dissociate and often repel each other. Since excimer formation is promoted by high bimolecular interaction, it is encouraged to source for use polymer material that is less prone to excimer formation.

9.2 Appendix II

Ultrasonic cleaning mechanism

Ultrasonic cleaning mechanism involves the rapid and complete removal of contaminants from objects immersed in a liquid impregnated with high frequency sound waves (ultrasound waves - which in effect are mechanical waves). These non-audible sound waves mimic a scrubbing brush action within the liquid (particularly at the interface between the liquid and a solid object) as a result of the conversion of their high frequency electrical energy by an implanted transducer, into ultrasonic energy (that is, high frequency sound energy) which enables the cleaning process since it is mechanical energy. Therefore, the piezoelectric effect is the basis of operation of the USB since this effect involves the conversion of either electrical or magnetic energy to mechanical energy (or vice versa) by a transducer. The cleaning power depends on the performance of the transducer. The ultrasonic energy spreads within the liquid and stirs up the rapid build-up and collapse of minute bubbles, the phenomenon of which is called cavitation. These bubbles rapidly increase in size until they implode against the surface of the immersed solid item awaiting surface cleaning. The implosion releases an enormous amount of energy, which scrubs and lifts

the contamination off the surface of the solid item like a substrate. As the bubbles implode and cavitation takes place, the cleaning solution rushes into the gap left by the bubble. Due to its effectiveness in cleaning even the innermost recesses of intricately shaped parts like hinges and box joints, ultrasonic cleaning method is employed in the cleaning of many precision and surgical instruments in industry and medicine. However, the USB process cannot be applied in the cleaning of soft solids like rubber.

9.3 Appendix III

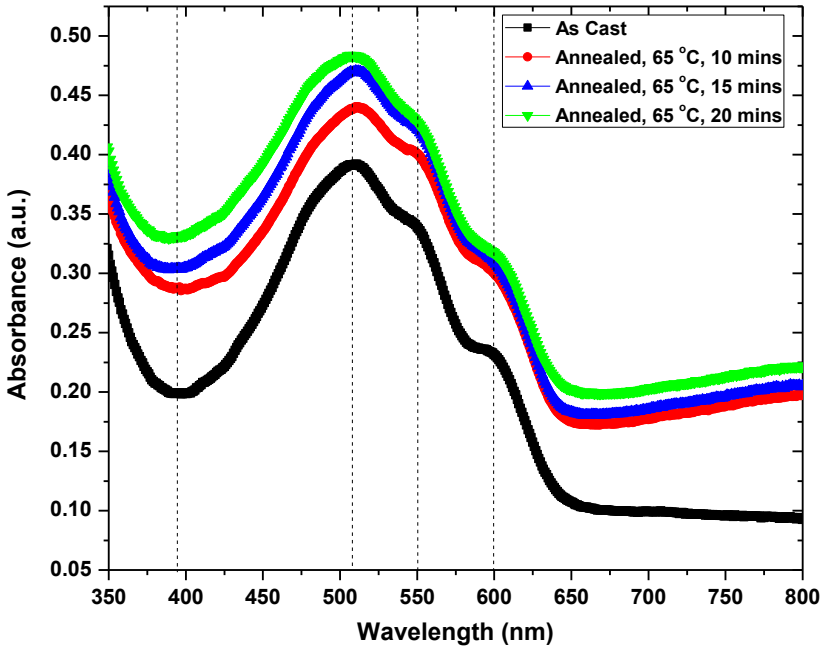

In the figure we show results for low temperature thermal annealing of the P3HT:PCBM based solar cells, at the same temperature, but at different time durations and note that absorbance increases with annealing times.

Publications and Conferences

Publication Papers under Review

1. Chiguvare Z, Jhamba L and Wamwangi D, *Charge injection at metal-polymer interfaces*: *an experimental investigation into why the efficiency of organic solar cells is low at high incident light intensities*

2 Jhamba L and Wamwangi D. *Opto-electrical mechanisms linking the threshold open circuit voltage at which the efficiency of polymer-fullerene solar cells starts to decrease with voltage regimes at metal-active layer junctions of P3HT:PCBM devices*

Conference attendance and presentations

1 Oral presentation of paper entitled "Influence of light intensity on the efficiency of organic solar cells." Paper presented at the November 3–8, 2013 in **Taiwan,** Haulien city under the Engineering Conferences International, New York, USA Program. The conference theme was: Carbon-Based Nano-Materials and Devices

2 Attended the 2012 annual South African Institute of Physics at the University of Pretoria from 9th July to 13th July 2012 and made an oral presentation of the paper entitled "Charge injection at metal-polymer interfaces."

Papers for Publication Submissions

1 Influence of active layer thickness on optical characteristics of spin-coated polymer-fullerene based BHJ solar cells of ITO/PEDOT:PSS/P3HT:PCBM/Al configuration

2 An analysis of transformations in the surface morphology of P3HT:PCBM film blend for differing film thicknesses (2D – treatment)

3 Effect of different active layer thicknesses on charge injection mechanisms at electrical contacts in the dark in ITO/PEDOT:PSS/P3HT:PCBM/Al devices

4 Influence of post-fabrication thermal annealing at different temperatures on the opto-electrical characteristics of P3HT:PCBM based solar cells

5 Dark and illuminated J(V) characteristics of ITO/PEDOT:PSS/P3HT:PCBM/Al devices due to thermal annealing at different temperatures